# Ferromagnetic Resonance Investigation of GaMnAs Nanometric Layers

Khashayar Khazen

Université Paris VI – Pierre et Marie Curie
Institut des NanoSciences de Paris

# THÈSE

pour l'obtention du diplôme de

## DOCTEUR DE L'UNIVERSITÉ PARIS VI

Spécialité : Physique des Solides

Présentée par

**Khashayar KHAZEN**

Sujet :

# Ferromagnetic Resonance Investigation of GaMnAs Nanometric Layers

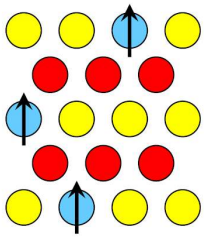

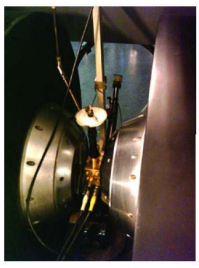

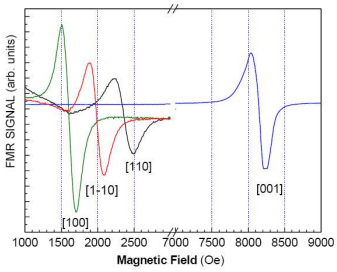


Soutenue le 11 juillet 2008 devant le jury composé de :

| | | |
|---|---|---|
| M. | Bret Heinrich | Rapporteur |
| M. | Tomas Jungwirth | Rapporteur |
| M. | Claude Chappert | Examinateur |
| M. | François Gendron | Examinateur |
| M. | Alain Mauger | Examinateur |
| M. | Hans Jurgen vonBardeleben | Directeur de thèse |

*To The Four Angels Of My Life:*

**Hossein, Fereshteh, Sanaz and Roxana**

*"I am among those who think that* ***science has great beauty****. A scientist in his laboratory is not only a technician: he is also a child placed before natural phenomena which impress him* ***like a fairy tale****."*

Marie Curie

# Abstract

This thesis is dedicated to the study of the magnetic properties of GaMnAs nanometric layers by the ferromagnetic resonance (FMR) technique.

Three series of samples have been studied to investigate independently the influence of the strain, the hole concentration and the Mn concentration on the magnetic properties of GaMnAs.

In the first series, the $Ga_{1-x}Mn_xAs$ samples with x=0.07, grown on GaAs (compressive strain) and GaInAs (tensile strain) substrates are studied. The results of magnetization, resistivity and Hall effect measurements are presented. From the FMR measurements the easy axes of magnetization and the type of magnetic anisotropy are determined. The angular variations of the FMR spectra are studied in detail and the g-factor, Curie temperature and the magnetocrystalline anisotropy constants are determined as function of temperature. Spin wave resonance were equally observed and interpreted. The observations are compared to the proposed phenomenological models and the spin stiffness and the exchange integral between the Mn ions are deduced.

The second study concerns a series of GaMnAs samples with the same Mn doping level of 7% atomic concentration in which the hole concentrations was varied via a hydrogen passivation technique. The hole concentrations are deduced from Hall effect measurements in high fields and low temperatures. The measured hole concentrations correspond to different conductivity regimes from insulating to impurity band and metallic regimes. The samples are characterized by SQUID magnetometry and resistivity measurements. The magnetization as a function of hole concentration is compared to the predictions of the RKKY model. ERDA measurements are performed to determine the concentration of hydrogen in the ferromagnetic sample with the lowest hole concentration. The domain structure of this samples is investigated by magneto-optical Kerr effect microscopy. The FMR spectra are analyzed in details and the hole concentration corresponding to the onset of ferromagnetism is estimated to $10^{19}cm^{-3}$. The g-factors depend on the hole concentration and temperature. The relation between the g-factors and the theoretically calculated hole polarization of the samples is presented. The anisotropy studies of the samples have provided the investigation of the magnetocrystalline anisotropy constants as a func-

tion of the hole concentration and the temperature. Their variations are compared to the theoretical models. The energy surfaces deduced from the measured magnetocrytalline anisotropy constants are calculated as a function of magnetization and applied field orientations and magnitudes.

The influence of increasing the doping level from 7% to 21% atomic concentration is studied in the third series of samples. Contrary to the theoretical predictions, the critical temperature is not increased above 180K. The FMR parameters are compared to those of standard GaMnAs sample doped with 7% atomic concentration of Mn. The reason for no further increase in $T_C$ is attributed to high level of magnetic compensation. The measurements are also compared to the theoretical predictions based on the mean field approximations.

The relaxation of the magnetization is studied as a function of strain, hole concentration, Mn concentration as well as temperature. The damping constants were found to be anisotropic. This anisotropy however depends strongly on the process whose contribution is dominant for a specific configuration of the system.

# Introduction

Magnetic semiconductors have been the object of numerous studies in the past decades. Both intrinsic magnetic materials such as EuO and GdN but also diluted magnetic semiconductors (DMS) where the magnetism is introduced by doping have been investigated. The advent of spintronics where the manipulation of spin polarized currents is the basic phenomenon has stimulated the search for ferromagnetic semiconductors and the discovery of long range ferromagnetism in p-type manganese doped GaAs by Ohno et al in 1995 has initiated a worldwide research program on this material.

In line with the requirements for spintronics applications the study of these materials concerns mainly thin epitaxial layers with typical thickness of a few nanometers. This is at the same time an advantage and a challenge: modern growth techniques for thin layers such as low temperature molecular beam epitaxy (LTMBE) allow the doping of DMS semiconductors at concentrations largely above their high temperature equilibrium solubility but the small thickness of them introduces also an increasing dependence on the interface quality for the performance of these materials in multilayer structures. In this context heteroepitaxies of metals on semiconductors such as Fe on (100)GaAs have turned out to be particular challenging. Very recently, all semiconductor based GaMnAs trilayers have shown encouraging high values of tunnelling magnetoresistance.

In GaMnAs the ferromagnetism is carrier (hole) induced and occurs for Mn concentrations above x=0.01. In spite of being a diluted magnetic semiconductor most of its basic properties can be well modelled in the framework of the kinetic exchange mean field theory. The GaMnAs system is distinctly different from metallic ferromagnets such as Co and Fe as in GaMnAs the demagnetization fields are much smaller than the magnetocrystalline anisotropy fields. Further, the spin orbit interaction is much stronger in this p-type semiconductor with metallic conductivity. All anisotropies are related to the particular valence band structure of GaAs which is very sensitive to strain and applied magnetic fields. In addition the Fermi level position, which can be varied quite largely, will further modify the basic magnetic properties.

A major drawback of the GaMnAs system is its relatively low Curie tempera-

ture which up to now seems to be limited to about 200K. However this is not a fundamental limit as various theoretical works have predicted that room temperature ferromagnetism should be achievable for a Mn doping concentration of x=0.10 and a carrier concentration of $10^{21} cm^{-3}$. Most of the past studies have focussed on lower (x=0.05..0.07) Mn doped layers as they can be easily and reproducibly grown by LT-MBE. More recently, an important progress in the growth has been made and epitaxial layers with a doping concentration of x=0.21 free of precipitates have been successfully grown. In this work we have focussed on the magnetic properties of nanometric single layers grown by LTMBE on GaAs and GaInAs substrates. As we have outlined above, this system presents a number of interesting problems concerning the influence of strain, hole concentration and magnetic ion concentration on the magnetic properties. It presents also a material challenge for doping levels above x=0.05. These aspects have been investigated in this thesis by the ferromagnetic resonance spectroscopy which has been our main experimental technique. This technique is particularly well adapted to the study of nanometric layers due its high sensitivity, its excellent energy resolution and the rich information which can be obtained from an analysis of the resonance fields and lineshapes. It allows further to study the dynamics of the magnetization by a linewidth analysis via the determination of the so called Gilbert damping factor.

It should be mentioned that the particular non equilibrium growth of these highly doped layers gives rise to high concentration of point defects which can not be neglected in the interpretation of the results. Typical problems are the simultaneous introduction of Mn on the normal substitutional Ga site and on interstitial sites where their magnetic and electrical properties are different. Further, arsenic antisite defects which are double donors can modify strongly the electrical compensation in as grown layers. Post growth annealing to improve the magnetic properties has thus become a standard and unavoidable procedure for these layers. They must however be well controlled in order to avoid the formation of Mn precipitates.

In the course of this work it turned out to be necessary to perform additional measurements: static magnetization measurements by SQUID have been systematically performed on all layers, the problem of interstitial Mn ions has been addressed by channelling RBS investigations. The samples with extremely low carrier concentrations, leading to a paramagnetic state, have been analyzed by electron paramagnetic resonance.

This thesis is composed of six chapters:

In the first chapter I present a short overview of some fundamental concepts in different ferromagnetic materials (metals, molecular crystals and semiconductors) in the context of spintronics and I summarize the basic properties of GaAs and the Mn dopant. A brief description of the main theoretical approaches for the carrier induced ferromagnetism is also given.

In the second chapter I outline the main concepts of ferromagnetic resonance

spectroscopy. This technique has a long history in the study of metallic bulk and metallic thin layer samples but its application to ferromagnetic semiconductors, which introduces new aspects, is a relatively recent development linked to the study of the GaMnAs system. I further present our experimental set-up composed of two X-band and Q-band variable temperature spectrometers. In the next chapters I present the principal experimental results which are regrouped in three themes: the influence of the strain in the GaMnAs layers on the magnetic properties is presented in chapter III. We have studied two model systems GaMnAs on GaAs and GaMnAs on GaInAs which represent the two cases of compressive and tensile strained layers respectively.

In the next chapter IV, I present the results concerning the influence of the hole concentration on the magnetic properties. We have been able to vary this parameter by co-doping a given layer by various amounts of hydrogen. In this way the hole concentration could be varied over several orders of magnitude from $10^{21}cm^{-3}$ to below $10^{18}cm^{-3}$. The results obtained are compared to the predictions of the main field theory. This study has been done in collaboration with another laboratory (LPN/Marcoussis) which has performed the growth, hydrogenation and the structural and electrical analysis of these layers. We have further used another technique (elastic recoil detection analysis) to characterize the hydrogen content in these layers.

In chapter V we present the results obtained for very highly doped layers (up to x=0.21), which had been supplied by Prof.Tanaka (University of Tokyo). The interest of these layers is to shift the Curie temperature above the previous limit of 180K. These layers have been investigated in addition to FMR spectroscopy by Rutherford Backscattering channelling in order to analyze the contribution of interstitial Mn ions.

In the last chapter VI we have studied the dynamic properties of the magnetization via a determination of the Gilbert damping factor. Such measurements have been performed for various type of samples to investigate the influence of strain and hole concentration on the magnetization relaxation.

The main results obtained are summarized in the general conclusion.

# Contents

# 1

# Magnetic semiconductors and Spintronics

After the discovery of transistors in 1925/1947 and the first revolution in electronic technology, research in electronic technology had three objectives: higher performance and faster data processing, smaller devices and lower energy consumption. While the giant electronics engineering and technology is continuing its own way producing the devices which are being optimized for the requirements and the desires of the market, the researchers in their laboratories have always asked until where it can continue? How far they can be fast, small and economical. Today microelectronics seems to approach these limits. The integrated circuits in which more than 1 million transistors are integrated in $1mm^2$ and flash memories of $1.5cm^2$ with 16GB capacity are approaching their final limits due to the noise and breakdown of dielectrics resulting from their small size prevents the companies to satisfy their market.

One of the alternative options is the application of another degree of freedom, the spin of the carriers. Already spintronic plates are used in the field of mass-storage devices and have led to compressing massive amounts of data into a small area, at approximately one trillion bits per square inch ($1.5 Gbit/mm^2$). The storage density of hard drives follows an exponential growth curve. The doubling period for the areal density of information storage is twelve months.

Recently IBM scientists have announced a next-generation nonvolatile memory dubbed "RaceTrack" which is expected to initially replace flash memory and eventually mechanical magnetic hard-disk drives. The prototype encodes bits into the magnetic domain walls along the length of a silicon nanowire, also known as RaceTrack. This method allows "massless motion" to move the magnetic domain walls along the silicon nanowire for the storage and retrieval of information. Such drives will be able to store data nearing 1 Terabytes on a single 3.5inch (8.9cm) drive.

The most successful spintronic device to date is the spin valve, due to its widespread application in disk read/write heads. This device includes a layered structure of thin

films of magnetic materials in which the electrical resistance depends on the applied magnetic field direction. It is based on the giant magnetoresistance effect. In a spin valve, one of the ferromagnetic layers has its magnetization direction which remains fixed and the magnetization of the other ferromagnetic layer is "free" to rotate with the application of a magnetic field. When the magnetic field aligns the free layer and the pinned layer magnetization vectors, the electrical resistance of the device is at its minimum. When the magnetic field causes the free layer magnetization vector to rotate in a direction antiparallel to the pinned layer magnetization vector, the electrical resistance of the device increases due to spin-dependent scattering.

Devices have been demonstrated with GMR ratios as high as 200% with typical values greater than 10%. This is a vast improvement (hence the term "giant") over the anisotropic magnetoresistance effect in single layer materials which is usually less than 3%.

Future applications may include a spin-based transistor, which requires the development of magnetic semiconductors exhibiting room temperature ferromagnetism. The operation of MRAM or magnetic random access memory is also based on spintronic principles. Spintronics-based non-volatile 3D optical data storage has also been proposed.

The ad-mixture of the nano-scale science (nanoscience) and the spintronics, in which the performance of the related effects such as TMR and GMR are enhanced, not only have increased the technological interests for investing in this field, but also have attracted the attention of many fundamental research groups. In the following sections we will discuss the fundamental concepts and requirements of this new field together with the choice of the materials. Diluted magnetic semiconductors and particular case of GaMnAs will be presented in more detail as a good candidate.

### *1.1 Fundamental concept*

Spintronics or magic-electronics was officially born after the discovery of the giant magneto-resistance (GMR) effect by Albert Fert and Peter Grunberg [1,2] in 1988 via independent studies. During their studies on Fe/Cr/Fe super lattices and tri-layers (respectively) they observed that the resistivity for the electric current from one layer to other depends on the relative alignment of the magnetization in each Fe layer ($\Delta R \approx 80\%$). While this effect concerned ferromagnetic metallic layers separated by a non-magnetic metallic layer, a similar effect was observed in replacing the non-magnetic layer by an insulating layer. This tunneling magnetoresistance (TMR) effect had been discovered even earlier than GMR by Michel Jullier in 1975 [3] in Fe/MgO/Fe. The relative resistivity measured by Jullier was about $\Delta$ R $\approx$ 16 % which was too small for applications.

Just after these two discoveries the researchers discovered the ability to apply the coupling between the electric state of the charge (information) carriers with their

magnetic state (the additional degree of freedom) in the conventional electronic technology. This gave them the perspective of increasing the performance of the speed of information processing by applying both the charge and spin state of the information carriers (compared to the pure charge state in electronics and computer since with 0 and 1 bit states). Moreover it gave them the perspective of the unification of the memory and processing units for smaller sizes since the magnetism is the base of information storage and charge is the base of its processing.

The coupling between the magnetic moments and the charge carriers is provided by the kinetic exchange interaction. This coupling is then the key feature for spintronics applications. In spintronics this interaction is crucial from two points of view. First of all for generating a spin polarized current can be achieved by coupling between the spins of the carrier and the magnetic moments in the material, in this case the exchange coupling will align the spin of the carriers parallel to each other. Second, this spin polarized current can be used to measure the magnetization state of a layer via the magnetoresistance effect. In this latter case, again it is the exchange interaction which determine the resistivity of the material. This is the basic process in GMR and TMR based devices.

## *1.2 Concerning systems and materials*

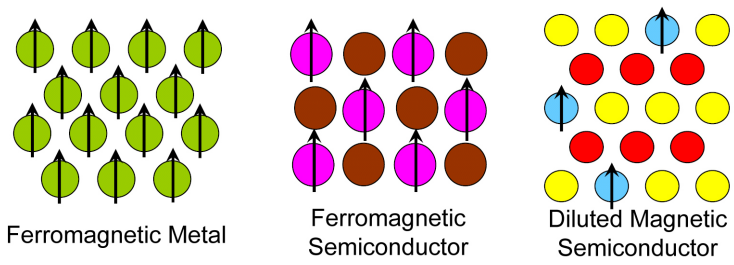


**Figure 1.1:** Schema concerning different materials which can be applied in spintronics

The use of the spin state of the carriers requires materials in which the charge and spin degree of freedom of carriers are strongly coupled. This feature is present in the ferromagnetic materials in which the exchange interaction have large values. Ferromagnets are the basic systems for the so-called magneto-electronics technology. They can be categorized into different categories depending on their potential use in spintronic devices.

### 1.2.1 Ferromagnetic metals (FM)

The ferromagnetic metal systems such as the Fe, Co and Ni in sophisticated configurations as Multilayers to clusters where among the first studied systems in spintronics. The transition metals, are constitute of 100% magnetic moments (fig.1.1). The ferromagnetic order in such materials is a carrier mediated order where the 3d electrons are delocalised and provide the magnetic state. The spin-orbit coupling in these materials is quenched because of the large crystal field contribution. These materials are already used for their high concutivity in addition to their high Curie temperatures. The application of GMR, TMR, AMR (anisotropic magnetoresistance), spin-torque, spin valve and spin pumping effects based on the single and multi layer and nanostructures have led to the production of new devices such as read/write magnetic heads, magnetic memory tripes, etc.

However their difference to the semiconductors-based electronics complicates the integration of their mono-crystalline thin films in standard electronic systems.

### 1.2.2 Ferromagnetic molecules

The members of this family are the complex molecules (i.g. [4]). Although they are expected very promising for the application in magnetic-electronics because of their special magnetic properties but they are not considered as as compatible material with the recent electronic generation. The complicated electronic structure and conductivity process together with their structural instability require to be more fundamental studies before the application can be achieved.

### 1.2.3 Ferromagnetic semiconductors (FS)

This given name to this category may be somewhat misleading since it can be mixed-up with the next group. It refers to semiconductors in which, at least one element constituting the unit cell of the material is magnetic (fig.1.1). Materials such as EuO and GdN shows ferromagnetic order below their Curie temperature which is usually low due to the weak exchange integral between the localized electrons of the f-shell that builds the magnetic moment and the d-electrons in the conduction band. These materials were studied strongly in 1970's and then abandoned for a certain time. The arising interest toward these materials can be seen more and more in recent years after the appearance of spintronics domain [5, 6]. The difficult growth process of these materials as single crystal thin films on the standard substrate, the incapability of codoping them because of the large density of intrinsic defects their low Curie temperature are among the points which should be solved before their application in spintronics domain.

Another interaction which leads to further spintronic functionalities in the spin-orbit (S-O) interaction. This interaction is weak in the metallic systems due to the

domination of the crystal field, whereas it is large in the case of semiconductors which increases the interest for their application.

### 1.2.4 Diluted magnetic semiconductors (DMS)

A very interesting family of magnetic materials can be obtained from the semiconductors already applied in micro-electronics. The largely studied materials such as Si, GaAs and GaN are among the semiconductors which are widely used not only for their electrical properties (as processing unit devices) but also for their opto-electronic properties (LED).

Of course these performing materials are not intrinsically magnetic. In order to introduce magnetic properties to these systems they have to be doped by magnetic ions such as the transition metal ions. In this case some of these materials present ferromagnetism (with different $T_C$) and become useful in spintronics.

The advantages of using semiconductor systems instead of the metallic systems lies in the capability of the manipulation of the magnetic state of these materials via optical, electrical and structural control (this case will be discussed in more details in following sections). The longer mean free path of the spin-polarized carriers in these materials and the stronger spin-orbit interaction are other advantages. Also the unification of the processing and storage units in information is made possible in their application.

The very important and major drawback of these materials is their low $T_C$. At present time, the critical temperatures are still far below the room temperature and prevent their direct application.

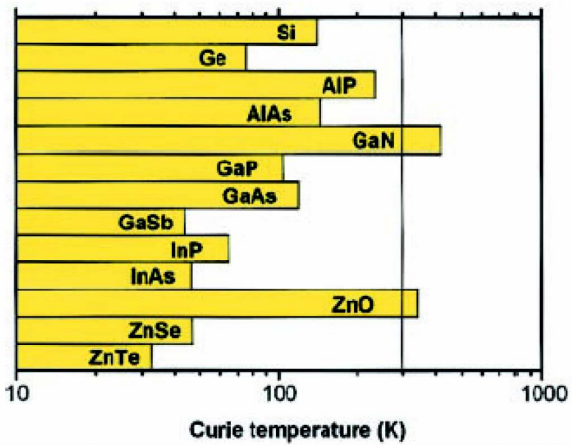


**Figure 1.2:** Predicted $T_C$ for different semiconductors doped by 5% of manganese and for hole concentration (p-type) of $\approx 10^{20} cm^{-3}$ based on mean field approximation calculations [7]

Dietl et al. in a highly cited article [7], reported a theoretical study of the

magnetic properties of different p-type semiconductors doped by manganese(fig.1.2). They predicted from the mean field (MF) theory, the Curie temperatures above the room temperature for the two cases of GaN and ZnO sytems.

However, the experiments, up to this date, have not yet confirmed these theoretical predictions. The ZnO, for example, has not shown even intrinsic ferromagnetic order. This feature is attributed to the high density of native defects which prevents the growth of p-type conductive samples. The magnetic freezing in Mn-doped ZnO (and more or less other II-VI family members) is found to be the antiferromagnetic or spin-glass order (cf. [8]). The solubility of transition metal ions in group IV semiconductors such as Si and Ge is very small. However, recent reports on the injection of the spin-polarized current into Si [9] have attracted other groups to study the magnetic properties of implanted Si samples [10].

So far, the only III-V DMS members which have shown high single-phase intrinsic ferromagnetism are GaMnAs and InMnAs. The former material has been the object of numerous studies, just as the GaAs host material. The very high compatibility of this material with the electronic technology, in addition to its Curie temperature which has increased from its first observation at T$\approx$ $50K$ ( [11]) to T=180K in recent samples ( [13]) in only 10 years, both have motivated us to investigate its magnetic properties and the $T_C$ related parameters. We were interested both in its fundamental properties and the material aspects which would allow to push the critical temperature up to room temperature.

### *1.3 DMS hosted by III-V semiconductors*

The "III-V group" materials are already well integrated in electronic technology. In addition to this fact, the intrinsically large spin-orbit interaction in III-Sb and III-As valence-band states makes these hosts ideal candidates for exploring various spintronic issues such as optical control of magnetization and spin transport properties.

Transporting the spin information between layers, in GMR or TMR based devices, is sensitive to spin-coherence times in the system. While the spin-orbit interaction plays an important role in some specific spintronic applications the strong spin-orbit coupling reduces the spin coherence length in DMSs. Nevertheless functional spintronic trilayer devices have been built with (Ga,Mn)As-based tunneling structures where large MR effects have been measured.

### *1.4 GaMnAs*

The GaMnAs for reasons indicated in previous sections and the ones which will be shown in future was chosen as the main subject of this thesis. In this section as

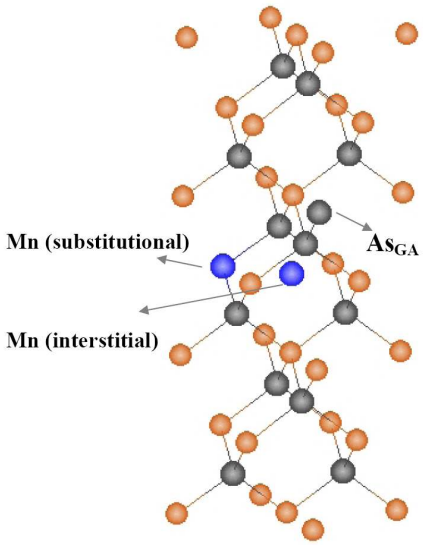


**Figure 1.3:** Crystalline stucture of host GaAs material and the sites occupied by Mn impurities

we focus on the aspects which are needed to interpret our results. For more details we invite the reader to consult the review article of Tomas Jungwirth et al. (cf. [14]) which contains an almost complete bibliography on this system.

### 1.4.1 GaAs, the host material (structural and electrical properties)

GaAs is one of the most largely studied semiconductors because of its very particular properties which can be found nowadays in many electronics and semiconductors handbooks. It is used to make devices such as microwave frequency integrated circuits (i.e. MMICs), infrared light-emitting diodes, laser diodes and solar cells.

The crystal structure of this material is shown in fig. 1.3. It is a Zinc-blende structure with four Ga(or As) atoms per lattice. The lattice parameter of stoichiometric material is $a = 5.653A°$. Usual techniques used for growing epitaxial GaAs layers include Molecular beam epitaxy (MBE), Low pressure epitaxy (LPE), VPE and Molecular Chemical Vapor Deposition (MOCVD). In its epitaxial form it contains both donor and acceptor impurities and the relative concentration of these impurities determine the p or n-type of GaAs.

GaAs is a direct band gap semiconductor with gap energy of 1.519 eV at $T \approx 0K$ which decreases as a function of temperature. The As has the higher contribution to the hybrid valence band. On the high pressure this band gap will change also into an indirect band gap.

### 1.4.2 Mn impurity centers

All the electrons in the GaAs are hybridized and shared between the Ga and As atoms. In order to give magnetic properties to GaAs one practical way is to dope it with magnetic ions, specially the 3d transition metals. There are different elements which can be used, among which, the manganese has particular features that have made it a promising candidate.

In a GaAs matrix, the Ga ions have the electrical configuration of $3d^{10}4s^24p^1$ and As ions the configuration $3d^{10}4s^24p^3$. When a Mn ion is substitudet for Ga, it takes the configuration Mn $3d^{10}4s^2$. The $Mn^{2+}$ ion together with a hole moderately bound to it, forms a neutral $A^0(d^5+\text{hole})$ acceptor. Its 5 electron in d-shell will occupy three bonding sp-d $t_{2g}$ state of $3d_{xy}$,$3d_{yz}$ and $3d_{xz}$ and two antibonding states of $3d_{x^2-y^2}$ and $3d_{z^2}$ which are split by the tetrahedral crystal field. All five electrons, after the Hund's rule, have the same spin orientation and give rise to ${}^6S$ ground state. The hole introduced by this Mn ion will then occupy one of the anti-bonding state of $3d_{xy}$,$3d_{yz}$ and $3d_{xz}$ above the Fermi level which have the a dominant As$4p$ character. The binding energy of this hole is $E_B$=112.4 meV as determined from infra-red spectroscopy [15]. Increasing the Fermi level (for example by applying a positive voltage bias as in STM experiment [16–18]) delocalizes the hole and the Mn acceptor will be charged negatively; $A^-$. This is one of the particularities of manganese in GaAs host matrix that, independent of the Fermi level position, the Mn will retain its 2+ charge state with S=5/2, contradictory to the case of GaN where the manganese can be either in the $Mn^{2+}$ or $Mn^{3+}$ state [19].

The five electrons in the quasi-localize d-levels of Mn, each has a spin s=1/2, so the Mn ion provide the material with a total spin of 5/2.

The filled Mn d-level is deep in the valence band and the empty d-level is above the Fermi level and high in the conduction band, The repulsion of states with the same spin polarization pushes the energy of valence-band states up relative to the energy of valence-band states which is considered as the hybridization of the $d$ and $sp$ levels. This results in an antiferromagnetic coupling between valence-band states and local Mn spins.

### 1.4.3 Mn solubility and layer growth techniques

The case explained above concerned an individual Mn ion in the GaAs matrix. Evidently, this single ion renders the material paramagnetic but can not provide a ferromagnetic order in the system. To induce a ferromagnetic state manganese concentrations x>0.01 have to be introduced [20]. When the concentration of the Mn increases the impurity state above the valence band transforms into an impurity band (Mott transition). Again the same picture of hybridization which couples the holes in the impurity band and the localized electrons is applicable in this regime.

These interactions give rise to :

1. A direct antiferromagnetic interaction between the itinerant holes and the localized Mn magnetic moments
2. An indirect ferromagnetic interaction between the Mn magnetic moments resulting from their coupling to the holes.

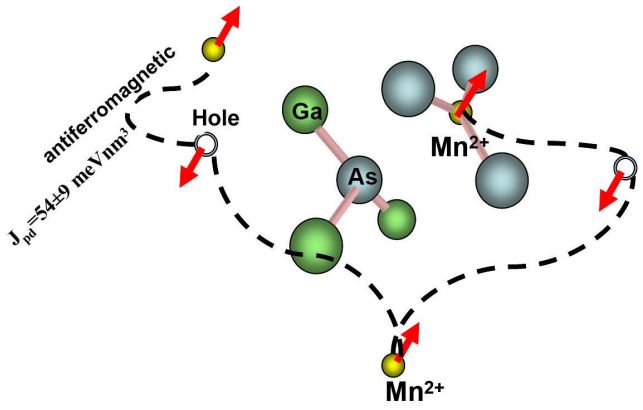


**Figure 1.4:** Schematic presentation of two coupled ordered sub-systems in GaMnAs

Note that in low doping regime the holes are weakly bound to the Mn acceptors, and a long range ferromagnetic order can not be mediated between the manganese ions.

The solubility of Mn in the GaAs matrix, under normal high temperature ($600°C$)in growth conditions is less than 0.1%. Therefore one challenge for growing the ferromagnetic GaMnAs layers was to find a suitable technique to overcome this limitation. This has been achieved with low temperature molecular beam epitaxy (LT-MBE) which has become the standard technique to grow highly doped semiconductor layers. Ohno et al. [21] in 1992 were the first group to grow the InMnAs layers with Curie temperature $\approx 7K$. They showed that growing the layers via low temperature ($\approx 250°C$) molecular beam epitaxy (LT-MBE) provides high quality monocrystalline layers in which one can increase the doping level up to 1%. Applying the growth process at low temperatures prevents the formation of MnAs segregations [22].

By this technique, the researchers nowadays grow standard samples with up to 5% of Mn in substitutional sites. Recently the need for higher Curie temperature have pushed the researchers to further increase the manganse concentration over 10%. The detailed study of these samples is presented in chapter 5 and we just note

here that while the LT-MBE is a well known technique to grown thinlayers (from 2nm to micron scales) with about 5-7% of doped Mn, it fails for heavily doped samples. At high concentration of Mn, the tendency of the manganese to bond to arsenic and precipitate as MnAs clusters increases. One solution was found very recently by Ohya et al. (cf. [23]), who suceeded in increasing the doping concentration up to $x = 0.21$ by lowering the growth temperature and decreasing the layer thicknesses to 10-20nm (more details in chapter. 5). However LT-MBE technique is followed by the creation of new types of undesirable defects in the films.

### 1.4.4 Point defects

Two major types of defects are introduced by applying LT-MBE growth for highly doped Mn concentrations:

#### *1.4.4.1 As antisites*

The most frequent defect is the arsenic antisite. Its concentration strongly increases as the growth temperature decreases. The As ions which occupy the Ga sites are double donor with levels at $E_C = -0.75eV$ and $E_C = -1.0eV$. Therefore each $\mathrm{As}_{Ga}$ ion compensates two holes from the valence band.

These defects are stable up to $T \approx 450°C$, a temperature higher than the growth temperatures [24]. So practically no post-growth temperature treatment can diminish their concentration. However, the application of $As_2$ dimers as the source of MBE growth are found to decrease the probability of the formation of As antisites [25]. Recently Furdyna et al also have proposed the co-doping of the sample with Si in order to decrease the $As_{Ga}$ concentration. Myers et al. [26] used the control of the As:Ga flux ratio to decrease the concentration of this defect.

The typical concentration of this defect for samples with Mn concentration of $x \approx 0.05$ (growth temperature $\approx 250°C$) is estimated to $\approx 10^{19}\mathrm{cm}^{-3}$ [27].

The presence of $As_{Ga}$ defects leads also to a significant expansion of the lattice. According to full-potential supercell calculations (Masek and Maca [28]) they contribute to the variation in lattice constant with a factor $0.46 \cdot x_{As_{Ga}}$.

#### *1.4.4.2 Interstitial Mn*

The high doping level of Mn leads to another crucial undesirable defect: Mn interstitials. They are double donors and can occupy three possible lattice sites (in principle), two of which are the interstitial $T_D$ sites surrounded either by the Ga or As. Total energy calculations predict that these positions are energetically equivalent. The third one is the hexagonal interstitial site, which is less probable since the formation energy is higher. The particle induced X-ray emission (PIXE) experiments performed by Yu et al. [29] have been able to evidence the preferential occupation

of tetrahedral sites by these defects. These measurements were performed in lower doped samples. On the contrary no experimental results are available for highly doped samples. The minority spin d-electrons of interstitial Mn ions form a weakly dispersive band $\approx 0.5eV$ below the Fermi energy. This case is less treated both experimentally and theoretically in the literature [30].

Since the $Mn_{int}$ donors are positively charged, as a result of the high Coulomb interactions, they tend to form pair defects with substitutional manganeses impurities. The superexchange interaction between these ions then result in an antiferromagnetic coupling which seems to be effective even at temperature of 300K.

Apart from this magnetic compensation, because of their charge state each $Mn_{int}$ compensates two holes from the system. It is thus important to control these defects which degrades considerably the magnetic properties of the GaMnAs films.

### 1.4.5 Post growth annealing

The $Mn_{int}$ ions are rather mobile defects with an activation energy of E=1.4eV. It is thus possible to out-diffuse them by appropriate annealing treatments. The details of the annealing process have been always a matter of experience and different groups have reported their particular method of annealing. This includes the annealing in the presence of a capping layers such as GaAs [23] or As [31] as well as in different atmospheres such as vacuum, oxygen, nitrogen and air. Also the temperature and duration of the annealing is an important factor to be optimized. This feature can be controlled by in-situ electrical resistivity measurements. The resistivity tends to decrease as the interstitial manganese are removed from the matrix. Some early works on the annealing optimization showed the initial decrease in the resistivity and a further increase as a function of the duration of the process [32] where as the more recent studies have shown that the resistivity tends to saturate after a certain time and remains constant for longer durations [13].

Previous studies such as resistance-monitored annealing studies combined with Auger surface analysis concluded that the the interstitial Mn ions migrate toward the free surface, but one can not exclude the diffusion to the interface which would result in a symmetric gradient of the Mn profile following the annealing process. Such a diffusion model has been applied by Furdyna et al. In following chapters (cf. section 5.3) we present an RBS channeling study of the Mn concentration profile in an annealed layer.

The increase in the conductivity of the samples after the annealing treatment, shows well their out-diffusion from the matrix. Three possibilities have been invoked to explain the annealing effects and they are still matter to debate. One possibility is the formation of the MnAs clusters which should be either ferromagnetic or superparamagnetic (if the size of the clusters is very small). Nevertheless no associated FMR spectrum justifying this model have been reported. The other possibility is the

formation of metallic Mn clusters which are diamagnetic and might be observed at the surface via XPS measurements . Both these possibilities are favored if a capping layer is used or the annealing is done in a non-oxygen containing atmosphere.

A third case arises if the annealing performed under oxygen. In this case the Mn ions which reach the surface will be oxidized and form different MnO compounds which can be anti/ferromagnetic depending on the stoichiometry of the $Mn_xO_y$ compound.

In all cases the saturation of the resistivity with time, indicates that the Mn out-diffusion has saturated. To further improve the annealing, multiple annealings in oxygen with surface layer etching have been proposed ( [13]).

Most authors have chosen annealing temperatures close to $200°C$. However for heavily doped layers, Ohya et al. perform it at lower temperature ($= 140°C$) for longer durations. The heavily doped layers they have studied are very sensitive to temperature as MnAs precipitation can easily occur.

### 1.4.6 Magnetic phase and ordering

The magnetic phase and the interactions which give rise to the ordering in GaMnAs depend strongly on the conductivity regime (Hole concentration) and Mn (magnetic moments)concentration. It has been shown qualitatively how a carrier mediated ferromagnetic order in this material can be formed and how it can be explained via the bi-ordered system conception.

Studying the system more quantitatively, requires the use of different the theoretical models to interpret the quantities deduced from the measurements. For this the different parameters and interactions supporting and describing fundamentally the system such as those determining the magnetic order must be known.

In GaMnAs, because of the DMS nature of the magnetic moments, one can neglect the dipole-dipole interactions, which leaves the electron spin, the repulsive Coulomb interactions and the Pauli exclusion principle , as the main parameters determining the magnetic order.

There are different type of interactions and associated models which were used to explain the magnetic ordering in different systems:

For spins carried by itinerant electrons, exchange interactions are provided through Stoner's itinerant exchange [33] which is responsible for the magnetic ordering. The type of the order in this case depends on the system and it is not always the ferromagnetic order which is favored. The instability of Stoner is $U\chi^\circ(q) = 1$, where $\chi^\circ(q)$ is the susceptibility of the gas of free carriers in the Fourier space. the $\vec{q}$ vector of the magnetic structure is the one which maximize the $\chi^\circ(q)$ by satisfying the condition : $U\chi^\circ(q) \geq 1$. Because the kinetic (band) energy is minimized by double occupation of each Bloch state, the Stoner ferromagnetic instability occurs in systems with a large density of states at the Fermi energy. Nevertheless, this model

does not apply to GaMnAs (or in general for DMS sytems) where the magnetic moments have local character and the Fermi level is much smaller than in metals.

Heisenberg direct exchange [33] between two local spins originates from the Pauli principle. Kramers superexchange interaction [34] applies to local moments that are separated by a nonmagnetic atom. In a crystal environment, an electron can be transferred from the nonmagnetic atom to an empty shell of the magnetic atom and interact, via direct exchange, with electrons forming its local moment. The nonmagnetic atom is polarized and is coupled via direct exchange with all its magnetic neighbors. The resulting superexchange interaction between local moments depends on the relative sign of the two direct-exchange interactions [35,36]. In GaMnAs this interaction gives rise to an antiferromagnetic order between the $Mn_{Ga}$ first neighbors (it is one of the major competing interactions and in low hole concentrations or high Mn concentrations become a dominant one).

Zener's double-exchange mechanism [37] also assumes an intermediate nonmagnetic atom. In its usual form, this interaction occurs when the magnetic atoms have a different number of electrons in the magnetic shell and hopping through the intermediate nonmagnetic atom involves magnetic-shell electrons. Combined with the Hund's rule, double exchange couples magnetic moments ferromagnetically. Parallel spin alignment is favored because it increases the hopping probability and therefore decreases the kinetic energy of spin-polarized electrons. For the case of manganese ions for example, this interaction is efficient if the matrix would contain both $Mn^{2+}$and $Mn^{3+}$ acceptors, which is usual case in host materials such as GaN. For this material, it was discussed that the substitutional Mn acceptors have the particularity to retain their "2+" charge state for all system states. Despite of this fact a similar version of double exchange is valid for the case of GaMnAs in the low Mn concentrations or low carrier densities where Mn acceptor states form an impurity band with mixed spd character. In this picture electrical conduction and Mn-Mn exchange coupling are both realized through hopping within an impurity band. Because of the resemblance of this picture to the double exchange interaction it is referred to by this termology.

Zener's kinetic-exchange [37] or indirect-exchange interaction is the model which is used to describe the ferromagnetism in systems with local, usually d-shell or f-shell, moments whose coupling is mediated by s or p-band itinerant carriers. The local moments can have a ferromagnetic direct exchange interaction with band electrons on the same site and/or an antiferromagnetic interaction due to hybridization between the local moment and band electrons on neighboring sites [38,39]. Polarization of band electrons due to the interaction at one site is propagated to neighboring sites.

When the coupling is weak, as in the case of weak band carrier polarization, the situation is described by RKKY theory, which was originally applied to carrier-mediated indirect coupling between local d-shell moments in metals [37,40,41]. The

range of this interaction is limited by the mean free path of the holes. Interactions between separate local moments can be either ferromagnetic or antiferromagnetic and tend to vary in space at the length scale of the itinerant band's Fermi wavelength. Unlike the double-exchange case, magnetic order in this case does not lead to a significant change in the width of the conducting band.

There is no sharp distinction between impurity-band double-exchange and kinetic-exchange interactions; the former is simply a strong-coupling, narrow-band limit of the latter [14].

Note that the appropriate model for long range ferromagnetic order in GaMnAs, depends strongly on the interplay of all these interactions and their competition as a function of crucial parameters such as the carrier and magnetic moment concentrations. The number of local moments participating in the ordered state and the number of holes may differ from the number of subtitutional Mn impurities in the system due to the presence of charge and moment-compensating defects. A qualitative overview on the magnetic ordering in different regimes considering the experimental investigations reveals [14] different conduction regimes with their relevant exchange interaction models:

- For very weak doping levels the average distance between Mn impurities $r_c = (3/4\pi N_{Mn})^{1/3}$ is much larger than the impurity effective Bohr radius $a* = \epsilon\hbar/m * e^2$, where $N_{Mn} = 4x/a^3$ is the number of Mn impurities per unit volume, $\epsilon$ and $a$ are the semiconductor dielectric function and lattice constant respectively, and m* is the effective mass near the top of the valence band. In this case the spacial distance between the Mn ions are great and the holes remain localized around the isolated ions. Here even in insulating limit a ferromagnetic exchange interaction between Mn local moments mediated via thermally activated band carriers was proposed [42].However, experiments [43] measured it as a paramagnet with g=2.77 from the EPR experiments.

- Experimentally, ferromagnetism in (Ga,M))As is observed when Mn doping reaches approximately 1% [44, 45] for a system close to the Mott insulator-to-metal transition. In low Mn (/hole) concentrations, or in highly compensated GaMnAs systems (in the limit where the overlap of intermediate bound holes (the impurity states) creates an impurity band), i.e. in semi-insulating regime, the localization length of impurity-band states is extended to a degree that allows them to mediate ferromagnetic exchange interaction between Mn moments, even though the moments are dilute. As mentioned above because of the hopping nature of conduction and the presence of a impurity band with a mixed spd characteristic the interaction is referred to as the double exchange interaction.

- At even higher Mn concentrations, the impurity band gradually merges with

the valence band [46] and impurity states become delocalized. In these degenerate ferromagnetic semiconductors, the proposed model describing the coupling between Mn local moments is the p-d kinetic-exchange mechanism [47–51]. Note that this model is proposed for an upper limits of with x≈0.05 and hole concentrations≈$4^{20}$. In higher Mn concentrations the higher probability of the Mn acceptors to be near neighbors in the lattice implies the domination of super exchange interactions that alter this simple model. In future chapters we will discuss this situation more in detail.

## *1.5 Theoretical approach*

Several theoretical models have been applied to interpret the experiments which have been performed on and the results obtained for GaMnAs and will be presented briefly

### 1.5.1 The first principal calculation (ab-initio)

The main technical challenge in DFT applications is the development of numerically efficient methods that provide accurate solutions of single-body Schrodinger equations for studying the microscopic origins of magnetism and for predicting electronic, magnetic, and ground-state structural properties. The advantage of this method is that it does not rely on any phenomenological parameter. However, the exact form of the exchange correlation energy functional is unknown. Applying local spin density approximation (LSDA) as solution also comes across certain difficulty due to the DMS nature of the magnetic ions which reduces the accuracy and complicates numerical implementation. There are also other problems. The Fermi wavelength of valence-band carriers is longer than the atomic length scale which increases the number of independent magnetic degrees of freedom that should be included in a DFT simulation of DMS materials.

In order to overcome theses shortcomings, the CPA and supercell approaches combined with DFT calculations have been used to address those physical parameters of GaMnAs that are derived from total energy calculations, including lattice constants, formation and binding energies of various defects, and type of magnetic order. It is a good choice since it leads to good results even when the range of Mn-Mn spin interaction is larger than the lattice constant.

As Jungwirth et al. have indicated in ref. [14] LSDA predictions for spectral properties, like the local DOS, are less reliable than predictions for total energy-related properties. LSDA also fails to account for strong correlations that suppress fluctuations in the number of electrons in the d shell. This leads to an underestimation of energy splitting between the occupied and empty d states in spin density functional (SDF) theory and to an overestimate of the strength of p-d exchange which affects

directly the crucial informations such as damping factor. It also fails to account for strong correlations that suppress fluctuations in the number of electrons in the d shell; the case which was mentioned as the particularity of Mn in GaMnAs. One solution to this problem was found via LDA+U which uses the combination of SDF theory with the Hubbard description of strongly correlated localized orbitals. Additional parameters from the Hubbard model are added to the energy functional; they are obtained by fitting to experiment.

### 1.5.2 Tight binding model

Another approach is the use of Anderson many-body Hamiltonian theory treated in the tight-binding-approximation. This approach takes into consideration Coulomb interactions up to second nearest neighbor only to describe the host semiconductor and terms describing hybridization with nonmagnetic impurities and Mn. Here the local changes of the crystal potential at Mn and other impurity sites are represented by shifted atomic levels parametrized from experiment. This makes the TBA approach a semiphenomenological theory. It has the advantage of treating disorder microscopically. The disadvantage of this model is the neglect of Coulomb interaction which influence the charge and spin densities.

According to the references in [14], the Curie temperatures, magnetizations, the lifetimes of Bloch quasiparticle states, the effects of doping and disorder on the strength of p-d exchange coupling, and the effective Mn-Mn magnetic interaction are among the problems that have been analyzed using this approach.

### 1.5.3 k.p calculations

In the regime where the band holes are itinerant (metallic conductivities) length scales associated with holes in DMS compounds are long enough that a k.p envelope function description of semiconductor valence bands is appropriate. In this framework, the Kohn-Luttinger (KL) Hamiltonian matrix is solved taking into account the spin-orbit interactions for 6 to 8 bands in a set of basis functions (dimension of the matrix) ranging from 6 to 8 [52].

The kinetic-exchange effective Hamiltonian approach [37] in this regime is based on the localized character of the five $Mn_{Ga}$ d-orbitals and describes hole states in the valence band using the KL Hamiltonian and assuming the p-d exchange interaction between $Mn_{Ga}$ and hole spins. k.p model assumes that all relevant wave vectors are near the Brillouin-zone center and states near the Fermi energy mainly have the character of the host semiconductor valence band (which exclude the variation of S-O coupling due to the GaMnAs nature of the material even in the high doping levels when the material tends to be an alloy), even in the neighborhood of a substitutional Mn. From symmetry considerations the spin dependent part of the effective coupling

between Mn and band spins is an isotropic Heisenberg interaction (this feature is discussed in chapter 6 ). The KL Hamiltonian parameters are taken from the known values for the host III-V compound [53], the strength of this exchange interaction $J_{pd}$ can be extracted experiments and used to predict all other properties [48–50,54].

One advantage of this approach is that it uses no free parameters to model ferromagnetism in these systems since the value of $J_{pd}$ can be obtained from experiments in a paramagnetic state. KL kinetic-exchange Hamiltonian takes the form:

$$\mathcal{H} = \mathcal{H}_{hole} + J_{pd} \sum_{i,I} S_I \cdot s_i \delta(r_i - R_I) \tag{1.1}$$

$\mathcal{H}_{holes}$ includes the k.p KL Hamiltonian and the interactions of holes with the random disorder potential and with other holes. The second term is the p-d exchange interaction. Refinements for disorder can be treated via other approximations, and the hole-hole Coulombian interaction as well.

This model fails if the $p-d$ exchange is too strong and the Mn acceptor level is too deep in the gap. As it will be discussed the latter condition can be true for high quality samples.

### 1.5.4 Other phenomenological models

In addition to the mentioned models which apply for the samples in metallic conductivity regime (valence band conduction) there are other basically phenomenological models in which holes are assumed to hop between Mn acceptor sites where they interact with Mn moments via phenomenological exchange interactions [55–58].

Applying these models in the low-Mn-density limit enables to investigate, at least qualitatively, the complicated situation of ferromagnetic order in an insulating regime. In chapter.4 we have tried to investigate the dependence of ferromagnetism in this regime experimentally.

Some theoretical works have tried to model the systems between localized hole and the impurity band regime (i.e. the density of localized holes is much smaller than the density of Mn ions). This leads to a polaron picture in which a single hole polarizes a cloud of Mn spins [59, 60]. Note that no experimental results has been published which supports this model.

## *1.6 Mean field model and Curie temperature prediction*

Among the most important parameters studied both theoretically and experimentally in GaMnAs systems is the Curie temperature. While the experiments on samples with different doping levels and hole concentration until today have shown a high $T_C \approx 176$K, the theoretical studies try to simulate and investigate the material properties affecting this parameter. The first works reported by Dietl et al. in 1999

and by Jungwirth et al. in 2000 were based on k.p calculations. This accounts for the strong spin-orbit interaction present in the host valence band, which splits the three valence bands into a heavy-hole, light-hole, and split-off bands with different dispersions and plays an important role in suppressing magnetization fluctuation effects and therefore in stabilizing the ferromagnetic state up to high temperatures [61].

However the calculations omit, for example, the suppression of $T_C$ in low-hole-density GaMnAs materials due to the direct antiferromagnetic superexchange contribution to the coupling of near neighbor Mn pairs [14] (This feature is discussed in chapter 4 and it seems that even in low hole concentration the measurements are in good agreement with the model and it is not disturbed by antiferromagnetic superexchange interactions). The whole model inevitably breaks down in DMS systems with holes strongly bound to Mn acceptors or with large charge fluctuations on $Mn_{Ga}$ d-shells.

Nevertheless this approach has been capable of interpreting and explaining many experimental results of this system. Therefore, we shall adopt also this model to interpret out experimental results. In particular the mean-field approximations together with k.p calculation has enabled the estimation of Curie temperature for metallic GaMnAs samples. we will test its predictions concerning the influence of the Mn and carrier densities of the magnetic properties.

The model is based on the assumption of a homogeneous distribution of $Mn_{Ga}$ ions and it neglects the role of other defects, apart from their potential contribution to hole or moment compensation.

It starts with the Anderson Hamiltonian (for many-body problem):

$$H = \sum_{s,k} \epsilon_k n_{k,s} + \sum_{d,s} \epsilon_d n_{d,s} + U n_{d\uparrow} n_{d\downarrow} + \sum_{k,s} (V_{k,d} c^{\dagger}_{k,s} c_{d,s} + c.c) \qquad (1.2)$$

written here, for simplicity, for a single localized orbital and a single itinerant band. k represent band states and d represents localized impurity state, with spin s, $\epsilon$ is the single-particle energy, and n and c are standard second quantization operators. The last term is the hybridization of the localized d-states of Mn and the GaAs valence band provides the antiferromagnetic coupling between magnetic moments and the delocalized carriers, which then establish the ferromagnetic order in the GaMnAs system. When hybridization between the local-moment and band-electron states is weak it can be treated perturbatively. The Schiffer-Wolff transformation reduces this hybridization term to an effective exchange interaction between the localized spins and the spins of the free carriers [62].

This approach is used for relatively weak hybridization and the canonical transformation should also be applied to operators representing observables. The Schrieffer-Wolf transformation also leads to a spin-independent interaction [62] which is normally neglected in comparison with the stronger spin-independent long-range part

of the Coulomb potential.

Assuming the both initial and final states are at the Γ point we can approximate $\sum_{k,k'} j_{k,k'} s_d s_{k,k'}$ by $J_0 s_d \cdot s_{k=0}$. $J_0$ corresponds to the average value of $J(R_i - r)$ experienced by the k=0 Bloch state over the ith unit cell and the exchange integral between the holes and the magnetic moments is presented as $J_{pd} = J_0 \Omega_{u.c.}$, where $\Omega_{u.c.}$ is the GaAs unit cell volume. This is the effective exchange parameter that can be evaluated by experiments.

In a virtual-crystal mean-field approximation, the p-d exchange potential due to the Mn impurities in a $Ga_{1-x}Mn_xAs$ DMS, $xN_0\Omega_{u.c.} \sum_{R_{u.c.}} J(R_{u.c.} - r) \langle S \rangle \cdot s$, has the periodicity of the host crystal. $\langle S \rangle$ is the mean-field Mn spin. The valence-band states in this approximation experience an effective single-particle kinetic exchange field $h_{MF} = N_{Mn} J_{pd} \langle S \rangle$, where $N_{Mn} = xN_0$ is the $Mn_{Ga}$ density. ($J_{pd}$=54±9 meVnm$^3$ inferred from photoemission data [63]). It follows that each local $Mn_{Ga}$ moment is described by a Hamiltonian $S_I \Sigma H_{MF}$ where $S_I$ is the $Mn_{Ga}$ local spin operator, $H_{MF} = J_{pd} \langle s \rangle$, with $\langle s \rangle$ the mean spin density of the valence-band holes.

In the mean field approximations , the dependence of $\langle S \rangle$ on temperature and molecular field $H_{MF}$ is [64]:

$$\langle S \rangle = \frac{\mathbf{H}_{MF}}{H_{MF}} S B_S(S |H_{MF}| k_B T) \tag{1.3}$$

with $B_S$ the Brillouin function. The Curie temperature is found by linearizing $H_{MF}$ and $B_s$ around $\langle S \rangle$=0:

$$H_{MF} \approx J_{pd}^2 N_{Mn} \langle S \rangle \chi_f \tag{1.4}$$

$$B_S \approx \frac{S+1}{3} \frac{S |H_{MF}|}{k_B T_C} \tag{1.5}$$

with itinerant hole spin susceptibility:

$$\chi_f = \frac{ds}{dH_{MF}} = \frac{d^2 e_T}{dH_{MF}^2} \tag{1.6}$$

where $e_T$ is the total energy per volume of the holes. Solving this equations one obtains:

$$k_B T_C = \frac{N_{Mn} S(S+1)}{3} J_{pd}^2 \chi_f \tag{1.7}$$

Applying a single spin-split band and an effective mass m* model, the kinetic-energy contribution $e_k$ to the total energy of the band holes gives a susceptibility:

$$\chi_{f,k} = -\frac{de_k^2}{d^2 h_{MF}} = \frac{m * k_F}{4\pi^2 \hbar^2} \tag{1.8}$$

where $k_F$ is the Fermi wave vector. By replacing $k_F$ with $p^{1/3}$ one obtains the dependence of the Curie temperature to Hole and Mn concentration as $T_C \propto xp^{1/3}$.

Using a realistic band Hamiltonian,the six-band KL Hamiltonian of the GaAs host band leads to a more quantitative prediction for the Curie temperature. Based on k.p calculations using the mean field approximation room-temperature ferromagnetism in GaMnAs is expected for ≈10% $Mn_{Ga}$ doping in weakly compensated samples. The results of these calculations are resumed in a fig.1.8 reported by Jungwirth et al. [65]. Hole-hole Coulomb interaction can also be considered by adding the hole exchange contribution to the total energy [66]. As it is shown in fig.1.8 the resulting Stoner $T_C$ enhancement (using six band KL Hamiltonian) which is 10-20% higher, but still $T_C$ is roughly proportional to $xp^{1/3}$ [65].

This model neglects the discrete random $Mn_Ga$ positions and other interactions such as the near neighbor superexchange. This phenomenological model fails when the Fermi wavelength approaches atomic length scales. Also the k.p band structure, the use of the host material band parameters, and the neglect of momentum dependence in the $J_{pd}$ parameter all become less reliable as the hole density increases to very large values. However it is predicted that the approximations are valid even for x≈10% and for any degree of compensation.

Also in very low hole concentration (high compensation levels) antiferromagnetic superexchange can dominate the near-neighbor $Mn_{Ga}$-$Mn_{Ga}$ coupling [67] leading to a reduced Curie temperature.

### *1.7 Band structure*

As already discussed the delocalized carriers in degenerate GaMnAs films (where the k.p calculations are valid) are in the band of the GaAs host material. The band can be described by the composition of 6 sub-bands (four $\Gamma_8$ and two $\Gamma_7$). The total Hamiltonian is constituted of the Kohn-Luttinger k.p Hamiltonian, the p-d exchange term, the strain Hamiltonian and the one related to the Zeeman effect. In this case the general form will be as follow:

$$H_{tot} = H_{k.p} + H_{exchange} + H_{strain} + H_{Zeeman} \tag{1.9}$$

In the absence of the exchange interactions (hybridization) and the strains, the heavy holes (J=3/2 $j_z = \pm 3/2$) and the light holes (J=3/2 $j_z = \pm 1/2$) constitute the band $\Gamma_8$ which is four time degenerated in the center of the Brillouin zone. They are mainly composed of the hybridized sp orbitals for which the contribution of As is dominant. The band $\Gamma_7$ (J=1/2) is separated ≈340meV from the former bands due to the large S-O coupling.

The origin of the exchange Hamiltonian has been already explained in previous sections. It is presented as:

$$H_{exchange} = \sum_{i,j} J(r_{ij}) \vec{S} \cdot \vec{s} \tag{1.10}$$

The exchange Hamiltonian between the valence and conduction bands and the localised 3d electrons of manganese can be written as:

$$H_{sd} = -x_{Mn} N_0 \alpha \left\langle \vec{S} \right\rangle \cdot \vec{s} \tag{1.11}$$

$$H_{pd} = -x_{Mn} N_0 \beta \left\langle \vec{S} \right\rangle \cdot \vec{s} \tag{1.12}$$

symbol $\beta$ used here is for comparison with the case of DMS II-VI where its is used instead of $J_{pd}$ and $N_0$ instead of $J_0$. While the experimental and theoretical values for $J_{pd}$ was presented in previous section, there is no report concerning experimental measurement of $N_0\alpha$. Its value for II-VI hosts has been measured =0.2eV [68]. Although these values should be host independent, $J_0$ tends to be larger in larger-gap, smaller-lattice-constant hosts [14].

For the non-zero magnetization parallel to z-direction, the displacements of the conduction band and valence band due to this interactions are : $\Delta E_c = x_{Mn} N0\alpha \langle S_z \rangle s_z$ and $\Delta E_v = x_{Mn} N0 \frac{\beta}{3} \langle S_z \rangle j_z$, which indicates a displacement of the energy of heavy holes 3 times larger than that of the light holes.

The tetragonal deformation of the lattice induced by the lattice parameter difference between the substrate and the film (which does not relaxes even up to the thickness of ≈500nm) lifts the degeneracy of the light and heavy hole bands. Its contribution to the splitting is $2bQ_\epsilon$. b presents the deformation parameter which is =1.7 for GaAs. If the hydrostatic deformations are negligible, one can express $Q_\epsilon$ as a function of the tensorial deformation components $\epsilon_{ij}$ and the strains $C_{ij}$.

$$Q_\epsilon = \epsilon_{zz} - \frac{\epsilon_{xx} + \epsilon_{yy}}{2} = \epsilon_{xx} \left[ 1 - 2\frac{C_{12}}{C_{11}} \right] \tag{1.13}$$

It is obvious that the relevant sign of the epitaxial strains is the direct influence on the relative position of the heavy and light holes in the center of the zone. It is shown that the effect is opposite for the layers under compressive or tensile strains. The relative separation of the bands is in the order of 20meV for the standard sample, in the absence of the exchange contribution.

In the center of the Brillouin zone, the exchange coupling can be expressed in terms of the reduced magnetization as:

$$\Delta\epsilon_{HH} = 6B_G m_z \quad \Delta\epsilon_{LH} = 2B_G \sqrt{m_z^2 + 4m_{xy}^2} \tag{1.14}$$

where $B_G$ is the hole splitting parameter ($B_G = \frac{\beta M}{6g\mu_B}$) and $m_z = \frac{M_Z}{M}$ and $m_{xy} = \frac{M_x^2 + M_y^2}{M^2}$ the reduced in-plane and normal-to-plane magnetizations, respectively. The

different behavior of the LH and HH bands for the splitting results from their wave functions. At the center of the Brillouin zone (as an example or an approximation), While the heavy holes are the pure spin states of:

$$|\frac{X+iY}{\sqrt{2}}\uparrow> \quad for j_z = 3/2$$

$$and$$

$$|\frac{X-iY}{\sqrt{2}}\downarrow> \quad for j_z = -3/2$$

the light holes are the mixed states of

$$|\frac{X+iY}{\sqrt{2}}\downarrow> \; mixed\, with\, Z\uparrow \quad for j_z = 1/2$$

$$and$$

$$|\frac{X-iY}{\sqrt{2}}\uparrow> \; mixed\, with\, Z\downarrow \quad for j_z = -1/2$$

Note that while the Fermi level for high hole concentrations lies deep in the valence band the terms light and heavy holes loose their distinction and they mix together.

### *1.8 Magnetic anisotropies*

The anisotropy of the valence band also plays an important role and generates anisotropy in the exchange integral and damping factors and it generates magneto-crystalline anisotropy.

The mean field model, has taken in account most of the effects of this anisotropy and has tried to explain its origin in a quantitative approach. Note, that the exchange interaction, itself, is considered isotropic, since the corresponding Hamiltonian contains no spatial coordinates; however we shall comment this feature in the last chapter.

In usual ferromagnetic metals, the dominant source of the anisotropy is the magneto-static anisotropy. It is related to the presence of the demagnetization field which is strong in the case of ferromagnetic metals (the strong dipole-dipole interactions). This field is proportional to the magnetization. The tensor of the proportionality N is a geometry dependent factor. Demagnetization field energy, depends not only on the shape of the sample but also on the relative direction of magnetization along the different axes of anisotropy and will be discussed in details (for the case of GaMnAs thin films) in the section 2.1.2.

Although the role of this field is important in ferromagnetic metals, it plays a minor role in the case of diluted magnetic semiconductors, because of the diluted

nature of the magnetic moments and hence the low magnitude of the magnetization. note that a typical magnetization for annealed $Ga_{1-x}Mn_xAs$ samples with x=0.05 is in the order of $M \approx 50 emu/cm^3$ at T=4K.

On the other hand, the magneto-crystalline anisotropy field depends on the anisotropic interaction of randomly distributed atomic charge of the Mn ions (spin $\vec{S}$) with the local electric field and so on the spin-orbit interaction. This interaction, being weak in the metallic systems, is dominant in the semiconductors.

An electron with the velocity $\vec{v}$ in the atomic lattice feels the S-O interaction as an effective magnetic field $\vec{H}_{SO} \propto \vec{S}(\vec{v} \wedge \vec{E})$ which can be expressed as $H_{SO} \propto -\vec{L} \cdot \vec{S}$, in which $\vec{L}$ is the orbital momentum of the atom and depends on the symmetry of GaAs matrix.

Since L=0 for the substitutional manganese $Mn^{2+}$ion, the spin-orbit interaction has a negligible effect on the electrons in the 3d-shell. On the other hand, the delocalized charge carriers feel the spin-orbit coupling effect which affects the spin polarization of the holes and consequently modifies the magnetization of the Mn ions.

In mean field calculations, there are only two (uniaxial and cubic) anisotropy constants (neglecting the biaxial compositions of them which results in a considerable approximation compared to th real case). The cubic and uniaxial anisotropy fields and their relevant constants can be estimated from calculations with the external field along [001], [110],[1-10] and [100] directions [69]. The results of these calculations is illustrated in fig.1.5 (6-band approximation).

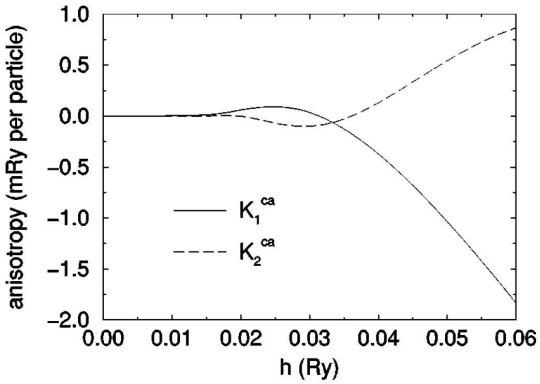


**Figure 1.5:** Six-band model, Zeeman effective local field seen by the holes h=0.01 Ry, results for the cubic magnetic anisotropy coefficients in units of Ryd per particle (main plot) and in $kJ/m^3$ (inset)

One important parameter, to which two important chapters of this thesis are dedicated, is the influence of hole concentration. The charge carrier density not only has direct influence on the Curie temperature of the layer but also modifies the

anisotropy of the valence band due to modifications to the position of Fermi level.

A qualitative picture of this effect for a sample under compressive strain is shown in fig.1.6. For a low enough hole concentration, the holes occupy only one sub-band, namely the Heavy holes (HH) band with $j_z = -3/2$ in which case the exchange interaction between the manganese ions ($H_{pd} \propto \vec{j}\vec{S}_{Mn}$) is maximized for the magnetization perpendicular to the plane. Therefore the easy axis of magnetization is along [001] direction for low hole concentration.

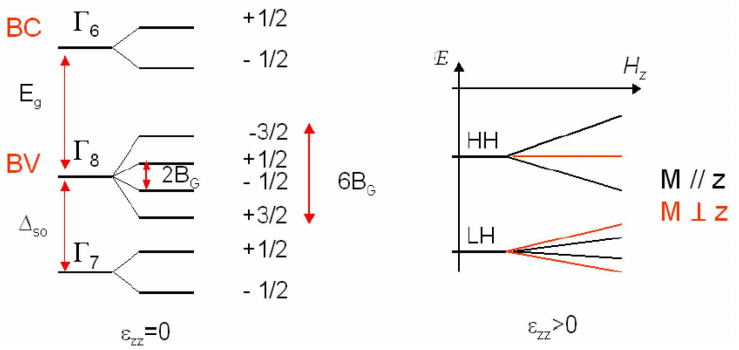


**Figure 1.6:** Schema of band splitting due to different interactions (left) and splitting of the HH and LH band for Zeeman effect in sample under compressive strain for two orientations of magnetization (right)

On other hand, for higher carrier densities, the Fermi level interferes with light hole band (competition between two bands) and in which case the easy axis of magnetization is in-plane.

As a function of the strains in the layer, the theoretical calculations based on mean field approximation (by Dietl et al. in 2001 [7]) have demonstrated the reorientation of the easy axis of magnetization from inplane directions (for compressive strain) to [001] direction (for tensile strain) due to the different contribution of heavy and light holes, as it was discussed (Fig.1.7).

The results show that for a layer under tensile strain, the modification to the hole concentration follows the same criteria as the compressive strained one but the HH and LH are inverted.

Other parameters which influence the orientation of the easy axis of the magnetization are Mn concentration which modifies the Zeeman splitting and temperature which in addition to the latter effect modifies directly the Fermi level in low hole concentration regimes. All these parameters and their contribution to the determination of the easy and hard axes of magnetization are discussed in detail in following chapters.

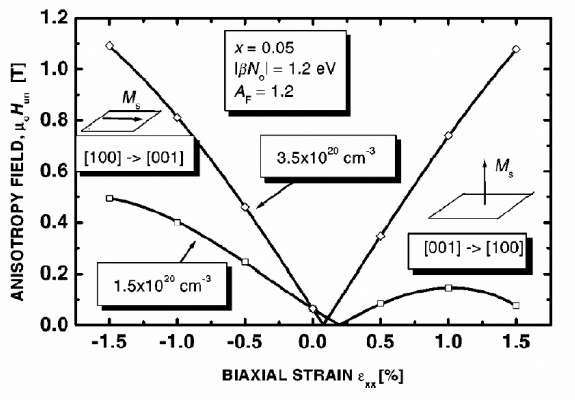


**Figure 1.7:** The points indicate the field required to reorient the magnetization from one axis to other as indicated. Calculations are based on mean field approximation for anisotropies as a function of strain. [7]

## *1.9 Toward higher $T_C$ in GaMnAs (different affecting parameters)*

The dependence of the Curie temperature on the hole and Mn concentrations have led researchers to try to increase this parameter by increasing these densities. Almost all models and theoretical approximations accept that rigorously by $[Mn] \approx 10\%$ doped manganse and hole concentration$\approx 10^{21} cm^{-3}$ one can expect $T_C$ is above room temperature in GaMnAs thin layers. Naturally, many groups have worked but a signifacant change in $T_C$ has net yet been achieved probably due to a high degree of compensation [70] or the formation of second phases. However one should note that while the theoretical studies are based on homogeneous samples with intermediate hole concentrations of the order $\approx 10^{20} cm^{-3}$, the case is less justified for the extreme cases were, for example, the competion of different interactions become paramount.

In this thesis we have investigated the effect of both parameters on $T_C$, up to high manganese and hole concentrations ($x \approx 0.21$ and $p \approx 10^{21} cm^{-3}$).

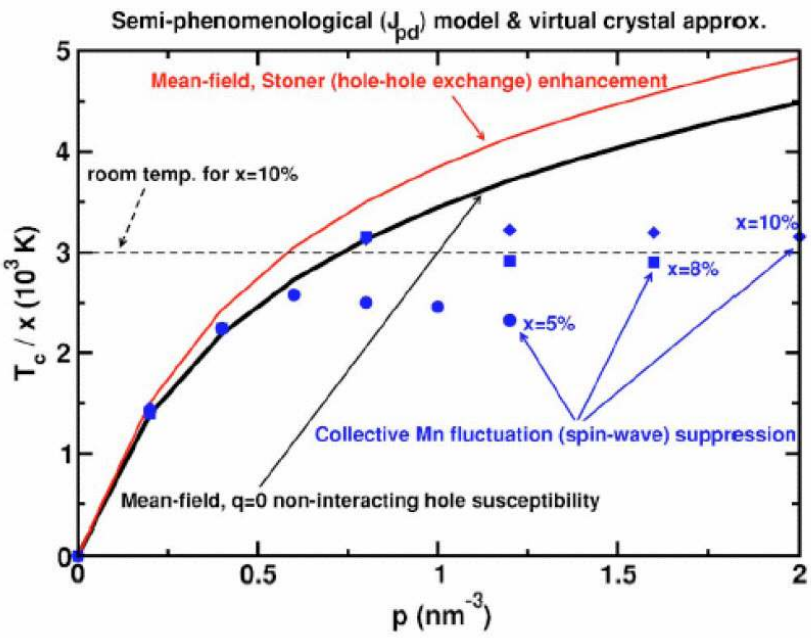


**Figure 1.8:** Calculated Curie temperature based on k.p calculation with different approximations [14]

# Bibliography


[1] P. Grunberg, R. Schreiber, Y. Pang, M. B. Brodsky, and H. Sowers *Physical Review Letters* 57 (19) 2442 - 2445 (**1986**).

[2] M. N. Baibich , J. M. Broto, A. Fert, F. Nguyen Van Dau, F. Petroff, P. Eitenne, G. Creuzet, A. Friederich, and J. Chazelas Physical Review Letters 61 (21): 2472 - 2475 (1988).

[3] M. Jullliere, Phys. Lett. 54A, 225 (1975).

[4] DC Ralph, G Schon, S Maekawa J. M. M. M. e343ñe345 (2007).

[5] K. Khazen, H. J. von Bardeleben, J. L. Cantin et al. Phys. Rev. B 74, 245330 (2006).

[6] F. Leuenberger, A. Parge, W. Felsch, K. Fauth, and M. Hessler, Phys. Rev. B 72, 014427 (2005).

[7] T. Dietl, H. Ohno, and F. Matsukura, Phys. Rev. B 63, 195205 (2001).

[8] AB Mahmoud, HJ von Bardeleben, JL Cantin et al., J. Appl. Phys. 101, (2007).

[9] BT Jonker, G Kioseoglou, AT Hanbicki, CH Li et al., Nature Phys. (2007).

[10] HW Wu, CJ Tsai, LJ Chen Appl. Phys; Lett., (2007).

[11] Van Esch, A., L. Van Bockstal, J. De Boeck, G. Verbanck, A. S. van Steenbergen, P. J. Wellmann, B. Grietens, R. B. F. Herlach, and G. Borghs, Phys. Rev. B 56, 13103 (1997).

[12] M. Julliere, Phys. Lett. 54A, 225 (1975).

[13] K. Olejnik, M.H.S. Owen, V. Novak, J. Masek, A.C. Irvine, J. Wunderlich, T. Jungwirth arXiv:0802.2080v1 (2008).

[14] T. Jungwirth,J. Sinova, J. Masek et al. Rev Mod. Phys. 78, (2006).

[15] Linnarsson, M., E. JanzÈn, B. Monemar, M. Kleverman, and A. Thilderkvist, Phys. Rev. B 55, 6938 (1997).

[16] A. M.Yakunin, A. Y. Silov, P. M. Koenraad, J. H. Wolter, W. Van Roy, J. De Boeck, J. M. Tang, and M. E. FlattÈ,Phys. Rev. Lett. 92, 216806 (2004).

[17] D.Kitchen, A. Richardella, and A. Yazdani, , J. Supercond. 18, 23. (2005).

[18] D. Kitchen, A. Richardella,P. Roushan, J.M. Tang and M. E. Flatte and A.Yazdani J. Appl. Phys. 101, 09G515 (2007).

[19] N Nepal, AM Mahros, SM Bedair, NA El-Masry et al., P Appl. Phys. Lett. 91, 242502 (2007).

[20] M. B. L. Sheu, R. C. Myers, J.-M. Tang, N. Samarth, D. D. Awschalom, P. Schiffer, M. E. FlattÈ arXiv:0708.1063v1 (2007).

[21] H. Ohno, H. Munekata, T. Penney, S. von Moln·r, and L.L. Chang, Phys. Rev. Lett. 68, 2664 (1992).

[22] P. Mahadevan, and A. Zunger, , Phys. Rev. B 68, 075202 (2003).

[23] S Ohya, K Ohno, M Tanaka, Applied Physics Letters (2007).

[24] D. E. Bliss, W. Walukiewicz, J. W. A. III, E. E. Haller, K. T. Chan, and S. Tanigawa, J. Appl. Phys. 71, 1699 (1992).

[25] R. P. Campion, , K. W. Edmonds, L. X. Zhao, K. Y. Wang, C. T. Foxon, B. L. Gallagher, and C. R. Staddon, J. Cryst. Growth 251, 311(2003).

[26] R. C. Myers, B. L. Sheu, A. W. Jackson, A. C. Gossard, P. Schiffer, N. Samarth, and D. D. Awschalom, Phys. Rev. B 74, 155203 (2006).

[27] L. X. Zhao, C. R. Staddon, K. Y. Wang, K. W. Edmonds, R. P. Campion, B. L. Gallagher, and C. T. Foxon, , Appl. Phys. Lett. 86, 071902 (2005).

[28] J. Masek, and F. Maca, eprint cond-mat/0508760 (2005).

[29] K. M. Yu, W. Walukiewicz, T. Wojtowicz, W. L. Lim, X. Liu, U. Bindley, M. Dobrowolska, and J. K. Furdyna,Phys. Rev. B 68, 041308 (2003).

[30] J. Masek, and F. Maca, Phys. Rev. B 69, 165212 (2003).

[31] M Adell, L Ilver, J Kanski, V Stanciu, P Svedlindh, Appl. Phys. Lett. 86, 112501 (2005).

[32] S. J. Potashnik, K. C. Ku, S. H. Chun, J. J. Berry, N. Samarth, and P. Schiffer, Appl. Phys. Lett. 79, 1495 (2001).

[33] N. W.Ashcroft, and N. D. Mermin, , Solid State Physics (Saunders, Philadelphia)(1976).

[34] P. W. Anderson, Phys. Rev. 79, 350 (1950).

[35] J. B. Goodenough, J. Phys. Chem. Solids 6, 287 (1958).

[36] J. Kanamori, J. Phys. Chem. Solids 10, 87 (1959).

[37] C. Zener, Phys. Rev. 81, 440 (1951).

[38] A. K. Bhattacharjee, G. Fishman, and B. Coqblin, Physica B and C 117-118, 449 (1983).

[39] T. Dietl, in Handbook of Semiconductors, edited by S. Mahajan (North-Holland, Amsterdam), Vol. 3B, p. 1251 (1994).

[40] T. Kasuya, Prog. Theor. Phys. 16, 45 (1956).

[41] K. Yosida, Phys. Rev. 106, 893 (1957).

[42] E. A. Pashitskii and S. M. Ryabchenko, Sov. Phys. Solid State 21, 322 (1979).

[43] J. Schneider, U. Kaufmann, W. Wilkening, M. Baeumler, and F. K^hl, Phys. Rev. Lett. 59, 240 (1987).

[44] Y.Ohno, D. K. Young, B. Beschoten, F. Matsukura, H. Ohno and D. D. Awschalom, , Nature (London) 402, 790 (1999).

[45] S. J. Potashnik, K. C. Ku, R. Mahendiran, S. H. Chun, R. F. Wang, N. Samarth, and P. Schiffer, , Phys. Rev. B 66, 012408 (2002).

[46] P. M.Krstajic, F. M. Peeters, V. A. Ivanov, V. Fleurov, and K. Kikoin, , Phys. Rev. B 70, 195215 (2004).

[47] T. Dietl, A. Haury, and Y. M. d'Aubigne, Phys. Rev. B 55, R3347 (1997).

[48] T. Dietl, , H. Ohno, F. Matsukura, J. Cibert, and D. Ferrand, Science 287, 1019 (2000).

[49] F. Matsukura, , H. Ohno, A. Shen, and Y. Sugawara, Phys. Rev. B 57, R2037 (1998).

[50] T.Jungwirth, W. A. Atkinson, B. H. Lee, and A. H. Mac-Donald, Phys. Rev. B 59, 9818 (1999).

[51] T. Jungwirth, J. Sinova, A.H. MacDonald, B.L. Gallagher et al. Phys. Rev. B 76, 125206 (2007).

[52] J. M. Luttinger and W. Kohn, Phys. Rev. 97, 869 (1955).

[53] I. Vurgaftman and J. R. Meyer, Phys. Rev. B 64, 245207 (2001).

[54] J. Konig, H. H. Lin, and A. H. MacDonald, Phys. Rev. Lett. 84, 5628 (2000).

[55] M. Berciu and R. N. Bhatt, Phys. Rev. Lett. 87, 107203 (2001).

[56] G. Alvarez, M. Mayr, and E. Dagotto, Phys. Rev. Lett. 89, 277202 (2002).

[57] R. N.Bhatt, M. Berciu, M. P. Kennett, and X. Wan, J. Supercond. 15, 71 (2002).

[58] G. A. Fiete, G. Zarand, and K. Damle, Phys. Rev. Lett. 91, 097202 (2003).

[59] A. C. Durst, R. N. Bhatt, and P. A. Wolff, Phys. Rev. B 65, 235205 (2002).

[60] A. Kaminski and S. Das Sarma, Phys. Rev. Lett. 88, 247202 (2002).

[61] Konig, J., T. Jungwirth, and A. H. MacDonald, Phys. Rev. B 64, 184423 (2001).

[62] J. R. Schrieffer and P. A. Wolff, Phys. Rev. 149, 491 (1966).

[63] J. Okabayashi, A. Kimura, O. Rader, T. Mizokawa, A. Fujimori, T. Hayashi and M. Tanaka, Phys. Rev. B 58, R4211 (1998).

[64] J.Kˆnig, J. Schliemann, T. Jungwirth, and A. H. MacDonald, , in Electronic Structure and Magnetism of Complex Materials, edited by D. J. Singh and D. A. Papaconstantopoulos (Springer Verlag, Berlin), p. 163 (2003).

[65] T. Jungwirth, K. Y. Wang et al., Phys. Rev. B 72, 165204 (2005).

[66] Mahan, G. D., Many-Particle Physics (Plenum, New York)(1981) .

[67] J. Kudrnovsky, I. Turek, V. Drchal, F. Maca, P. Weinberger, and P. Bruno, , Phys. Rev. B 69, 115208 (2004).

[68] J. A. Gaj, J. Ginter and R. R. Galazka, Phys. Status Solidi B 89, 655 (1978).

[69] M. Abolfath, T. Jungwirth, J. Brum, and A. H. MacDonald, Phys. Rev. B 63, 054418(2001).

[70] K. Y. Wang, K. W. Edmonds, R. P. Campion et al. J. Appl. Phys. 95, 6512 (2004).

# 2

# Experimental techniques

## *2.1 Ferromagnetic Resonance Spectroscopy*

In order to investigate the magnetic properties of ferromagnetic thin layers, ferromagnetic resonance spectroscopy is extremely powerful. It has been applied since the fifties to many metallic systems and it achievements have been reviewed at many occasions [1–4]. Among the important parameters which can be measured by this technique are the magnetocrystalline anisotropy constants, the g-factor, the magnetization (specially interesting in the case of ultrathin layers and thin≈30nm DMS layers where the conventional SQUID magnetometry can not provide reliable measurements), the Gilbert damping factor, the Curie temperature, the spin stiffness (via spinwave excitation detection) and even the homogeneity of the layers. Combined with its high energy resolution this makes the FMR spectroscopy an interesting technique for an in depth investigation of thin magnetic layers and multilayer structures.

FMR has been applied with success to the study the interlayer exchange coupling in metallic multilayers structures. Its high sensitivity allows even the investigation of magnetic quantum wells where one wants to study the effect of the subband occupation on its magnetic state.

In the case of spintronics, the compatibility of the studied systems, mainly ultrathin layers with the possibilities of this technique has made it a major source for experimental results. After many years of studies of metallic samples, now by the contribution of semiconductors to this field, new perspectives have opened for the application of FMR.

We have used FMR (and the related techniques EPR and SWR) as our principal technique in this work. In addition we have also used several other techniques: RBS,PIXE, XPS, magneto-optical Kerr microscopy and SQUID measurements to obtain complementary information on our samples. In this chapter we present the basic elements and theoretical background of the FMR spectroscopy.

The FMR spectroscopy is sensible to the magnetic part of the free energy of a

system which contains in addition to the Zeman term the contributions from the demagnetization and magnetocristalline anisotropy fields. The resonance fields (of the uniform mode) measured by FMR can be derived from the free energy expression. In the case of DMS thin epitaxial layers like GaMnAs on GaAs the magnetocristalline anisotropy fields are the dominant contribution in X-band spectroscopy. For this reason I will introduce first the concept of the magnetic free energy density and the magnetocrytalline anisotropy fields of strained GaMnAs layers.

### 2.1.1 Magnetocrystalline anisotropy and magnetic free energy

The magnetocrystalline anisotropy energy (MAE) is the difference in the free energies of the system for different directions of the magnetization in the crystal. The spontaneous orientation of the magnetization is therefore given by the equilibrium condition where the magnetic part of the total energy of the system is minimal. We have already mentioned the different contributions to the anisotropy in the GaMnAs system. The anisotropies are measured experimentally as a set of phenomenological magnetocrystalline anisotropy constants $K_i$.

For the zinc-blende structure of undoped GaAs we would, a priori only expect contributions from the cubic fourth order anisotropy constants to the free energy density [5, 6]. But as has been shown before, the lattice mismatch between the GaMnAs layer and the GaAs substrate introduces a biaxial compressive strain which leads to strong in-plane and perpendicular uniaxial deformations (anisotropies).

In GaMnAs, the magnetocrystalline anisotropy of the film reflects the anisotropy of valence band and the contributions of the heavy and light hole bands. While the spin-orbit interactions due to the Mn moments with L=0 and Zeeman splitting for these thin films are negligible [5], the p-d exchange interaction between the magnetic ions and the holes ( 0.1 $eVnm^3$) and the spin-orbit interaction in the GaAs host material ($\lambda$=0.34 eV) give the largest contributions to the splitting of the six fold degenerate valence band. Thus the Fermi level position and the valence band splittings are the crucial parameters determining the contribution of each type of holes to the magnetic properties. The strain induced splitting is predominant for the preferential alignment of the free hole magnetic moments in the film [5].

The intrinsic cubic and strain induced biaxial anisotropies can be well described by introducing four magnetocrystalline anisotropy constants (two uniaxial and two cubic), which we shall present below. They result in four high symmetry axes of magnetization in the GaMnAs crystal: [001], [110], [100] and [1$\bar{1}$0] axes.

The coefficient $K_{2\perp}$ reflects the difference in energy of system for magnetization perpendicular and parallel to the film plane. Its main origin is the biaxial strain resulting from the lattice mismatch between the film and the substrate. This results in a tetragonal distortion of the cubic symmetry of GaMnAs. The sign of $K_{2\perp}$ is opposite for compression and extension of the film. Usually, for a thin film, this

term has the highest contribution to the anisotropy part of the free energy. The films are of macroscopic dimensions and $K_{2\perp}$ is coupled to the shape anisotropy term through a $4\pi M - 2K_{2\perp}/M$ term known as $4\pi M_{effective}$. The crucial role of this term in the reorientation of the magnetization especially in PMA cases shows the importance of this constant.

$K_{4\perp}$ and $K_{4\parallel}$, the cubic anisotropies for [100] and [110] directions of the matrix are equal in the case of a net cubic system, whereas in the presence of additional tetragonal or trigonal deformations they are different and thus also magnetic energy for magnetization.

The in-plane uniaxial anisotropy constant $K_{2\parallel}$ is often related to the way the first layer of the film is grown on the [001] substrate surface plane, which can be an As or Ga layer. It has been related to the dimerisation of the surface atoms in the [110] or [1$\bar{1}$0] directions [7]. This dimerisation of As or Ga atoms in the first layers, results in an anisotropy along the [110] and [1$\bar{1}$0] directions. Since the growth is performed at low temperature, the absence of the dislocations because of the energy cost leads to the transfer of the anisotropy to the next layers. The anisotropy field corresponding to each constant is obtained by $H_i = 2K_i/M$.

The appropriate free energy F expression includes thus second order and fourth order magnetocrystalline anisotropy coefficients is given as:

$$F = \frac{1}{2}M[-2H\,[cos\theta cos\theta_H + sin\theta sin\theta_H cos(\phi - \phi_H)] + 4\pi M cos^2\theta \qquad (2.1)$$

$$-H_{2\perp}cos^2\theta - \frac{1}{2}H_{4\perp}cos^4\theta - \frac{1}{2}H_{4\parallel}\frac{1}{4}(3 + cos4\phi)sin^4\theta - H_{2\parallel}sin^2\theta sin^2\left(\phi - \frac{\pi}{4}\right)]$$

The first term in eq.2.1 represents the Zeeman energy, the second the dipolar demagnetization energy for thin film geometry and the last two terms describe the second and fourth order anisotropy energies. As a consequence of the strong magnetocrystalline anisotropy the magnetization is no longer aligned with the applied magnetic field for a general orientation of the magnetic field. Two different polar angles have thus to be used to describe the respective orientations of the magnetization M($\theta$,$\phi$) and the applied field H($\theta_H$,$\phi_H$)(fig.2.1). Contrary to the case of conventional ferromagnetic materials like Co, Fe in GaMnAs the demagnetization fields are much smaller than the magnetocrystalline anisotropy fields.

### 2.1.2 Relation between the energy and the resonance frequency

In the ferromagnetic materials, since the magnetic moments (spins) are correlated, one can consider all individual spins as a macro spin which in the presence of an external applied field, from a classical point of view (the assumption of macro

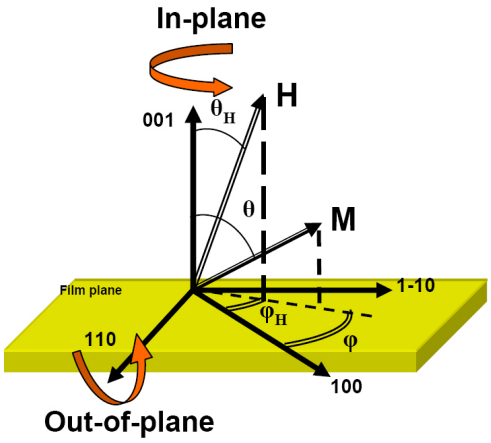


**Figure 2.1:** The definition of the polar angles$\theta_H$,$\phi_H$ and $\theta$,$\phi$ of the applied magnetic field and the magnetization respectively. The two rotation planes explored in the FMR measurements are also indicated.

system) precess around the effective magnetic field, composed of the applied field and the internal magnetic fields.

The motion of magnetization in presence of a magnetic field, $\vec{M}$, can be described by:

$$\frac{1}{\gamma}\frac{\partial \vec{M}}{\partial t} = -\left[\vec{M} \times \vec{H}_{eff}\right] + \vec{R} \tag{2.2}$$

where $\vec{H}_{eff}$ is the effective field which consists of external as well as internal fields, $\gamma$ is the gyro-magnetic ratio given by $g\mu_H/\hbar$ where g is the g-factor. The first term on the right hand side represents the precessional torque and the second one represents the damping term which may be written in different phenomenological forms (e.g. Gilbert, Landau-Lifshitz, Bloch- Bloembergen).

For the uniform precession in the classical limit without any dephasing of the spins (k=0), the spin motion can be described by the Landau-Lifshitz (LL) equation of motion:

$$\frac{1}{\gamma}\frac{\partial \vec{M}}{\partial t} = -\left[\vec{M} \times \vec{H}_{eff}\right] + \frac{\lambda}{\mu_0 \gamma^2 M^2}\left(\vec{M} \times \vec{M} \times \vec{H}_{eff}\right) \tag{2.3}$$

Here$\lambda$ is the LL damping parameter. For small damping the LL term can be replaced by the Gilbert damping term resulting in the Landau-Lifshitz-Gilbert (LLG) equation of motion [8].

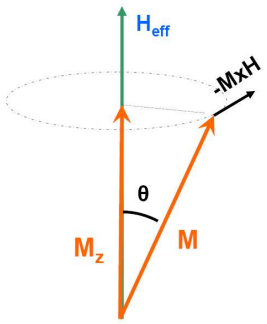


**Figure 2.2:** Schematic drawing of the precession of the magnetization in resonance condition

$$\frac{1}{\gamma}\frac{\partial \vec{M}}{\partial t} = -\left[\vec{M} \times \vec{H}_{eff}\right] + \frac{\alpha}{\gamma M}\left(\vec{M} \times \frac{\partial \vec{M}}{\partial t}\right) \tag{2.4}$$

where $\alpha$ is the dimensionless damping parameter and is related to the Gilbert damping parameter G, according to: $\alpha = G/\gamma M$.

The resonance equation can be derived by solving the LLG equation and considering the dynamical effects of exchange/conductivity and of surface anisotropy.

Here we have used the free energy approach developed by Smit and Beljers [9] which allows only to derive the resonance equations [3, 4]. The sample is assumed to be homogeneously magnetized ,i.e. the absence of the domain formation and we include the surface in an effective bulk anisotropy. To consider the symmetry of the given lattice it is always helpful to use polar coordinates. For the calculation of the resonance field we neglect the magnetic damping effect, therefore, the precession of the total magnetic moment in the resonance condition can be described by the first term in LLG equation of motion. In Fig.2.2 a schematic illustration of this precession is given.

According to Fig.2.2 the motion of magnetization can be described as:

$$\dot{\theta} = \gamma H_{eff,\phi} \qquad \dot{\phi} = -\frac{\gamma}{sin\theta} H_{eff,\theta} \tag{2.5}$$

The different contributions to $H_{eff}$ have to be taken into consideration through the free energy density F (the detailed form of free energy density for GaMnAs system has been presented just before).

The different contributions to $H_{eff}$ have to be taken into consideration through the free energy F.

$$dF = \vec{H}_{eff} \cdot d\vec{M} \tag{2.6}$$

Considering the equilibrium conditions for different orientations of the magnetization one can define the free energy partial derivatives.

$$F_\theta = \frac{dF}{d\theta}|_{\theta_{eq}} = 0 \qquad F_\phi = \frac{dF}{d\phi}|_{\phi_{eq}} = 0 \tag{2.7}$$

For small precession angles:

$$\delta_\theta = \theta(t) - \theta \qquad delta_\phi = \phi(t) - \phi \tag{2.8}$$

Equations 2.5 and 2.8 combined with eq.2.7 result in:

$$-\frac{M}{\gamma} sin\theta \frac{\partial(\delta\theta)}{\partial t} = F_{\phi\theta}\delta\theta + F_{\phi\phi}\delta\phi \qquad \frac{M}{\gamma} sin\theta \frac{\partial(\delta\phi)}{\partial t} = F_{\theta\theta}\delta\theta + F_{\theta\phi}\delta\phi \tag{2.9}$$

By assuming $\delta\theta$,$\delta\phi \propto exp(i\omega t)$, the precession of a total magnetic moment with free energy F occurs at the resonance frequency $f = \frac{\omega}{2\pi}$ given by:

$$\left(\frac{\omega}{\gamma}\right)^2 = \frac{1}{M^2 sin^2\theta}\left[\frac{\partial^2 F}{\partial\theta^2}\frac{\partial^2 F}{\partial\phi^2} - \left(\frac{\partial^2 F}{\partial\theta\partial\phi}\right)^2\right] \tag{2.10}$$

Which is known as the Smit-Beljers formalism.One can do the same calculation without neglecting the damping effect. then, the resonance equation including the damping parameter becomes:

$$\left(\frac{\omega}{\gamma}\right)^2 = \frac{1+\alpha^2}{M^2 sin^2\theta}\left[\frac{\partial^2 F}{\partial\theta^2}\frac{\partial^2 F}{\partial\phi^2} - \left(\frac{\partial^2 F}{\partial\theta\partial\phi}\right)^2\right] \tag{2.11}$$

Although eq.2.11 is mathematically correct, it is physically not convenient, because the Smit-Beljers equations are not defined for $\theta = 0$ Baselgia et al. [10] proposed to replace it by the following relation:

$$\left(\frac{\omega}{\gamma}\right)^2 = \frac{1+\alpha^2}{M^2}\left[\frac{\partial^2 F}{\partial\theta^2}\left(\frac{1}{sin^2\theta}\frac{\partial^2 F}{\partial\phi^2} + \frac{cos\theta}{sin\theta}\frac{\partial F}{\partial\theta}\right) - \left(\frac{1}{sin\theta}\frac{\partial^2 F}{\partial\phi\partial\phi} - \frac{cos\theta}{sin^2\theta}\frac{\partial F}{\partial\phi}\right)\right] \tag{2.12}$$

The partial derivatives are evaluated at the angles $\theta$ and $\phi$ which minimize F. Note that the resonance frequency is given by the second derivatives of F, and thus is essentially a measure of the curvature of F, or the stiffness of M. In a conventional ferromagnetic resonance (FMR) experiment the magnetization is perturbed at a constant microwave frequency $\omega_m$ and F is modified by varying an applied external field. The field needed to change F such that $\omega/\gamma = \omega_m/\gamma$ is referred to as the resonance field, $H_{res}$. If the magnetization is oriented along an orientation corresponding to

free energy minimum or easy direction of the magnetization, the curvature of F is increased and the applied field needed to make the resonance frequency equal to the microwave frequency $H_{res}$ is decreased. Similarly, if the magnetization is oriented along a free energy maximum, (the hard direction of the additional energy) $H_{res}$ is increased. An increased value of $H_{res}$ with respect to the resonance field of the easy direction therefore corresponds to a hard direction and a decreased value of $H_{res}$ corresponds to an easy direction.

For a biaxially strained GaMnAs thin film and following the approach of Smit-Beljers, that considers the equilibrium condition of the magnetization under a steady field and neglecting magnetic damping effects (because of its small value), the value of the applied field corresponding to the resonance condition can be written as:

$$\left(\frac{w}{\gamma}\right)^2 = \left[\left(H_{res}\times a_1 + b_1\right)\left(H_{res}\times a_1 + b_2\right) - b_3^2\right] \tag{2.13}$$

where:

$$a_1 = cos\theta cos\theta_H + sin\theta sin\theta_H cos(\phi - \phi_H)$$

$$b_1 = -\left[4\pi M - H_{2\perp} + H_{2\parallel}cos^2(\phi + \frac{\pi}{4})\right]cos^2\theta$$
$$+H_{4\perp}\frac{cos(2\theta) + cos(4\theta)}{2} + H_{4\parallel}\frac{cos4\theta - cos2\theta}{2}\frac{3 + cos4\phi}{4}$$
$$b_2 = -(4\pi M - H_{2\perp})cos^2\theta + H_{4\parallel}sin^2\theta(cos4\phi - cos^2\theta\frac{3 + cos4\phi}{4})$$
$$+H_{4\perp}cos^4\theta - H_{2\parallel}\left\{sin2\phi + \left[cos\theta cos(\phi + \frac{\pi}{4})\right]^2\right\}$$

In the special case that the magnetic field is along one of the the four high symmetry axes of the crystal, as a good approximation the applied field and the magnetization can be assumed parallel which simplifies the eq.2.13:

$$\left(\frac{\omega}{\gamma}\right)^2 = \left(H_{res} - 4\pi M + \frac{2K_{2\perp}}{M} + \frac{2K_{4\perp}}{M}\right)\left(H_{res} - 4\pi M + \frac{2K_{2\perp}}{M} + \frac{2K_{4\perp}}{M} - \frac{2K_{2\parallel}}{M}\right) \tag{2.14}$$

$$\left(\frac{\omega}{\gamma}\right)^2 = \left(H_{res} + \frac{2K_{4\parallel}}{M}\right)\left(H_{res} + 4\pi M - \frac{2K_{2\perp}}{M} + \frac{2K_{4\parallel}}{M} + \frac{K_{2\parallel}}{M}\right) \tag{2.15}$$

$$\left(\frac{\omega}{\gamma}\right)^2 = \left(H_{res} - \frac{2K_{4\parallel}}{M} - \frac{2K_{2\parallel}}{M}\right)\left(H_{res} + 4\pi M - \frac{2K_{2\perp}}{M} + \frac{K_{4\parallel}}{M}\right) \tag{2.16}$$

$$\left(\frac{\omega}{\gamma}\right)^2 = \left(H_{res} - \frac{2K_{4\parallel}}{M} + \frac{2K_{2\parallel}}{M}\right)\left(H_{res} + 4\pi M - \frac{2K_{2\perp}}{M} + \frac{K_{4\parallel}}{M} + \frac{2K_{2\parallel}}{M}\right) \quad (2.17)$$

for $H_{app} \parallel [001], [100], [110] and [1\bar{1}0]$ respectivley.

One should note that eqs. 2.14-2.15 are only valid for the saturated condition, i.e., H is strong enough to align all magnetic moments parallel to its direction.In an FMR experiment, however, for specific anisotropy values the resonance condition can also be fulfilled when the magnetization is not parallel to the external magnetic field direction. This causes an additional resonance at smaller fields with lower intensity (unsaturated mode). However due to the coercivity fields of GaMnAs which are much lower than the resonance fields of such modes they have not been observed in our case. In order to find the dispersion relation (frequency versus field) for the unsaturated mode (unsaturated branch) numerical calculation is needed.

In GaMnAs the four high symmetry axes, and the four Smit-beljers equations along these axes constitute an equation system which can be solved to calculate the anisotropy constants K. Note that in order to determine the these parameters one has to know the magnetization saturation value at various temperature. This is usually achieve by SQUID magnetometry measurements. The intensity of the FMR spectra, which are proportional to the total number of spins in the layer can also be used to deduce this value. This will we shown in following section and will be treated experimentally in chapters 4 and 5.

Different to the case of metallic systems where usually the number of unknown parameters are less than in our case the g-factor in GaMnAs thin films can be only obtained from the fit of the angular variation of the out-of-plane resonance field. In a different approach the g-factor can also be measured via a two frequency measurement.

### 2.1.3 experimental details

In a conventional FMR experiment a magnetic system is exposed to a sinusoidal electromagnetic radiation at a fixed frequency typically in the Gigahertz range. As shown above the resonance frequency is determined by the effective field which includes both external and internal fields. Therefore, the magnetic system can be driven through the resonance condition by sweeping a static external field. When measuring the absorption of the microwave radiation by the sample, the resonance field is found at maximum absorption. In order to enhance the signal to noise ratio, the magnetic field is modulated at 100kHz to use phase sensitive detection. As a consequence, the measured FMR signal is proportional to the field derivative of the imaginary part of the susceptibility ($d\chi^{''}/H$). In the other words the FMR technique is based on measuring microwave losses in a magnetic sample as a function of the

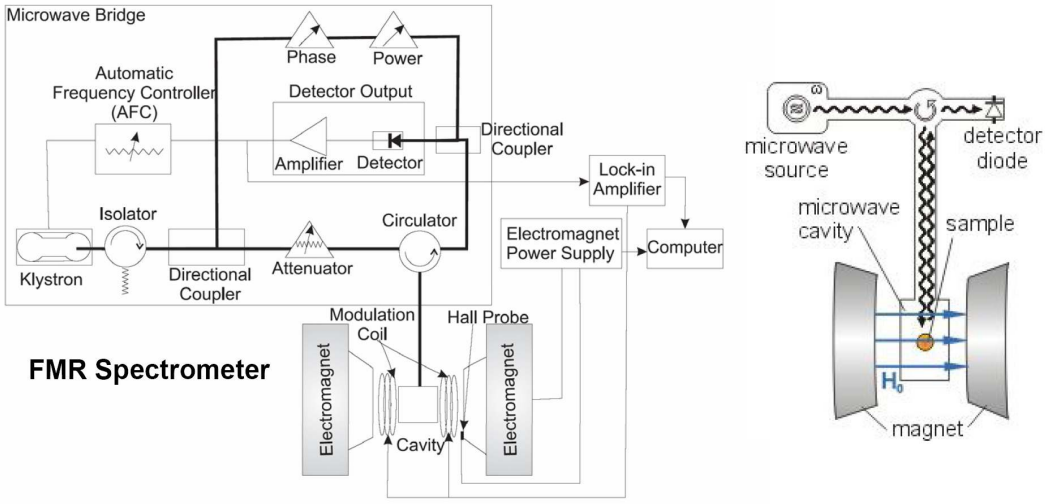


**Figure 2.3:** Schema of FMR spectrometer(left) and cavity setup (right)

external dc magnetic field. The absorbed power P is directly proportional to the imaginary part of the transverse rf-susceptibility.

The schema in fig.2.3 presents the our FMR setup and the microwave circuit. The studied sample are located in the center part of a rectangular $TE_{102}$(/cylindrical $TE_{011}$) cavity for measurements at microwave frequencies of 9.47GHZ(/35GHz), which is between the poles of the electromagnet. A The cavity is coupled to the rectangular wave guide by a small coupling hole (iris). The reflected power from the microwave cavity is monitored by a microwave diode detector. The reflected microwave power is proportional to the absorption of microwaves in the magnetic sample. The sample is cooled to 4K in either an oxford flow cryostat (9GHz X-band) or is immersed with the cavity in the low temperature cryostat.

### 2.1.4 FMR lineshape

The FMR lineshape can be derived from the LL equation and is expected to be Lorentzian. By assuming only small deviations of the magnetization from equilibrium one can (the applied field along x direction) $\vec{M} = (M_x, M_y, M_z) \approx (M_s, m_y, m_z) \approx \vec{M}_s + \vec{m}(y, z, t)$ where $\vec{m}(y, z, t)$ is the radio frequency component of $\vec{M}$ . If one considers only the linear response of the rf driving field $\vec{h}_{rf} = (0, h_y = h_0, 0)$ (linearized equation of motion) the higher order terms in $\vec{H}_{eff}$ can be neglected. By assuming

a simple $exp(i\omega t)$ for time dependence of the oscillatory field the LLG equation of motion gives [3]:

$$\frac{i\omega}{\gamma}m_{\parallel} + \left(H_1^{anis} + \frac{i\omega\alpha}{\gamma}\right)m_{\perp} = 0 \tag{2.18}$$

$$\left(H_2^{anis} + \frac{i\omega\alpha}{\gamma}\right)m_{\parallel} - \frac{i\omega}{\gamma}m_{\perp} = M_s h_0 \tag{2.19}$$

where $m_{\parallel}$ and $m_{\perp}$ are parallel and perpendicular rf magnetizations components with respect to the film surface (i.e. $m_y$ and $m_z$) and $h_0$ is the rf field perpendicular to $\vec{M}_s$; the saturation magnetization. $H_1^{anis}$ and $H_2^{anis}$ are linear combinations of anisotropy fields which depends on the system and the order of anisotropy; i.g. neglecting the effect of $K_{4\perp}$ in this configuration (since the corresponding effective field is proportional to the third power of the r.f. perpendicular magnetization component and it can therefore be neglected in the linearized equations of motion) express them as:

$$H_1^{anis} = H_0 cos(\theta - \phi) + 4\pi M_s - \frac{2K_{2\perp}}{M_s} + \frac{K_{4\parallel}}{2M_s}(3 + cos4\phi) + \frac{K_{2\parallel}}{M_s}(1 + cos(2(\phi - \phi_m)))$$

$$H_2^{anis} = H_0 cos(\theta - \phi) + \frac{2K_{4\parallel}}{M_s}cos4\phi + \frac{2K_{2\parallel}}{M_s}cos(2(\phi - \phi_m))$$

Then the rf-susceptibility can be easily derived from these equations:

$$\chi_y = \frac{m_{\parallel}}{h_0} = \frac{\mu M_s\left(H_1^{anis} + i\frac{\alpha\omega}{\gamma}\right)}{\left(H_1^{anis} + i\frac{\alpha\omega}{\gamma}\right)\left(H_2^{anis} + i\frac{\alpha\omega}{\gamma}\right) - \left(\frac{\omega}{\gamma}\right)^2} \tag{2.20}$$

where $\mu$ is the permeability. It can be shown, from this susceptibility, that the absorption curve has a Lorentzian lineshape. By replacing $H_2^{anis}$ by $H_{res} + \delta H$ in eq.2.20, utilizing the resonance condition to simplify the resulting denominator and then keeping terms that are linear with $\delta H + (\omega/\gamma)(G/\gamma M_s)$ one obtains:

$$\chi_{\parallel} = \frac{\mu M_s}{H_2^{anis,res} + H_1^{anis,res}} \frac{H_1^{anis,res} + \delta H + i\frac{\alpha\omega}{\gamma}}{\delta H + i\frac{\alpha\omega}{\gamma}} \tag{2.21}$$

The imaginary part of the susceptibility can be expressed as:

$$Im[\chi_{\parallel}] = \mu M_s \frac{H_1^{anis,res}}{H_1^{anis,res} + H_2^{anis,res}} \frac{1}{\Delta H_{HWHM}} \times \frac{1}{1 + \left(\frac{H - H_{res}}{\Delta H_{HWHM}}\right)^2} \tag{2.22}$$

comparing this equation y the conventional Lorentzian function $\frac{A}{1+x^2}$ gives the amplitude of the absorption peak via relation:

$$A = \mu M_s \frac{H_1^{anis,res}}{H_1^{anis,res} + H_2^{anis,res}} \frac{1}{\Delta H_{HWHM}} \tag{2.23}$$

It is shown that the FMR intensity is proportional to the magnetization, film thickness and an ellipticity factor $\frac{H_1^{anis,res}}{H_1^{anis,res}+H_2^{anis,res}}$.The r.f. normal modes of the thin film system generally correspond to elliptically polarized oscillations of the magnetization around its equilibrium orientation. When the applied field and the magnetization lie in the film plane the amplitude of the inplane component $m_{\parallel}$ is larger than the amplitude of the perpendicular component $m_{\perp}$ for $4\pi M_{eff}$ greater than zero. When $4\pi M_{eff}$ is negative, the case is inversed. This factor can be calculated from the anisotropy fields.

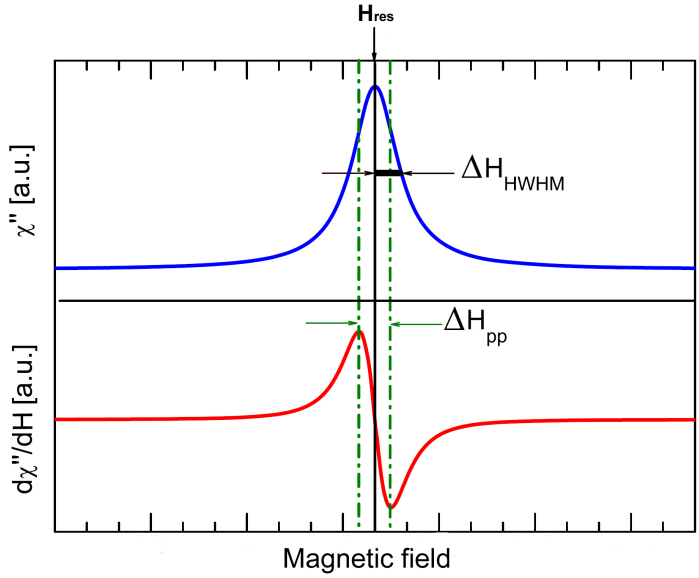


**Figure 2.4:** Standard FMR Lorentzian absorption and its modulated (derivative) spectrum

The FMR absorption line is characterized by the following parameters: resonance field $H_{res}$, the resonance linewidth $\Delta H_{HWHM}$ (half width at half maximum) and the intensity which is proportional to the sample magnetization and the ellipticity factor. In fig.2.4 a schematic FMR spectrum is shown. The signal-to-noise ratio is improved by using a small AC modulation of the external field. The amplitude of the modulation has to be much smaller than the FMR linewidth. The measured signal corresponds to the field derivative of the imaginary part of the transverse

susceptibility. In this case it can easily be obtained from the peak-to-peak linewidth, $\Delta H_{pp}$ which is related to $\Delta H_{HWHM}$ according to:

$$\Delta H_{pp} = \frac{2}{\sqrt{3}} \Delta H_{HWHM} \tag{2.24}$$

The FMR spectra are fitted by the appropriate lineshape functions for resonance field, intensity and linewidth measurements. In general, since due to modulation of the absorption spectra the derivative of them with respect to applied field is detected, the fitting function:

$$y = -A \frac{16 \frac{x - H_r}{W}}{3 + \left( \frac{\frac{x - H_r}{0.5}}{W} \right)^2} \tag{2.25}$$

is used where A,$H_r$ and W are the amplitude, resonance field and linewidth respectively.

Although the case of symmetrical Lorentzian lineshapes are generally accepted, but the noncolinearilty of M and H can also give rise to asymmetric lineshapes which can be modelized by mixed absorbtion and dispersion contributions. this feature can be affected sometimes resulting in the asymmetric lineshapes of the samples. It was mentioned that due to anisotropy reasons, the rf magnetization can have an elliptical polarization in the film plane. Taking account of both positive and negative frequency components (both circular components of exiting linearly polarized microwave field) results in a mixture of absoption-dispersion phases in the output spectra. In this case the fitting function can be used as:

$$y = \frac{a \left( \frac{H_r - x}{W} + 9b - 3b \left( \frac{H_r - x}{W} \right)^2 \right)}{\left( 3 + \left( \frac{H_r - x}{W} \right)^2 \right)^2} \tag{2.26}$$

Where a and b denote the amplitude of the absorption and disperssion signals,respectively. While the relation is valid independent of the origin of the phase mixing, this feature have attributed to different reasons. Ivanshin et al. have considered the metallic character of the sample as the origin of this anomaly, where the skin effect drives the magnetic and electric microwave components out of phase [11], whereas Peter et al. have reasoned that the dynamical character of the susceptibility can also be responsible for this issue [12].

Another type of lineshape often found in epilayers is the Gaussien lineshape. In low quality, inhomogeneous samples the presence of the magnetic regions with slightly different magnetization orientations not only contributes to the linewidth brodening but because of the arbitrary orientation of the magnetizations the form

of the spectra may change into a Guassian lineshape. For these types of spectra one can use the following function for fitting process:

$$y = -A\frac{1.65\frac{x-H_r}{0.5}}{W}e^{\frac{-0.5\frac{(x-H_r)^2}{0.25}}{W^2}} \tag{2.27}$$

# Bibliography


[1] S. V. Vonsovskii, "Ferromagnetic Resonance" (Oxford Pagamon), (1966).

[2] B. Heinrich and J. A. C. Bland, "Ultrathin Magnetic Structures", II-III, Springer, Heidelberg

[3] B. Heinrich and J. F. Cochran, Advances in Physics, 42:5, 523 - 639 (1993).

[4] M. Farle, Rep. Prog. Phys. 61, 755 (1998).

[5] Sawicki, M., F. Matsukura, A. Idziaszek et al. , Phys. Rev. B 70, 245325 (2004).

[6] X Liu, Y Sasaki, JK Furdyna, Phys. Rev. B 67, 205204 (2003).

[7] X. Liu and J. K. Furdyna, J. Phys.: Condens. Matter 18, R245 (2006).

[8] T. L. Gilbert, Phys. Rev. 100, 1243 (1955).

[9] J. Smit and H. G. Beljers, Phillips Res. Rep. 10, 113 (1955).

[10] L. Baselgia, M.Warden, F.Waldner, L. Hutton, E. Drumheller, Y. Q. He, P. E.Wigen, M. Marysko, Phys. Rev. B 38, 2237 (1988).

[11] V. A. Ivanshin, J. D. Deisenhofer et al. Phys. Rev. B, 61 6213 (2000).

[12] M. Peter, D. Shaltiel et al., Phys Rev 126, 1395 (1962).

[13] T. Jungwirth,J. Sinova, J. Masek et al. Rev. Mod. Phys. 78, (2006).

# 3

# The Effect of Strain on the Magnetic Properties of GaMnAs (Tensile vs. Compressive strain)

[1–5]

### *3.1 Influence of the substrate on the strain in the GaMnAs layer*

The quality of epitaxially grown thin layers depends largely on the choice of the substrate and its crystallographic orientation. In order to achieve a high quality epitaxial growth a substrate with the same crystalline structure and preferably with very similar lattice constants is required. In the case of GaMnAs the substrate of choice is of course GaAs which is available in the form of substrates and epilayers with controlled impurity and dislocation densities due to its large use in microelectronics. Nevertheless, the presence of the Mn dopant atoms in the GaMnAs layer, even at some at% concentration will result in a change of the lattice parameters which introduces a mismatch with undoped GaAs substrates. The variation of the lattice constant of relaxed GaMnAs layers with the Mn concentration has been recently determined ( Fig.3.1 ) [22].

If the sample is co-doped with hydrogen in the percent range further modifications of the lattice constants can be expected and have been indeed observed in our study.

Due to the many alloy systems of the III-V compounds a lattice mismatch between the GaMnAs layers can also purposely be introduced in order to engineer the strain in the GaMnAs layer. GaInAs substrates are a good example for this as the strain can be varied by large amounts via the In composition of the substrate. It has been shown by X-ray diffraction that for both substrates, GaAs and GaInAs, the GaMnAs layer will be biaxially strained. In this work all layers have been grown on (001) oriented GaAs or GaInAs substrates. But other orientations have equally been

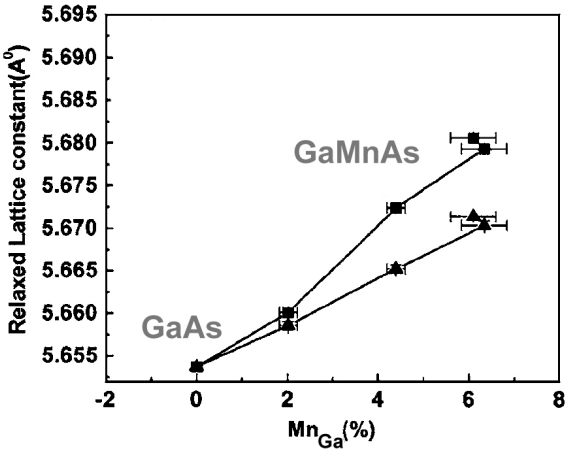


**Figure 3.1:** Relaxed lattice constants for the 50nm-thick GaMnAs films before annealing (squares) and after annealing (triangular) as a function of substitutional Mn content [22].

reported in the literature. The strain induced anisotropy of the magnetic properties can easily be determined by FMR spectroscopy: uniaxial/ biaxial/ trigonal cases symmetries might be expected. Typical values of the strain are$\epsilon_{xx} =\approx 0.17\%$ for $x = 0.05$ and (100)GaAs substrate.

As the Mn doping of GaAs leads to an increase of the lattice constant, layers grown on GaAs buffers are under compressive strain.

On other hand in the case of an GaInAs substrates with (x=0.09) the lattice constants of the substrates are bigger than those of GaMnAs with x=0.05 and the layer will be under tensile strain. In fact, as the lattice constants can be continuously varied by the In compositions the strain can be varied in the same way and actually even strain free layers can be grown.

As mentioned before (see section 1.4), the strain will modify the valence band structure and in particular invert the order of the highest light and heavy hole subband. These shifts and their implications for the magnetic properties have been calculated quantitatively by Dietl et al. [6] Under compressive strain it is the heavy hole band which is uppermost valence band whereas in the opposite case the light hole band lies highest. In addition to the strain splitting of the valence band the hole concentration, which determines the Fermi energy level position, must be considered when evaluation the magnetic anisotropies; in fact, in highly doped metallic samples both subbands will be populated and a distinction between light and heavy holes is no longer possible. A direct consequence of the strain is the orientation of the easy and hard axes of magnetization and layers with either perpendicular or parallel easy axes can be obtained.

Ferromagnetic resonance spectroscopy allows a simple determination of the hard and easy axes of magnetization by the position of the resonance fields. In addition

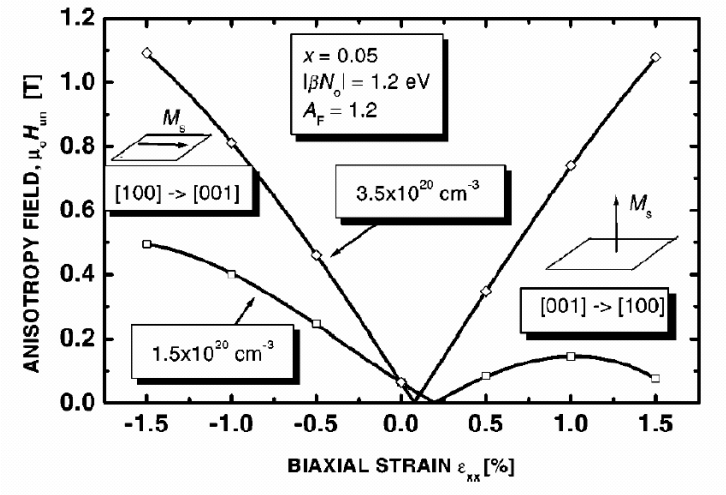


**Figure 3.2:** The points indicate the field required to reorient the magnetization of a GaMnAs sample doped with 5% of Mn as a function of the biaxial strain in the film and different hole concentrations, from one axis to other as indicated. Calculations based on mean field approximation for anisotropies as a function of strain.

it allows to determine quantitatively the magneto-crystalline anisotropy constants and the energy barriers between the different orientations of the magnetization. Let us just keep in mind that the easy and hard axes depend in addition to the strain on the hole concentration and the temperature.

In the following we will examine this aspect and verify the predictions of the mean field model.

## *3.2 Sample preparation*

### 3.2.1 GaMnAs/GaAs

$Ga_{0.93}Mn_{0.07}As$ layers of 50nm thickness have been grown at $250°C$ by low temperature molecular beam epitaxy (LTMBE) on semi-insulating (100) GaAs substrates. A thin GaAs buffer layer has been grown previously to the deposition of the magnetic layer. The as-grown sample were annealed for 1 hour at $T = 250°C$ in air.

### 3.2.2 GaMnAs/GaInAs

The 50 nm thick $Ga_{1-x}Mn_xAs$ layers on GaInAs were equally prepared by LTMBE under very similar conditions. However special care had to be employed to avoid dislocation formation in the relaxed GaInAs layer itself deposited on a

semi-insulating [001] GaAs substrate. To minimize the number of threading dislocations emerging in the magnetic layer [7]the following protocol was adapted. The $Ga_{1-y}In_yAs$ buffer consists first of a ≈0.5nm thick layer grown by increasing monotonously the In content y from 0% to 9.8%. Then 2 to 3nm of $Ga_{0.902}In_{0.098}As$ were grown above before depositing the $Ga_{1-x}Mn_xAs$ layer. The graded $Ga_{1-y}In_yAs$ layer prevented the formation of a too large amount of misfit dislocations, sources of threading dislocations propagating along <011> toward the surface, as usually observed at abrupt mismatched interfaces. Here, dislocations were distributed along the graded layer, which limits the nucleation of threading dislocations [7]. Indeed, a very low density of emerging dislocations,$\approx 4 \pm 2 \cdot 10^4 cm^{-2}$, was measured using an anisotropic revealing etchant. Moreover, the substrate temperature was set to $400°C$ during the growth of the buffer to avoid the formation of three-dimensional strain-induced islands, a process favoured at higher temperature. The $Ga_{1-x}Mn_xAs$ layer was deposited at $250°C$.

The quality of the surface was verified by the means of optical differential interference contrast microscopy. It revealed a rough surface originating from bunches of misfit dislocations propagating along [110] and $[1\bar{1}0]$ inside the graded layer.

The [In,Ga]As layer was shown by x-ray diffraction to be almost completely relaxed (at 80%).This fact insured the existence of the tensile strain in the $Ga_{1-x}Mn_xAs$ layer.

The concentration x was estimated to be ≈ 0.07, by comparison with similar layers grown on the GaAs substrates. Finally, a part of the sample was annealed under nitrogen atmosphere for 1 h in a tube furnace at $250°C$ to out-diffuse the interstitial Mn atoms, in order to improve magnetic properties (cf. section 1.4.5 ).

## *3.3 Magnetization measurements*

### 3.3.1 GaMnAs/GaAs

The magnetization of the GaMnAs/GaAs as grown sample is shown in fig. 3.3 as a function of temperature for different in-plane orientations of the applied field H=20Oe. The diamagnetic contribution of the thick substrate and buffer layers (≈600 microns) does not permit the application of higher fields. On the other hand one should notice that for this sample this low applied field can not align all the magnetic moments to their saturation state. The figure indicates an easy axis along [100] at T=4K which reorients along the $[1\bar{1}0]$ direction from T≈25K.

Figures 3.4 and 3.5 present the magnetization of the annealed sample as a function of applied magnetic field and temperature respectively. Note that the M(T) spectra were measured for an applied field of H=20Oe again. The easy axis is found to be along $[1\bar{1}0]$ direction for this sample. Although the wide peak around 130K along [110] is normally attributed to an easy axis reorientation, no such event is

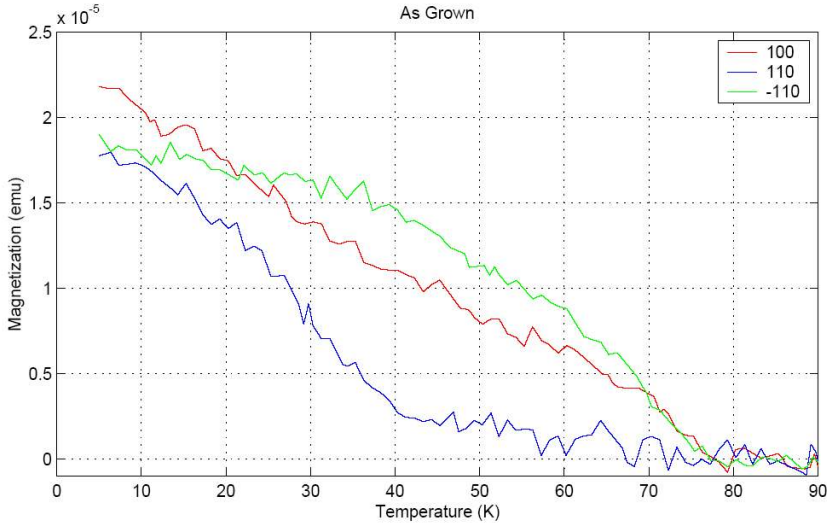


**Figure 3.3:** Magnetization as a function of temperature for in-plane easy axes of GaMnAs/GaAs as-grown sample ($x \approx 0.07$) measured by SQUID device in the presence of an applied field = $20Oe$ . The size of the sample is $4mm \times 4.5mm \times 50nm$

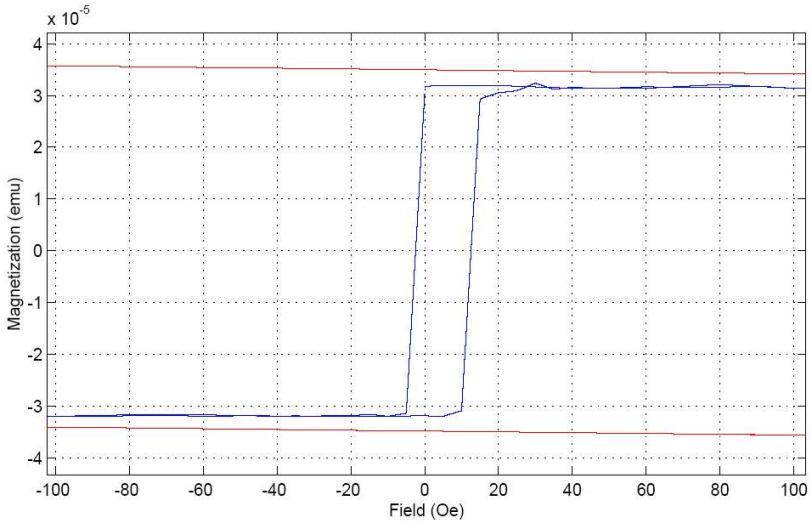


**Figure 3.4:** Magnetization as a function of applied magnetic field for in-plane $[1\bar{1}0]$ axis of GaMnAs/GaAs annealed sample ($x \approx 0.07$) measured by SQUID device.The size of the sample is $4mm \times 4.5mm \times 50nm$.

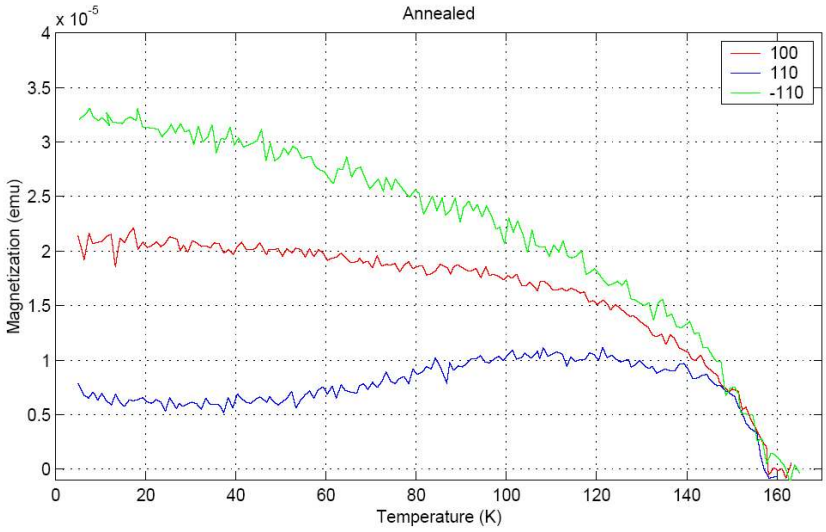


**Figure 3.5:** Magnetization as a function of temperature for in-plane easy axes of GaMnAs/GaAs annealed sample ($x \approx 0.07$) measured by SQUID device in the presence of an applied field = $20Oe$. The size of the sample is $4mm \times 4.5mm \times 50nm$.

observed for the other two axes. The M(H) curves present a square-like hysteresis curve along $[1\bar{1}0]$ direction. This feature is what is usually observed along an easy axis orientation.

These measurements will be further discussed in the context of the magnetic anisotropy constants in section 3.4.3.

### 3.3.2 GaMnAs/GaInAs

The electrical resistivity curves shown in fig.3.6 illustrate the enhancement of the Curie temperature (although they do not allow a precise measurement of the Curie temperature) for the annealed sample (section 1.6 and [9]) as well as a considerable decrease in the resistivity (e.g. at T=4K from 13 to 2.58 m$\Omega$); a similar variation is observed for the sample under compression strain.

Fig.3.7 (a) and (b) are the Hall hysteresis loops extracted from the transverse resistivity. In GaMnAs like in all other semiconductors the anomalous Hall effect $\rho^a_{xy}$ is dominant over the normal Hall effect. Although this feature is still not completely understood and its origin is out of the scope of this thesis, it is expected to be induced through spin-orbit coupling, by anisotropic scattering of the spin-up and spin-down carriers. It is proportional to the perpendicular projection of the magnetization $M_\perp$ along the film's normal direction.

$$\rho^a_{xy} = R_a(\rho_{xx})M_\perp \tag{3.1}$$

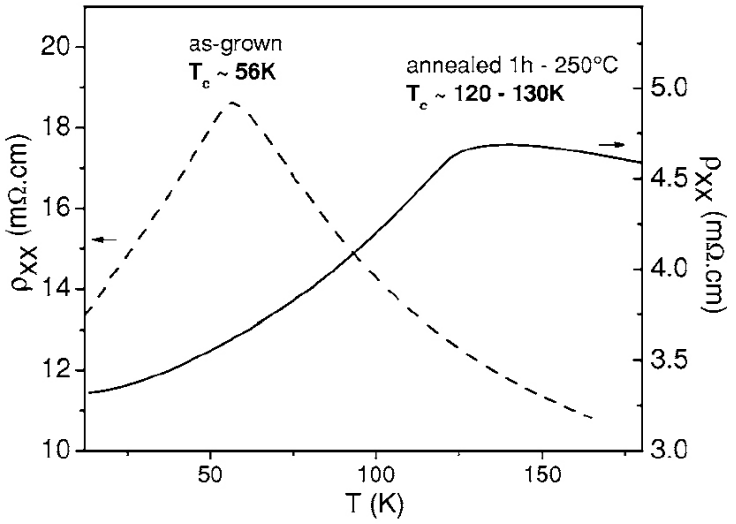


**Figure 3.6:** Thermal dependence of the longitudinal resistivity for the as-grown (Ga,Mn)As film (dashed line, left), and for the annealed sample (full line, right) [8].

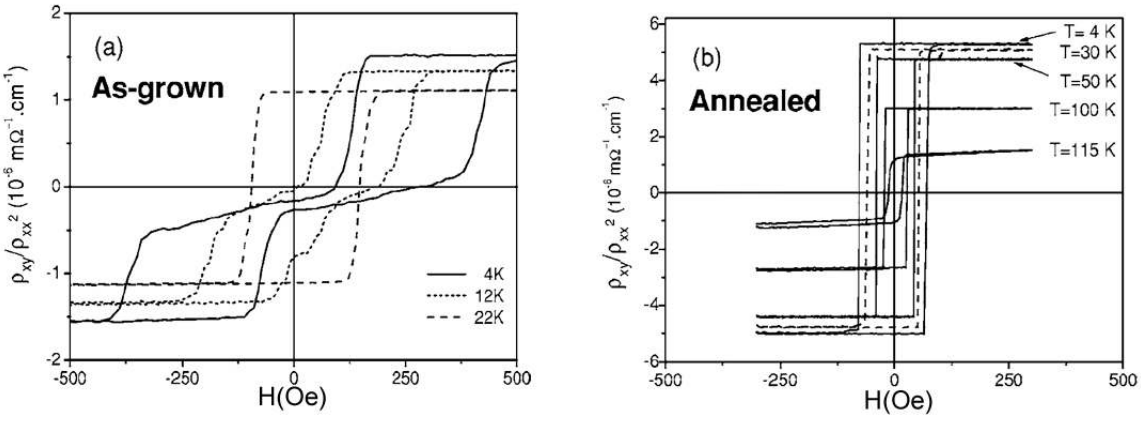


**Figure 3.7:** Magnetic hysteresis loops measured by the Hall resistivity at low temperatures: (a) as-grown and (b) annealed GaMnAs/GaInAs 50nm thick films ($x \approx 0.07$). Sweeping rate of the magnetic field is 17 Oe/s.

where $R_a$ which presents the anomalous Hall term is proportional to $\rho_{xx}^{\gamma}$ the sheet resistivity. The value of the power factor $\gamma$ is still a matter of debate (cf. [10]). It is in the range of $1 \leq \gamma \leq 2$. However, for high quality samples this value is found to be equal to 2 [11].Thus, here the value $\rho_{xy}/\rho_{xx}^2$ is proportional to the magnetization of the sample along the growth direction. As is shown in fig.3.7 for the as-grown sample, from T=22K the Hall resistivity presents a hysteresis feature which indicates the existence of the easy axis normal to film plane. Whereas, at lower temperatures the hysteresis curve has a more complicate form. This feature which is explained in the frame of the valence band structure in section 1.7 and which will be treated experimentally in the following section 4 is attributed to the low concentration of charge carriers and the Fermi energy level and the resulting anisotropies which favor an in-plane easy axis for these temperatures. Since in this chapter the subject is strain related magnetic anisotropies of the films, we will leave this feature to be studied in its own section. The annealed sample on the other hand shows a hysteresis cycle for all investigated temperatures. For this sample an easy axis along the [001] direction is measured for all temperatures up to $T_C$.

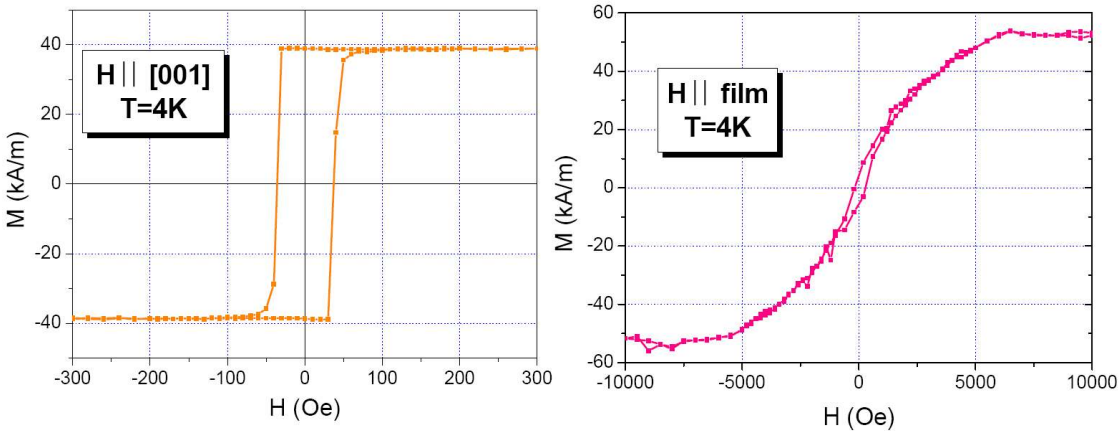


**Figure 3.8:** GaMnAs/GaInAs 50nm thick annealed sample ($x \approx 0.07$) magnetization as a function of applied field for [001] perpendicular to film plane (left panel) and parallel to in-plane hard [110] axis (right) measured by SQUID device. (in order to compare with other figures note that $kA/m \equiv emu/cm^3$)

The SQUID magnetization curves of the sample as a function of applied field, are shown in fig. 3.8 for both the in-plane and perpendicular directions. While for the [001] direction of the applied field the magnetization along the field presents a good square hysteresis cycle with a coercivity field of ≈40Oe (for a slow field sweep of 0.08 Oe/s), the in-plane magnetization for H‖film plane shows no hysteresis cycle and the saturation magnetization is not achieved before an applied field of about

6000Oe. Both curves saturate coherently at about 40(emu/cm$^3$). Considering the estimated 7% Mn doping level, the fraction of the magnetically active Mn ions in the sample is 55% (or via a simple model ≈22% interstitial Mn ions. Here we have neglected the negative contribution of the holes to the total value of M due to their minor role in this case 4.7.

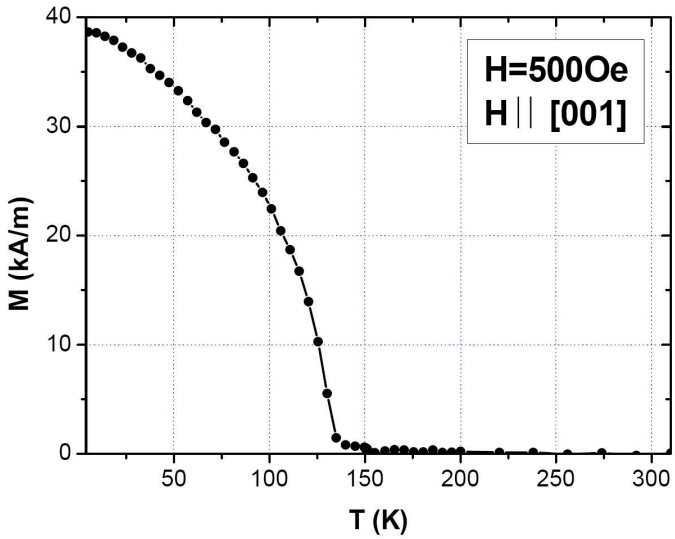


**Figure 3.9:** GaMnAs/GaInAs 50nm thick annealed sample ($x \approx 0.07$) magnetization as a function of temperature in the presence of applied field H=500Oe along [001] direction of the film measured by SQUID device.

The variation of the magnetization with temperature M(T) is presented in fig. 3.9 for a magnetic field of 500Oe oriented perpendicular to the film plane. It can be well fitted by a Brillouin function for S=5/2. This feature predicts the absence of any second ferromagnetic phase as well as the reorientation of the easy axis at any temperature. The critical temperature is $T_C$=140K.

The Curie temperature deduced from the temperature dependence of the intensity of the FMR spectra is slightly higher as one measured by SQUID due to the presence of a stronger applied magnetic field imposed by the resonance condition.

### *3.4 FMR measurements*

In this section we will present the results of the FMR measurements of as-grown and annealed GaMnAs films under both tensile and compression strains. It is shown how FMR measurements can be applied to investigate the effect of strain in the samples. Fig.3.10 presents the FMR resonance field corresponding to two tensile and compressive strained annealed samples. The high symmetry axes of magnetization

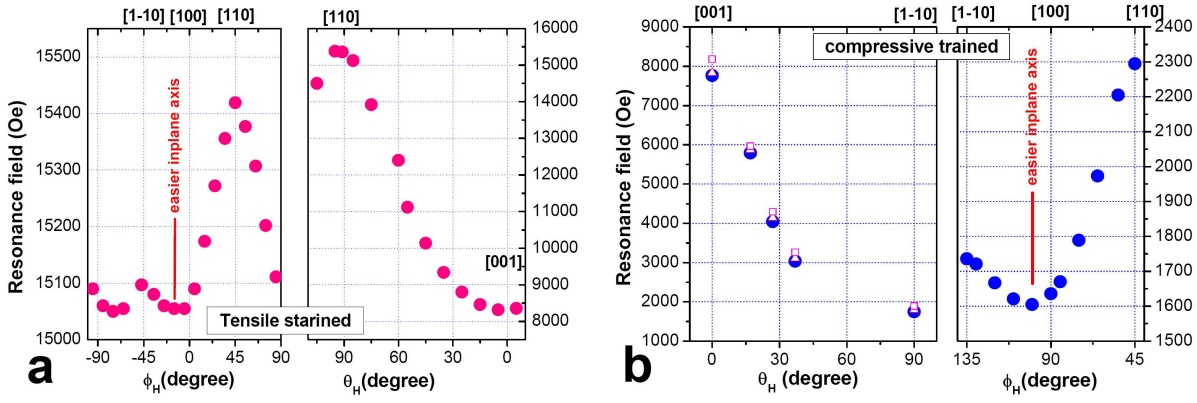


**Figure 3.10:** Angular variation of FMR resonance field for different orientations of applied magnetic field in [001] and /[1$\bar{1}$0] planes (presented by $\phi$ and $\theta$ respectively ) for GaMnAs/GaInAs (a) and GaMnAs/GaAs (b) annealed samples($x \approx 0.07$).

in GaMnAs matrix are labeled by their orientation. And the resonance fields along different axes are obtained by changing the orientation of the applied field with respect to the film in two [110] (/[1$\bar{1}$0]) (out-of-plane) and [001] planes; as it is described in section 2.1.1. The four axes correspond to different resonance fields which denotes the anisotropy of the magnetization. The rotation of applied field in [1-10] axis, which is called the out-of-plane configuration, reveals a two-fold symmetry in this plane. It is a usual case for ferromagnetic thin films epitaxied on a substrate with different lattice parameter. As it was explained in chapters 1 and 2 and also in section 3.1, this results in a strain in the sample. The strain in this direction can be simply expressed as a uniaxial perpendicular anisotropy constant ($K_{2\perp}$) in the free energy density of the system and because of the cubic structure of GaAs the in-plane axes should have a four-fold symmetry (the anisotropy between axial and diagonal directions). In addition to the strain, there is the contribution of another parameter including in $K_{2\perp}$. We will see in next chapter how one can distinguish these two contributions applying mean field approach for GaMnAs.

In fig.3.10, the panels corresponding to inplane configuration (different orientation of magnetic applied filed ($\phi_H$) in plane [001]), show that while there exists a four-fold symmetry of cubic crystalline structure (difference of resonance field between H along cubic axis [110] and diagonal axis [100]), it is slightly disturbed by an additional anisotropy along [110] and [1$\bar{1}$0] directions. Although the origin of this anisotropy is still a matter of debate, the proposed models have attributed it to the substrate influence on the layer. For the (001) GaAs substrates that were used for growing our samples, the last layer is composed of As or Ga atoms with electrons which are not bound. In this case they tend to form dimers which results in the

reconstruction of the surface of GaAs. Since the dimers are along specific axes, a supplementary stress is applied to the layer [23]. A supplementary model proposed the incorporation of the manganese ions along the As dimers during the growth, which results in a trigonal strain and the relevant sheer stress ($\epsilon_{xy} \neq 0$) [24].

Note that while the form of the angular variation for both samples are quasi-similar, the respective resonance fields which indicates the order of the axes are different. While the resonance field measured for $H \parallel [001]$ has the largest value among the four high symmetry axes (and so it considered as the hard axis of magnetization) in the GaMnAs/GaAs sample, the resonance field for the same direction of applied field in the tensile strained sample denotes that it is the easy axis of magnetization. The relative order between the inplane axes are

In following subsections the preferential magnetic axes as well as the Curie temperatures and the magneto-crystalline anisotropy constants will be discussed in more details and a comparison between the two samples and to the prediction of mean field theory model will be made. the particular case of relaxation of magnetization will be studied in chapter 5. Both in order to be able to obtain the essential informations for relaxation discussion and because of some special aspects of our samples the FMR measurements were performed via both X-band and Q-band microwave fields.

### 3.4.1 X-band measurements (9.47GHz)

The angular variations of the uniform mode spectra were measured in the two different in-plane and out-of-plane rotation planes (cf. section 2.1.1).

#### *3.4.1.1 GaMnAs/GaAs*

In fig.3.11 we present the spectra obtained for the as-grown sample for B‖[001] obtained in "out-of-plane" configuration and the resonance spectra for three in-plane high symmetry orientations at 4K. The spectra present clearly an easy axis along [100] and the hard axis along the [001] direction. These directions are in agreement with the SQUID measurements (cf. fig.3.3). The spectrum along the [001] direction, which has a mixed absorption / dispersion lineshape, is composed of one main resonance line and additional small intensity resonances. The resonance with the highest intensity at ≈7800Oe is the FMR uniform mode of this film. The second resonance is attributed to the first mode of spin-waves (k=1). While in the absence of higher spin-wave modes to justify this claim, this could also be the result of a sample inhomogeneity composed of regions with different magnetic moments, the additional resonance spectrum near H=3300Oe reinforces the spin wave model interpretation. Our observation are different from those of Rappoport et al. [12] who have reported the disappearance of the spin-waves for GaMnAs/GaAs layers for thicknesses below

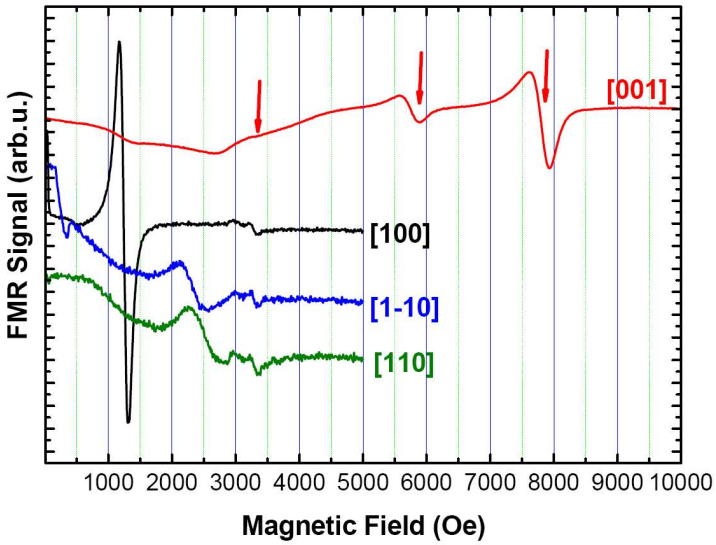


**Figure 3.11:** FMR spectra for GaMnAs/GaAs 50nm thick as-grown sample ($x \approx 0.07$) at T=4K for four high symmetry axes as indicated. Along [001] hard axis direction the spin-wave modes are shown by arrows, included the first spin-wave mode which can be considered as the uniform mode. (microwave frequency=9.47GHz)

100nm. The extension of the resonance fields from hard to easy axis for this as-grown sample is particularly large (compare to the other similar reported works). The single and uniform line-shapes and relative small line-widths for this sample show its high quality.

The FMR spectra for this sample were measured as a function of temperature between 4K and 85K. At a temperature of ≈40K an easy axis reorientation along the $[1\bar{1}0]$ direction is observed. For H ∥ [001], the hard axis, the spin-wave resonance is observable up to 80K. The Curie temperature for this sample is slightly lower than 85K, taking in account the 3000Oe applied field in FMR. The evolution of the FMR spectra are shown in fig.3.12.

The same approach was followed for the annealed sample. In fig.3.13 the spectra of the annealed sample in the out of plane configuration are shown for T=4K. As can be observed, the second low intensity resonance has become very weak compared to the main resonance. This sample can be considered as perfectly homogeneous. The line-widths of the spectra are reduced which indicates that the annealing conditions are quite optimized. Here again the large field extension of the spectra from hard to easy axes is very particular for this samples. Increasing the gain by a factor ×12.5, a third resonance very lightly separated from the first one is observed which because of the weak separation can be ignored. The spectra taken with a higher gain show the existence of a fourth resonance. However we will treat this case in

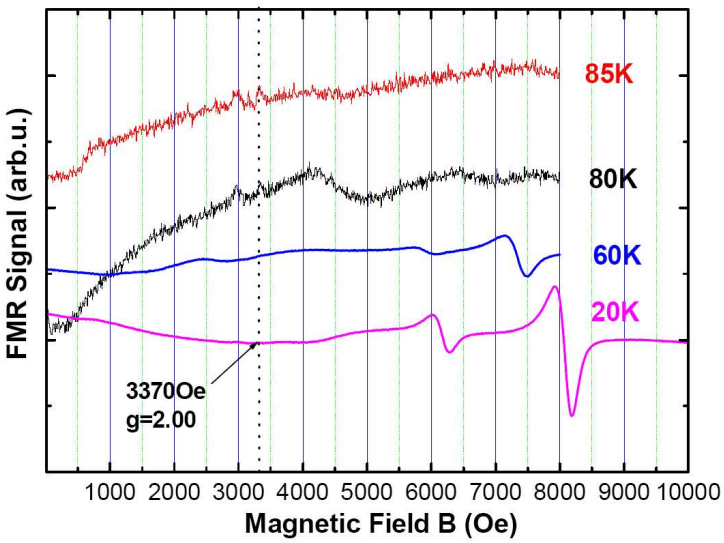


**Figure 3.12:** FMR spectra of GaMnAs/GaAs 50nm thick as-grown sample ($x \approx 0.07$) for applied static field along [001] axis of the film as a function of temperature. The dotted line indicated the field H=3370Oe corresponding to g=2.00. (X-band)

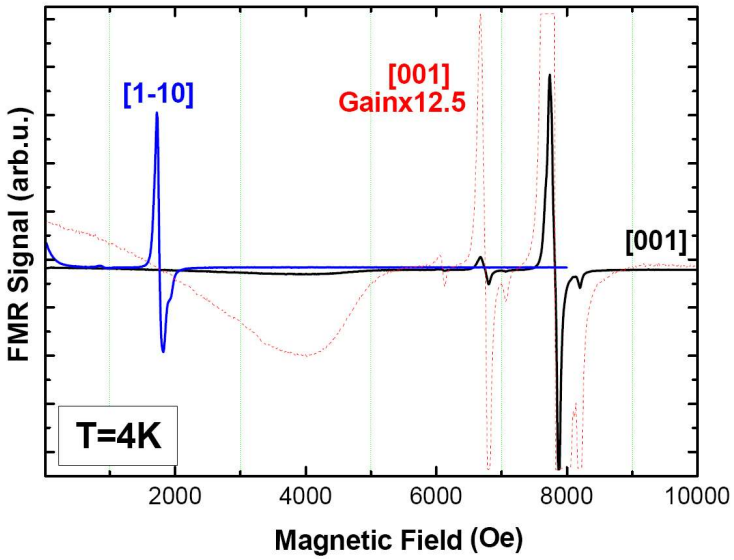


**Figure 3.13:** FMR spectra of GaMnAs/GaAs 50nm thick annealed sample ($x \approx 0.07$) along [1$\bar{1}$0] and hard [001] axes at T=4K. The red dotted line presents the same spectrum along [001] direction but with a gain 12.5 times larger. (X-band)

a next sections (see section 3.5). Thsse additional spectra can be attributed to the spin waves of higher modes (K≠0). Also note that in the spectrum H‖[1$\bar{1}$0] two other resonances in addition to the intense uniform mode are observed: one at lower field with H≈900Oe and one at higher field.

The easy axis orientation is particular for this sample. It is not exactly along one of the four high symmetry orientations of the zinc-blende structure but in between [100] and [1$\bar{1}$0] with 10° deviation from the former. The [100] direction is an easier axis than the [1$\bar{1}$0] direction. Such subtle misorientations related to competing cubic and uniaxial anisotropies cannot be determined by SQUID M(T) measurements (fig.3.5).

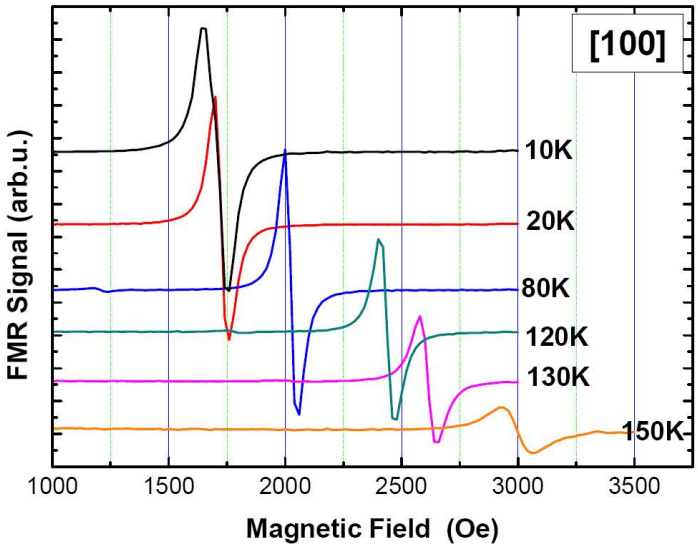


**Figure 3.14:** FMR spectra of GaMnAs/GaAs 50nm thick annealed sample ($x \approx 0.07$) along [100] axis as a function of temperature. (X-band)

The Curie temperature of this sample is investigated by FMR measurements in higher temperatures. Spectra in fig.3.14 shows $T_C$ ≈170K. This value is higher than the SQUID measurements which presents the $T_C$=157K.

#### *3.4.1.2 GaMnAs/GaInAs*

In this case the tensile strain induced by the substrate leads to a perpendicular [001] easy axis. The as-grown sample how ever is a special case (cf. 3.3 ). This sample shows an in-plane easy axis for temperatures below 20K. This feature is attributed to the competition between the hole concentrations and the strain spitting of the valence band which will be discussed in section (4.11.1).

The annealed sample was measured in detail by FMR in both in-plane and out-of-plane configurations. This sample also has some special features. The first particularity of the spectra is their different lineshape, which is a Gaussian lineshape. Whereas the Lorentzian lineshape is the natural shape expected from the LL equation, a Gaussian lineshape is a clear indication of an inhomogeneous sample. In order to get more information on the inhomogeneous aspect of this sample follow the discussion in section 6.4.2.

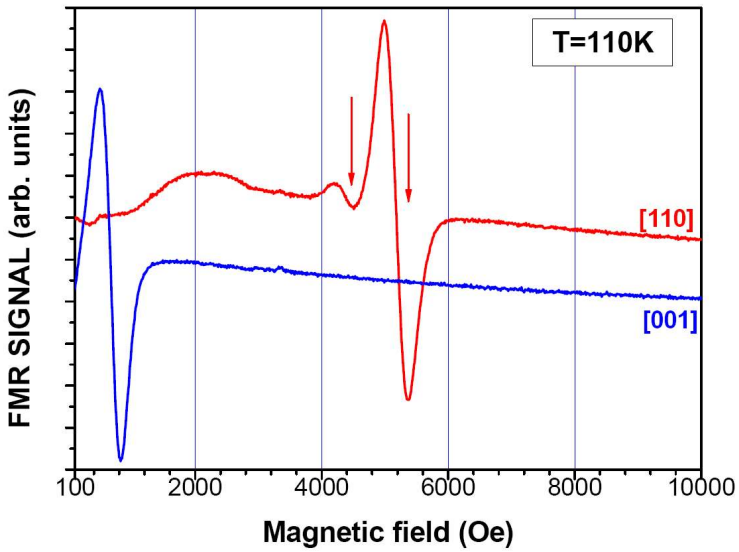


**Figure 3.15:** FMR spectra of GaMnAs/GaInAs 50nm thick annealed sample ($x \approx 0.07$) in out-of-plane configuration for two [001] easy and [110] hard axes of magnetization at T=110K. The two resonance fields corresponding to spin-wave modes along the hard axis are marked by arrows. (X-band)

At T=110K both the out-of-plane and in-plane variations show a "normal" FMR spectrum consisting of one dominant anisotropic FMR single line spectrum. As can be seen in fig.3.15 and 3.16 while the hard axis lies in-plane along the [110] direction the easy axis is perpendicular to the layer. A small intensity additional line is observed (red arrow) along the [110] which is attributed to either a spin-wave mode or a small magnetic inhomogeneity in the sample. Fig.3.17 shows the out-of-plane angular variation of the resonance field. One notices the appearance of a second resonance for $\theta_H = 30°$. This second resonance which disappears as we get close to the in-plane directions is attributed to the first mode of spin-waves. Considering its disappearance above a critical angle and the probable presence of surface pinning centers its attribution to spin wave seems probable [12].

We have started this subsection with the presentation of the high temperature spectra since as shown in fig.3.18 at lower temperature -below 80K- no FMR spec-

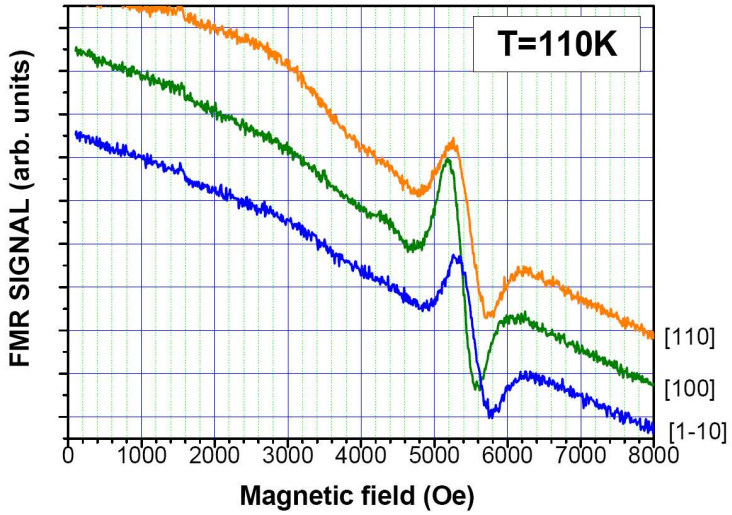


**Figure 3.16:** FMR spectra of GaMnAs/GaInAs 50nm thick annealed sample ($x \approx 0.07$) for three in plane high symmetry axes at T=110K. (X-band)

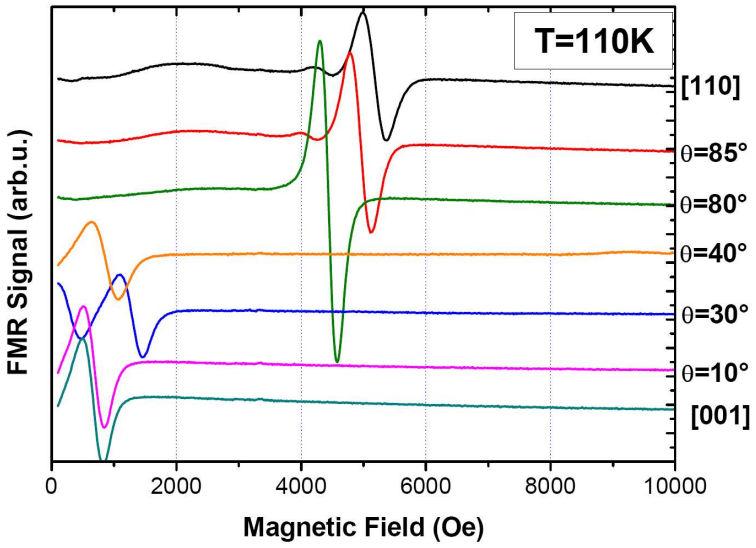


**Figure 3.17:** FMR spectra of GaMnAs/GaInAs 50nm thick annealed sample ($x \approx 0.07$) for different orientations of the applied field with respect to the [001] direction of the film for rotation around the $[1, \bar{1}, 0]$ axis, at T=110K. (X-band)

trum can be observed at X-band for the easy axis orientation H||[001]. This is the second particularity of this sample. In this case again [110] is the hard axis and there is no modification of the order of the other two axes as a function of temperature.

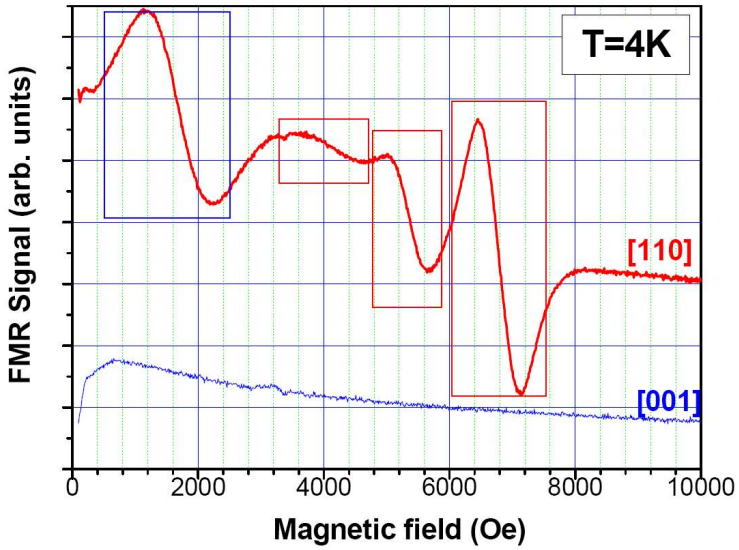


**Figure 3.18:** FMR spectra of GaMnAs/GaInAs 50nm thick annealed sample ($x \approx 0.07$) for applied field along hard, [110], and easy, [001], axes of magnetization at T=4K. (X-band)

Contrary to the simple situation observed at T=110K (one dominant single line FMR spectrum) we observe for B||[110] at T=4K at least four resonance lines. For the three high field spectra (red squares) two models can be proposed:

1. one uniform mode FMR line at 6800G with two resolved spin waves (fig. 3.18, 3.28 )

2. three FMR lines which are the manifestation of an important magnetic inhomogeneity of the sample

The low field line (blue square) is:

1. either the result of differently magnetized part of the film with an easy in-plane axis or

2. an unsaturated mode which can be found as a second solution of the FMR equation

To distinguish between the different models the angular variation of the FMR spectra has to be analyzed.

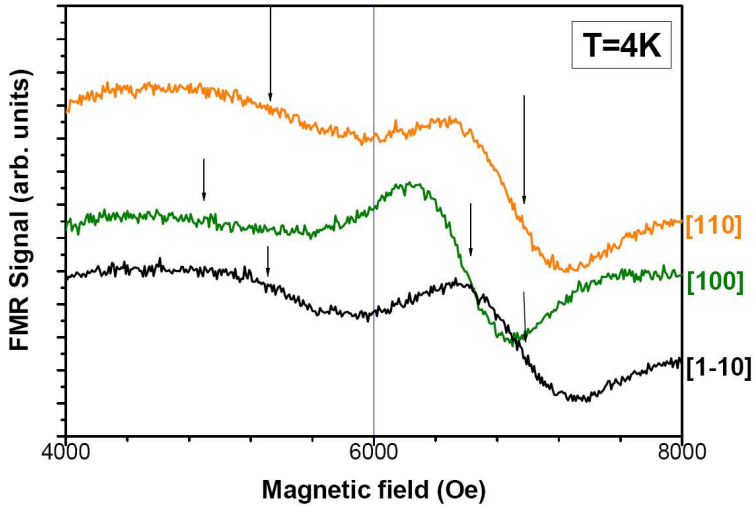


**Figure 3.19:** FMR spectra of GaMnAs/GaInAs 50nm thick annealed sample ($x \approx 0.07$) for applied field along three hard in-plane axes of magnetization at T=4K. (X-band)

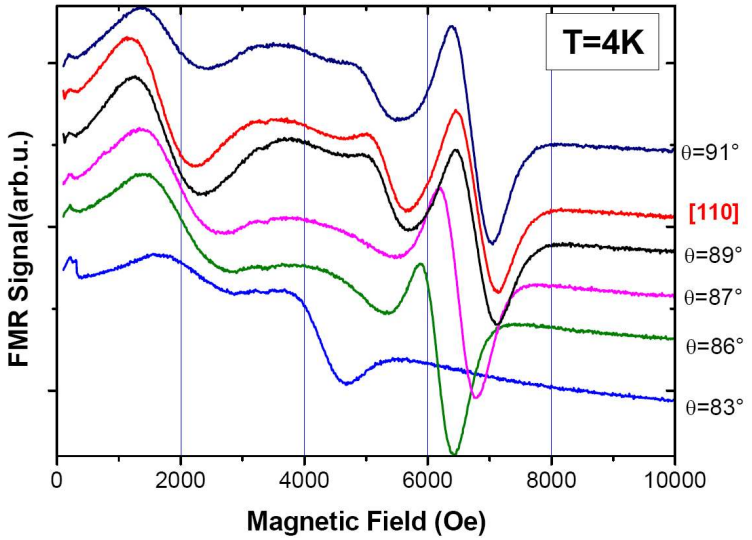


**Figure 3.20:** FMR spectra of GaMnAs/GaInAs 50nm thick annealed sample ($x \approx 0.07$) for angular variation of applied field in th $[1\bar{1}0]$ plane at T=4K. (X-band)

For slight deviations ($\pm 10°$) of the applied field from the $[1\bar{1}0]$ axis, we observe different angular variations for these lines (fig.3.20). The high field lines move to lower fields as expected for this "hard axis" orientation whereas the low field line moves to higher fields in line with an easy in-plane axis model.

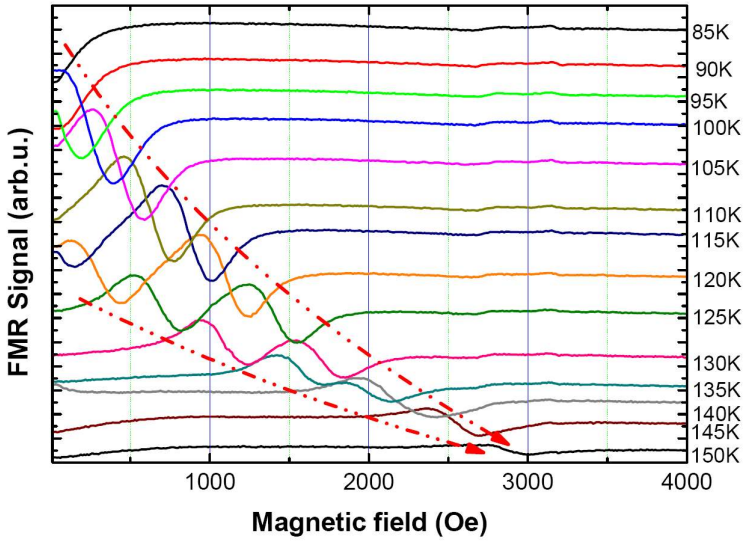


**Figure 3.21:** FMR spectra of GaMnAs/GaInAs 50nm thick annealed sample ($x \approx 0.07$) for applied fields along [001] easy axis as a function of temperature. The two dashed lines are guidelines to present the evolution of the two separated resonance spectra as a function of temperature.(X-band)

For orientations of the magnetic field $> 10°$ from the [110] direction all resonance lines broaden drastically and no spectrum is detectable for any field orientation (fig. 3.18). In particular for $B \parallel [001]$, the easy axis of magnetization, no FMR spectrum is observed at all which excludes an quantitative analysis of the FMR spectra. In order to understand the current situation the FMR for easy axis is measured progressively as a function of decreasing temperature from T=85K. The result which is shown in fig.3.21 indicates that for temperatures lower than 90K the easy axis resonance moves to negative fields. As the difference between the [001] and in-plane axes resonance fields is determined by the perpendicular uniaxial strain, hence, in tensile strained GaMnAs films the easy axis of magnetization ([001]) coincides with the strong uniaxial second order anisotropy direction. For that reason no FMR resonance can be observed at temperatures below T≈90K for the easy axis orientation H‖[001] at X-band. One should note the appearance of the second resonance for temperatures ≈120K. This particular case is distinguished by both the variation of two resonances and their relative intensities as a function of temperature. The case is discussed in the spin-waves section (3.5). In order to obtain more quantitative

information of magnetic properties of the film for this range of temperature the measurements were continued in Q-band in which the shift of all spectra to higher fields gives access to the resonance spectra which lie in negative fields in application of X-band measurements.

Fig.3.21 shows the evolutions of the resonance spectra as a function of temperature from 4K to $T_C$ which is measured to be 150K (again note the 3300Oe applied field).

### 3.4.2 Q-band measurements (34GHz)

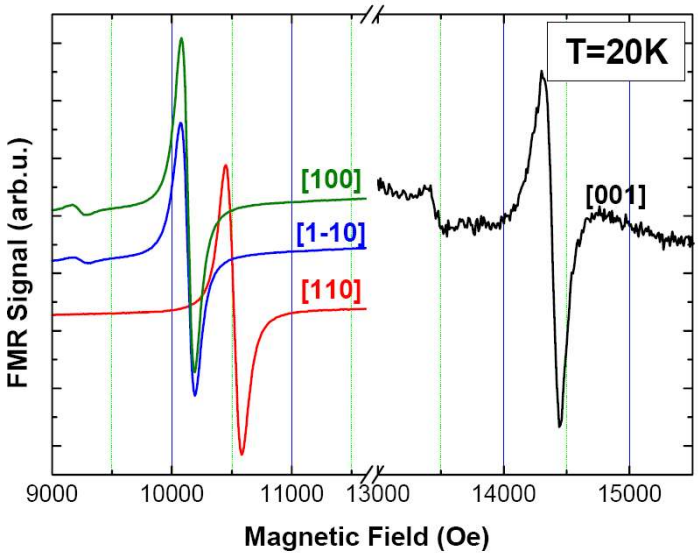


**Figure 3.22:** FMR spectra of GaMnAs/GaAs annealed sample ($x \approx 0.07$) for applied field along the in-plane and normal-to-plane high symmetry axes of film at T=20K (Q-band)

The same measurements as in X-band were also performed at Q-band for two annealed samples. This not only enables us to deduce further information on the relaxation processes and the corresponding damping factor, but also in the case of GaMnAs/GaInAs sample gives supplementary information that was missing due to the non observation of the resonance field along easy axis at low temperatures.

Fig.3.22 presents the FMR spectra for GaMnAs/GaAs annealed sample at T=20K for different orientation of applied magnetic field. As shown in the figure the lineshape still fit with the first derivative of Lorentzian absorption curve. The spectra have kept their relative distances and are only shifted by 9000Oe to higher fields. Their width has also increased by approximately a factor 2. The latter feature will be discussed in detail in the section 6.4.1. Despite of this broadening the first

spin-wave mode is still observable for H||[001] but the resonance spectra which was attributed to the slight inhomogeneity of this sample is no longer observed.

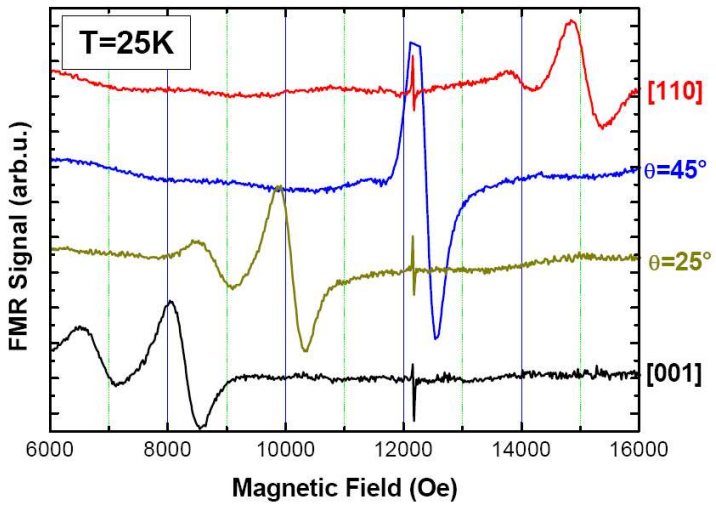


**Figure 3.23:** Angular variation of the FMR spectra for GaMnAs/GaAs 50nm thick annealed sample ($x \approx 0.07$) as a function of different applied field orientations in $[1\bar{1}0]$ plane at T=25K (Q-band)

Fig. 3.23 shows the FMR spectra of tensile strain sample at T=25K. As the same as former case here also the spectra have kept their initial form as X-band measurement. As one observes a second low field resonance is systematically observed at X-band and Q-band; it is attributed to a spin wave resonance.

### 3.4.3 Simulations, anisotropy constants and discussions

As the GaMnAs/GaAs sample presents a good example of a high quality sample, it will be treated as a reference sample for further investigations in this essay. Thus the magnetic properties of this sample are studied in detail.

The angular variation of the resonance field for both FMR configurations which were presented in section 2.1.1, are demonstrated in fig. 3.24 of the two samples. For the GaMnAs/GaInAs sample the application of Q-band measurements enabled us to deduce the resonance fields missing in X-band measurements. Hence the angular variation shown in fig.3.24 are shown in different bands for the two samples. It should be recalled that because of the high Curie temperature of the samples the resonance fields do not have a considerable change between 4K and 20K, thus the presented simulations can be compared in a good approximation. The measured data were fitted using the equations 2.1, 2.10 and the equilibrium conditions of the magnetization. As it is presented the simulated angular variations were fitted for

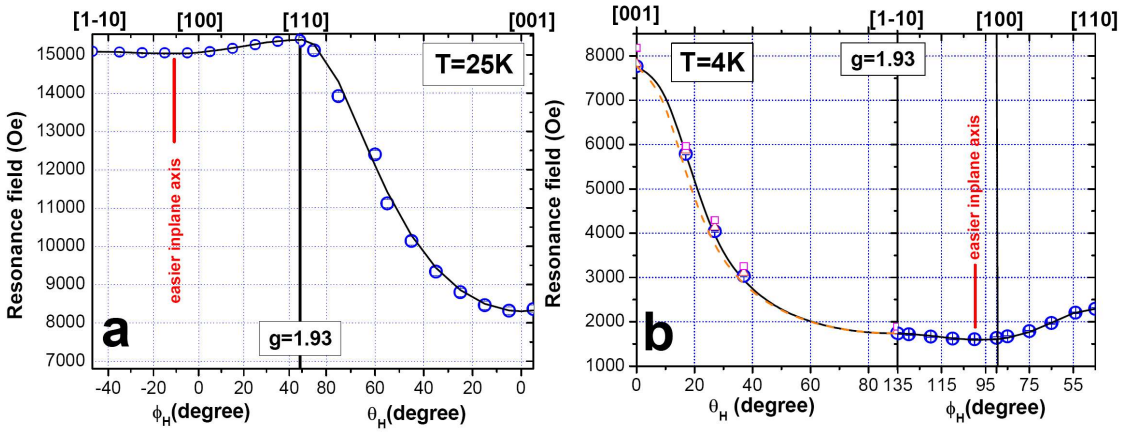


**Figure 3.24:** FMR resonance field as a function of angular variation of the applied field orientations with respect to film axes for (a) GaMnAs/GaInAs sample at T=25K (Q-band) and (b) GaMnAs/GaAs sample at T=4K (X-band). For both samples $x \approx 0.07$. The open triangles and squares in panel b represents the weak intensity resonance fields found superposed to the main one in each direction.

both samples using same LandÈ factors. From these fits the best simulation is found for g=1.93. For the sample under compression strain the dashed line presents the simulation with g=2.00. The parameters influencing the g-factor are discussed in section 4.10 . This value which is in good agreement with transport measurement justifies our claim about the metallic behavior of the sample. The supplementary resonances, a part from the main FMR uniform mode are presented on the graph in order to show their variation. As it is shown their separation become smaller for intermediate orientations of the applied field. These simulations enables us also to determine the deviation between the magnetization and the applied field orientations for different directions in the film. This is where we conclude for sure the orientation of the "real" easy axis of magnetization for both samples lies along the 10° from the in-plane [100] to $[1\bar{1}0]$ axis.

It is observed that the difference between the $[1\bar{1}0]$ as the harder axis and the [100] as the easier axis is small which indicates the small magnitude of in-plane anisotropy (cf. section 2.1.1). The other particular characteristic is the relatively high difference between the [110] and $[1\bar{1}0]$ resonance fields which is usually very weak.

As it was discuss further above (section3.3 and fig.3.5), there was a contradictory easy axis determination between SQUID and FMR measurements and the fact was promised to be explained in this section. The key to explain this difference lies in the real easy axis of magnetization of this sample. As it was mentioned, the SQUID

measurement were done in the presence of an applied field of 20Oe. From the FMR angular variation simulations one discovers that the even fields as high as 1700Oe can not align the magnetization along the [100] direction. Since the minimum of the energy surface resides in the vicinity of this axis and as concerns the energy surface (for details on the energy surface description see section 4.12 ) the moments prefer to align it that direction. In fact if we consider the minima as the valley and the maxima as the peaks of the mountain, the [100] direction lies exactly on the slope between the [110] peak and the minimum valley. Our further investigation show that in order to align 100% of the magnetic moments along [100] one requires a field of the order $10^4$Oe or more. This is where as the two [110] and $[1\bar{1}0]$ directions are the metastable equilibrium orientations of the magnetization. It means that a large field is enough to align the magnetic moments along these axes. But both of these axes are in-plane hard axes of the magnetization since their energy level is higher than [100] direction. In a normal case where the difference between the axes are large enough,i.e. for H‖[110] and [100] directions, the M(T) measurements are able to distinguish it and so determine the easier axis. This is whereas for the cases like our sample where the $[1\bar{1}0]$ and [100] show a small difference, M(T) measurements should be performed in much higher fields. For example in the case of the 20Oe applied field along [100] direction it is natural that the moments prefer to align themself in 10° away from this axis, so magnetization in this axis will always show only the projection of $M_{sat}$ along this axis. On the other hand, along $[1\bar{1}0]$ direction all the moments will be aligned for this applied field.

As it is remarked, it is crucial to take into account the fundamental definition of the easy and hard axes which were created, as words, from the energy point of view. FMR measurements because of their intrinsic nature are sensible to the energy levels of the axes. It should also be noticed that all the above discussion are made with the assumption of a single domain structure. In the case of multi domains one is obliged to investigate the mentioned feature above the coercivity field of the sample, otherwise the contribution of the magnetic domains will influence the results.

To be able to quantitatively discuss these issues, one requires to deduce the magnetocrystalline anisotropy fields and constants. Figures 3.25 and 3.26 illustrates the anisotropy fields and constants respectively. At low temperatures the $H_{2\perp}$ and the corresponding anisotropy constant $K_{2\perp}$ are the dominating ones with a negative sign. The other three constants are negligible. The negative sign of the perpendicular uniaxial anisotropy field which after subtracting from the demagnetization field $4\pi M$ creates the $4\pi M_{eff}$ term is the key which dominates a hard axis perpendicular to the film surface for the compression strained layers (see section 1.8). As the temperature is increased the latter becomes comparable to the other three constants which invokes the isotropy of the resonance field near $T_C$. For the GaMnAs/GaInAs sample the anisotropy fields are calculated in Q-band for T<80K and in X-band for T>80K, hence the non-monotone variation of $4\pi M_{eff}$ and $H_2\perp$ terms from 80K

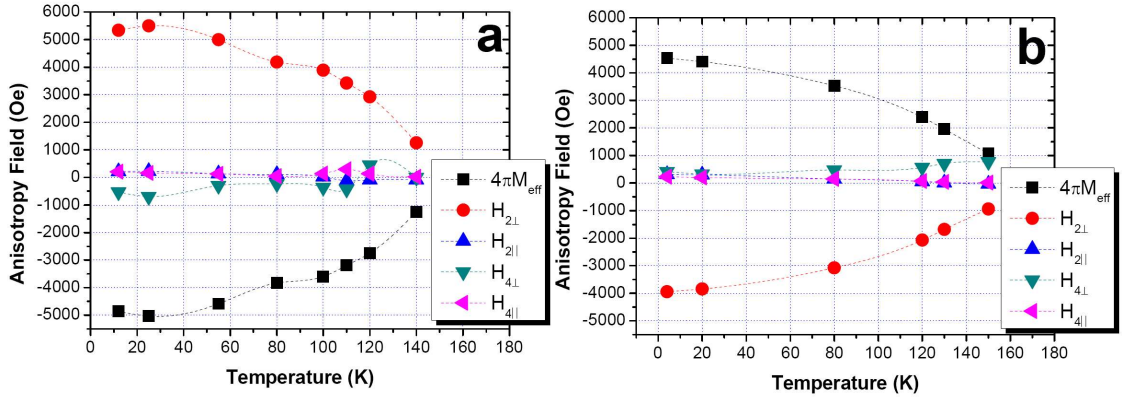


**Figure 3.25:** Magnetocrystalline anisotropy fields for (a)GaMnAs/GaInAs and (b) GaMnAs/GaAs 50nm thick samples-$x \approx 0.07$-as a function of temperature.

to 110K can be related to this fact, where the change in the cavity conditions and temperature controll has slightly lowered our precision.

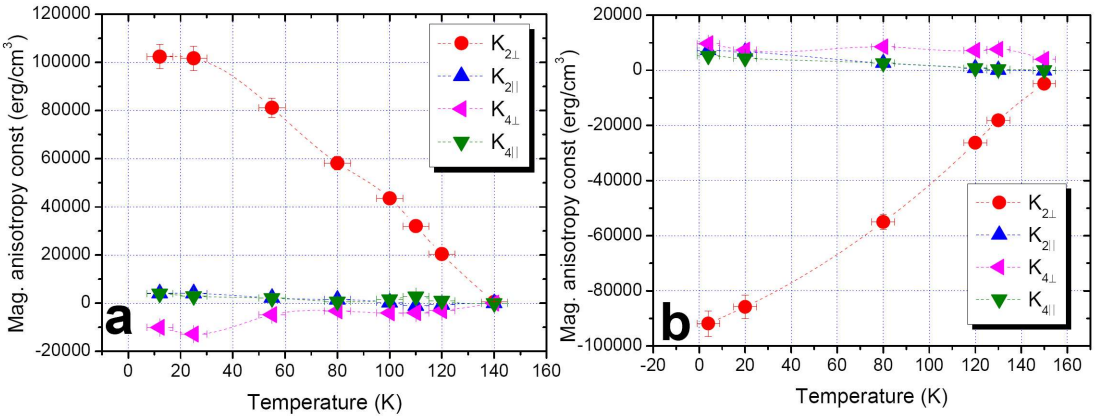


**Figure 3.26:** Magnetocrystalline anisotropy constants for (a) GaMnAs/GaInAs and (b) GaMnAs/GaAs 50nm thick annealed samples -$x \approx 0.07$- as a function of temperature.

Note how the positive sign of $K_{2\perp}$ constant invokes in-plane hard axis of the magnetization.

## *3.5 spin-wave studies*

As was mentioned in section3.4, the uniform FMR spectra were accompanied by satellite resonance spectra which are suspected to be the spin waves. The spin-wave observation in FMR measurements is not a completely controllable phenomenon. Despite this fact there are many groups working on this aspect because of the crucial informations one may obtain studying them and they have tried to put this subject in a experimental frame and determining the parameters which give rise to their excitations. In the case of GaMnAs ultrathin layers it is clearly observed that it is a sample dependent process; e.g. following the systematic studies of Furdyna et al. [12, 13] and Goennenwien et al. [14] the spin wave resonance is not detectable for samples thinner than 100nm. The fact that the reported spin-wave resonance studies on GaMnAs samples are limited to few works which can be found in ref. [12–15] and each one with different and sometime even contradictory (from the mode numbers and boundary conditions to the angular dependence and the resonance separations), indicates the need of more experimental data to reveal and elucidate this issue. Here in this section we follow our studies on the two samples under compressive and tensile strains from this point of view. Note that in our samples we obviously observed at least two supplementary modes excitations for different directions of the applied field and temperatures which have the behavior of the spin-waves. This enables us not only to deduce the spin stiffness parameter and thus the exchange integral between the manganese ions and between the manganese ions and charge carriers in both layers but also to contribute to the development of the general SWR studies.

### 3.5.1 Spinwaves in GaMnAs/GaAs sample

Take a look at the fig.3.11. In this figure one can obviously observes three resonances along the hard axis of the as-grown sample. Fig.3.12 presents the evolution of these spectra as a function of temperature. One can note that while at low temperatures these resonances are separated with almost equal distances as the temperature get close to $T_C$ their separations increase as a function of the mode numbers (for beginning one may desire to numerate the mode with n=0,1 and 2 in the order of the resonance field). Note that at T=20K the second resonance is observed close to H=3370Oe and for T=60K it is in the other side of the g=2.00 related field. However note again that its relative intensity is increased in this case and is now more intense than the n=1 mode. In 1958 Kittel [21] reported a quadratic dependence of the resonance field separation between the spin-wave modes $\Delta$H for a homogeneous ferromagnetic film along the normal-to-plane axis for surface pinned SW condition as:

$$H_n = H_0 - n^2 \frac{D\pi^2}{g\mu_B L^2} \tag{3.2}$$

where D is the exchange stiffness constant, n is the spin-wave mode number and $H_n$ its respective resonance field. $H_0$ evidently is the uniform mode resonance field. This model considers the pinning of the magnons on the surfaces of the film.

In 1963 A.M.Portis in his article attributed the equidistant spin-wave resonance separations in contradiction to the quadratic dependence prediction of Kittel to the inhomogeneity (non-uniformity) of the magnetic properties in a thin film [16]. While different groups after him attributed this inhomogeneity to different probable parameters as a depth dependent magnetization, Goennenwein et al. used the general model proposed by Hoekstra et al. [17] to simulate the spin-wave resonance fields in GaMnAs films. They add a general effective field to the resonance equation:

$$\frac{\omega}{\gamma} = H_{ext} + H_{eff} - DK^2 \tag{3.3}$$

where they assumed a z dependent effective field linearly varying from 0 to L (the film thickness) and deduced its variation via investigation of etched samples. The relation they proposed is as follows:

$$\Sigma(n) = H_{ext,0} - H_{ext,n} = D^{1/3} H_l^{2/3} \left\{ \frac{3\pi}{2} \left( n + \frac{1}{4} \right) \right\}^{2/3} \tag{3.4}$$

Here $H_l$ determines the dependence of the effective magnetic field on the position in the layer. However one might comment that the etching process, as it modifies the surface conditions and changes the internal anisotropy fields is not an appropriate technique to investigate this issue. As the eq.3.4 shows, they acquired a $\propto n^2$ dependency of the magnon resonances assuming the *un-pinned* spin waves at the surface.

Liu et al. (ref. [13]) have recently tried to adapt the same model to the case of GaMnAs in which the dominant anisotropy field in due to the perpendicular uniaxial anisotropy field ($H_{2\perp}$) and its relevant $4\pi M_{eff}$ term. In their model they assumed a symmetrical parabolic variation of $4\pi M_{eff}$ along the film z-direction ($-L/2 \leq z \leq L/2$); and supposed symmetric boundary conditions at both the surface and the interface. The origin of the gradient of the anisotropy field is attributed to different facts such as an oxide surface layer, an abrupt change in the hole concentration and magnetization close to the surface, as well as a gradient of the hole concentration along the z-direction of the film due to the out diffusion of the interstitial Mn ions. (Here I would like to make a comment on this assumption considering its indication in many reports of Furdyna et al. Although the out diffusion of the Mn ions, for sure, creates a concentration gradient, the metallic behaviour of the ferromagnetic GaMnAs will lead to a homogenous carrier distribution and even in a semi-insulating sample where the holes are in the impurity *band* and the characteristic of a band is that it is extended all over the material). They proposed a linear dependence of the spin wave resonance fields with their respective modes:

$$H_n = H_0 - \left(n - \frac{1}{2}\right)(4/L)\left(4\pi M^0_{eff}\epsilon\frac{D}{g\mu_B}\right)^{1/2} \tag{3.5}$$

where $\epsilon$ is a phenomenological factor called "distortion parameter", used to define the profile of the magnetic anisotropy along z diction of the film. Their calculations of the relative resonance field and intensity of the spin-waves showed the validity of the surface pinning assumption. Note that by applying this equation, one considers that in the case of the magnon excitations the uniform mode completely disappears (it decomposes into excited higher modes) and the first mode (n=1) is shifted to lower fields. Since the intensity of the higher modes decrease drastically with the mode number, the authors supposed that the first mode can be considered with good approximation as the uniform mode. In their model, the uniaxial anisotropy constant $K_{2\perp}$ is the dominant parameter whose variation along the growth direction leads to a transition from the Kittel model to a Portis-like model. Now, as the temperature increases the diminution of this constant because of the decrease in magnetization magnitude (cf. section 3.4.3) will reduce its influence in line with the proposed explanation for the temperature evolution of spin-wave resonances in fig.3.12. Thus, from T=60K, for the as-grown sample one can expect the classic Kittel-like spin wave dispersion to hold. One can observe a digressive decrease in the separation between the respective modes as a function of the temperature. As it will shown later in this section there is a linear relation between the exchange stiffness constant D and the exchange integral J between the Mn ions. The reduction in the polarization of the holes due to increasing thermal fluctuations and hence the decease in the coupling between the Mn ions is at the origin of this decrease.

But the very particular feature of these spin waves are observed in the annealed sample. In fig.3.13 (the solid line) the spectra along the [001] axis of the film reveal two well-resolved modes. The dotted line is the same spectrum with a gain increased by a factor 12.5. As one notices, not only a third mode is now observable but one can also observe the exact fine structure of the uniform FMR mode (first SW mode) reflected in the higher modes. As it was mentioned in previous sections the slight deformation of the uniform mode is due to the superposition of two or more resonances. These resonances which are causeattributed to the inhomogeneity of the magnetic moment distribution in GaMnAs diluted system, present different respective anisotropy constants. As the boundary conditions for the spin-wave excited modes are determined by the anisotropy fields and their variation along the film growth direction (for [001] direction), *a priori*they must be different for each of the partially superposed spectra. This issue is not yet understood and requires more detail investigation, in particular as a function of different thicknesses.

The SWR spectra as a function of the angular variation of the applied field in the [110] plane at T=4K is shown in fig.3.27.

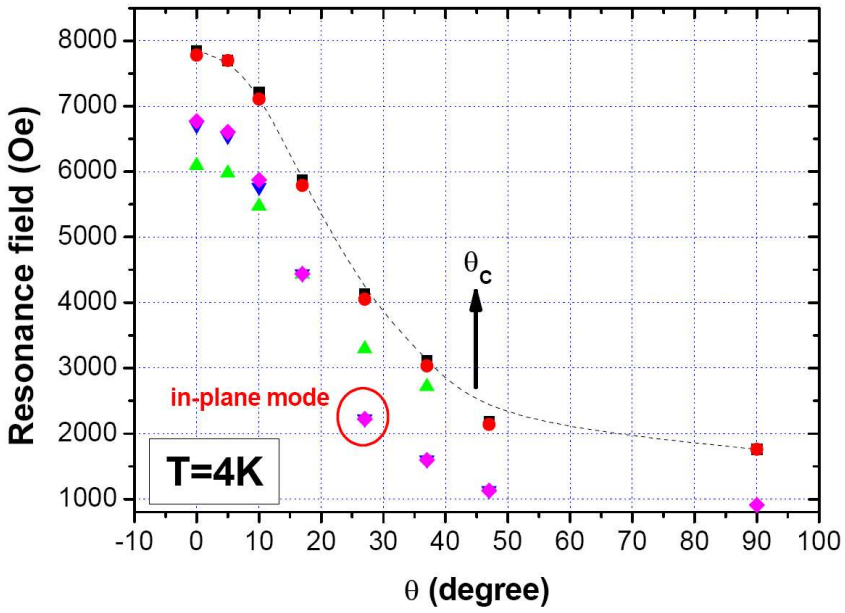


**Figure 3.27:** Spin-wave resonance fields as a function of angular variation of applied field in [110] plane (out-of-plane) at T=4K measured via X-band microwave frequency. The squares and circles presents the two uniform modes separated for inhomogeneity reasons; the diamonds and downward triangles are the respective successive modes of the former and the upward triangles present the second SW modes. The critical angle of the -out-of-plane spin-wave modes is marked by an arrow.

For $\theta_H$=0 the two resolved uniforms modes and their respective first spin-wave modes are labled. The second modes are mixed with each other in our resolution as a result of their low intensity and very small field separation.

Note the fact that, if one label the modes by successive n=0,1 and 2 (as proposed by Goennenwein et al. for un-pinned boundary conditions [14]) or by even numbers (as proposed by Furdyna et al. for pinned boundary conditions [12]) the modes do not follow the $n^{2/3}$ neither the linear dependent dispersion relation. As the applied field in rotated from the perpendicular direction the SW mode change initial separation relation contradictory to what was reported for the samples of Furdyna et al. At $\theta \approx 18°$ only one mode is detected which is probably the second excited mode (based on the respective linewidth tracing of the modes as a function of angular variation); however in the fig.3.27 it is shown as the superposition of both modes due to its complicated situation.

In 1995 Han used the volume inhomogeneity (VI) model proposed by Portis and deduced a critical angle for the observation of spin-wave modes [18]. He calculated $\theta_C = 52°$. Furdyna et al. measured this critical angle arround 19° followed by the appearance of a new mode in higher fields than the uniform mode called the " *surface mode*" [13]. They attribute this to the model proposed by Puszkarski in 1970 [19]. In his model, he introduced a surface anisotropy field which allows the excitation of an exchange-dominated nonpropagating surface mode and thus there will be a critical orientation where only a single uniform FMR mode is observed. In Puszkarski's surface inhomogeneity (SI) model the spin pinning condition at each film surface can be described by an effective parameter:

$$A^* = 1 - (g\mu_B/2S\zeta J)\,(\mathbf{K}_{surface} \cdot \mathbf{m}) \tag{3.6}$$

where S is the atom (in our case Mn) spin, J is the Heisenberg exchange interaction parameter between two nearest spins, $\zeta$ is the number of nearest-neighbor spins in a crystal lattice, $\mathbf{K}_{surf}$ is the effective surface anisotropy field, and $\mathbf{m}$ is the unit vector parallel to the magnetization M. Physically,parameter A* is a measure of the pinning strength of the surface spins at the surface.

He then comments that when A*<1, surface spins are pinned and a series of bulk SWR modes with real values of the wave vectors k are observed. For H||[100] these modes conform to the quadratic law (Kittel model), and for H||[001] they are distorted to obey the linear law (Portis model). As H tilts away from either the [001] or [100] direction,A* increases, so that the surface spin pinning fades away. At the critical-angle orientation corresponding to A*=1 only one resonance peak, corresponding to the uniform mode with k=0, remains. This situation corresponds to the disappearance of surface anisotropy. When H continues to approach the [110] or [1$\bar{1}$0] direction, the weak higher-field mode observed several hundred oersteds above the strongest mode can be identified as a nonpropagating surface mode (i.e.,

k is imaginary for that mode), consistent with the case A*>1. At this condition the surface spins are unpinned.

Furdya et al. even go further and find the critical angles in this model consistent with the angles at which the resonance field becomes independent of the small change in magnetic anisotropy (i.e. $\partial H_R/\partial H_{2\perp} or \partial H_R/\partial H_{4\parallel}$=0). In our measurements (cf. fig.3.27) this angle is the angle where the the first SW mode disappears. But the disappearance of the second mode happens for angles $\approx 45°$ which is more consistent with Han VI model. The surface modes in these sample are not detected which must be the result of their very low intensity. Instead for angles $\approx 25°$ a new mode emerges. This new mode which coexist with the second out-of-plane mode before the latter disappears has completely different nature. The line width for this mode which is about 250Oe and decreases as the applied field approaches the in plane directions, together with its intensity which is considerably higher than the second out-of-plane SW mode and its lower resonance field, all indicate its different nature.

The resonance separations between the modes have decreased considerably which should be the sign in the decrease in the spin stiffness constant. In the following chapters, I will show how the g-factor varies as a function of hole concentration and it will be shown how this factor reflects the hole polarization in each sample (cf. section 4.10).

The successive study of g-factor in section 5.5 reveals once more how the g-factor in high hole concentration increases again after a certain minimum value as well as the relevant hole polarization. As mentioned above, the decrease in hole polarization is considered as the dominant parameter which reduces the spin stiffness (the exchange integral) in as-grown sample as a function of temperature. Here, the reason for the decrease of the spin stiffness (and so the exchange integral between the manganese moments) can be explained with the same criterion. As it will be shown this annealed sample presents a very high degenerated behavior. Thus the spin-orbit and so the hole polarization will be reduced. For the in-plane applied field, no spin wave was detected.

These modes were detected as well in Q-band measurements (fig.3.22).

### 3.5.2 Spinwaves in GaMnAs/GaInAs sample

The case of additional excited modes for this annealed sample is very special since the hard axes of the magnetization lies in the film plane for all temperatures. Note that in this chapter and specially in this section the focus of the study is on the annealed samples; where as the mentioned similar studies were performed upon as-grown samples. The shift of the resonance fields along in-plane axes to higher fields enables one to better study the more resolved excited modes. The better separation of the modes and the inhomogeneity contributed resonances for these orientation due to the large value of perpendicular uniaxial anisotropy adds to this peculiarity.

As it is presented and briefly discussed on fig.3.28, the [110] related resonance spectrum in the out-of-plane direction is composed of four components. Its decomposition is shown in fig;3.28.

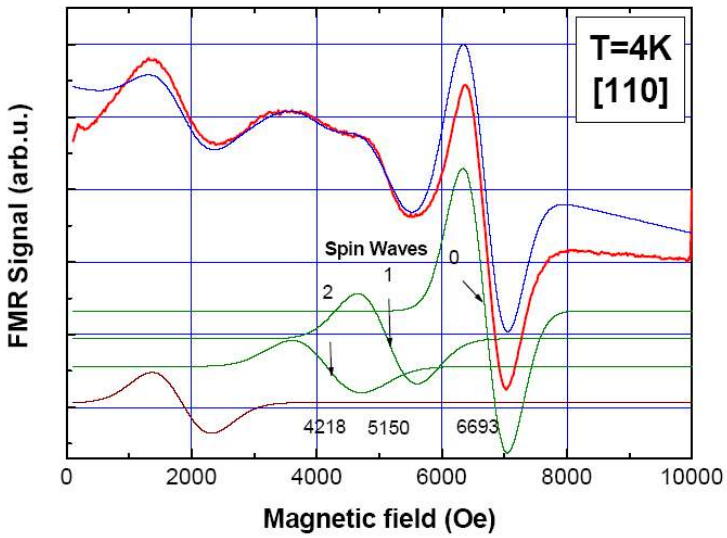


**Figure 3.28:** The FMR spectrum of GaMnAs/GaInAs 50nm thick annealed sample -$x \approx 0.07$- for applied field along the hard [110] direction in out-of-plane configuration at T=4K is decomposed in three spin wave resonances and a low field inhomogeneity caused modes. The red solid line presents the resulted simulated spectrum from all components.

The evolution of the spectra as a function the angular variation of the applied field in out-of-plane configuration (fig.3.28) is used to identify the modes. As the high field modes vary largely with the orientation of the applied field and superposed on each other for 7° from the in-plane direction, the modes which lies in lower fields shifts very slowly to higher fields. This behavior reveals the fact that the origin of the latter mode is not the same as other ones and thus it is attributed to the inhomogeneity of the sample or the second result of the Smit-Beljers equation. For in-plane configuration of SWR measurements (cf.3.19) the modification to cavity condition has decreased our resolution to study these modes; however the first excited mode is marked by arrows in the figure.

As the case is discussed previously in the text, in order to study the FMR (or SWR) spectra at low temperatures one should apply the Q-band microwave frequency measurements. For T=20K the spectra in fig.3.29 show the uniform mode and the two respective excited SW modes for the applied field angle $\theta_H = 20°$.

In fig.3.30 the angular variations of the resonance fields for different applied field angles are presented. The resonance fields do not follow a linear dependence. As one observes for $\theta_H \approx 25°$ the second mode is nearly vanished. The first excited mode has vanished (or superposed) to the uniform mode at critical angle $\theta_H \approx 60°$

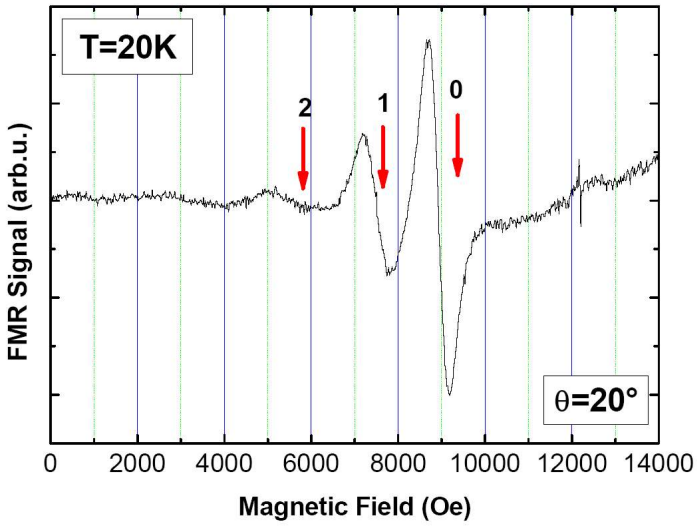


**Figure 3.29:** The SWR spectrum of GaMnAs/GaInAs 50nm thick annealed sample -$x \approx 0.07$- for applied field along $\theta_H = 20°$ with respect to [001] direction in out-of-plane configuration at T=20K. The arrows show the respective spin-wave excited modes. The labels are with respect to their resonance field order.

from the perpendicular [001] direction. This is again, as the case for GaMnAs/GaAs sample, more consistent with the Han model. In this sample the in-plane SW modes have a particular characteristic. Fig.3.30 presents the spin-wave resonance field as a function of different orientations of the applied field in in-plane and out-of-plane configurations at T=25K.

Note once again the emerging of an in-plane spin-wave mode, right after the critical angle. The SW mode retains its distance from the uniform mode and follows exactly the same angular variation as the main mode. Contradictory to the case studied by Furdya et al. (cf. [13]) and their proposed model upon the theoretical studies of Puszkarski, the in-plane mode does not vanish nor is it superposed to the uniform mode.

The model proposed both by Furdyna et al. and Han has considered symmetrical boundary conditions for both the surface and the interface of the film. They applied a model in which the gradient of the anisotropy field (inhomogeneity profile) grows from the middle of the film and has a quadratic dependence on z (from the middle point). What they consider is either a magnetization which varies from bulk to the surface or the hole concentration symmetrical variation toward the surfaces because of the $Mn_{int}$ profile. As it will be discussed in coming chapters, our results on the profile of the $Mn_{int}$ after the annealing process reveals the migration of these moments toward the free surface and not to the interface. Whereas for the as-grown sample the profile is considerably more homogeneous along this direction. Consider-

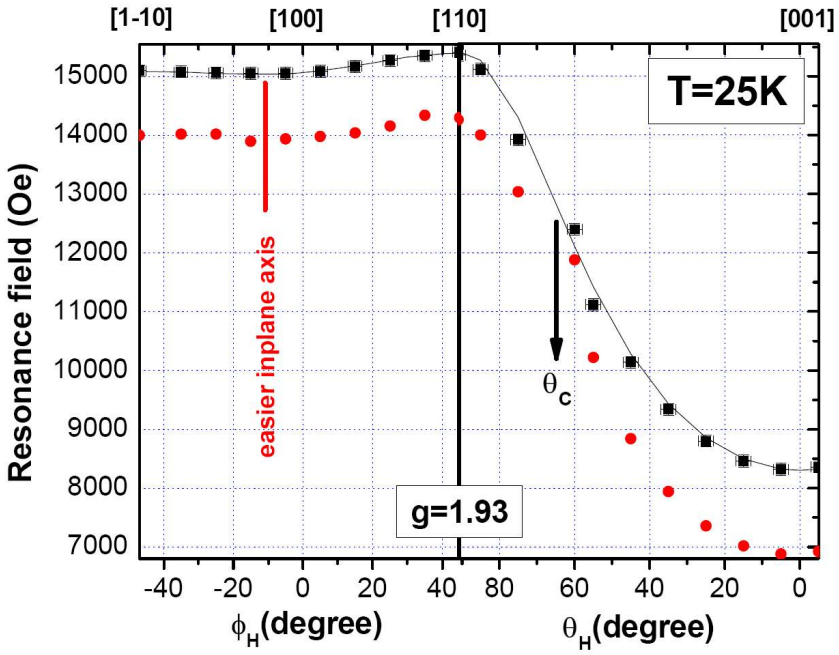


**Figure 3.30:** The spin-wave resonance field of GaMnAs/GaInAs 50nm thick annealed sample -$x \approx$ 0.07- as a function of different orientation of applied field in in-plane and out-of-plane configurations at T=25K. The out-of-plane critical angle is marked by an arrow.(Q-band)

ing the metallic character of both annealed and as-grown samples, this observation indicates without doubt a homogeneous distribution of the hole concentration over the sample. So I would like to emphasize four facts:

1. Although the existence of the surface and interface for the ultra-thin ferromagnetic films,where the strains in the film are not relaxed because of the small thickness, causes the introduction and variation of the uniaxial anisotropy field along the growth direction ([001] direction here), but the effect of a gradient of manganese interstitial profile ,which contributes strongly to the modification to the GaAs lattice parameter is much more important and this should be considered as the dominant origin of a depth dependent anisotropy field and so the boundary conditions should be taken as 0<z<d, where the interface correspond to the zero value.

2. The ferromagnetic order in GaMnAs samples is carrier mediated and these carriers are in the valence band, thus the hole concentration is homogeneous over all the sample.

3. The surface boundary conditions and the studied theoretical models correspond to the out-of-plane modes they can not explain the emergence of the in-plane SW modes (some groups have attributed their excitation due to the existence of macroscopic defects in the layer volume, however the essential periodic character which they require to be the boundaries for these modes do not correspond to our diluted epitaxied samples).

4. Considering the growth conditions, it is more logical to use a non-symmetrical profile. Moreover, while basic models are based upon an asymmetrical boundary condition, it is not valid to assume a symmetrical parabolic $4\pi M_{eff}$ along the growth direction.

The other particularity of this sample is shown in fig.3.21. As a function of temperature from 110K, one observes the shift of the spin-wave mode along [001] direction to the positive fields in X-band measurements. The case of such comparable spin-wave modes are also mention in ref. [13] and even more complicated cases are even observed in inhomogeneous metallic samples. Here, to be consistent with the rest of the text, we label the mode in higher field the uniform mode; however in this case calling it as the uniform mode is not a right action. Tracing both modes as a function of temperature, which is done in the figure by red solid arrows, reveals how from 120K the intensity of the first SW mode dominates to the uniform mode and they are superposed at T=140K. This particular fact is not understood for the moment, where as the diminution of the mode separation is attributed simply to the digressive decrease in exchange integral as a function of temperature up to the curie temperature at T=170K.

Now a similar fact can be observed in fig.3.17. There is was shown that from $\theta_H = 30$ to 40 the resonance field of the spin-wave which is emerging from the "negative" fields disappears and there is a decrease in the uniform mode resonance field. This fact which could not be explained by the anisotropy field can be attributed to the same process which was responsible for the particular spin-wave behavior in previous paragraph.

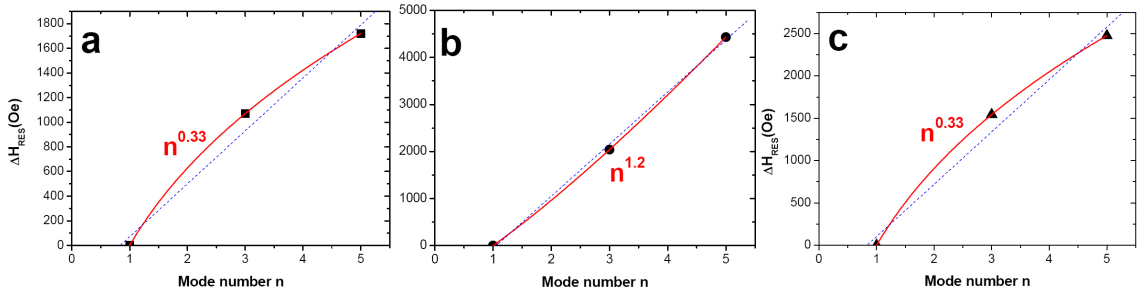


**Figure 3.31:** Spin wave resonance fields for different excited modes for (a) GaMnAs/GaAs annealed and (b) as-grown samples at T=4K for applied field along [001] direction. For GaMnAs/GaAs annealed sample (c) the resonances are for applied field along [110] direction and T=4K. The modes are labeled assuming the pinned spin-wave mode at the surfaces. The solid line are the polynomial fits with respective mentioned powers. The dashed lines are the linear fits

After all these qualitative studies the most important parameter to be studieD is the spin stiffness and the exchange integral between the magnetic moments in our samples. The different but few studies and models which were proposed for SWR measurements on GaMnAs films have already explained and commented briefly. As one has noticed, not only they are not adequate, but also contradictory due to the complicated character of the system and complicated model they were seeking do not provide one with reliable results.

In fig.3.31 the resonance fields of the three modes are plotted. Goennewein et al. have used successive n=0,1,2,.. mode numbers and based on this they have attributed a $n^{2/3}$ dependence of the mode resonances. Where as for the same system Rapapport et al. have found a linear dependence by labeling the modes by even numbers, justified by the pinned spin-wave boundary condition [12]. Note that in the other article they applied the same model for perpendicular orientation of the applied field but adjusting the mode numbers to the odd ones, consistent with the classical model applied by Kittel for ferromagnetic films due to the surface state and anisotropy. In this model they have well accepted that the uniform mode break into magnon excitations and so the first observed mode is not the uniform one but the mode corresponding to n=1.

In our case accepting the general fact that the surface anisotropy should con-

tribute to the pinning of the magnons at the surface we have used the same numbering. It should be noted that in the case of using the successive numbers one could find the same $n^2/3$ dispersion law between the modes as Goennenwein. In each panel of fig.3.31 two linear and polynomial fits are shown. Although one is able to distinguish the better fit, the difference for just three first modes is not drastic. Note that in panel (b) the modes satisfy merely a linear dispersion relation were as in annealed samples the relation is more deformed from the classic Kittel model.

In absence of a completely satisfying theoretical model for the dispersion relation of magnon modes, we have applied the existing models to our samples. The results obtained are presented in table.3.1.

| Sample | *Classic SW model (Kittel)* | | *Inhomogeneity SW model (Furdyna)* | | | | |
|---|---|---|---|---|---|---|---|
| | Respective modes | Exchange stiffness constant **D** ($T.nm^2$) | Respective modes | Distortion parameter **ε** | Exchange stiffness constant **D** ($T.nm^2$) | Spin stiffness **A**(pJ/m) | Exchange integral $\mathbf{J_{MnMn}}$(meV) |
| GaMnAs/GaAs Annealed | **3,4** | **1.8** | **3,5** | **0.23** | **2.685** | **0.063** | **0.23** |
| GaMnAs/GaAs As-grown | **3,5** | **3** | **3,5** | **0.95** | **2.432** | **0.039** | **0.17** |
| GaMnAs/GaInAs Annealed | **3,4** | **2.6** | **3,5** | **0.3** | **3.496** | **0.064** | **0.23** |

**Table 3.1:** The spin-wave modes adjusted to two classical and inhomogeneity models and respective calculated parameters obtained from each model

As one observes from the table, the SW mode numbers are not very different in both models, moreover the compressive strained as-grown sample can be fitted by the same mode number in both cases. The exchange stiffness constant D for classical and inhomogeneity models are deduced from equation 3.2 This model has been proposed by Furdyna et al. for [100] orientation of the applied field [13]. The value of the distortion parameter is calculated from eq.3.5. The stiffness parameter A is related to D by relation:

$$D = 2A/M_0 \tag{3.7}$$

where $M_0$ is the saturation magnetization. The exchange integral between manganese magnetic moments is given by the relation:

$$J = Dg\mu_B/(2Sr_s^2) \tag{3.8}$$

where S is the total spin of each Mn ion and $r_s$ is the distance between the moments calculated as $r_s=(4\pi x N_0/3)^{-1/3}$ with x the concentration of magnetically active Mn ions and $N_0$ the concentration of cation sites.

The calculated stiffness in both models are not considerably different, nevertheless the relative values corresponding to annealed and as-grown GaMnAs/GaAs samples do not seem to have the same characters in both models. While they increase in classical model for as-grown sample, consistent with the our proposed scenario, it seems to be constant (or rather reduced) in Furdyna's model. Note that the distortion parameter is increased largely for the as-grown sample as compared to both annealed ones.

But the most particular aspect of the results, which is model independent is their small magnitude (One order of magnitude smaller) compared to the previous reported works ( [12–14]) and theoretical calculated ones [20] (fig.3.32).

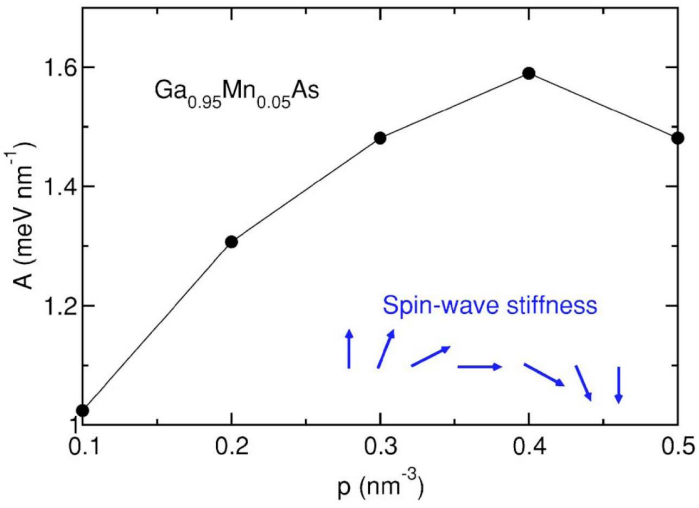


**Figure 3.32:** Theoretical spin-stiffness parameter in $Ga_{0.95}Mn_{0.05}As$ as a function of the hole density calculated using the Holstein-Primakoff representation of fluctuating Mn local spins and the KL kinetic-exchange description of hole bands. The arrows are schematic picture of stiffness [20].

These values which are in very good agreement with the values obtained from recent magneto-optical measurements on the same samples shown in fig.3.33 [4]. They are attributed (as it will be shown in sections 4.10 and 5.5) to the reduction of the hole polarization which is again consistent with the measured LandÈ factor,

because of the high hole concentration in these metallic samples; in the other reports the studied samples were as-grown samples.

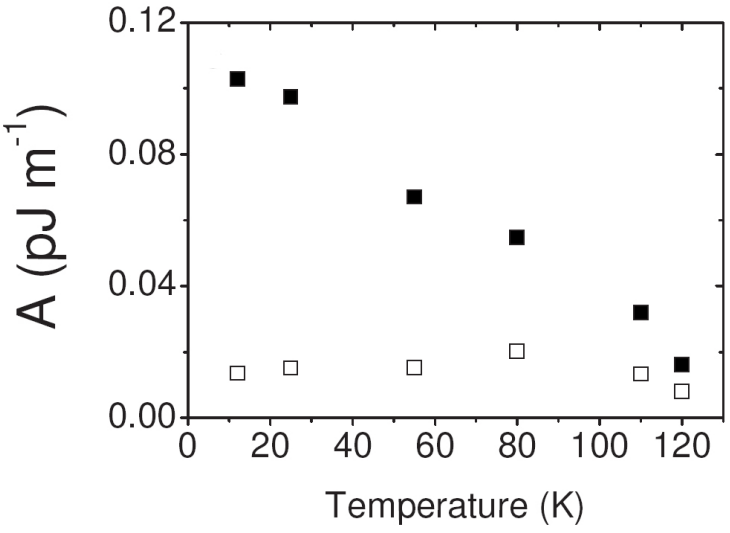


**Figure 3.33:** Stiffness parameter values as a function of temperature for GaMnAs/GaInAs annealed sample measured by magneto-optical Kerr effect. [4]

The other very special feature is the same value of the exchange integral for both compressive and tensile strained samples. Consistent with the other characters of the tensile strained system (as it will be discussed in section 6.4) is the augmentation of the distortion parameter in this sample compared to its compressive strained counterpart.

### *3.6 Conclusion*

We have studied in very detail the possible aspects of the magnetic properties of GaMnAs samples under the tensile and compressive strains. Although there were some particularities of each film specially from the magnetocrystalline anisotropy point of view and the easy magnetization axes,in general the intrinsic characteristic parameters of the films such as the g-factor,Curie temperature and the $J_{MnMn}$ exchange integral are the same for the annealed samples. After the structural parameters the key to this similarity is found in the magnitude of the strain in the samples. One concludes that choosing the substrate properties is of great importance in modifying and adjusting the magnetic properties of the layer; as it was predicted by the theoretical predictions. In this chapter we have presented the capability of the structural control over the magnetic properties of the GaMnAs system; an advantage which is missing in the case of the most of metallic systems.

The spin-wave resonance study of the samples revealed a particular and at the same time complicated dispersion relation of the magnons in this material. It was shown that despite of the global similarities with the case of metallic layers, one can not explain all the complicated behavior of the spinwaves in GaMnAs. The special case of the observation of in-plane spin-wave modes can not be described by the inhomogeneity models applied for conventional out-of-plane modes. The reason for the excitation of these modes is still unclear. However, as an approximation they fit well to the classical pinned-to-surface modes of Kittel, which enabled us to measure the exchange stiffness factor and the exchange integral fo coupling interaction between the Mn ions. These measurements were well consistent with the magneto-optical Kerr effect microscopy results. Both techniqued revealed a J value at least 5 times lower than the predicted and measured values for the as-grown samples with lower Mn concentrations. However, the general trend of the calculated stiffness factor to decrease at high hole concentrations illustrates that this event was expected. Together with the results which will be presented in the following chapters, we have attributed a part of this difference to the lower level of polarization for samples with higher Mn and hole concentrations.

As the last remark, we would like to note that the diluted nature of the spin in a periodic matrix modify the classical dispersion relation of the spinwaves which is based on the assumption of the periodic localization of these spins, and not just because of the inhomogeneity of the anisotropy fields.

# Bibliography


[1] "Damping and magnetic anisotropy of ferromagnetic GaMnAs thin films", Kh.Khazen, H.J.vonBardeleben et al. submitted to Phys. Rev. B.

[2] A. Dourlat, V. Judi, C. Gourdon, Kh. Khazen, H.J. vonBardeleben et al., IEEE Trans. Mag. 43 3022 (2007).

[3] A. Dourlat, C. Gourdon, Kh. Khazen et al., J. Appl. Phys. 102, 023913 (2007).

[4] C. Gourdon, V. Jeudi, Kh.Khazen et al. Phys. Rev. B 76, 241301(R) (2007)

[5] A. Dourlat, V. Judi, C. Gourdon, Kh. Khazen, H.J. vonBardeleben et al., Physica E 40 1848 (2008).

[6] T. Dietl, H. Ohno, and F. Matsukura, Phys. Rev. B 63, 195205 (2001).

[7] J. C. Harmand, T. Matsuno, and K. Inoue, Jpn. J. Appl. Phys., Part 2 28, L1101 (1989).

[8] L. Thevenard, L. Largeau, O. Mauguin et al. Phys. Rev. B 73, 195331 (2006).

[9] V. Novak, K. Olejnik, J. Wunderlich, M. Cukr, K. Vyborny et al., eprint arXiv:0804.1578v1

[10] J. Sinova1, D. Culcer, Q. Niu, N. A. Sinitsyn, T. Jungwirth and A. H. MacDonald, Phys. Rev. Lett. 92, 126603 (2004).

[11] K. W. Edmonds, R. P. Campion, K. Y. Wang, A. C. Neumann et al. J. Appl. Phys. 93, 6787 (2003).

[12] T. G. Rappoport, P. Redlinski, X. Liu et al. Phys. Rev. B 69, 125213 (2004).

[13] X. Liu, Y. Y. Zhou, and J. K. Furdyna Phys. Rev. B 75, 195220 (2007).

[14] S. T. B. Goennenwein, T. Graf, T. Wassner, M. S. Brandt, M. Stutzmann, J. B. Philipp, R. Gross, M. Krieger, K. Z¸rn, P. Ziemann, A. Koeder, S. Frank, W. Schoch, and A. Waag, Appl. Phys. Lett. 82, 730 (2003).

[15] D. M. Wang, Y. H. Ren, X. Liu, Y. J. Cho, J. K. Furdyna, M. Grimsditch, and R. Merlin, AIP Conf. Proc. 893, 1175 (2007).

[16] A. M. Portis, Appl. Phys. Lett. 2, 69 (1963).

[17] B. Hoekstra, R. van Stapele, and J. Robertson, J. Appl. Phys. 48, 382 (1977).

[18] Z.-Q. Han, J. Magn. Magn. Mater. 140, 1995 (1995).

[19] H. Puszkarski, Prog. in Suface Science. Vol. 9. pp. 191-247 (1979).

[20] J. Konig, T. Jungwirth, and A. H. MacDonald, Phys. Rev. B 64, 184423 (2001).

[21] C. Kittel, Phys. Rev. 110, 1295 (1958).

[22] L. X. Zhao, C. R. Staddon, K. Y. Wang, K. W. Edmonds, R. P. Campion, B. L. Gallagher, and C. T.

[23] X. Liu and J. K. Furdyna, J. Phys.: Condens. Matter 18, R245 (2006).

[24] Steven C. Erwin and A. G. Petukhov, Phys. Rev. Lett., 89 227201 (2002).

# 4

# Investigation of the influence of the free hole concentration

[1–3]

As the ferromagnetism in GaMnAs is a carrier mediated process, the free hole concentration plays a major role in the exchange interaction coupling the Mn moments. This fact implies a dependence of $T_C$ on the free hole concentration, which is indeed predicted by the mean field model(eq.1.6). The double role of the Mn dopant providing at the same time the magnetic ions and the holes renders any separate variation of one of these two parameters difficult. May be that is the reason why the experimental results showing the dependence of the magnetic properties on the hole concentrations have been reported only occasionally [4]. It would be desirable to dispose of more such results for further refined modeling of the magnetic properties of GaMnAs layers. The modification to free hole hole concentration not only results in the variation of Curie temperature of the samples but has also a direct influence on the uniaxial and cubic magneto-crystalline anisotropy constants of the film. The calculations, based on mean field approximations (cf. [5]), predict quantitatively such constants. According to them a reorientation of the hard and easy axes of the magnetization is expected which definitely has its own technological application promises.

This chapter is dedicated to our investigation of the influence of the free carrier concentration on the magnetic properties of GaMnAs films, as well as verifying the validity of the predictions based on calculation within the mean field approximation.

The first problem to be solved is the one how the hole concentration can be conveniently modified. Different approaches have been proposed in the literature which I will overview in the next section.

## *4.1 Techniques to modify the hole concentration*

The hole concentration in a GaMnAs film can both be increased or decreased. Different techniques have been applied for this purpose; they present of course advantages and disadvantages. In the following I will overview the different investigations published in this context.

### 4.1.1 Variation of the manganese concentration

As the Mn dopant is electrically active, being a single acceptor, the modification of the Mn doping level is the most direct approach (and one of the first used techniques) to vary the hole density. Examples of the investigations using this technique can be found in [6, 7]. Sheu et al. have determined the onset of ferromagnetism for the Mn doping level as 1% which sets the minimum Mn and hole concentraton which can be obtained holes of $\approx 10^{20} cm^{-3}$.As parallel to the charge concentration the concentration of the magnetic ions is equally modified it is only of limited interest. Further, the extension of the hole wavefunction increases with the Mn concentration, whereas the average distance between the manganese moments decreases.

In a somehow similar approach, the post-growth annealing can serve to increase the hole concentration by more than 30% (cf.1.4.5)as compared to the as grown state. Once again the total concentration of magnetically active Mn ions is modified.

### 4.1.2 External electric field control

The hole concentration can be modified by applying an external electrical field of some MV/cm (depending on the dielectric constant of the insulating layer and its breakdown field) through a gate in a field effect transistor structure (FET). The induced field modulates the charge carrier concentration positively or negatively depending on the sign of the field. Examples of this technique for the case of III-V:Mn can be found in [8–13]. These authors have studied the Mn $\delta$-doped GaAs layers (in which the homogeneity of the samples is not obvious ); Chiba et al. achieved to extend the work to homogeneous GaMnAs layers, [14]. The variation of the hole concentration can be derived from:

$$\Delta[p] = \left(\frac{\epsilon_r}{e}\right)\frac{E}{t}$$

where $\epsilon_r$ is the relative electrical permitivity of the layer,$t$ is the thickness of the film and $E$ the applied external field. The authors succeeded to measure an absolute variation of some $10^{13} cm^{-3}$ over the measured total $[p] \approx 10^{20} cm^{-3}$, leading to a change in $T_C$ of some 5K.

Yet, the complex configuration required to prepare such samples and the problem of the ohmic contacts used to apply the gate voltage make this technique rather complicated.

The limitations of the technique resulting in the limitations of the charge modulation (e.g. the breakdown field) and the required low thickness of the film are other inconveniences of its application. The application of the technique on the as-grown (and not the usual annealed) samples is still unclear. This maybe the result of the disagreement of the measured data and the mean field predictions obviously observable in ref. [14].

### 4.1.3 Electrical modification via an acceptor or a donor co-doping

The co-doping of the samples with acceptors such as Be and donors such as Si or Te can increase or decrease the hole concentration respectively [15–18]. Since in order to have each desired hole concentration one has to grow a new sample the reproducibility of the samples with exactly the same amount of manganese is not guarantied. Moreover, as the dopant ions occupy the Ga sites, this technique progressively reduces the solubility of the Mn ions in the matrix. The increase of the incorporation of the interstitial Mn in this case leads to a saturation of [p]. Thus this is not a desirable technique for samples with high concentration of manganese.

Recently Cho et al. [19] has shown that the co-doping of silicon in highly Mn doped samples can increase the hole concentration (contradictory to the low Mn concentration case ) by reducing the density of As antisites.

### 4.1.4 Modulation doping via another layer

The $\delta$-doping technique is used to provide a high concentration of holes in a $\delta$-function like hole profile along the growth direction([001]). Layers of 5 and 13 nm Be-doped GaAlAs were deposited on a 5nm layer of GaMnAs with x=0.06. The $\delta-$doping is used to provide a high concentration of Be in a $\delta$-function-like profile along the growth direction. The delocalized holes provide as by Be co-doping the enhancement of the free hole density [20]. This concept has been adopted as well by Johnston et al. in a super-lattice structure.

As in the previous technique, for each hole concentration a new sample must be grown under different conditions which can be expected to modify also the Mn concentration. The presence of a depletion layer which forms at the interface of the two layers and the profile of the diffused ions, specially in the highly doped samples are two points to be taken into consideration.

### 4.1.5 $As_{Ga}$ control of hole compensation

Each $As_{antisite}$ double donor compensates two holes from the valence band. The existence of these defects is due to the growth condition of the samples and thus it was not considered as a fully controllable process. But recently Myers et al. (cf. [4]) succeeded to vary the density of these defects, making this technique a promising approach in order to modify the free charge carriers in a sample. By changing the ratio of the As and Ga during the growth process, the authors produced As-riched and Ga-riched layers respectively. They showed than while in the As-riched samples the excess of arsenic ions leads to an increase in the $As_{Ga}$ concentration, in Ga-riched samples the accumulation of the group-III ions on the surface during growth suppresses substitutional Mn incorporation leading to lower p and $T_C$ values. A strong deviation from the usual $T_C \propto p^{1/3}$ behavior was demonstrated with $T_C \propto p^{0.09}$ for x=1.5%. This dependence applies equally well to stoichiometric (Ga,Mn)As as it does to heavily $As_{Ga}$ compensated (Ga,Mn)As. This change in the hole density dependence of $T_C$ occurs in the doping region where the effects of a Mott gap and disorder are expected to alter the mechanism of ferromagnetism. This can be considered as an interesting approach to reduce the hole concentration.

### 4.1.6 Hydrogen passivation

While Hydrogen passivation of the acceptors in GaMnAs matrix itself can be categorized as a co-doping technique, its nature provides some special properties which makes it an ideal approach to decrease the hole density in a controllable, relatively simple and reversible procedure. This technique will be discussed in detail in the following section.

## *4.2 Hydrogen passivation*

Hydrogen has been shown to act differently from the previous co-doping methods. Hydrogen doping is an exceptionally efficient approach to decrease the hole concentration of a film by several orders of magnitude [22–25]. As the hydrogen passivation of the electrical activity of the Mn acceptor proceeds without modification of the magnetic moment of the $Mn_{Ga}$ ions this opens the way to manipulate the hole concentration in a film without changing its Mn concentration. This is one of the privileges of the hydrogen passivation which enables to study independently the role of hole concentration on the magnetic properties of GaMnAs structures.

### 4.2.1 Hydrogen atom in GaMnAs; bonds

Hydrogen has an extremely high solubility and mobility in GaMnAs. The $H^+$ ions passivate the free holes via the formation of acceptor complexes , i.e. As-Mn-H

complexes. The effect of hydrogen incorporation and Mn acceptor passivation were investigated by secondary ion mass spectroscopy and by local vibrational mode spectroscopy, respectively [22, 25, 26].The hydrogen passivation does not modify the spin of the $Mn_{Ga}$ acceptor due to the delocalized character of the hole and the anti-bonding configuration of the H atom. Thus irrespective of the charge state of the acceptor, the electronic configuration of the Mn ion in highly doped samples remains $3d^5$ with a spin S=5/2. The hydrogen atoms are believed to form H-As bonds in a Mn-As-H anti-bonding configuration, but other probable configurations such as As-H-Mn have also been considered [27]; so different models are still under discussion. Knowing that the bonding configuration will modify the spin state of the substitutional Mn, the EPR(FMR) spectroscopy is the technique of choice to investigate the hole dependence of the magnetic properties.

The extremely high solubility and mobility of hydrogen in GaMnAs (cf. [24]) allows the complete passivation of even x=0.07 Mn acceptors. Hence this controllable passivation process provides us with samples with any desired amount of carriers.

As the samples become paramagnetic below a certain hole concentration this offers even the possibility of lateral magnetic patterning [28]without any etching.

The hydrogen doping is possible by using atomic hydrogen produced by the use of hydrogen plasma. The in-diffusion is a thermally activated process which can be handled conveniently at a substrate temperature of $150°C$. Considering the growth and degradation temperatures (cf. 1.4.3), this treatment is not expected to modify the GaMnAs samples otherwise.

### 4.2.2 Activation energy; post-hydrogenation annealing effect

The (H,Mn-As) complexes are stable up to about $100°C$ fig.4.1. The activation energy in order to dissociate this complex has been calculated as $\approx 0.4-0.66eV$ [27]. At higher temperature the hydrogen atoms are separated from the complex and out-diffuse toward the free surface of the layer, where they recombine and form $H_2$ molecules. As the out-diffusion profile can be adjusted by the annealing period t, one can control the amount of hydrogen (and so the hole concentration). As the passivation process itself is more difficult to control quantitatively, the post-passivation annealing of a fully passivated sample has been used in this study.

All the mentioned properties of the hydrogen co-doping makes it an exceptional technique to reduce the hole concentration without modification of the Mn concentration and distribution.

## *4.3 Hydrogenated series preparation*

The initial sample was a standard $Ga_{0.93}Mn_{0.07}As$ film of 50nm thickness grown by LTMBE at $260°C$ on a (100) GaAs substrate. After the growth the film was

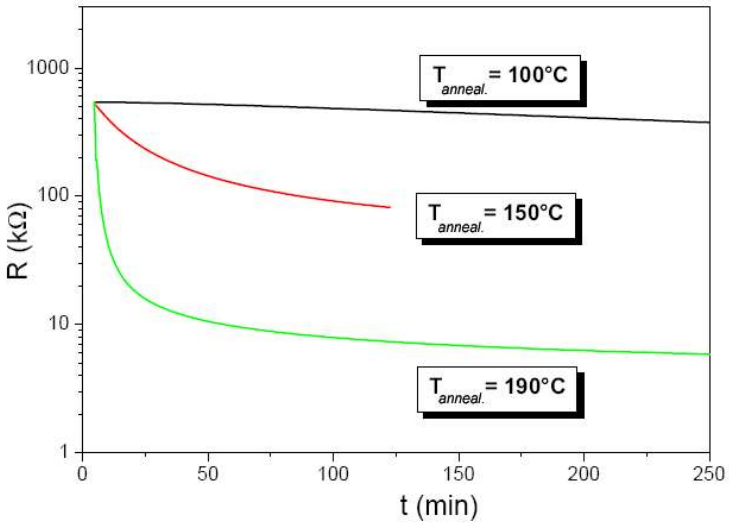


**Figure 4.1:** The resistivity of the samples as a function of the annealing time for different annealing temperatures. The resistivity is normalized to an initial value. [29]

annealed at 250°$C$ four 1 hour under nitrogen to optimize its magnetic properties. The annealed films have a critical temperature of $T_C \approx 140$K. Then the film was hydrogen doped by exposure to an radio frequency hydrogen plasma (13.56 MHz, 80 mW.cm$^{-2}$, 1 mbar) at 130°$C$ during 3 hours. The hydrogenation parameters were chosen such as to fully passivate the film. The hydrogen concentration and profile were verified by secondary ion mass spectroscopy. The hydrogenated wafer was then cut in different pieces which were partially depassivated by vacuum annealing at 150°$C$ for durations between 6 min and 3000 min. We thus obtained a series of samples with hole concentrations between $10^{18}$ and $10^{21} cm^{-3}$. These samples were further characterized by X-ray diffraction, Hall measurements and static magnetization measurements with a superconducting quantum interference device (SQUID). For more details on the preparation and characterization of these films see ref [3, 25, 29].

## *4.4 Modification of the lattice parameter*

The Hydrogen incorporation in the GaMnAs layer is accompanied by a slight modification of the lattice parameters. XRD results of hydrogenated samples are given in table 4.1. They show a variation of the lattice parameter (strain) with respect to GaAs, as a function of hole concentration which is directly related to the hydrogen concentration. It is found to vary from 0.33% (compared to the GaAs lattice parameter) for the sample.A to 0.17% for the reference sample which contains

no more hydrogen.

## 4.5 Resistivity and Hall effect measurements

The optimization of the temperature and duration of the passivation conditions was provided by monitoring the change of the resistivity of the layer before and after the hydrogenation. For a fully passivated sample resistivity values greater than $40M\Omega$ were obtained, proving that they are highly resistive. This value, considering the mobility of H:5 $cm^2/Vs$ (cf. [23]) provides an upper limit for $p \approx 6 \cdot 10^{16} cm^{-3}$, indicating the high mobility of hydrogen even at temperatures as low as $130°C$. Higher passivation temperatures -above $170°C$- lead to lower resistivity values for a same exposure times and thus a lower H incorporation(fig.4.2).

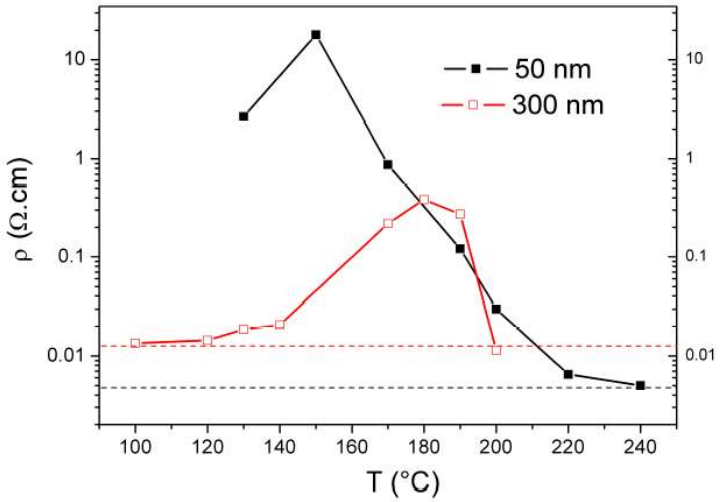


**Figure 4.2:** Electrical resistivity of GaMnAs/GaAs sample with $x \approx 0.7$ measured in-situ during the passivation process. The measurement is performed as a function of the substrate temperature during the passivation treatment. two 50nm (filled squares) and 300nm (empty squares) are compared. The maximum value of the resistivity corresponds to the highest passivation; it depends on the layer thickness. ( [24])

The resistivity measurements were performed after the post-passivation annealing at $190°C$. Figure 4.3 shows the evolution of the resistivity with annealing time. The reference sample was exposed to the same annealing process in order to have a reference sample with the same thermal history. As it is shown in the figure 4.3, the reference sample shows no notable change during the 3000 minutes of annealing. Different from previous studies on which had shown the degradation of the film after long time annealing, these measurements are consistent with the recent work of Olejnik et al. [30] who also observed the establishment of a saturated state after thermal annealing.

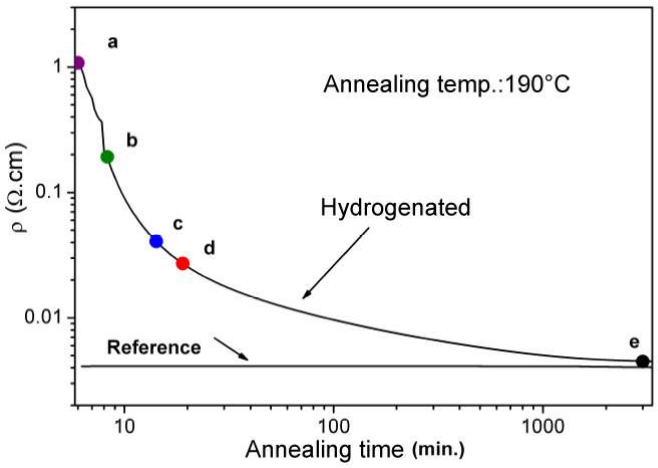


**Figure 4.3:** Resistivity vs. post-passivation annealing time monitored during the annealing. The circles represent the series of samples studied here. The Reference sample was annealed independently for the same annealing duration as the other samples and the result is is shown by the lower solid line. [24].

The hole concentration has been determined by low temperature (T=1.8 K) high field (10T) transport measurements in order to limit the contribution from the anomalous Hall effect. The hole concentrations were obtained from the relation

$$\rho_{xy} = H/pe + C\rho_{xx}^2 M_\perp$$

where $\rho_{xy}$ and $\rho_{xx}$ are the Hall and sheet resistivity respectively. $M_\perp$ presents the perpendicular magnetization and $C$ is a proportionality constant. (for more details on determination of hole concentration in this series see [29]).

These measurements were limited to the regimes in which the samples had a sufficiently high carrier density, i.e. for the fully passivated and the samples with very short annealing times the hole concentration could not be measured in this way.

The resistivity as a function of temperature is shown for different samples in fig.4.4. The transport measurements have shown that the samples have different conductivity regimes. Samples C, D, E and "reference" are metallic whereas samples A and B show a thermally activated behavior at low temperature [24].

Table4.1 summarizes the basic properties of the investigated samples. As it is shown, the initial hydrogen passivation leads to a complete electrical compensation reducing the hole concentration to values below $10^{18}\text{cm}^{-3}$.

The critical temperatures $T_C$ of these films vary from 25K and 140K. They were deduced from electrical transport and magnetometry (SQUID) measurements and they have been independently verified by our FMR measurements. The peak of the resistivity gives only an approximate value of the critical temperature. [31](cf.

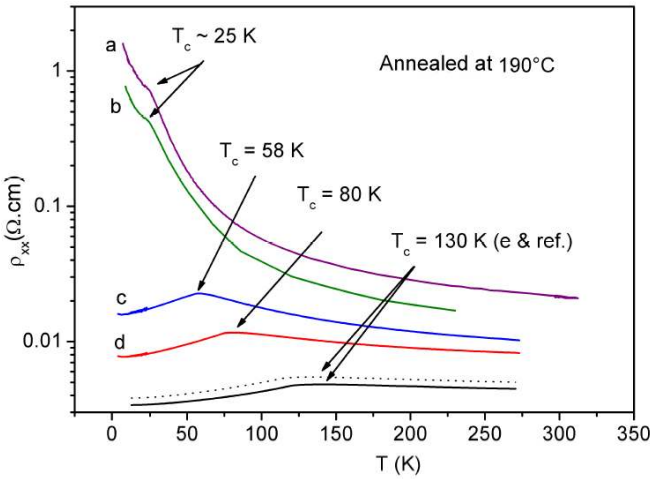


**Figure 4.4:** Electrical resistivity of the GaMnAs/GaAs samples as a function of temperature. The arrows show the approximative Curie temperatures of samples A to E and the Reference sample. [24]

fig.4.4). For the low hole concentrations the values estimated from the resistivity curves differ slightly from those obtained by SQUID and FMR measurements as shown in the table table:hydrogentable. The $T_C$ of 140K for the reference sample decreases to 25K for sample A. The hydrogenated sample is paramagnetic.

## *4.6 Elastic recoil detection (ERDA) spectroscopy*

ERDA measurements have been performed in order to determine the hydrogen content in the samples. For sensitivity limitations, we present ERDA measurements on the sample.A only.

For the ERDA measurements the samples were irradiated with a $He^{2+}$ beam of 3MV energy at a beam current of 3nA. The beam section was circular with a diameter of 0.5mm. The sample was tilted at an angle of 65° with respect to the probing beam and the detection angle was chosen to 35°. In order to protect the detector from the forward scattered $\alpha$-particles a thin mylar film of $13\mu m$ was placed before the detector.

For the calibration of the measurements in absolute units (hydrogen atoms per $cm^2$) a reference sample of $H_8C_8$ (polystyrene), grown on a Si substrate was used; it contains $3 \cdot 10^{17}$ hydrogen atoms per $cm^2$.

To verify a eventual hydrogen loss due to the beam exposure several successive measurements at equal doses were performed at a same point of the sample; each dose corresponds to $1\mu C$. The results given in table.4.2 show no degradation.

Typical ERDA spectra for sample.A and the polystyrene reference samples are

**Table 4.1:** Annealing time, Curie temperature $T_C$, hole concentration $p$ , biaxial strain $\epsilon_{xx}$ and magnetization $M$ at 1kOe and T=4K for the set of the reference and hydrogenated samples. The reference sample has equally been annealed for 3000min in order to eliminate any effects related to the purely thermal anneal.

| sample | Reference | E | D | C | B | A | Fully passivated |
|---|---|---|---|---|---|---|---|
| $T_c$ (K) | 142 | 137 | 86 | 72 | 42 | 25 | Para magnetic |
| Annealing Time (min) | 3000 | 3000 | 19 | 14 | 8 | 6 | 0 |
| Hole concentration ($10^{19}$ cm$^{-3}$) | 100 | 79 | 11 | 3.2 | 2 | - | 0.01 |
| $\varepsilon_{xx}$ (%) | -0.17 | -0.18 | -0.27 | -0.30 | -0.31 | -0.32 | -0.36 |
| Magnetization at 4K (emu/cm$^{-3}$) | 44.25 | 40.29 | 36 | 32.76 | 30.96 | - | - |

shown in fig.4.5

There is a slight background signal which maybe due to a residual contamination in the chamber. It was $\approx 42 counts/\mu C$.

The counts rate for the two samples are:

- polystyrene: 3000-42×2=2916±56
- Sample.A: 785-42×4=617±31

Since the samples are very thin, the energy loss of the He beam across the sample is negligible, therefore the number of hydrogen atoms per $cm^2$ can be simply calculated from the following expression:

$$N_{H/cm^2} = 300 \times 10^{15} H/cm^2 \times (2/4) \times (617/2916) = 31.7 \pm 1.7 \times 10^{15} H/cm^2$$

Where H stands for Hydrogen atoms. Assuming that the total amount of hydrogen is contained only in the 50nm thin GaMnAs layer we deduce a concentration of $\approx 6.3 \times 10^{21} H/cm^3$ which is 6 times larger than the Mn concentration.

From the ERDA spectra simulation we can also deduce the distribution of the hydrogen atoms within the sample. The measurements show a flat concentration profile with a H concentration of 11% for the first $290 \cdot 10^{15}$ atoms/cm$^3$. Supposing the theoretical density of GaAs=$4.5 \cdot 10^{22}$/cm$^3$ it corresponds to:

**Table 4.2:** The ERDA count rates measured for sample.A and the polystyrene sample for different beam dose

| Sample | Dose | Count rate |
|---|---|---|
| Sample A | 1 μC | 186 |
| Sample A | +1 μC | 366 |
| Sample A | +1 μC | 577 |
| Sample A | +1 μC | 785 |
| Polystyrene | 1 μC | 1542 |
| Polystyrene | +1 μC | 3000 |

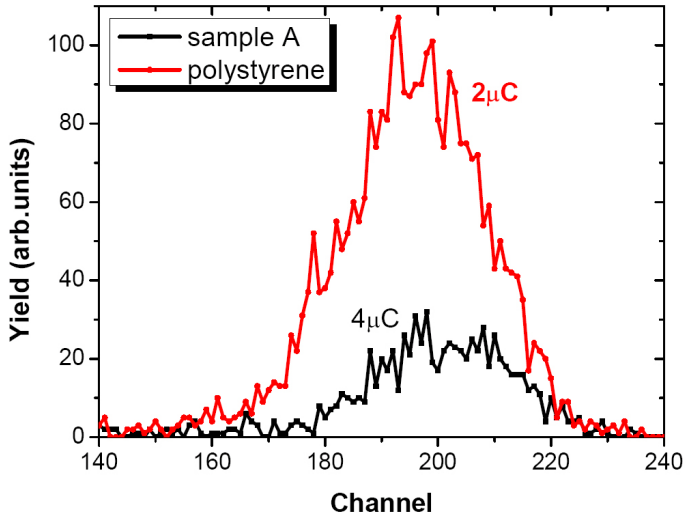


**Figure 4.5:** ERDA spectra for samples A (black/dark) and polystyrene (red/light) as reference.

$$290 \times 10^{15} at/cm^2 / 4.5 \times 10^{22} / cm^3 = 64nm$$

Our result show that the hydrogen has also been diffused in the substrate layer.

### *4.7 SQUID measurements and results*

The magnetization M(H) of the samples were measured with a commercial superconducting quantum interference device (SQUID)with the field aligned H‖[110] (fig.4.6.a) and for H‖[001] (fig.4.6.b). For the in-plane orientation the coercive field varies progressively from 500 to 1200 Oe for samples reference to B respectively; the opposite behavior is observed for H‖[001]. The saturation magnetization decreases with increasing hole concentration for this field orientation.

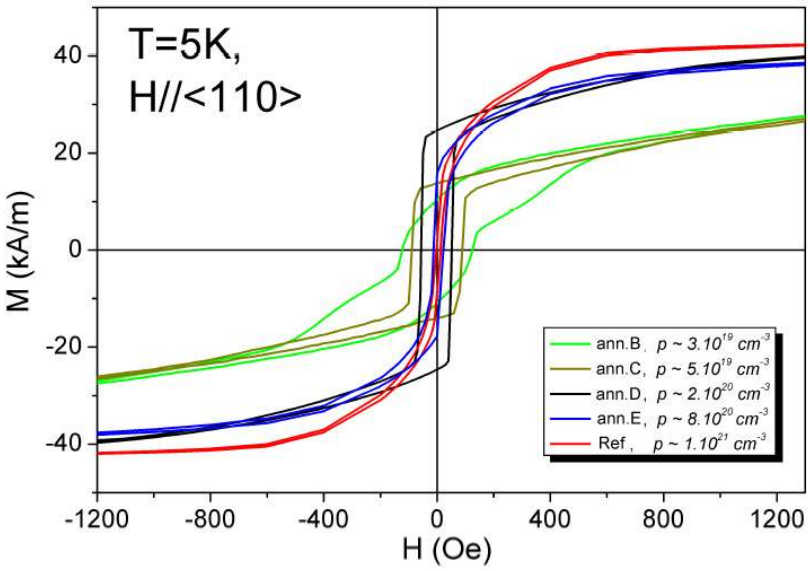


**Figure 4.6:** Magnetization of the hydrogen passivated series (as indicated in the figure) as a function of applied field for H‖[110];T=5K.

For H‖[110] the hysteresis loops become wider as the hole concentration decreases. This fact is attributed to an increasing inhomogeneity and a change in the anisotropy constants (for example see [32, 33]).

The magnetization at T=5K and H=0.3T decrease with increasing hydrogen concentration. They vary from 44 emu/cm$^3$ for the reference sample to 31 emu/cm$^3$ for sample B (table 4.1). Such a reduction is expected from the decrease of the exchange interaction strength with decreasing hole concentration. In the mean field approach (cf. [34]) Mauger et al. have calculated (via RKKY model) this variation

for Mn ions in CdTe and in the antiferromagnetic phase as:

$$J_{eff}\left(R_{ij}\right) = \frac{9\pi}{2}\frac{p^2}{E_F}J^2\frac{sin\left(2k_FR_{ij}\right) - 2k_FR_{ij}cos\left(2k_FR_{ij}\right)}{\left(2k_FR_{ij}\right)^4}$$

where the effective exchange integral J is proportional to the second power of the hole concentration $p$. k and E are the wave vector and the energy of the Fermi level of the delocalized holes. Considering the $k_F^3 \approx$p hence the saturation magnetization should vary as $[p]^{1/3}$ as is actually observed (fig.4.7).

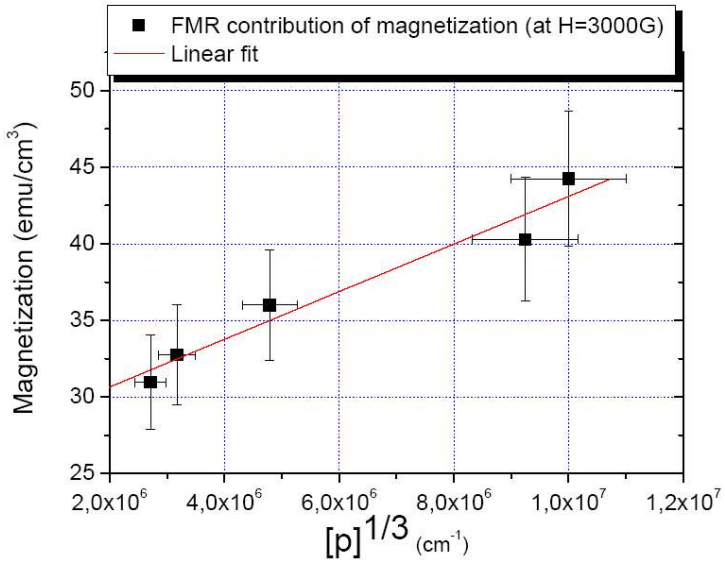


**Figure 4.7:** Magnetization as a function of the hole concentration in the presence of H=3kOe. The solid line is a linear fit to the measurements. H‖[110] and T=5K.

The magnetization measurements (fig.4.6) show that the fully passivated sample is paramagnetic and that sample A is the sample with the lowest hole concentration for which ferromagnetism is observed. As it was explained in section4.5 it is difficult to be more precise for the threshold hole concentration corresponding to the on-set of ferromagnetism at T=4K; it should be considered as an upper limit ( $10^{19}$cm$^{-3}$). After the longest annealing time of 3000 minutes (sample E) the film is completely depassivated and the initial properties are nearly restored. Nevertheless, we still observe a 10% difference in the magnetization and a 20% smaller hole concentration between the 'fully depassivated' sample E and the reference samples. Different hypotheses might be proposed to explain this difference. Either the sample is not yet fully depassivated or more probably, the hydrogenation and/or the 3000 min

depassivation treatments have degraded the sample slightly. In fact, it is well known that exposure to a ion plasma can etch the sample surface and thus degrade its magnetic properties.

The M(H) measurements (fig.4.6) require some further comments. The saturation magnetization of the reference sample is already significantly lower than expected from the doping level. If all x=0.07 Mn ions were occupying substitutional sites and were magnetically active we should expect a magnetization of 72 emu/cm$^3$ where the negative contribution of the free holes, about 10% of the Mn magnetization [20], has been taken into account. Thus a large fraction of about 1/3 of the Mn ions is apparently not magnetically active, probably due to interstitial site occupation and/or the formation of antiferromagnetic complexes with substitutional Mn ions which have not been removed by the annealing treatment. Extending the magnetization measurements to fields above 1T we observe for the reference sample an increase from M 44emu/cm$^3$ to M 50emu/cm$^3$ (fig.4.8).

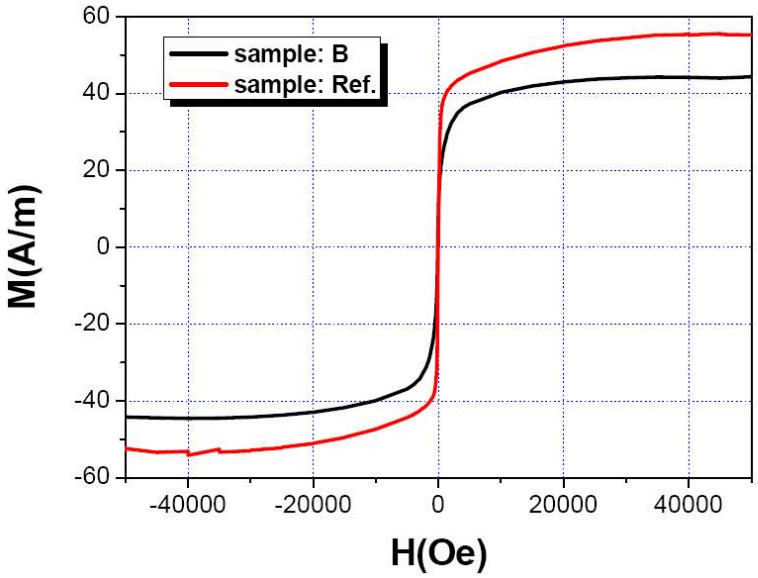


**Figure 4.8:** High field magnetization M(H) for samples B (black/dark line) and Reference (red/light line) at T=5K for H‖[110].

This increase, which is about 12% of the total magnetization, indicates the presence of a paramagnetic phase even in the reference sample. More detailed information on the magnetization cycles and transport measurements is given in reference [3]. The simultaneous presence of a paramagnetic fraction even for optimized thermal annealings is a general observation in LTMBE GaMnAs layers. Three facts can be attributed to the existence of this paramagnetic phase. The frustration of spins due to the defects in the crystal, a fraction of isolated interstitial manganese

ions, which are not associated with a nearest neighbor substitutional Mn ion and not fully ionized arsenic antisite ions. Specific microscopic measurements such as ion channeling and particle induced X-ray emission (PIXE) have been applied in a few cases to investigate this problem quantitatively [35] and section 5.3. They have confirmed the presence of interstitial Mn ions located on tetrahedral interstitial sites with As nearest neighbors. Extension of the SQUID measurements to higher fields show in all cases the presence of a paramagnetic phase superposed on the ferromagnetic phase.

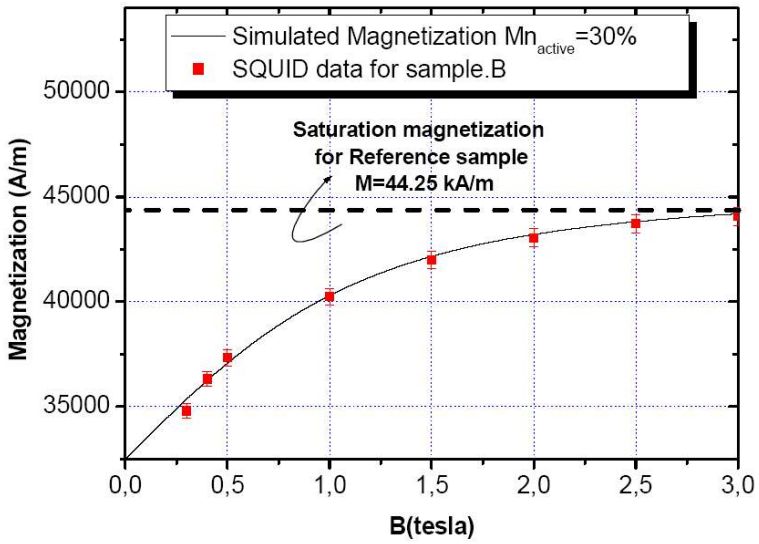


**Figure 4.9:** High field magnetization M(H) for sample B at T=5K as measured by SQUID (squares) and the simulation of its paramagnetic component by a Brillouin function with S=5/2 (line) to which the ferromagnetic contribution of the magnetization has been added as a constant offset. In order to compare the result with the magnetization of the reference sample its value has been indicated by a horizontal line (dashed line).

The case of samples A and B is different from the other ones as the hole concentration at low temperature falls in the $10^{19} cm^{-3}$ range for which localization effects can be expected to become important either in the form of impurity band conduction or polaron formation [36, 37]. As we still observe in these samples a ferromagnetic resonance spectrum with a well defined angular variation we know that they are homogeneously magnetized. The weak thermal activation energy shows that the conduction proceeds via an impurity band with thermally activated hopping. As shown in fig.4.9, contrary to the magnetization saturation behavior expected for a homogeneous ferromagnetic film, sample B presents as the other samples of this series a strong paramagnetic component in addition to the ferromagnetic one. The data from the SQIUD measurement can be fitted by a Brillouin function with S=5/2

and a corresponding Mn fraction of x=0.015, i.e. 30% of the magnetically active Mn centers. This can be attributed to either bulk or lateral inhomogeneous distributions of the hydrogen ions in the partially depassivated samples. Considering the possible gradient of the hydrogen profile along the growth direction this effect can be very possible.

The temperature dependence of the magnetization value was also measured for H‖[110] with H=500Oe. The results are shown in fig. 4.10 as the reduced magnetization vs temperature. The Curie temperature can be deduced from the temperatures where the magnetization becomes zero (since, a priori, the paramagnetic contribution for this amount of applied field is negligible). As the hydrogen concentration increases, there is a change in the form of the magnetization curve at temperature above $0.7T_C$. This change is attributed to either the increase in the concentration of paramagnetic centers or to the reorientation of the magnetic easy axis at these temperatures [38]. For these samples $T_C$ is deduced from fitting the magnetization curve with a Brillouin function.

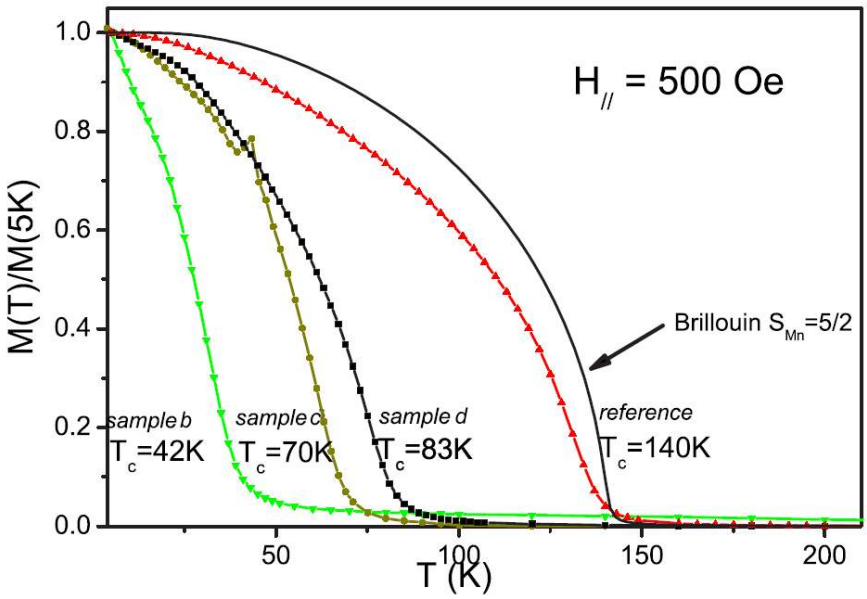


**Figure 4.10:** Temperature dependence of the normalized magnetization under a 500 Oe in-plane field for samples B,C,D,E and reference. The solid line corresponds to a Brillouin curve with $S_{Mn}=5/2$ and $T_C=140$K. Curie temperatures increase and curves become more convex with increasing hole density.

In the following we will present and analyze in detail the FMR results in order to deduce the hole concentration and temperature dependence of the magnetic anisotropies in these samples.

## *4.8 Magneto-optical Kerr microscopy*

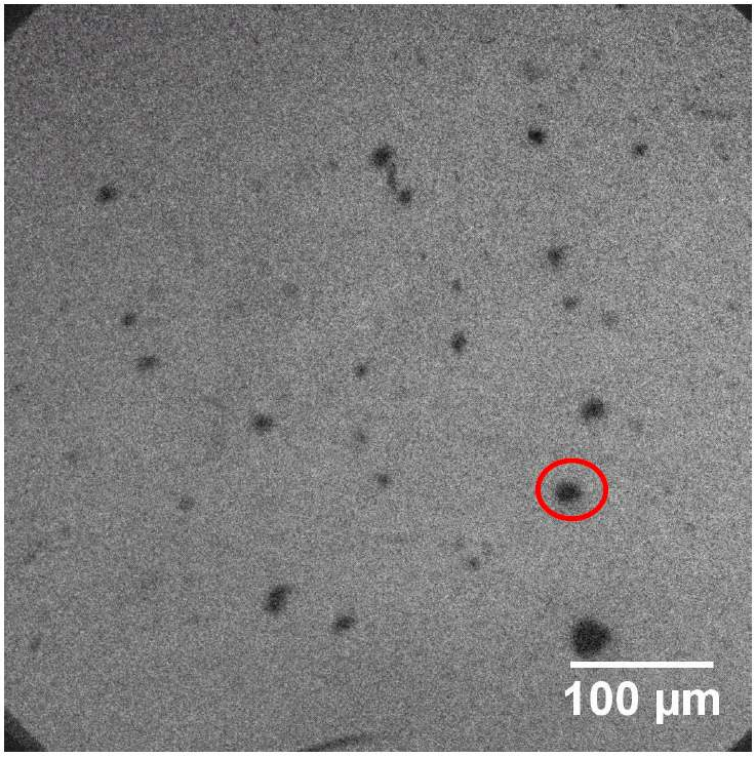


**Figure 4.11:** Magneto-optic Kerr image of sample.B for H=180Oe with H‖[001] -the easy axis- at T=3.5K

Fig.4.11 shows the image of sample.B taken via magneto-optical Kerr microscope at T=3.5K. The camera is fixed along perpendicular direction to the film plane. The image is obtained by dividing the image of the sample exposed to an applied field H=180Oe along the [001] axis by its image after being saturated at H=-600Oe. The black spots in the image present regions in which the magnetic moments possess lower values projected along the normal-to-plane axis (they are not saturated). Note that the application of a field of H=400Oe provides qualitatively the same image. This feature is retained up to T=10K, after which the magnetization reorients in both regions to the in-plane direction and therefore Kerr measurements are no longer possible.

In fig.4.12 the hysteresis curves of the magnetization are shown; they were obtained from the average intensity of the images with respect to a point of the film surface. The Kerr signal is normalized to the saturated value of the rest of the film which constitutes the higher curve ($305\mu$m·$305\mu$m centered on fig.4.11). The measured coercive field is well consistent with the SQUID measurements. The lower curve refers

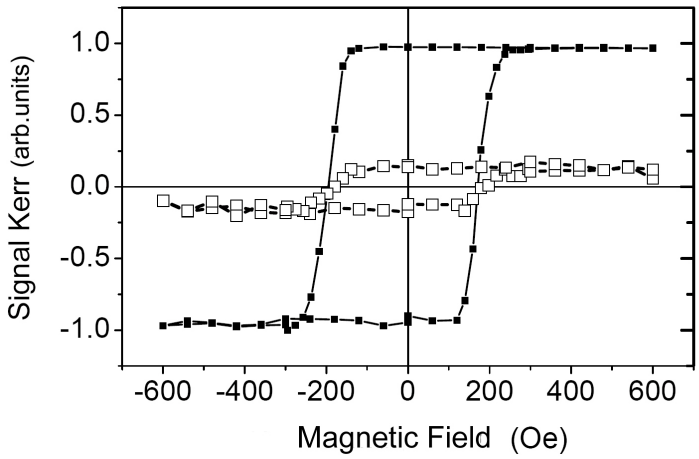


**Figure 4.12:** Hysteresis curves deduced from Kerr measurements for sample.B at T=3.5K. The filled squares correspond to the average intensity of the image in fig.4.11, the open symbols correspond to the defect regions shown in fig.4.11

to the magnetization of the region marked by the red circle in fig.4.11($10\mu$C·$7.6\mu$C). The spots are the ferromagnetic regions with the same ceorcivity field as the other parts of the image but with the magnetization ≈6.8 times lower.

For a better observation of how different region behave as a function of the applied field, we have presented in fig.4.13 the images taken while the field was progressively increased (note that the film was initially saturated in inverse direction). While most of the image in fig.4.13a is dark for H=100Oe, one can still observe the white traces. When the magnetic field is increased, the rest of the image starts to change its contrast. This feature is shown in fig.4.13c and d. The MOKE measurements on the samples with high hole concentrations has shown that the progressive alignment of the magnetization with applied fields, while the applied field is less than the coercive field, is achieved via the nucleation of the magnetic domains in the regions were the energy costs for flipping the moment is lower (i.e. in regions corresponding to structural defects) and then it is the domain wall propagation which is responsible for the total magnetization reversal process [32]. In the particular case of the sample.B however as is demonstrated in this figure, the magnetization reversal of the film occurs apparently as a uniform process. This might be due to the small size of the magnetic domains which are below the resolution of our system. The other particular aspect of the sample, is the emergence of the small zones surrounded by the white traces present in all four images in fig.4.13 and the corresponding Kerr hysteresis curve in fig.4.14. These regions, which are characterized by a lower magnetization, are the ones surrounded by macroscopic crystalline defects such as dislocations. On these defects since the energy cost to magnetization reversal is low, they are aligned with the applied field in more lower fields, whereas

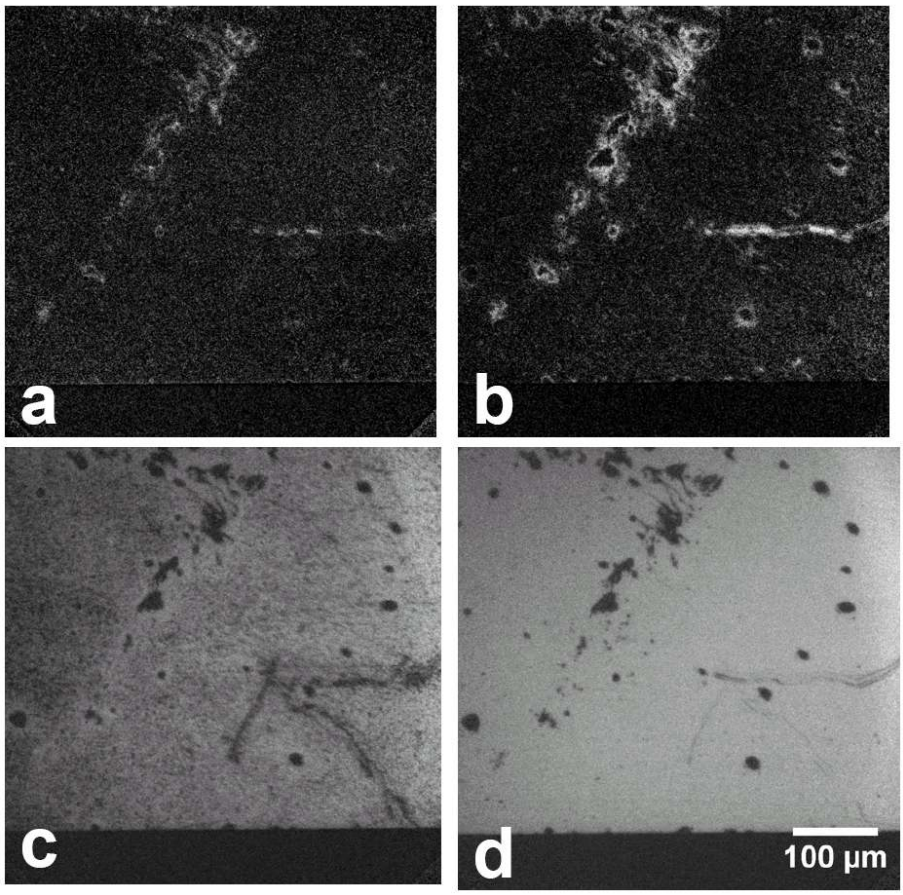


**Figure 4.13:** Kerr images of samples.B for the applied fields: (a)100Oe (b)150Oe (c)170Oe (d)300oe along [001] axis after saturated in opposite direction with H=600Oe. the images are divided to the image of sample in zero applied field after the saturation

hydrogen ions captured in them could not be easily out-diffused by post-passivation annealing process and yet therefore these are the regions which are more electrically compensated as the rest of the sample. The limitations of our spectrometer has not allowed us to extend the measurements to higher fields (above 600Oe).

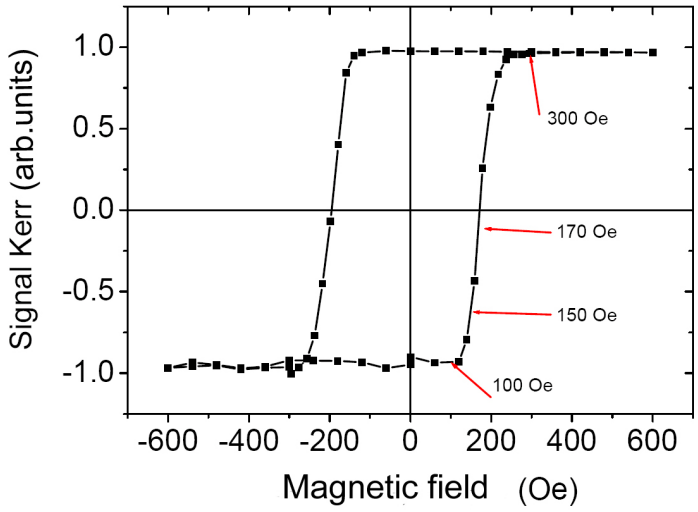


**Figure 4.14:** The hysteresis curve corresponding to the Kerr images in fig.4.13

## *4.9 FMR measurements*

The ferromagnetic resonance (FMR) measurements were performed with a standard X-band spectrometer with 100 kHz field modulation and first derivative detection. The angular dependence of the FMR spectra was measured for two rotation planes of the applied static magnetic field: (110) and (001), named out-of-plane and in-plane configurations respectively (cf.2.1). Samples B to E have been fully investigated by the FMR spectroscopy. Sample A showed a too large linewidth which combined with a low critical temperature of ≈25K did not allow reliable FMR measurements. It will not be discussed further in the following.

### *4.9.0.1 Reference Sample [p] =1·10$^{21}$ cm$^{-3}$*

In fig.4.15 we show typical FMR spectra of the reference sample for the in-plane and out-of- plane orientations at T=4K. The FMR lineshapes are slightly asymmetric due to the high conductivity of the film which leads to mixed absorption / dispersion line-shapes (cf. [39–41]). In addition to the main FMR line corresponding to the uniform mode, additional small intensity lines are visible. These satellite lines

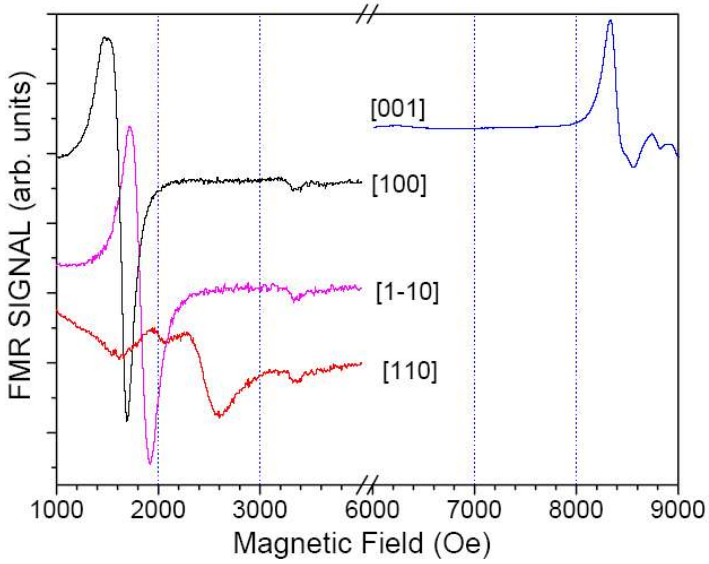


**Figure 4.15:** FMR spectra at T=4K of the reference sample (sample.R: GaMnAs/GaAs, 50nm thick, $x \approx 0.07$) for the four high symmetry orientations of the magnetic field. The small intensity additional high field lines visible for H||[001] are attributed to an inhomogeneity of the sample magnetization. They give also rise to the doublet structure for H||[110]

are not spin wave related but are attributed to sample inhomogeneities. Such inhomogeneities can result from locally different concentrations of the magnetic ions, an inhomogeneous hole concentration related to the compensating defects or strain variations which create the regions with different anisotropy fields; i.e the resonance field $H_res$. The effect of inhomogeneity is most easily seen for the hard axis orientation of the applied magnetic field. In the following sections (cf. 4.10) we show that the variation of resonance field is more sensitive in this direction compared to other axes. For the moment we will neglect these inhomogeneities and discuss only the dominating uniform mode FMR lines. In FMR the easy and hard axes of the magnetization can be directly deduced from the orientations for which the minima and maxima of the resonance field occur. The resonance positions for the four high symmetry orientations show that at 4K the in-plane [100] direction is the easy axis of magnetization while the hard axis is the [001] direction normal to the film plane. This is the "normal" configuration for annealed $Ga_{1-x}Mn_xAs$ with x≈0.05 layers with low electrical compensation grown on GaAs substrates, which due to the lattice mismatch are under strong compressive stress (table 4.1 ). Locally inhomogeneous magnetic properties of GaMnAs films are often observed in FMR even in thermally annealed samples. Whereas they are not easily detected by SQUID measurements (due to the sensibility of SQUID measurements to the average value of magnetization in the whole sample) they are easily separated in the FMR spectra

as lines with different resonant fields. The spectrum obtained at T=4K along [001] axis is decomposed in 6 different spectra with slightly relative different resonance fields with different respective intensities (fig. 4.16).

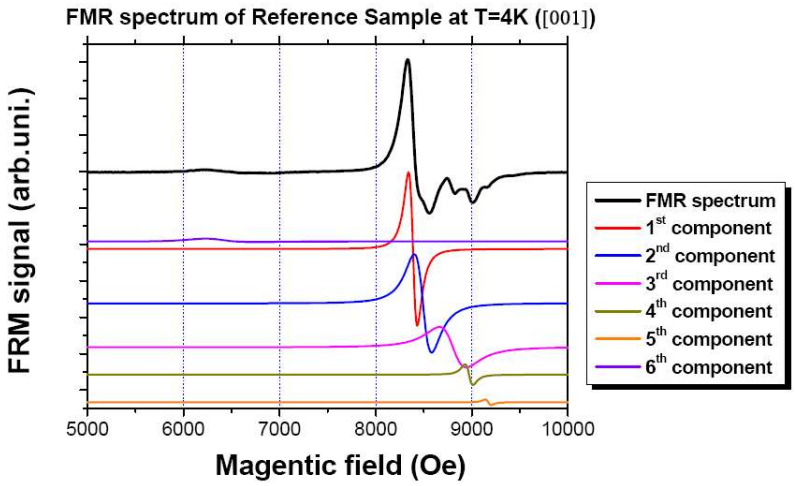


**Figure 4.16:** FMR spectra of the reference sample (sample.R: GaMnAs/GaAs, 50nm thick, $x \approx 0.07$) for H‖[001] at T=4K and its decomposition into six Lorentzian components.

Goennenwein et al [23] have used the analysis of the spin wave resonances to investigate the homogeneity of GaMnAs films. They observed an unexpected constant spacing of the spin wave resonance positions which they ascribed to a magnetization gradient over the sample thickness. Inhomogeneous distributions of interstitial Mn ions related to the post growth annealing process have often been evoked in this context but quantitative measurements supporting such concentration profiles are rare. The inhomogeneity of the as grown samples can be improved by annealing processes but apparently the initial annealing conditions chosen by us - the one's giving a minimal electrical resistivity- were not yet sufficient to fully homogenize the sample properties. The temperature dependence of the FMR spectra was measured between 4K and $T_C$. Fig.4.17 shows the FMR spectra for hard and easy axes orientation as a function of the temperature. We observe a monotonous shift of the resonance fields toward the paramagnetic limit (H=3400Oe / g=2.00) with increasing temperatures. As will be shown below (cf. 4.11.2), this is a result of the strong temperature dependence of the anisotropy constants which determine the resonance positions.

From the in-plane measurements we observe a change in the orientation of the easy axis from [100] for T<80K to [1$\bar{1}$0] for T≈110K (0.77 TC). The linewidths of the FMR spectra vary with the orientation of the applied field. The lowest linewidths are observed for H‖[100], the easy axis orientation and maximum linewidths for

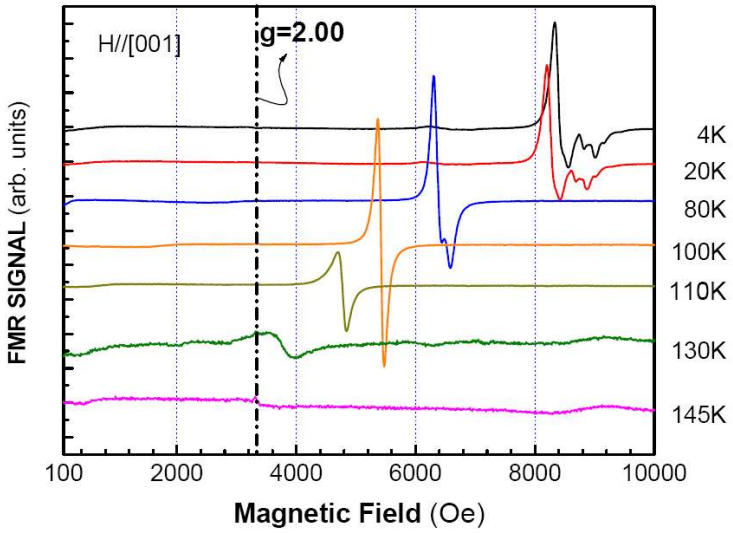


**Figure 4.17:** FMR spectra of the reference sample as a function of temperature for H‖[001].

H‖[110]. The linewidths vary only slightly with temperature with the exception of the temperatures range close to TC where they broaden significantly. Typical values at T=4K are approximately $H_{pp}$=300Oe for H ‖ [001] and $H_{pp}$=200Oe for H‖[100].

#### 4.9.0.2 Fully-depassivated sample E: [p]=7.9·10$^{20}$cm$^{-3}$

The low temperature (4K) FMR spectra of this sample are shown in fig.4.18 For this sample the recovery of the original hole concentration suggests that all the hydrogen atoms in the matrix have been out-diffused. We should thus expect similar resonance fields as for the reference sample which is actually observed. In addition, the FMR spectra show a remarkable improvement of the lineshape in particular for the H‖[001] orientation. As compared to the reference sample both the linewidth of the uniform mode spectrum is reduced and the small intensity side lines have been eliminated. This improvement is attributed to the additional 50 hours annealing accompanying the hydrogen out-diffusion treatment. As in the previous case there is a change of the easy axis from [100] to [1-10] at T≈110K ( 0.8 TC). At T≈135K the sample becomes paramagnetic.

#### 4.9.0.3 Sample D: [p]=1.1·10$^{20}$cm$^{-3}$

The angular variation of the FMR spectra for the in-plane configuration is shown in fig.4.19. We observe a strong variation of the linewidth with the lowest value for H ‖ [100], the easy axis of magnetization. The FMR lines are broader than in

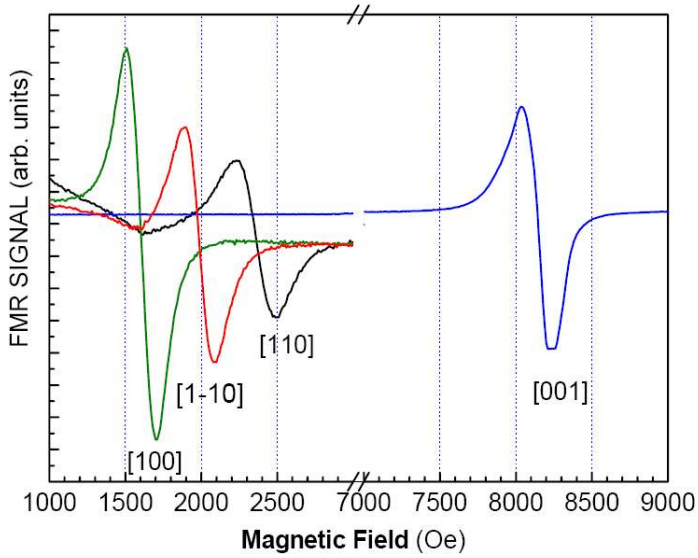


**Figure 4.18:** FMR spectra at T=4K of sample E for the four high symmetry orientations of the applied field. An obvious improvement of the line-shape and linewidth as compared to the reference sample is observed.

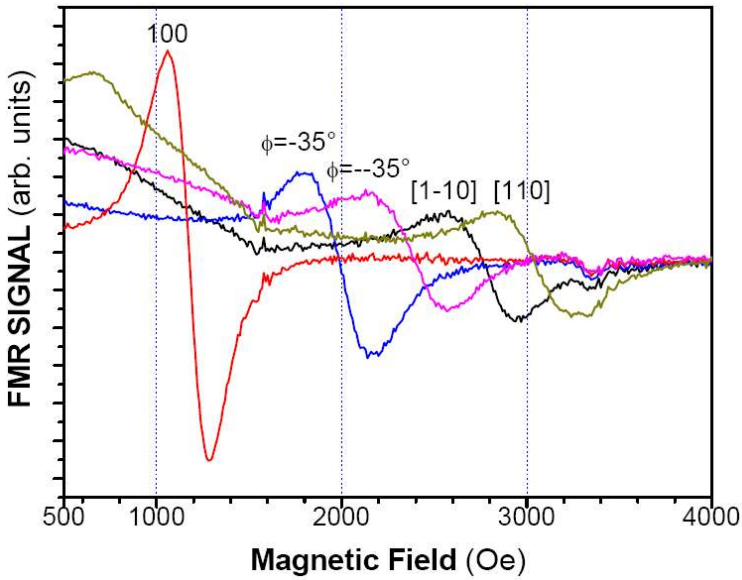


**Figure 4.19:** FMR spectra at T=4K of sample D for the in-plane angular variation of the applied field.

sample E and a slight deformation of the main FMR line by the small intensity inhomogeneous lines, which are no longer resolved, can still be noticed in the hard axis orientation. We observe at 4K a decrease of the extrema of the resonance fields for hard and easy axis orientation of the applied field as a result of the decreased effective magnetization $M_{eff}$ value. While the hard axis of the sample remains [001] for all temperatures up to $T_C \approx 86$K, the easy axis changes its orientation at T=70K ($0.8T_C$) from [100] to [1-10] direction. The evolution of the spectra as a function of the temperature is presented in fig.4.20. The extension of the resonance position for in-plane and hard axes orientation ([110] and [001] i.e. for out-of-plane configuration) first increases when the temperature is raised from 4K to 20K and then decreases monotonously up to the Curie temperature. This observation of increasing resonance fields with increasing temperatures between 4K and 20K is a quite general observation for GaMnAs layers with samples with intermediate to low hole concentrations; it does not seem to be related to a change in the hole concentration. One should note that although the extension of the resonance field from hard axis to [110] increases in from 4K to 20K its total extension from hard to easy ([100]) axis decreases globally.

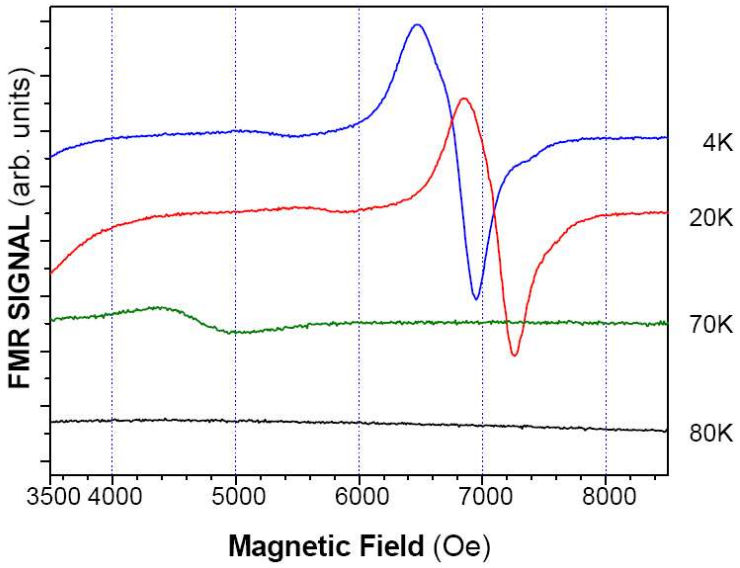


**Figure 4.20:** FMR spectra of sample D for H||[001] at different temperatures. Increasing the temperature from 4K to 20K shifts the resonance to higher fields.

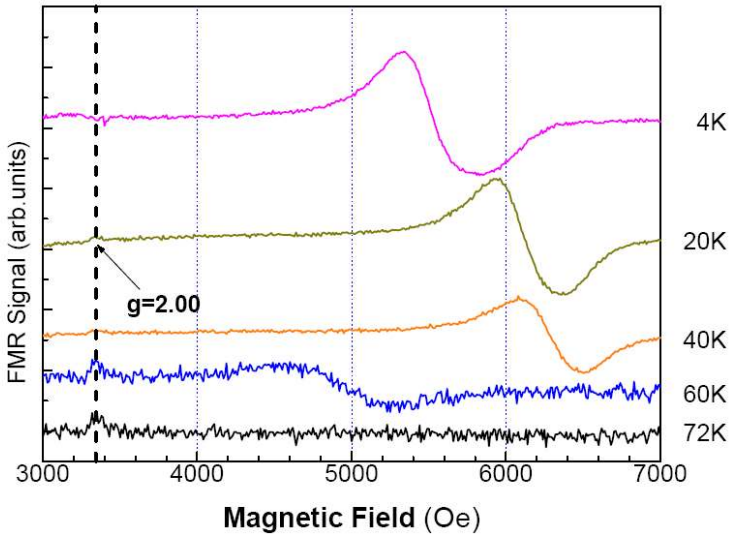


**Figure 4.21:** FMR spectra of sample C for H‖[001] for different temperatures between 4K and 72K.

#### 4.9.0.4 Sample C: [p]=3.2·10$^{19}$cm$^{-3}$

Sample C is the sample with the lowest hole concentration with a still metallic conductivity regime. As for the previous samples we observe a further increase in the linewidths and a reduction of the extension of the resonance fields between hard and easy axes(fig.4.21). The low temperature easy axis is still [100] and as for the samples with higher hole concentrations the easy axis orientation changes from[100] to [1$\bar{1}$0] at T=0.8T$_C$. Of course, since at this temperature the in-plane directions become nearly equivalent, the difference between the three in-plane axes becomes small. The critical temperature of this sample is reduced to T$_C$=72K. The out-of-plane FMR spectrum for H‖[001] goes to larger values when the temperature is increased from 4K to 40K and then rapidly decreases when approaching T$_C$.

#### 4.9.0.5 Sample B: [p] =2·10$^{19}$cm$^{-3}$

In sample B we still observe a ferromagnetic resonance spectrum but now with a highly increased linewidth of up to $\Delta$H $\approx$ 2000Oe at T=4K (fig.4.22). Both the reduction of the hole concentration, and thus the exchange integral J$_{pd}$, and the contribution of the paramagnetic inhomogeneities do contribute to this broadening. A hole concentration of 2·10$^{19}$cm$^{-3}$ is thus still sufficient for long range ferromagnetic order. The main change occurs for the low temperature easy axis of magnetization. From the inversion of the high field /low field resonances (Fig.4.22) we can conclude

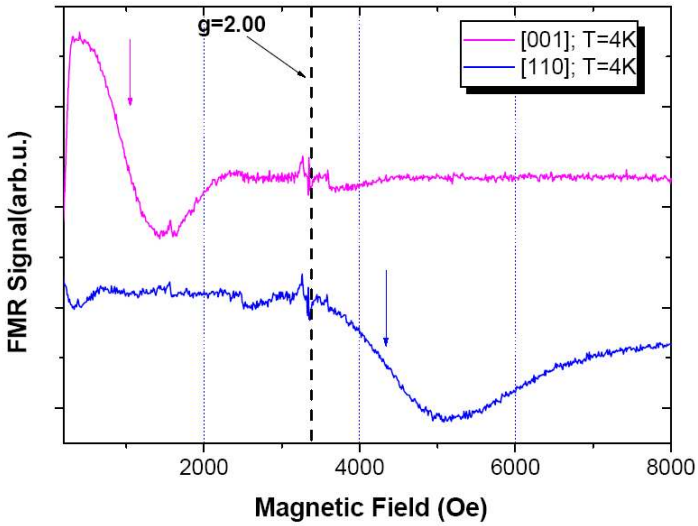


**Figure 4.22:** FMR spectra of sample B at T=4K for magnetic field orientations H‖[100] and H‖[001]; the easy axis of magnetization has switched to out-of plane; i.e. ‖[001].

that the easy axis of the sample has changed from in-plane [100] to the out-of-plane axis [001]. Such a change of the preferential magnetic axes with the hole concentration has been predicted by Dietl et al. [5] within the mean field theory. As the temperature is increased to T=10K ($0.23T_C$) the easy axis switches back to the in-plane [100] direction but the hard axis remains in the in-plane [110] direction. The linewidth decreases with increasing temperature and at T=23K it is reduced to ≈1000 Oe. Increasing the temperature to T=30K ($0.7T_C$) the out-of-plane [001] axis becomes the hard axis once again. As the hole concentration of this sample is low with in particular a thermally activated impurity conduction regime the magnetic coupling between the holes and the magnetic manganese ions is changed from that in the metallic regime. At these low hole concentrations a polaron model might a priori be considered to better describe the ferromagnetic state. The polaron model has been discussed by Kaminski et al [37]. They expected this regime to be of importance for hole concentrations of $10^{19}cm^{-3}$. According to these authors a characteristic feature of the polaron model is a particular shape of the magnetization curve M(T), which should present a concave curvature. However, this is not observed in our case (see sec. 4.7).

#### *4.9.0.6 Fully passivated sample and spin state*

The fully passivated sample still presents a low intensity electron paramagnetic resonance spectrum (fig. 4.23); its low intensity, resonance fields at g=2.00 and its temperature dependence confirm that this sample is paramagnetic. The resonance

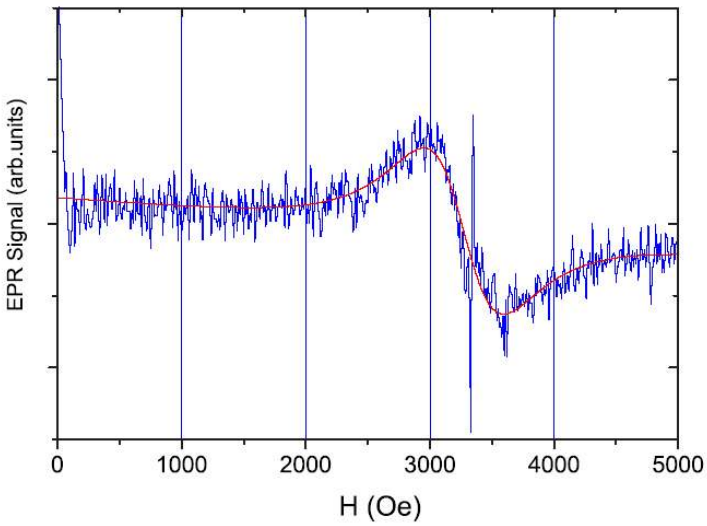


**Figure 4.23:** FMR spectra of the fully passivated sample at T=4K for magnetic field orientation H‖[001]. The red/dark line is a fit to the measurement corresponding to the first derivative of the Lorentzian absorption function.

field of 3300Oe corresponds to a g-factor of g=2.00, the signature of an $Mn^{2+}$ configuration for the manganese atoms, this spectrum is a good evidence for our claim that the there is no direct bond between the hydrogen ions and the substitutional Mn ions. The competing interactions of dipolar line broadening and exchange narrowing have transformed the fine structure and hyper-fine split multi-line spectrum of the isolated $Mn^{2+}$ ion in a single, structureless Lorentzian line. The paramagnetic spectrum is more difficult to observe due to the much lower sensitivity of the EPR spectroscopy. Fig.4.24 Nevertheless we were able to detect in addition to the $Mn^{2+}$ spectrum an additional spectrum composed of four separated lines of equal intensity. This spectrum corresponds to the well known spectrum of the arsenic antisite in its positive charge state. It is characterized by an electron spin of S=1/2 and a central hyperfine interaction with a 100% abundant I=3/2 nucleus (As). This observation allows us also to directly situate the Fermi level in this sample which is pinned by the $E_c$-0.75 and $E_v$+0.5eV levels of this defect.

The spectra were measured as a function temperature up to room temperature (fig.4.25). The EPR spectrum intensity decreases as expected with increasing temperature following a Curie or Curie-Weiss behavior. Note that even at room temperature the signal/noise ratio is still sufficient to quantitatively analyze the $Mn^{2+}$ EPR spectrum.

The spectra can be well fitted with a first derivative Lorentzian lineshape function as shown in fig.4.26 and 4.27. Note that the EPR resonance fields decrease slightly as a function of temperature; this temperature dependent shift is due to the

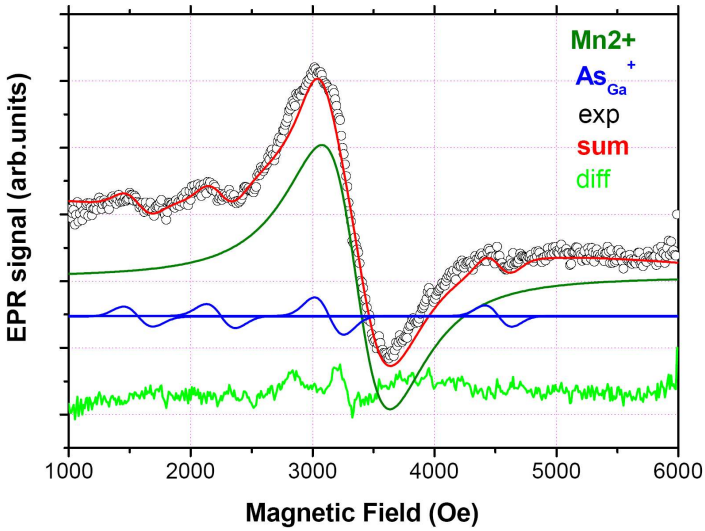


**Figure 4.24:** EPR spectra of the fully passivated sample at T=10K. The open circles present the measured spectrum which is decomposed in two spectra corresponding to $Mn^{2+}$ and $As^{+}_{Ga}$ centers.

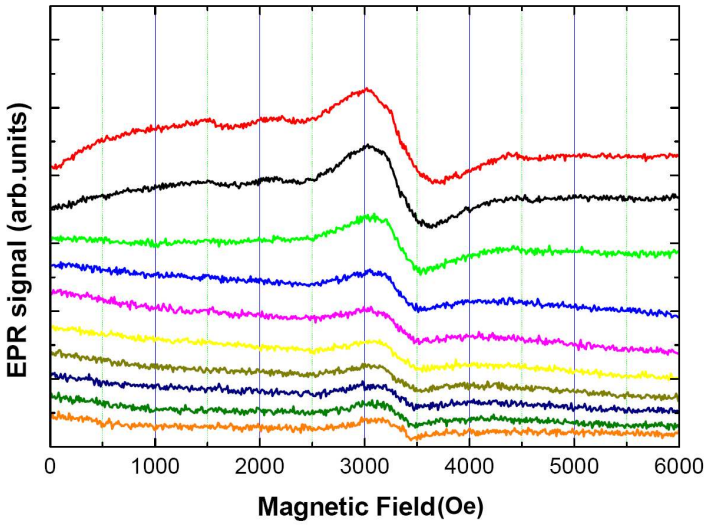


**Figure 4.25:** EPR spectra of the fully passivated sample measured as a function of temperature

contribution of the demagnetization field for H‖[001].

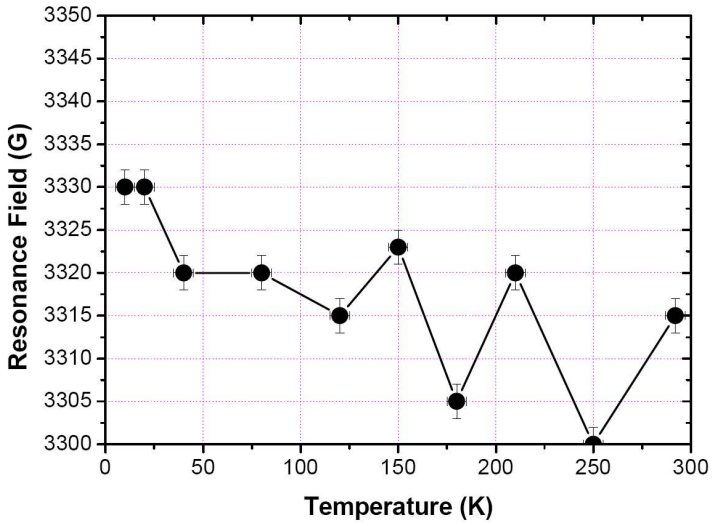


**Figure 4.26:** EPR resonance field of the $Mn^{2+}$ spectrum in the fully passivated sample as a function of temperature; H‖[001]

From a double integration of the simulated EPR spectra we have determined the spin density which will be used to determine the Curie-Weiss temperature of this defect. In fig.4.28 we plotted in the usual way $1/intensity$ as a function of temperature. While the low temperature the data can be well fitted by a line passing trough zero, the linear extrapolation of the high temperature gives a negative Curie-Weiss temperature of ($\approx -25K$).

This standard approach to determine the Curie-Weiss temperature of the sample demonstrates an anti-ferromagnetic coupling between the nearest neighbour Mn ions. Using the following epression:

$$\frac{J}{K_B} = -\frac{3}{2}\frac{\theta_0}{S(S+1)z} \tag{4.1}$$

the effective exchange integral can be derived from the Curie Weiss temperature; Its value is $J = 0.4meV$. In order to understand the origin of this interaction, remember that in section 1.4.6 it was discussed that the coupling between the substitutional Mn ion magnetic moments is the result of the competitions between different interactions. It is clear that, while for high charge carrier densities, the Zener kinetic exchange interactions leads to a ferromagnetic order, for very low hole densities the antiferromagnetic superexchange interaction between the first Mn neighbors will become dominant at low temperatures.

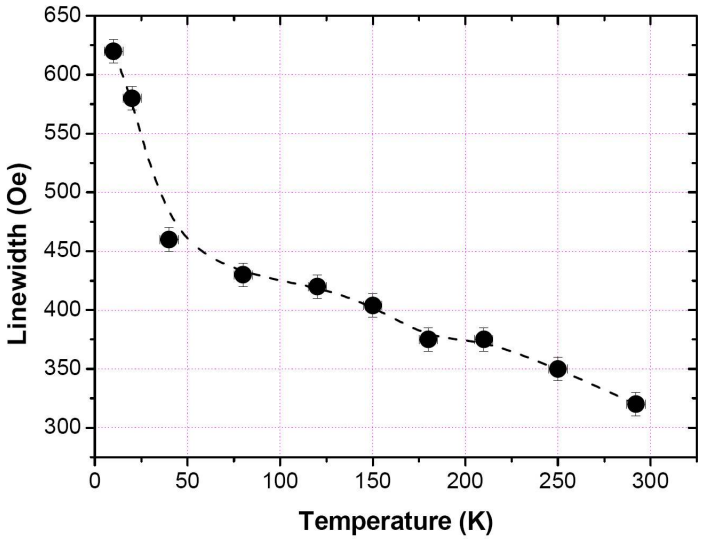


**Figure 4.27:** EPR linewidth of the $Mn^{2+}$ spectrum in the fully passivated sample as a function of temperature

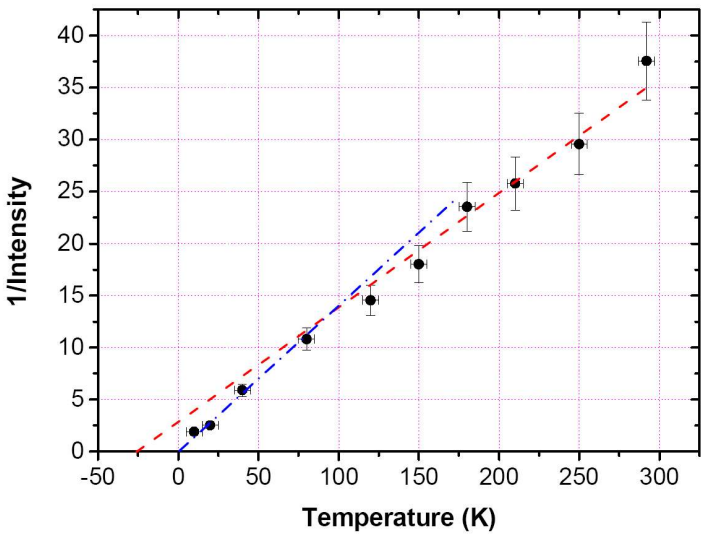


**Figure 4.28:** Curie-Weiss plot: Inverse of the $Mn^{2+}$ EPR spectra intensity of the fully passivated plotted as a function of temperature

### 4.9.1 easy axis reorientation

| Sample \ Axis | 001 | 100 | 110 | 1-10 |
|---|---|---|---|---|
| **Reference** 4K | 4 | 1 | 3 | 2 |
| 20K | 4 | 1 | 3 | 2 |
| 80K | 4 | 1 | 3 | 2 |
| 110K | 4 | 2 | 1 | 3 |
| **sample E** 4K | 4 | 1 | 3 | 2 |
| 20K | 4 | 1 | 3 | 2 |
| 80K | 4 | 1 | 3,2 | 3,2 |
| 110K | 4 | 2 | 1 | 3 |
| **sample D** 4K | 4 | 1 | 3 | 2 |
| 20K | 4 | 1 | 3 | 2 |
| 70K | 4 | 2 | 3 | 1 |
| **sample C** 4K | 4 | 1 | 3 | 2 |
| 20K | 4 | 1 | 3 | 2 |
| 40K | 4 | 1 | 3 | 2 |
| 60K | 4 | 2 | 3 | 1 |
| **sample B** 4K | 1 | 2 | 3 | 4 |
| 10K | 2 | 1 | 4 | 3 |
| 20K | 2 | 1 | 4 | 3 |

**Table 4.3:** Easy and hard axes for the magnetization at different temperatures between T=4K and $T_C$; 1 is the easiest axis and 4 the hardest axis respectively.

In table 4.3 and fig. 4.29 we summarize the four easy and hard axes of magnetization for all samples. We observe that for all hole concentrations three nonequivalent in-plane axes exist. The in-plane anisotropy increases with decreasing hole concentration. We will show below that this is mainly due to the increase of the cubic in-plane anisotropy constants. The angular dependence of the FMR spectra in this series of samples with decreasing hole concentrations show a change of the hard axis (easy axis) resonance position to the lower(higher) fields with decreasing hole concentration.

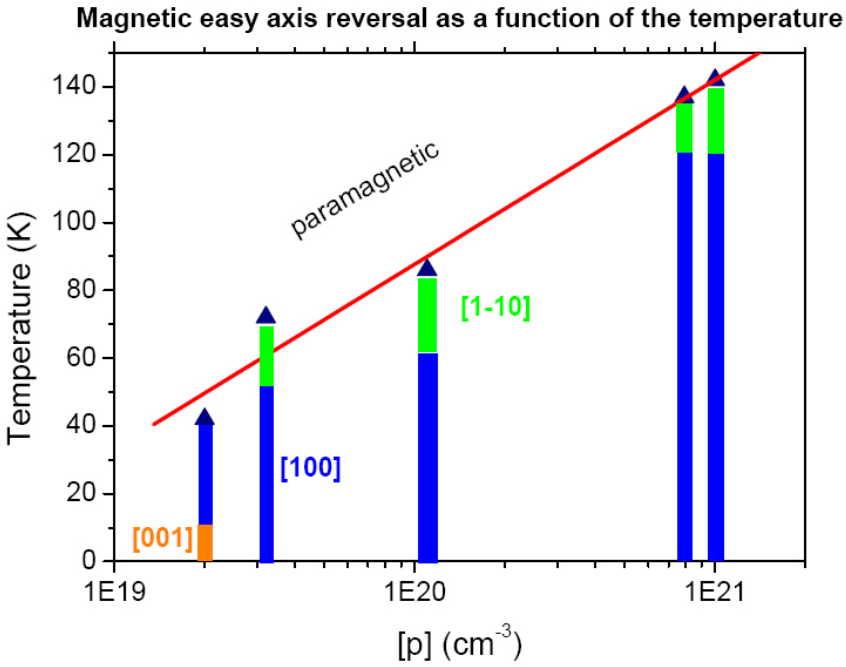


**Figure 4.29:** Easy axis orientations, as a function of the hole concentration and the temperature, for samples B, C, D, E and reference. The triangles indicate the Curie temperature of each sample. The red line presents the approximated frontier between paramagnetic and ferromagnetic behavior. For all samples a change of the easy axis is observed close to $T_C$

### 4.9.2 FMR intensity

The saturation magnetization of the samples, which has been deduced from the SQUID measurements, has been observed to vary with the hydrogen content (table4.1). To verify the intrinsic character of this change, we have determined it independently from the intensity of the FMR spectra. It is of interest to use the FMR spectra for the measurement of the magnetization as due to the resonance character of the FMR technique such measurements will not be perturbed by contributions from the substrate or any secondary phases in the FM layer. The FMR measurements allow measuring the magnetization quantitatively but only in arbitrary units; to obtain absolute values the comparison with a standard sample is required. In fig.4.30 we show the normalized FMR intensity, obtained from a double integration of the FMR spectra and compare them with the normalized magnetization determined from static SQUID measurements. We observe a linear correlation between the two results which shows that the decrease of the magnetization is an intrinsic property of the GaMnAs layer. The good correlation between the two techniques demonstrates the usefulness of FMR measurement to determine the magnetization in particular in the case of ultrathin ($<$20nm) GaMnAs layers which for sensitivity reasons are hardly accessible with SQUID measurements. The Curie temperature of the samples are deduced from the extrapolation of the FMR intensities to zero (which have not been corrected for the 3000Oe applied fields pushing the $T_C$ to higher values than the zero field values). The FMR values shows a fairly good agreement with the ones measured by SQUID. Concerning the FMR parameters we see that decreasing hole concentrations lead to a monotonous shift of the critical temperatures (fig 4.31)in agreement with the $p^{1/3}$ mean field prediction (cf. sec. 1.6), a reduction of the FMR resonance positions, an increase of the linewidths and lead finally to a paramagnetic transition.

### 4.9.3 FMR linewidth

We have observed in this series of samples widely different FMR linewidths which vary monotonously with the hole concentration and depend also on the orientation of the applied magnetic field and the temperature. The linewidth of the uniform mode FMR spectra is related to various parameters such as relaxation processes and the damping and reflects also sample inhomogeneities in the bulk and at the surface of the films. It is generally decomposed in a frequency independent inhomogeneously broadened part and an intrinsic damping related second component (see sec. 6.3).

In the past it has been generally assumed that the inhomogeneous linewidth is negligibly small in annealed samples [42] but our preliminary results have shown this not to be the case. Even in annealed samples the inhomogeneous line width is still comparable or even superior to the frequency dependent homogeneous one.

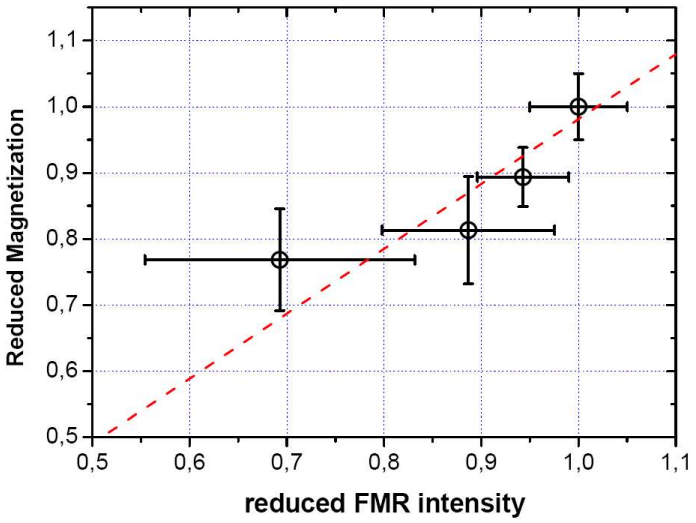


**Figure 4.30:** Normalized magnetization $M/M_{sampleE}$ measured at H=1kOe and T=4K by SQUID versus the normalized intensity $I/I_{sampleE}$ of the FMR spectrum obtained by a double integration. The figure shows the results for the four samples B to E.

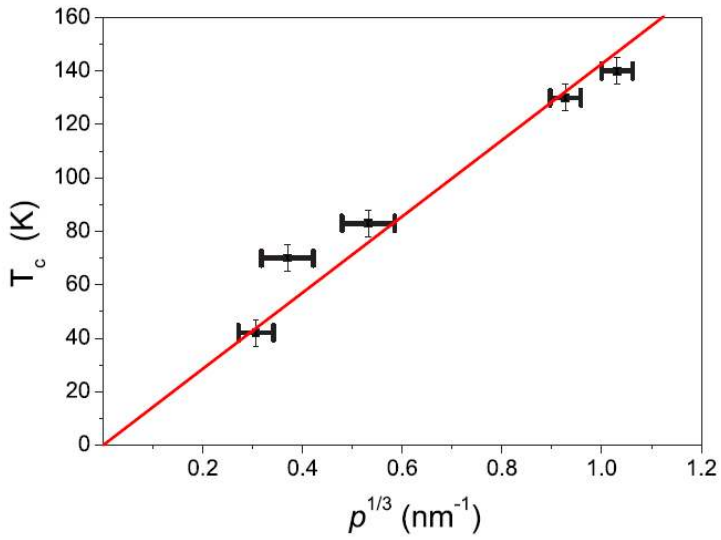


**Figure 4.31:** Curie temperature as a function of $p^{1/3}$,where p is the mean hole density between n=1 and n=2 fit results discussed in section 4.5 p.103. The full line is the fit to the mean-field expression $T_C \propto p^{1/3}$.

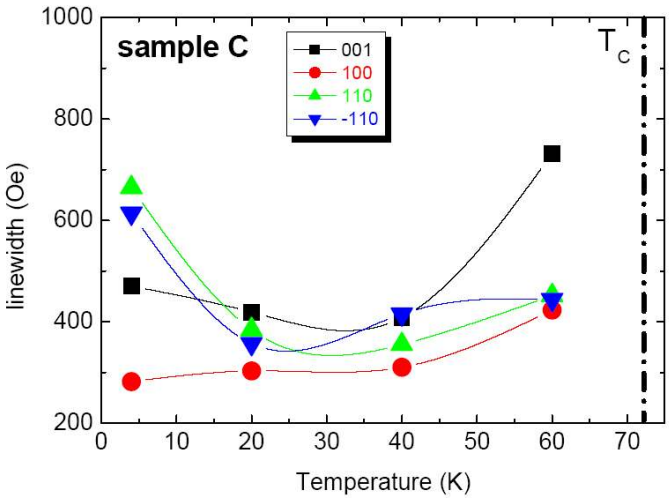


**Figure 4.32:** FMR linewidth (symbols) of sample C as a function of temperature for the four high symmetry orientations of the applied field. The lines are guides for the eyes.

Typical values of $\Delta H_{inh}$ for annealed non hydrogenated films are 100Oe to 200Oe. With a Gilbert parameter of G = $8{\cdot}10^7$ $s^{-1}$ the homogeneous broadening at 9GHz gives an additional linewidth of $\approx$ 60Oe. The actual situation is more complicated due to the additional orientation and temperature dependence of the linewidth. The variation of the parameters $\Delta H_{inh}$ and G with decreasing hole concentrations has not yet been determined. We know however from theory that lower hole concentrations are expected to further decrease the damping factor. In fig.4.32 we show the temperature variation of the linewidth for sample C which is typical for all samples: it is characterized by different behaviors for the orientation of the applied field parallel to the cubic [100], [001] and the [110], [-110] axes. For the field parallel to the cubic axes, the linewidths are approximately constant at low temperature and increase only close to the critical temperature. For H$\|$ [110], [1-10] we observe a different low temperature behavior, the linewidth increases by a factor of two. An orientation dependence of the linewidth can in principle be expected from the variation of the anisotropy fields. However, the observation of the smallest linewidth for the easy axis orientation [100] and highest linewidth for the in-plane hard axis orientation [110] is not in agreement with such a model which relates the linewidth to inhomogeneities of the anisotropy fields.

Our results show that the main change in the linewidth of the FMR spectra for a given temperature and orientation is related to the hole concentration. We observe a monotonous increase of the linewidth with lower hole concentrations (fig. 4.33 ). It would have been interesting to monitor the respective contributions of the two components of the linewidth but these results, which require FMR measurements at different microwave frequencies, are not yet available. Once again we see that

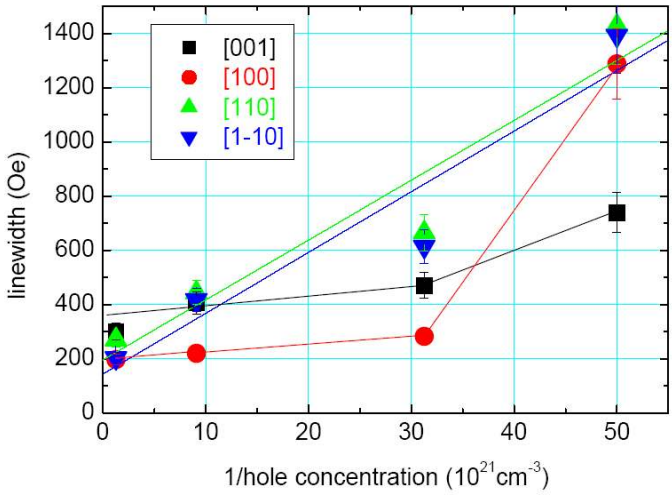


**Figure 4.33:** FMR linewidth (symbols) as a function of the reciprocal hole concentration $[p]^{-1}$ for the four orientations of the applied field. The lines are a guide for the eyes.

the linewidths vary similarly for H||[100], [001] and for H|| [110], [-110]. For H||[100] $\Delta H_{pp}$ increases from 100Oe for the reference sample to1500Oe for sample B. Phenomenologically we find that in the high hole concentration regime the linewidth varies for a given orientation and temperature approximately as the inverse of the hole concentration (eq.4.2)

$$\Delta H_{pp} \propto [p]^{-1} \tag{4.2}$$

The in-plane angular dependence of the linewidth show a simple behavior previously observed for quite different systems such as Fe/Ni bilayers. As shown in fig. 4.34 the in-plane linewidth follows closely the in-plane resonance field indicating that they have a common origin. We see from fig. 4.33 that the angular dependence of the linewidth increases equally with decreasing hole concentrations. These changes should be related to the valence band occupation but no model is available at this time which would allow to relate the linewidth to the hole properties.

## *4.10 g-factor measurement; comparison to mean field calculations*

In addition to the anisotropy constants a further parameter which can be deduced from the angular variation of the FMR spectra is the g-factor. In previous FMR works in GaMnAs the g-factor has generally be assumed to be a constant and equal to that of the ionized $Mn^{2+}$ acceptor in GaAs, i.e. $g_{Mn} = 2.00$ [43]. Liu et al [44] have very recently shown that this assumption is not always valid. The contribution of the free holes which are coupled antiferrmagnetically to the Mn moments to the

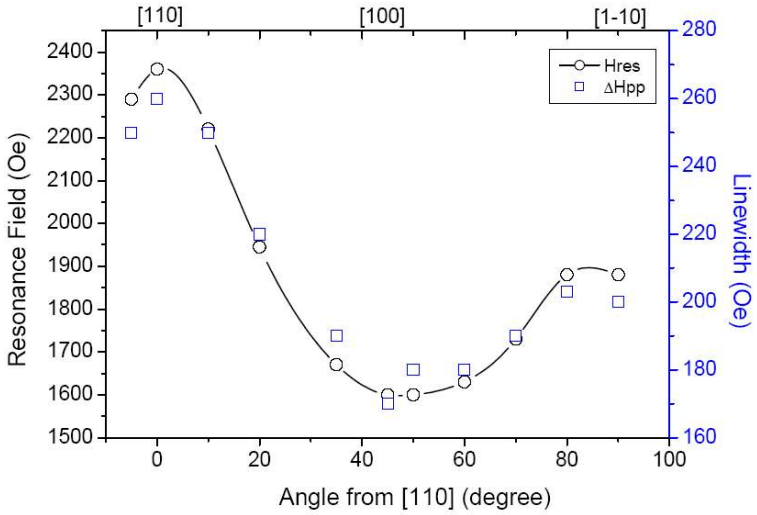


**Figure 4.34:** Angular dependence of the resonance field (left ordinate, black) and the FMR linewidth (right ordinate, blue) of sample E; the rotation plane is (001), T=4K.

total magnetization is negative. This results in a modification to the effective g-factor, which is measured in FMR. The effective g-factor can be smaller than 2.00 and is expected to vary with the hole concentration. The effective g-factors have been calculated for different Mn doping levels and hole concentrations [45].We have taken this fact into account in our parameter determination. The g-factor affects mainly the out-of-plane variation of resonance fields and we have deduced it from its contribution. The numerical values of the anisotropy constants depend on the g-values used in equation 3 and this should be kept in mind when comparing different published values. Based on the experimental results of Liu et al [20, 44] Sliwa et al [45] have proposed to use the following phenomenological relation (eq.4.3) to determine the effective g-factor:

$$\frac{n_{Mn} \cdot S \cdot g_{Mn} + M_c/\mu_B}{g_{eff}} = S \cdot n_{Mn} + s \cdot n_h \cdot P \tag{4.3}$$

where S and s are the Mn and hole spins, $g_{Mn}$ the g-factor of $Mn^{2+}$ and $M_C$ and P the hole magnetization and hole polarization respectively. The hole polarization can be deduced from the hole splitting parameter via eq:

$$P = \frac{2g\mu_B}{\beta p}\frac{\partial F_c(M)}{\partial M} \tag{4.4}$$

where $\beta$ is the exchange integral and $F_c$ is the hole contribution to the free energy. As Dietl et al. have well remarked in their article (cf. [5] ) one important question is: "what is the degree of hole polarization $P$ as function of [$p$] and splitting

parameter $B_G$ ?" This polarization parameter not only determines the magnitude of the anomalous Hall effect, as they mentioned, but it has also a direct effect on the relaxation (damping) in the layer by modifying the coupling between the holes and the Mn moments. Therefore it is crucial to be able to measure it for a specific system. Fig. 4.35 shows the relation between the splitting parameter and hole polarization

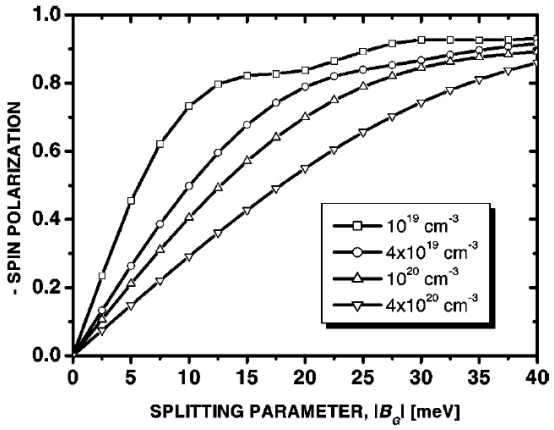


**Figure 4.35:** Calculated degree of the hole spin polarization as a function of the spin-splitting parameter for various hole concentrations in GaMnAs ($B_G$=-30 meV corresponds to the saturation value of Mn spin magnetization for x=0.05). [5]

for different hole concentrations [5]. One should note that although at first sight there is a decrease of the spin polarization with increasing the hole concentration one should notice that the splitting parameter changes also with the sample properties. In order to calculate the real polarization of the sample one needs to determine first this splitting parameter. The spin polarization is one of the most important aspects of the application of semiconductors in spintronics devices. As the metallic materials do not provide a 100% polarisation of the charge carriers, ferromagnetic semiconductors are expected to be superior in this aspect. Considering the direct relation between the effective g-factor and the hole polarisation in DMS samples, one can use this relation to determine this parameter.

In fig.4.36 we show the experimental angular variation of the resonance fields and the simulated one's calculated from the four anisotropy constants, the magnetization M and the effective g-factor g. We obtain a good agreement between the simulated resonance fields and the measured one's only for $g < 2.00$. The g-factor varies from 2.00 for sample B to g=1.90 for the reference sample with the highest hole concentration. The values of the g factors obtained from the fitting procedure are given in fig.4.37 as a function of the hole concentration at T=4K.

The sample related parameters used to deduce the effective g-factor were calculated by Sliwa and Dietl for the samples in the series (private communication). The

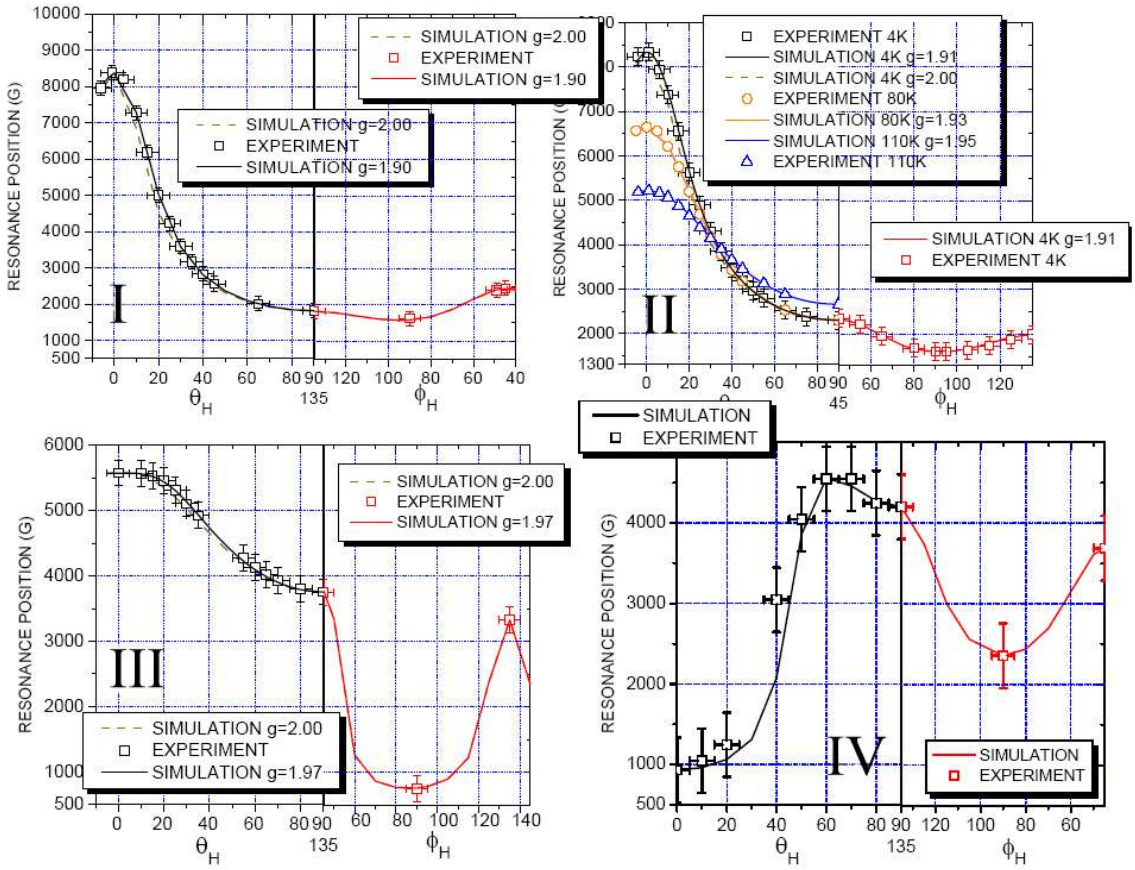


**Figure 4.36:** Angular dependence of the FMR resonance fields at 4K (squares) and the simulated (eq.2.10) angular variations (lines) for two different values of the g-factor: g=2.00 (dashed line) and the most appropriate g value obtained by a least square fit (solid line).(I) the reference sample, (II) the fully depassivated sample E, (III) sample C and (IV) sample B. For the fully depassivated sample E the variations are also shown for T=80K and 110K in the out-of-plane configuration.

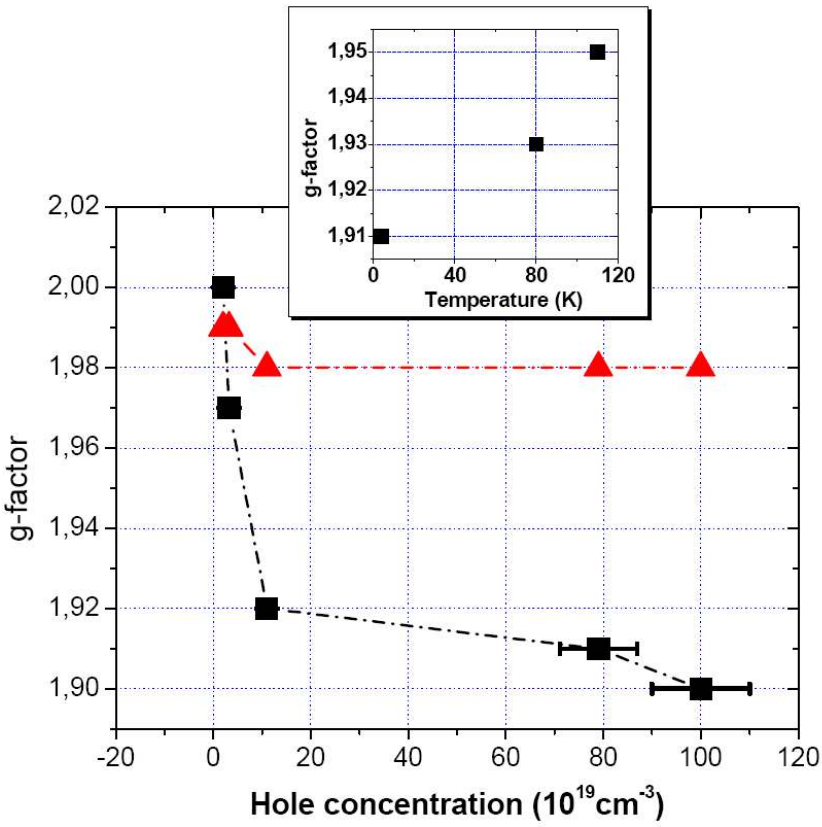


**Figure 4.37:** Experimental (squares) and calculated (triangles) g-factors at T=4K as a function of the hole concentration. The experimental values are obtained from the fitting of the out-of-plane angular variation and the calculated one's from eq.4.3

| SAMPLE | R | E | D | C | B |
|---|---|---|---|---|---|
| $B_G$ (meV) | -25,68 | -23,38 | -20,89 | -19,01 | -17,96 |
| $M_c$ (emu/cm$^3$) | -4,77 | -3,99 | -1,05 | -0,37 | -0,24 |
| $g_{eff}$ | 1,98 | 1,98 | 1,98 | 1,99 | 1,99 |

**Table 4.4:** Spin splitting ($B_G$), Magnetization of the holes ($M_c$) and the effective g-factors ($g_{eff}$) calculated via $k.p$ calculations using mean field approximations for all the samples in the series (private communications with C. Sliwa and T. Dietl)

results are shown in the table 4.4. Using these parameters we obtained the g-factor from the phenomenological equation 4.3. Comparing the experimentally determined g-values with the one's predicted by this equation, two important conclusions can be drawn.

- As the experimental values of the effective g-factor show a variation from 2.00 to 1.90 and tend to saturate for high hole concentrations (sample D,E and reference), the mean field calculation predict a smaller variation from 1.99 to 1.98 only.
- The concept of an effective g-factor has been born from the consideration of the negative contribution of the hole magnetization to the total g-factor. One may consider the reduction of this value directly with the hole concentration, the decrease of the hole polarization. Taking a look at the fig. 4.37, table 4.4 and the hole concentrations reveals that this is not true. While the sample.B has a polarization of ≈80% the parameters due to reference sample attribute a hole polarization of ≈20% or less. As a result the increase of the hole concentration decreases the hole polarisation.

A parabolic single band model can be useful to qualitatively explain these results. While for low hole densities with a Fermi level is close to the top of the VB the splitting of the spin up and spin down states is important with respect to the population in the band, for a highly metallic samples, with a Fermi level deep in the VB, the splitting of the band becomes less important. This tends the effective g-factor to saturate with increasing hole concentrations. One frequent question for these systems is whether the hole-hole or hole-Mn interaction breaks first when the temperature is increased close to the Curie temperature. Referring to the results in this section one may be able to answer this question. For samples with low hole concentration the polarization of the charge carrier is important but since the hole density is low the exchange integral between the magnetic moments and the holes is weak and Mn-h coupling will fade out first. For high hole concentrations, the hole polarization is weak and loose its coherence first when approaching $T=T_C$.

The insert in fig. 4.37 shows the temperature dependence of the g-factor of the fully depassivated sample E. In the metallic conductivity regime the temperature variation between 4K and 130K is not expected to change the hole concentration so that the change in the g-factor must be attributed to the strong variation of the polarizations and spin-splitting of the valence band [45].

### *4.11 Magneto-crystalline anisotropy constants*

In fig.4.38 we show the magnetic anisotropy constants obtained from eq.2.10 for the different samples as a function of temperature. From them the associated

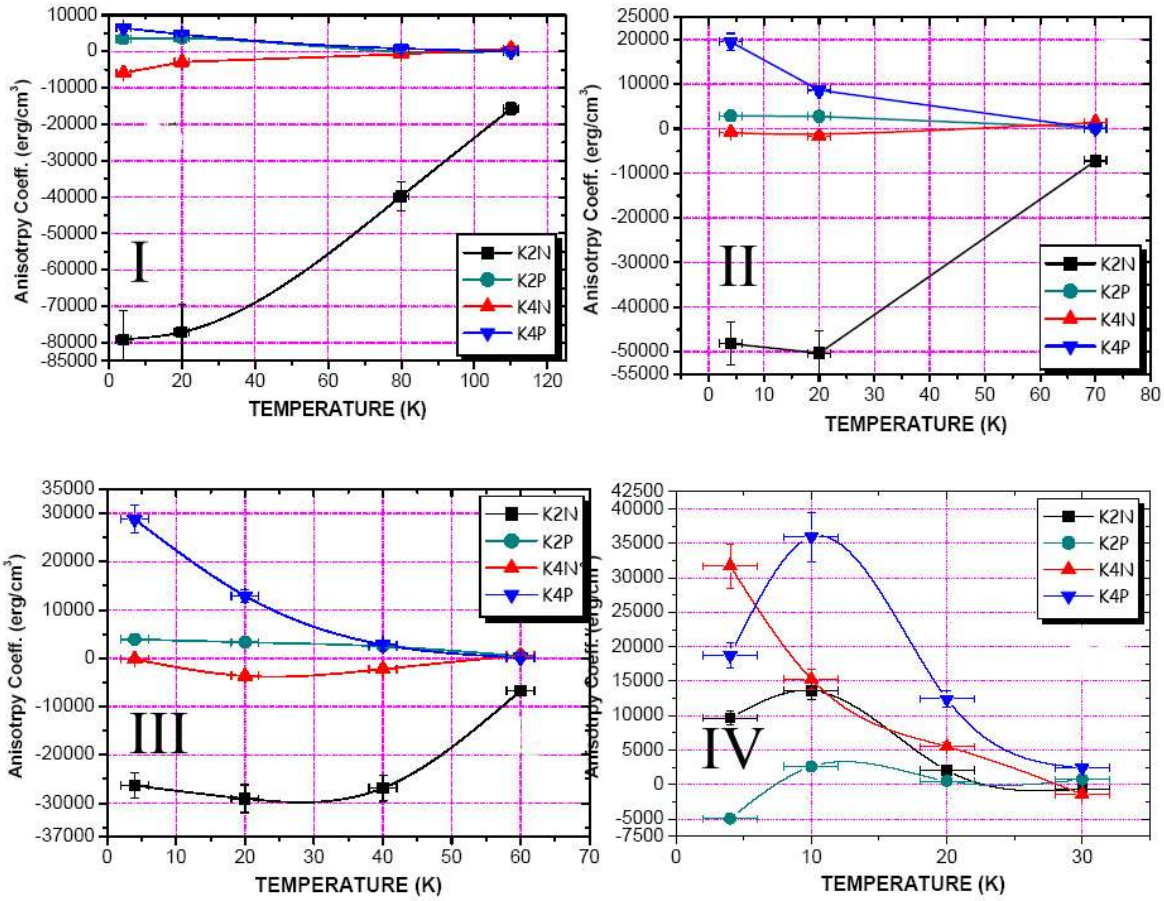


**Figure 4.38:** Variation of the four magnetocrystalline anisotropy constants $K_{2\perp}$ (squares),$K_{2\parallel}$ (circles),$K_{4\perp}$ (upward triangles),$K_{4\parallel}$ (downward triangles) as a function of temperature for the sample E (I), sample D (II), sample C (III) and sample B (IV). Symbols: experimental results, lines are guide for the eyes.

anisotropy fields, defined as $2K_i/M$, can be easily obtained (fig.4.38). As expected, the second order uniaxial contribution is predominant at low temperatures in the reference sample, the fully depassivated sample E and sample D with an associated anisotropy field of $2K_{2\perp}$ /M≈-4kOe. This value is comparable to the Zeeman field of 3.3kOe and much higher than the demagnetization field of ≈ -300 Oe. In sample C the uniaxial and cubic anisotropy constants have comparable numerical values but are of opposite signs. At T=4K the anisotropy constant $K_{2\perp}$ is in the -8·$10^4$erg/$cm^3$ range and decreases monotonously with the hole concentration in spite of an increasing strain (table 4.1 ). Its value is directly related to the strain i.e. the choice of the substrate and the doping level in the GaMnAs layer. But the lattice constants of the strained GaMnAs layer depend also on the substitutional and interstitial Mn ion concentrations and the hydrogen content. In our particular case of a same substrate and a constant Mn distribution in the layer we can analyze its variation with the hole concentration. The other significant point is that in samples with lower hole concentration the $K_{2\perp}$ constant has an extremum after 4K whereas in sample.E and the reference sample its value decreases progressively.

### 4.11.1 Comparison to mean field predictions

According to the mean field theory, the value of the constant $K_{2\perp}$ normalized to a constant strain is expected to vary linearly with the hole concentration. The dependence has been predicted by Abolfath et al. [46] in the low hole concentration [p]=0.01$nm^{-3}$ limit where only one hole subband is populated:

$$\frac{K_{2\perp}}{\epsilon_{xx}} = E \cdot [p] \tag{4.5}$$

Here $\epsilon_{xx}$ presents the biaxial strain and the coefficient E has a value of E=0.36 Ry. As shown in fig.4.39, such a linear behavior is experimentally observed even in the high hole concentration range $0.02nm^3$<[p]<$1nm^{-3}$. Nevertheless, the value of the proportionality coefficient E differs substantially from the value of 0.36 Ry by a factor of 200. The experimentally determined value for E approaches the predicted value in the lowest concentration range (sample B and C). Due to the absence of sufficient experimental values in this range we consider the agreement with the predictions as satisfactory. In sample B due to the change of sign of the constant $K_{2\perp}$ at T=4K, the easy axis in this sample is now perpendicular to the film plane. This configuration is normally observed in GaMnAs films grown on GaInAs substrates which are under tensile strain [6]; but sample B is still under high compressive strain; it is the low hole concentration which is responsible for the easy axis rotation. As shown in table 4.3, the easy axis of magnetization rotates back to the in plane [100] direction at T>10K.

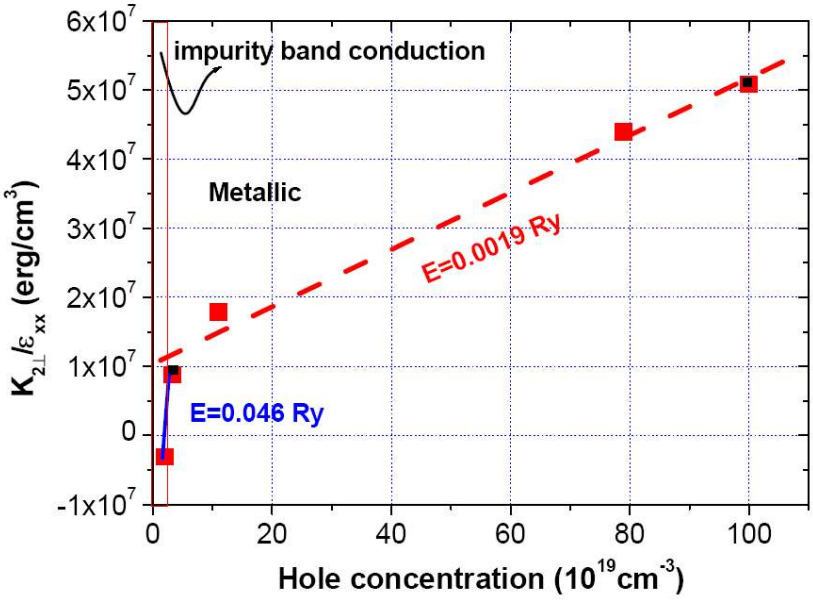


**Figure 4.39:** The uniaxial anisotropy constant $K_{2\perp}$ divided by $\epsilon_{xx}=\Delta a/a$, the bulk lattice mismatch, as a function of the hole concentration; T=4K. The two different regions with respect to the hole concentration (metallic/impurity band conduction) are indicated. A linear fit by eq. 4.5 in the two regimes gives a coefficient E of 0.046 Ry (impurity band) and 0.0019 Ry (metallic) regime.

With decreasing hole concentrations (fig. 4.39) one of the two cubic anisotropy constants, $K_{4\parallel}$, increases monotonously and becomes comparable to the value of $K_{2\perp}$ in sample B. The competition between these two constants causes the hard axis of magnetization to be no longer aligned along the [001] direction but at about 20° from the film normal. This type of competition occurs usually for intermediate Mn doping levels and results in the deviations of the equilibrium positions from the high symmetry orientations. This point is important for the equilibrium orientations of the magnetization. For all samples the value of $K_{2\parallel}$ is small compared to the other anisotropy constants.

### 4.11.2 temperature dependence

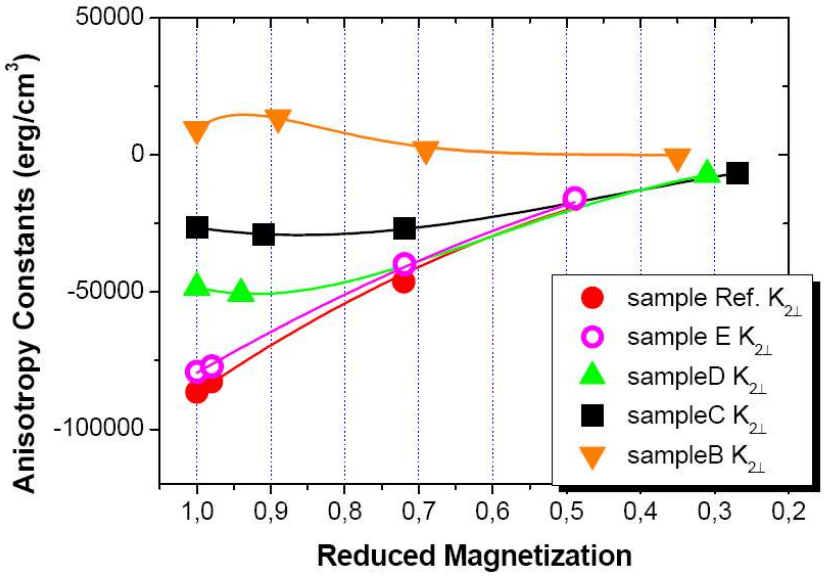


**Figure 4.40:** Experimentally determined second order uniaxial anisotropy constants $K_{2\perp}$ (symbols) as a function of the reduced magnetization and their fit (lines) by a polynomial development $P(\kappa_j^i)$ of the anisotropy coefficients $\kappa$ which include the contributions of second and fourth order terms. For the relationship between the parameters K and $\kappa$ see [47]. The power coefficients are given in table 4.5.

We have equally analyzed the temperature dependence of the anisotropy constants K. To do so, we have extracted the anisotropy coefficients $\kappa$ from which the K's can be derived as linear combinations [47]. The coefficients $\kappa_l(T)$ are the anisotropy coefficients of order $l$ at temperature T obtained from the expansion of the anisotropy part of the free energy in spherical harmonics. Callen et al. [48] have shown that the temperature dependence of the anisotropy coefficients $\kappa$ is different

in the low and high temperature regimes (eq. 4.6, 4.7 ):

$$\frac{\kappa_l(T)}{\kappa_l(0)} = m(T)^{l(l+1)/2} \qquad \textit{low temperatures} \tag{4.6}$$

$$\frac{\kappa_l(T)}{\kappa_l(0)} = m(T)^{l} \qquad \textit{high temperatures} \tag{4.7}$$

m(T) is the reduced magnetization. The two cases have been the subject of many experimental and theoretical articles [47–50]. But the lack of a precise model for systems other than a single ion [41], has prevented simple guidelines. Different results have been reported in the literature: Wang et al [50] reported a simple l power law, others have reported results closer to l(l+1)/2 variations [49]. Dziatkowski et al. [47] have investigated this problem for the case of non hydrogenated $(In_{0.53}Ga_{0.47})_{0.87}Mn_{0.13}As$ films of 50nm thickness grown on InP substrates. They found that none of the coefficients followed the power laws predicted by eqs. 4.6 and 4.7 but obtained much smaller values of the exponent of 1 and 2 respectively. They tentatively attributed these deviations to the simultaneous contributions of bulk and surface anisotropies which vary differently with temperature [47]. However, as the angular variation of the FMR spectra can be satisfactorily simulated with a single set of 'bulk' anisotropy constants we think that surface and interface anisotropy effects in 50nm thick layers are negligible. Thus a different process must be responsible for the particular temperature dependence observed in their case.

The magnetocrystalline anisotropy constants $\kappa$ are related to experimental anisotropy constants $K$ via linear equations:

$$K_{2\perp} = 0.94\kappa_2 - 5.31\kappa_{44} + 3.17\kappa_4 \tag{4.8}$$

$$K_{2\parallel} = -1.54\kappa_{22} \tag{4.9}$$

$$K_{4\perp} = -7.4\kappa_4 + 5.31\kappa_{44} \tag{4.10}$$

$$K_{4\parallel} = -7.08\kappa_{44} \tag{4.11}$$

In fig. 4.40 , 4.41 we have plotted the anisotropy constants $K_2$,$K_4$ as a function of the reduced magnetization for the different samples. The variation of the constants with temperature and thus the reduced magnetization does a priori not follow a simple power law as they are linear combinations of the coefficients $\kappa$ of second and fourth order. Nevertheless, the dependence of $K_{2\perp}$ follows a simple power law for the films with high hole concentrations where the coefficient $\kappa_2 >> \kappa_4$,$\kappa_{44}$ is dominant. In this case (table 4.5) $K_2$ follows a quadratic power law as expected from eq. 4.6 for the low temperature case. In the samples with lower hole concentrations (B, C) the increasing influence of the cubic coefficients leads to a different variation due to competing second order and fourth order coefficients. The cubic anisotropy

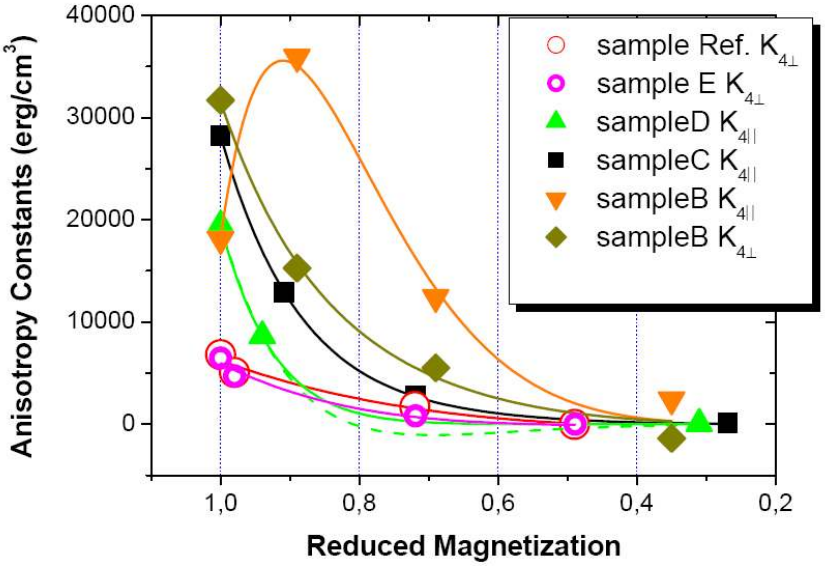


**Figure 4.41:** Experimentally determined second order uniaxial anisotropy constants $K_{4\perp}/K_{4\|}$ (symbols) as a function of the reduced magnetization and their fit (lines) by a polynomial development $\mathrm{P}(\kappa_j^i)$ of the anisotropy coefficients $\kappa$ which include the contributions of second and fourth order terms. For the relationship between the parameters K and $\kappa$ see [47]. The power coefficients are given in table 4.5

constant $K_{4\|}$ shows in the samples with the highest hole concentration a variation of $m^4$ due to the predominance of the coefficient $\kappa_{44}$; but for decreasing hole concentrations the overlap of the high and low temperature regions makes the variation more complicated (rather a combination of both laws as we have deduced by fitting). The lack of sufficient experimental data prevents us to treat this intermediate case in more detail.

| SAMPLE | $K_4$ | $K_2\perp$ |
|---|---|---|
| **B** | $K_{4\|}$: 6,10/ $K_4\perp$:4,10 | 10 |
| **C** | $K_{4\|}$:4,10 | 2,3 |
| **D** | $K_{4\|}$4,10 / 12 | 2.3,5.0 |
| **E** | $K_4\perp$: 3.7 | 1.8 |
| **Reference** | $K_4\perp$: 4.1 | 2.1 |

**Table 4.5:** The power coefficients of the anisotropy coefficients used to obtain the polynomial fitting curves of the variation of the anisotropy constants K with the reduced magnetization (fig.4.40,4.41)

## *4.12 Magnetic free energy surfaces*

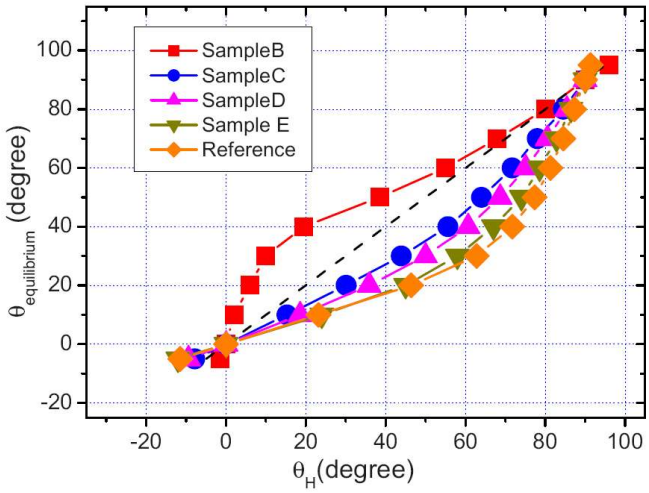


**Figure 4.42:** Equilibrium angle $\theta$ of the magnetization as a function of the angle $\theta_H$ of the applied magnetic field for the out-of-plane configuration; T=4 K. Results are shown for the reference sample and samples E, D, C, and B. The dashed line shows the variation which would be expected if M and H were collinear, which is not the case.

The switching of the magnetization from one orientation to another by a small external magnetic field is strongly influenced by the energy barriers introduced by the internal anisotropy fields. One of the consequences of the strong anisotropy fields in GaMnAs/GaAs is the fact that the magnetization is in general not aligned with the external applied field for small applied fields (fig. 4.42).The knowledge of the anisotropy constants allows us to calculate the free energy density and thus the internal energy barriers for reorientation. Due to the anisotropy of the internal magnetic fields it is not sufficient to consider only the variation of the magnetic free energy F with H for a fixed orientation; to model these barriers one should evaluate the free energy surfaces $F(\phi,\phi_H)_{H_0}$ and $F(\phi,H)_{\phi_{H0}}$. The energy surface depends on 8 parameters: the value of the applied field H, its orientation ($\theta_H$,$\phi_H$), the four anisotropy constants and the magnetization M. Examples of energy surfaces are given in fig. 4.43, 4.44 for the reference sample. We see that high symmetry orientations do not necessarily correspond to a minimum in the free energy and what is more important for switching, at low temperatures the minima are surrounded by anisotropic barriers the height of which depends on the value of the applied magnetic field. To illustrate this we present the in-plane energy surface of the reference sample at T=20K for an applied field H=200Oe as a function of the angles ($\phi$,$\phi_H$). For a very small applied field of H=10Oe it is impossible to switch the magnetization away from $\phi = 0°$ for any orientation of H due to the surrounding energy barriers.

Although, in low orders of applied field one must consider the magnetic domain regime and nucleation of the magnetic domains at fields well below the required fields to flip the entire coupled moments in the film. This is attributed to the presence of regions where the existence of defects or inhomogeneities will enable the magnetization to reorient with lower energy barriers. The domains increase their size via the propagation of the domain walls with lower energies (cf. [32]). On the contrary for a strong applied field of 3000Oe there are no barriers and M is always aligned with the applied field. The interesting case arises for intermediate fields (≈200Oe). Initially the magnetization is oriented at an angle of $-8°$ with respect to the [100] direction in which the magnetic field is applied. Then if we change the orientation of the applied field ($\phi_H$), the equilibrium orientation of the magnetization is given by the minimum energy at the cross section of the energy surface and the line $\phi_H = cte$. Up to about $\phi_H = 60°$ the magnetization is oriented at lower angles than $\phi_H$. For larger angles $\phi_H$, the magnetization switches to higher angles ($\phi > \phi_H$). From the point $\phi_H \approx 90°$ to 170° both magnetization and the applied field move collinearly. Contrary to what has been assumed in [20], the moments do not remain in one orientation until the barrier is overcome by an increased magnetic field. Now

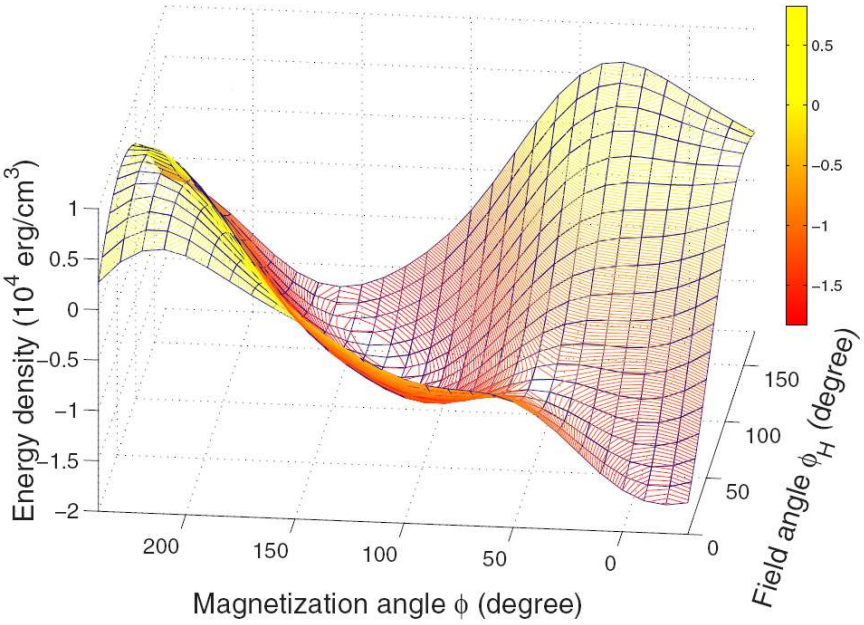


**Figure 4.43:** The energy density surface for the reference sample as a function of the polar angles $\phi_H$,$\phi$ for an applied field of H=200Oe , the configuration is in plane; $\theta = \theta_H = 90°$ and T=20 K.

let us consider the case (fig.4.44) where the orientation of the applied field is directed along the [110] direction ($\phi_H = 45°$) and we increase the applied field from zero. M

is initially oriented in any of the two equivalent directions $\phi = -45°$ and $\phi = 135°$ in the sample. As the field is increased, around 300Oe, the moments in the [-110] direction ($\phi = -45°$) become aligned along the [110] direction. It is not before 300Oe that the moments which were initially oriented in [-110] have fully switched to [110]. Instead, we observe a gradual shift of the magnetization angle; it does not change abruptly from the [-110] to the [110] direction as would have been deduced from a simple one-dimensional representation. These energy surfaces are in addition extremely sensitive to the temperature which introduces a further possibility for magnetization switching combining small applied fields and temperature variations. As a result both the application of a magnetic field along a particular orientation or the variation of its orientation can be used for magnetization switching.

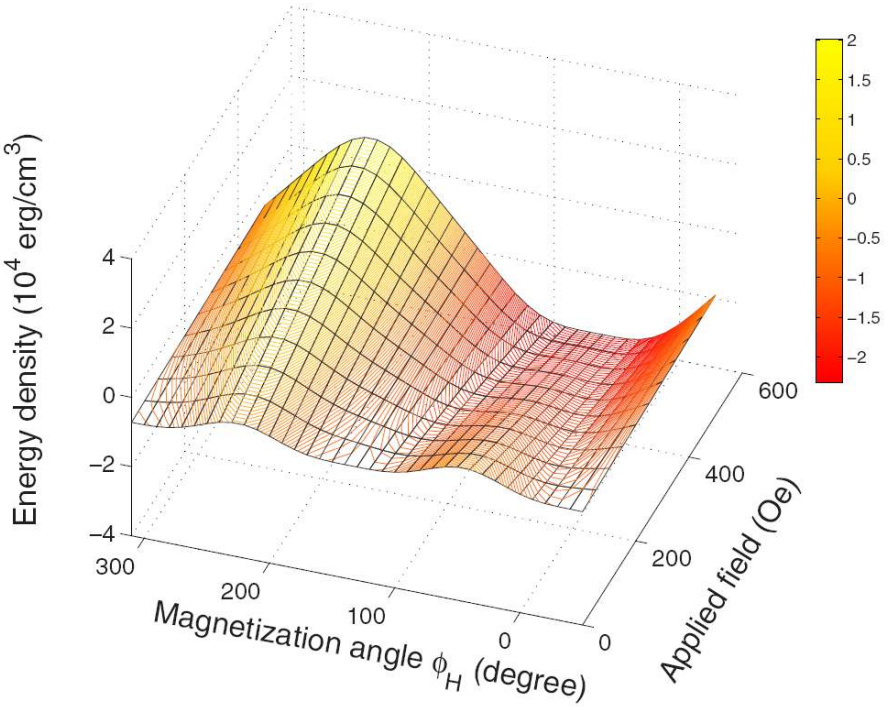


**Figure 4.44:** The energy density surface for the reference sample as a function of the applied field H and the polar angle $\phi$ of the magnetization for a constant value of $\phi_H = 45°$; the configuration is in plane $\theta = \theta_H = 90°$ and T=20 K.

## *4.13 Conclusion*

The micromagnetic parameters of ferromagnetic 50nm thick strained $Ga_{0.93}Mn_{0.07}As$ films have been investigated as a function of the hole concentrations by FMR spectroscopy. The variation of the basic parameters, i.e. the critical temperatures, easy

axes of magnetization and the anisotropy constants have been determined. Their numerical values and their variation with the hole concentration and the temperature are found to be in good agreement with the prediction of the kinetic Zener model for all the samples in the metallic and in the impurity band conduction regime. The uniform mode FMR spectra broaden rapidly with decreasing hole concentrations; their anisotropic linewidth reflect the symmetry of the valence band structure.

The measured g-factor values, interpreted in a phenomenological model based on the Zener kinetic exchange-type model, indicates a gradual decrease in the hole polarization level (for a specific layer) with increasing hole concentration. More direct measurements(via Andreev reflection technique) of the hole polarization of these samples are under way at this moment to further verify this issue. We have deduced from these measurements a lower Mn-Mn exchange integral as predicted previously.

The numerical values of the anisotropy constants and their evolution as a function of temperature were determined. The values obtained were used to test the predictions of the mean-field theory which relates the anisotropy constants to their microscopic origins.

We have shown the possibility to control the magnetic properties of DMS systems via the hole concentration which might itself be modified in space charge regions. Finally, the hydrogen passivation allows in the case of complete passivation a pattering of the films in ferromagnetic and paramagnetic regions which is an interesting alternative to conventional ion beam etching techniques.

# Bibliography


[1] Kh. Khazen, H. J. von Bardeleben, and J. L. Cantin et al., Phys. Rev. B 77, 165204 (2008).

[2] Kh. Khazen, H. J. von Bardeleben, J. L. Cantin, L. Thevenard et al., IEEE. Trans. Mag. 43 (2007).

[3] L. Thevenard, L. Largeau, O. Mauguin, A. LemaÓtre, K. Khazen, and H. J. von Bardeleben, Phys. Rev. B 75, 195218 (2007).

[4] R. C. Myers, B. L. Sheu, A. W. Jackson, A. C. Gossard, P. Schiffer, N. Samarth, and D. D. Awschalom, Phys. Rev. B 74, 155203 (2006).

[5] T. Dietl, H. Ohno, and F. Matsukura, Phys. Rev. B 63, 195205 (2001).

[6] X Liu, Y Sasaki, J.K. Furdyna, Phys. Rev. B 67, 205204 (2003).

[7] B. L. Sheu, R. C. Myers, J. M. Tang, N. Samarth, D. D. Awschalom, P. Schiffer and M. E. FlattÈ Phys. Rev. Lett. 99, 227205 (2007).

[8] H. Ohno, D. Chiba, F. Matsukura, T. Omiya, E. Abe, T. Dietl, Y. Ohno, and K. Ohtani, Nature London 408, 944 (2000).

[9] Y.D. Park, A. T. Hanbicki, S. C. Erwin, C. S. Hellberg, J. M. Sullivan, J. E. Mattson, T. F. Ambrose, A. Wilson, G. Spanos and B. T. Jonker, , Science 295, 651 (2002).

[10] H. Boukari, P. Kossacki1, M. Bertolini, D. Ferrand et al., Phys. Rev. Lett. 88, 207204 (2002).

[11] D. Chiba, M. Yamanouchi, F. Matsukura and H. Ohno, Science 301, 943 (2003).

[12] A. M. Nazmul, S. Kobayashi, S. Sugahara and M. Tanaka Jpn. J. Appl. Phys. 43 pp.L233-L236 (2004).

[13] D Chiba, M Yamanouchi, F Matsukura, H Ohno, J. Phys.: Condensed Matter, (2004).

[14] D. Chiba, F. Matsukura and H. Ohno, Appl. Phys. Lett. 89, 162505 (2006).

[15] F. Yu, C. Gao, S. Y. Jeong, P. B. Parchinskiy, D. Kim, H. Kim, and Y. E. Ihm, J. Magn. Magn. Mater. 304, e155 (2006).

[16] Y. Satoh, D. Okazawa, A. Nagashima, and J. Yoshino, Physica E (Amsterdam) 10, 196 (2001).

[17] S. E. Andresen, B. S. S¯rensen, F. B. Rasmussen et al., J. Appl. Phys. 94, 3990 (2003).

[18] M. A. Scarpulla K. M. Yu W. Walukiewicz and O. D. Dubon, AIP Conf. Proc. June 30, 2005 Volume 772, pp. 1367-1368 (2005).

[19] "Si co-doping of GaMnAs: a solution for removing As antisites", Y. J. Cho, X. Liu, J. K. Furdyna, Abstract Submitted for the MAR08 Meeting of The American Physical Society (2008).

[20] X. Liu, L. Lim, L. V. Titova, M. Dobtowolska, J. K. Furdyna, M. Kutrowski, and T. Wojtowicz, J. Appl. Phys. 98, 063904 (2005).

[21] J. Konig, T. Jungwirth, and A. H. MacDonald, Phys. Rev. B 64, 184423 (2001).

[22] M. S. Brandt, S. T. B. Goennenwein, T. A. Wassner, F. Kohl, A. Lehner, H. Huebl, T. Graf, M. Stutzmann, A. Koeder, W. Schoch, and A. Waag, Appl. Phys. Lett. 84, 2277 (2004).

[23] S. T. B. Goennenwein, T. A. Wassner, H. Huebl, M. S. Brandt, J. B. Philipp, M. Opel, R. Gross, A. Koeder, W. Schoch, and A. Waag, Phys. Rev. Lett. 92, 227202 (2004).

[24] L. Thevenard, L. Largeau, O. Mauguin, A. Lemaitre, and B. Theys, Appl. Phys. Lett. 87, 182506 (2005).

[25] A. Lemaitre, L. Thevenard, M. Viret, L. Largeau, O. Mauguin, B. Theys, F. Bernadot, R. Bouanani-Rahbi, B. Clerjaud, and F. Jomard, Proceedings of the 27th International Conference on the Physics of Semiconductors, edited by J. Menendez and C. G. Van de Walle (AIP, Melville, 2005), p. 363.

[26] R. Bouanani-Rahbia, B. Clerjaud, B. Theys, A. Lemaitre and F. Jomard, Physica B: Condensed Matter 340-342, 284-287 (2003).

[27] J. P. Goss, P. R. Briddon, and M. G. Wardle, Physica B 654, 376-377 (2006).

[28] L. Thevenard, A. Miard, L. Vila, G. Faini, A. LemaÓtre et al., Appl. Phys. Lett. 91, 142511 (2007).

[29] "...tude des propriÈtÈs ferromagnÈtiques de (Ga,Mn)As au moyen de l'hydrogÈnation", Laura Thevenard, Thesis (2006).

[30] K. Olejnik, M.H.S. Owen, V. Novak, J. Masek, A.C. Irvine, J. Wunderlich, T. Jungwirth arXiv:0802.2080v1 (2008).

[31] F. Matsukura, H. Ohno, and T. Dietl. Handbook of Magnetic Materials, vol. 14. Elsevier, Amsterdam (2002).

[32] A. Dourlat, V. Jeudi, C. Gourdon, Kh. Khazen, H.J. von Bardeleben et al., IEEE Trans. Mag. 43 3022 (2007).

[33] A. Pross, S. Bending et al., J. Appl. Phys. 95, 3225 (2004).

[34] A. Mauger, M. Escorne, Phys. Rev. B 35, 1902 (1987).

[35] K. M. Yu, W. Walukiewicz, T. Wojtowicz, W. L. Lim, X. Liu, U. Bindley, M. Dobrowolska, and J. K. Furdyna,Phys. Rev. B 68, 041308 (2003).

[36] T. Jungwirth, J. Sinova, A.H. MacDonald, B.L. Gallagher et al. Phys. Rev. B 76, 125206 (2007).

[37] A. Kaminski and S. Das Sarma Phys. Rev. Lett. 88, 247202 (2002).

[38] M. Sawicki, F. Matsukura, A. Idziaszek, T. Dietl, G. M. Schott, C. Ruester, C. Gould, G. Karczewski, G. Schmidt, and L. W. Molenkamp, Phys. Rev. B 70, 245325 (2004).

[39] C. J. Oates, F. Y. Ogrin et al., J. Appl. Phys. 91 1417 (2002).

[40] V. A. Ivanshin, J. Deisenhofer et al., Phys. Rev. B 61, 6213 (2000).

[41] K. Sugawara, C. Y. Huang, Phys. Rev. B 28, 4955 (1983).

[42] J. Sinova, T. Jungwirth, X. Liu, Y. Sasaki, J. K. Furdyna, W. A. Atkinson, and A. H. MacDonald, Phys. Rev. B 69, 085209 (2004).

[43] J. Schneider, U. Kaufmann, W. Wilkening, M. Baeumler, and F. Kohl, Phys. Rev. Lett. 59, 240 (1987).

[44] X. Liu and J. K. Furdyna, J. Phys.: Condens. Matter 18, R245 (2006).

[45] C. Sliwa and T. Dietl, Phys. Rev. B 74, 245215 (2006).

[46] M. Abolfath, T. Jungwirth, J. Brum, and A. H. MacDonald, Phys. Rev. B 63, 054418 (2001).

[47] K. Dziatkowski, M. Palczewska, T. Slupinski, and A. Twardowski, Phys. Rev. B 70, 115202 (2004).

[48] H. B. Callen and E. Callen, J. Phys. Chem. Solids 27, 1271 (1996).

[49] M. Farle, Rep. Prog. Phys. 61, 755 (1998).

[50] K. Y. Wang, M. Sawicki, K. W. Edmonds, R. P. Campion, S. Maat, C. T. Foxon, B. L. Gallagher, and T. Dietl, Phys. Rev. Lett. 95, 217204 (2005).

# 5

# Investigation of heavily doped GaMnAs layers (x>0.08)

Even though GaMnAs thin layers have been studied for several years now and important progress in the material quality and the critical temperatures have been made the current research encounters the problem that all efforts to increase the Curie temperature above its current record value of 180K have failed. An obvious reason for this limitation is the solubility problem which did not allow the growth of epitaxial layers with more than [Mn]=0.08 even under low temperature MBE conditions. The group of Prof.Tanaka has recently succeeded to overcome this problem and has shown that it is possible by further reducing the growth temperature and limiting the thickness to <2nm to incorporate up to x=0.21 Mn. In this chapter we present a FMR study of his epitaxial layers with x=0.15,0.17 and x=0.21.

The ferromagnetism in GaMnAs diluted magnetic semiconductors (from 2% to ≈5% of Mn doping) is based on the exchange interaction between delocalized carriers (holes) and localized Mn spins. Its properties are in good agreement with the predictions of the kinetic exchange Zener model [1]. As it was mentioned in section 1.6 according to this model the five 3d electrons of substitutional $Mn_{Ga}$ ions create the localized spins with a magnetic moment of $5\mu_B$; they contribute simultaneously to the holes delocalized in an impurity band mixed with the GaAs valence band (for hole concentrations of $10^{19}$ to $10^{21}cm^{-3}$) [2]. According to the Zener kinetic exchange model these moments are below the Curie temperature ($T_C$) coupled ferromagnetically via an antiferromagnetic interaction with the free holes in the impurity/valence band. This model predicts an enhancement of $T_C$ as a function of the magnetically active Mn concentration and the concentration of the charge carriers ($p^{1/3}$) and shows that the temperature of 180K is not a fundamental limit of this system. According to this prediction, it is possible to increase the Curie temperature of GaMnAs up to room temperature by substituting ≈10% of Ga ions with Manganese and keeping the hole concentration at a level of $10^{21}cm^{-3}$ [1] (it is worth noting here that all other theoretical models not based on the mean field

approximation arrived at the same conclusion 1.6).

The relatively low solubility limit of Mn in the GaAs matrix has made the sample growth a material challenge. Some reports have mentioned the formation of secondary phases like MnAs for more highly doped layers both in the as-grown and annealed samples ( for example see [4, 5]) and it was not until recently that the growth of homogeneous GaMnAs thin layers with x>0.1 by molecular beam epitaxy on GaAs substrates at temperatures as low as 169K could be achieved by Ohya et al. [6].

In this chapter these heavily doped samples are studied and their magnetic properties and will be compared to the standard x=7% reference sample. We will investigate further whether the requirements of the Zener model are really fulfilled in these layers.

### *5.1 Techniques to increase the Mn concentration*

In section 1.4.3 the problem of the manganese solubility in the GaAs matrix was explained and it was mentioned that in order to overcome this problem the crystal growers turned to the low temperature MBE technique in which the GaMnAs growth can be performed at a typical temperature of $200 - 250°C$. Since it has been shown that a further decrease of the growth temperature is possible by changing the growth parameters this is a very promising direction for growing higher doped layers [7], Sadowski et al. [9]

The first successful GaMnAs samples with high Mn content were reported in 2001 by Sadowski et al [8]. They found that in order to further decrease of the substrate temperature, without having excess arsenic adsorbed, the arrival rate of As dimers must be controlled precisely and they achieved this by modulating the shutters of the $As_2$, Ga, and Mn sources, and were thus able to decrease the growth temperature down to $150°C$. This special modification of the LTMBE technique was first reported by Horikoshi et al. [10] and is known as migration-enhanced epitaxy (MEE). Applying this technique Sadowski et al. have grown samples with 9 and 10% of manganese. The samples were 300nm thick; but the resistivity measurements showed the samples to be semi-insulating with a resistivity of about 0.1Ωcm. The as-grown samples had the $T_C$s around 75K but no values for the annealed samples were reported. A probable explanation is the formation of MnAs precipitates by the annealing process.

The second report of layers with even higher Mn concentrations was recently published by Ohya et al. from the Tokyo university [6]. They applied the same LT-MBE growth technique and worked at temperatures as low as ≈140K. To avoid the problems encountered by Sadowski et al., Ohya et al. limited the film thickness to values below 20nm. Thus they could overcome the precipitation problem and grew the films with Mn concentrations as high as 21%. The other mentioned problem

was the annealing process which is a standard and necessary technique to improve the films quality via out-diffusion of the interstitial Mn ions. Although for standard (x=0.05) samples, the temperature at which MnAs precipitates form is relatively high $350°C$ [4], at high Mn concentration its value decreases also. In order to prevent the segregation of MnAs clusters, the annealing process was performed at temperatures close to $140 - 160°C$ but for longer duration of 100 hours (compared to the standard annealing of 1 hour at $250°C$). In addition, they used a capping layer in order avoid the segregation of the MnAs particles on the surface during the annealing.

## *5.2 Sample preparation and properties*

We studied three highly doped ultra thin $Ga_{1-x}Mn_xAs$ epilayers with x=0.152, 0.176 and 0.213, (A, B and C respectively) grown via low temperature molecular beam epitaxy (LT-MBE) technique on pure GaAs substrates. A 50nm non doped GaAs buffer layer is grown as the intermediate layer. The properties of the samples are briefly presented in table.5.1.

| Sample | Mn: 15.2% 1.6$\mu_B$ | | Mn: 17% 1.1$\mu_B$ | | Mn: 21% 1.2$\mu_B$ | |
|---|---|---|---|---|---|---|
| GaAs cap. | 1nm | 168°c | 1nm | 159°c | 1nm | 159°c |
| GaMnAs | *10nm* | **168°c** | *20nm* | **159°c** | *10nm* | 152°c |
| Buffer layer | 50nm | 620°c | 50nm | 620°C | 75nm | 620°c |
| Semi insulating GaAs | 625nm | | 625nm | | 625nm | |

**Table 5.1:** Structural configuration and preparation condition of the heavily doped as-grown samples. Note that the magnetization per Mn atom indicated beside each sample belongs to the annealed sample.

The substrate temperature was decreased successively from 168 to $152°C$ for sample A to C during the buffer layer and GaMnAs layer growing process in order to increase the solubility of the Mn ions. The samples A and C are 10nm and sample B is 20nm thick. This feature enables to investigate also the effect of the thickness

on the magnetic properties of these heavily doped samples. all samples possess a capping layer of 1nm GaAs. These layers are predicted to prevent the segregation of the MnAs clusters on the surface after the annealing treatment. For the transport measurements an Indium layer is used to paste the sample on the block. For the FMR measurements of course this layer was removed.

After growing the films, one piece of each sample was annealed under conditions shown in the previous subsection. The temperature and duration of the annealing were optimized via an in-situ control of the electrical resistivity of the films. For annealing temperature of $160°C$ the resistivity decreases at first, indicating the out-diffusion of the interstitial Mn, but it increases while the process is performed longer than a few hours. For temperature as low as $140°C$ the decrease of the resistivity continues and saturates for durations over 90h. For this series of samples, the annealing was performed during 116 hours.

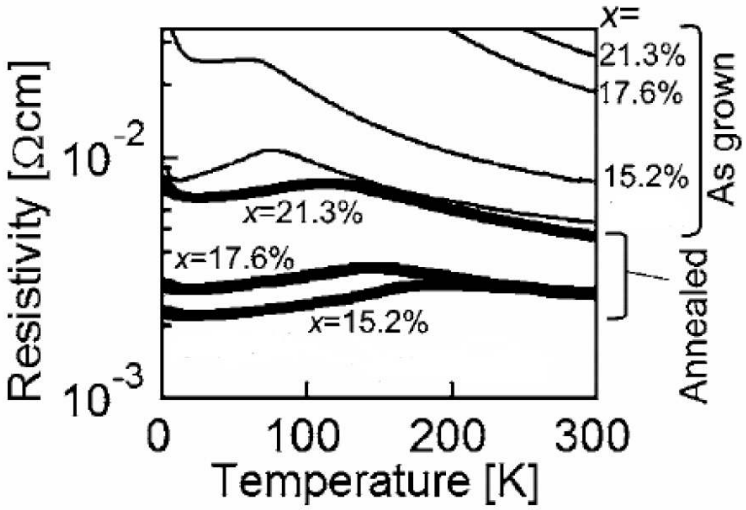


**Figure 5.1:** Resistivity measurements for heavily doped samples (as-grown and annealed) as a function of temperature (from ref. [6])

Fig. 5.1 shows the resistivity curves for different samples of the series. One immediately notes the considerable improvement in the electrical transport quality of the samples after the annealing process. The as-grown samples present such a high resistivity that could not be measured and are out of the graph. Yet it will be shown by FMR that even these samples are ferromagnetic but only at very low temperature. Their behavior is very similar to the hydrogen passivated samples (samples A and B; cf. chapter 4).

On other hand, the annealed samples show a metallic behavior. The sample B shown is not exactly the same sample which was measured by FMR. This sample is 10nm thick whereas the sample in our series was 20nm thick. The resistivity values

for samples A and B are found to be comparable to the one of the reference sample of the hydrogen passivated series.

The magnetic circular dichroism (MCD) measurements performed by these authors showed the absence of any secondary phase. This conclusion can be verified by the FMR measurements. No XRD measurements were obtained for these samples due to their small layer thickness. The SQUID measurements were reported very briefly at T=10K although one should take into account the high contribution of the substrate diamagnetism. Moreover, no SQUID measurement is available for the 20nm sample B.

## *5.3 c-RBS measurements; $Mn_{int}$ profile*

In order to obtain information on a possible Mn concentration gradient in these layers and to measure the relative concentrations of the substitutional and interstitial Mn ions, channeling Rutherford back-scattering (RBS) measurements were performed on one of the samples. We have done previously similar investigations on GaMnAs samples with x=0.07 Mn concentration [11]. Here only the sample B could be measured due to its higher thickness of 20nm.

Figure 5.2 shows random RBS spectra (non channeling orientation) for the (a) as-grown and (b) annealed sample, measured with a $He^+$ beam of energy of 1.6MeV with scattering angle of 165°. The Mn related spectrum is indicated by an arrow.

The total amount of Mn deduced from the peak area is $6.0 \pm 1.0 \times 10^{15}$ and $7.2 \pm 1.0 \times 10^{15} cm^{-2}$, respectively. Assuming the elemental composition of $Ga_{1-x}Mn_xAs$ and the volume density for non-doped GaAs ($4.39 \times 10^{22} atoms/cm^3$), x value is evaluated to be 13.7±2.0 and 16.4±2.0, respectively (consistent with the expected x=0.17). The thickness of the layer of 20nm had been measured in advance by electron microscopy. Considering the experimental errors, the total concentration of Mn before and after annealing has not been changed so much. However, the shape of Mn RBS spectrum for the annealed sample is significantly different from as-grown one. It can be seen in the Fig.5.2(b) that the scattering yield at higher energies, corresponding to the surface region, is increased. It indicates a non uniform Mn distribution after the annealing.

Figure 5.3 shows aligned spectra along (a,c) [001] and (b,d) [110] axis for as-grown and annealed samples, respectively. The backgrounds have been subtracted. A strong peak is clearly observed in both samples for the [110]-aligned spectra. On the other hand, a considerably smaller peak is observed in the [100]-aligned spectra.

We can determine the ratio of substitutional to interstitial Mn by comparing the backscattering yield between random and aligned spectra. We consider the interstitial sites of tetrahedral as well as randomly distributed Mn. If a Mn atom is located at a tetrahedral site, it will be detected for <110> beam alignment but not for the other directions <100> and <111> where this site is shadowed. On the

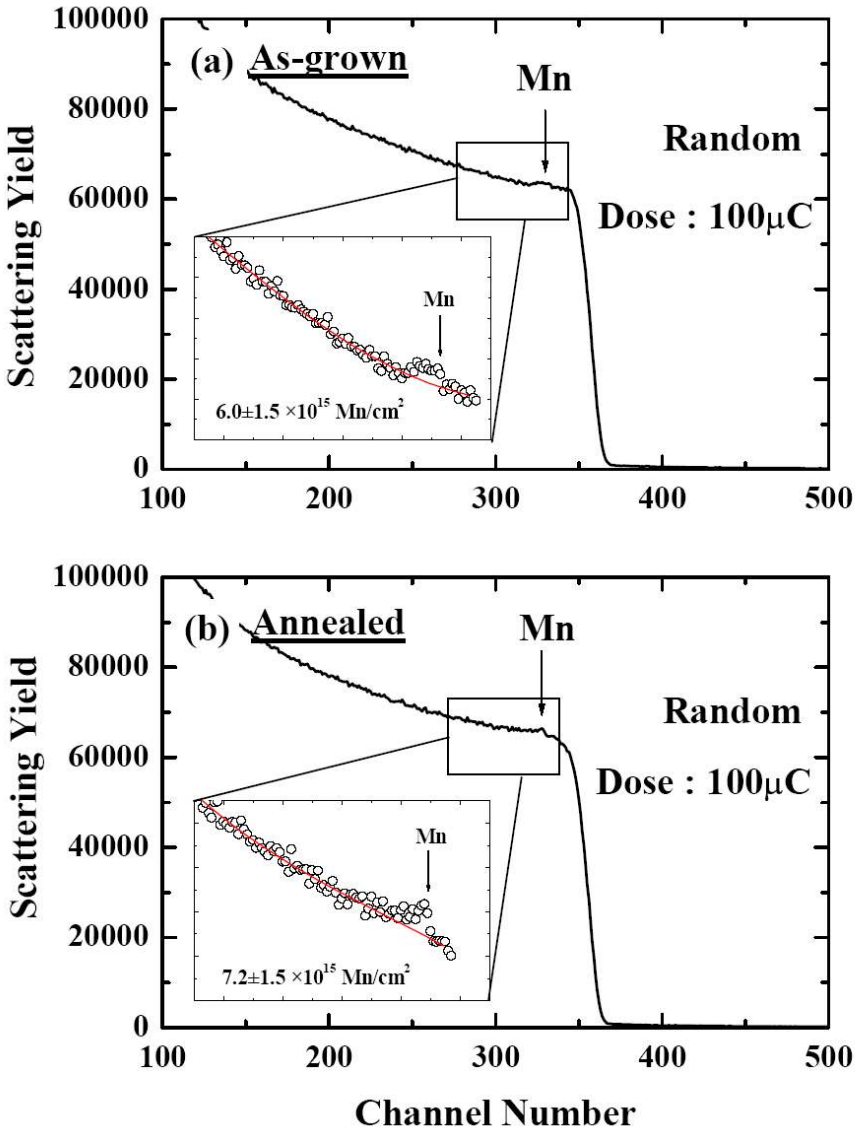


**Figure 5.2:** the RBS measurements of sample.B (a)as-grown and (b)annealed along random crystalline direction

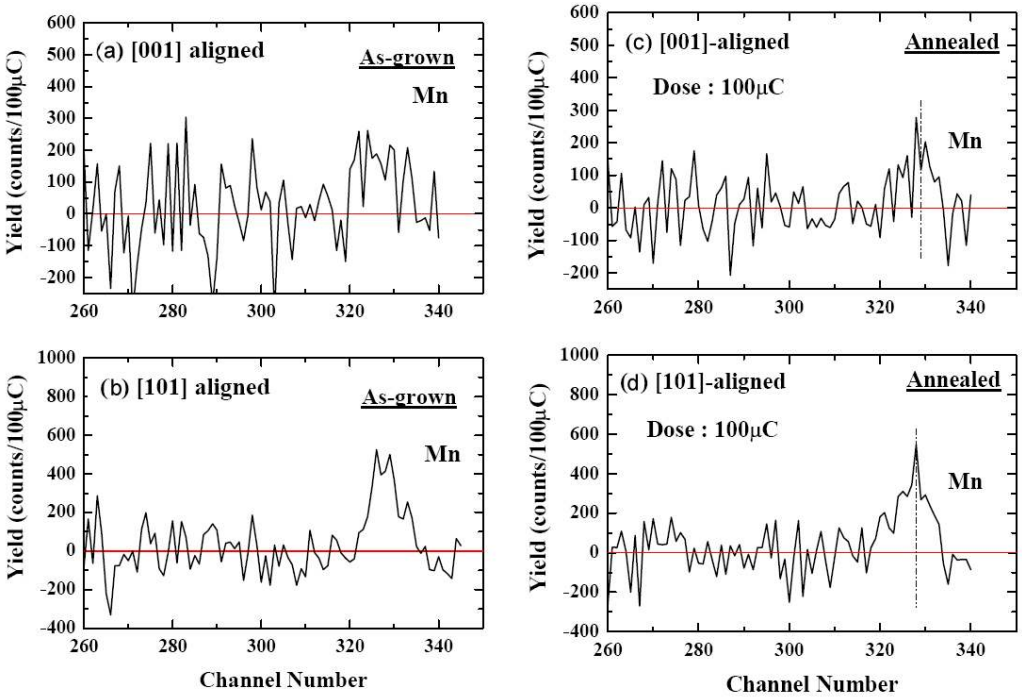


**Figure 5.3:** The RBS spectra of sample.B (a,c)as-grown and (b,d)annealed along (a,c)[001] and (b,c)[110] directions

other hand, randomly located Mn atoms will be seen for any beam orientation. In order to determine the fraction ($p_{[110]}$) of substitutional Mn, we can thus compare the scattering yield of the random spectrum to the <110>-aligned spectrum. It must be noted that the contribution of the surface peak of Mn has to be estimated. Then we performed Monte Carlo simulation of ion trajectories in the GaAs lattice to estimate the shadowing effect. We obtained the value of $3.2 \times 10^{15} Mn/cm^2$. The fraction ($p_{[110]}$) of substitutional Mn is calculated in the first approximation by the following relation.

$$p_{[110]} = \frac{y_{random} - y_{[110]}}{y_{random} - (3.2 \cdot 10^{15}) \cdot x} \tag{5.1}$$

The obtained fractions are shown in table 5.2. The small peak observed in the [100]-aligned spectrum can be explained in terms of the surface peak. The fact indicates that the amount of randomly distributed Mn is negligibly small for these two samples.

| | $p_{[110]}$ (%) |
|---|---|
| **As grown** | 81±5 |
| **annealed** | 85±5 |

**Table 5.2:** The measured fraction of substitutional Mn ions for as-grown and annealed samples

We observed small signals from the [001]-alignment. The fraction ($p_{[001]}$) of Mn aligned along the Ga or As atomic rows is estimated by the relation:

$$p_{[001]} = \frac{y_{random} - y_{[110]}}{y_{random} - (5.35 \cdot 10^{15}) \cdot x} \tag{5.2}$$

The $p_{[001]}$ value does not correspond to the fraction of the substitutional site because Mn atoms in both the tetrahedral and the hexagonal interstitial sites are also aligned in this geometry. Therefore, the $p_{[001]}$ value indicates the total fraction of the substitutional and interstitial Mn. We have determined a concentration of ≈100% for total Mn after and before annealing. This is a direct indication that, despite the assumption usually made in many papers, Mn ions do not get out of the matrix after annealing, but just migrate toward the surface.

In conclusion, we have experimentally observed the migration of the interstitial Mn ions toward the free surface of the sample after annealing process. The rest of the samples is shown to be left unchanged after annealing with ≈60% of magnetically active manganese ions.

## 5.4 FMR measurements

The ferromagnetic resonance (FMR) measurements were performed with both X-band and Q-band standard spectrometers with 100 kHz field modulation and first derivative detection. The angular dependence of the FMR spectra was measured for two rotation planes of the applied static magnetic field: (110) ("out of plane") and (001) ("in-plane"); for more detail see section 2.1.1.

These two set of measurements enable us to determine the resonance positions for the four high symmetry orientations of films: H||[110], [1-10], [001] and [100] from which the four anisotropy constants can be deduced. These axes are distinguished in-situ in growing procedure by in-situ reflection high-energy electron diffraction (RHEED) analysis. The FMR spectra were measured in both configurations as a function of temperature between 4K and their respective Curie temperatures. Both the as-grown and annealed samples were investigated via this technique.

### 5.4.1 Spectra analysis, FMR intensity

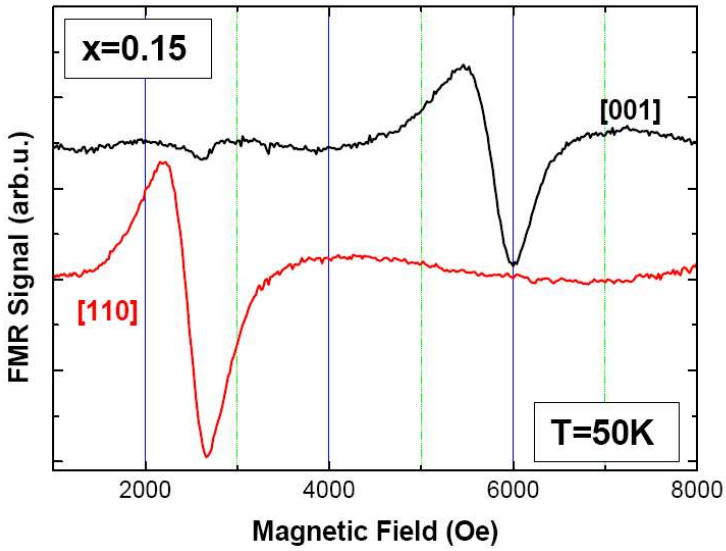


**Figure 5.4:** FMR spectra for as-grown sample with x=0.15 at T=50K for applied H||[001] and [110] directions in out-of-plane configuration.

#### 5.4.1.1 As-grown samples

Fig.5.4 is the FMR spectra measured for the as-grown sample with x=0.15 at T=50K. Along the hard axis [001] the spectrum presents a line-width about 350Oe

and for in-plane direction it rises to 420Oe. Comparing these linewidth to the reference sample and the hydrogen passivated series, one finds them of the same magnitude as in the sample with low hole concentration and high inhomogeneity. This is in agreement with the resistivity measurements. The good signal to noise ratio for this samples shows the power of ferromagnetic resonance spectroscopy for investigating the magnetic properties of ultra-thin layers in this range of thickness, where other conventional techniques such as SQUID and XRD and even resistivity measurements are not capable to provide information. The higher temperature spectra are shown in fig.5.5. From these observations we have estimated the $T_C \approx 70K$.

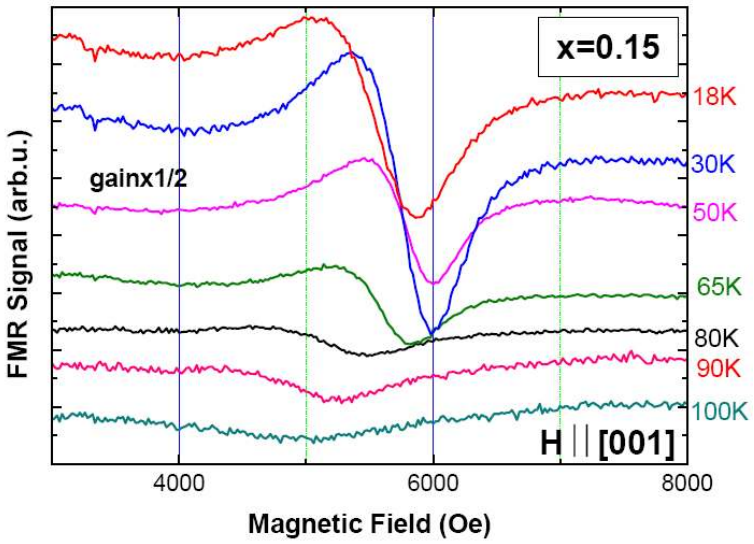


**Figure 5.5:** FMR spectra for applied field along the hard [001] direction in as-grown sample.A for different temperatures.

As the Mn concentration increases, the spectra become larger and the internal field inside the film decreases. This is what we observed in fig.5.6. The spectra are so wide that the resonance field can not be deduced without fitting the spectra. However we were able to determine the transition temperature also for this sample which is ≈65K. This value is about 3 or 4 time higher than what the transport measurements have determined for its 10nm thick counterpart. No FMR spectra were observed concerning the as-grown sample.C. This sample appears to be paramagnetic. However, Ohya et al. had reported this sample to be ferromagnetic for temperature lower than 20K ( [6]). In the following subsection we will discuss the FMR measurements on the annealed samples. We will see how the annealing process has greatly improved such samples.

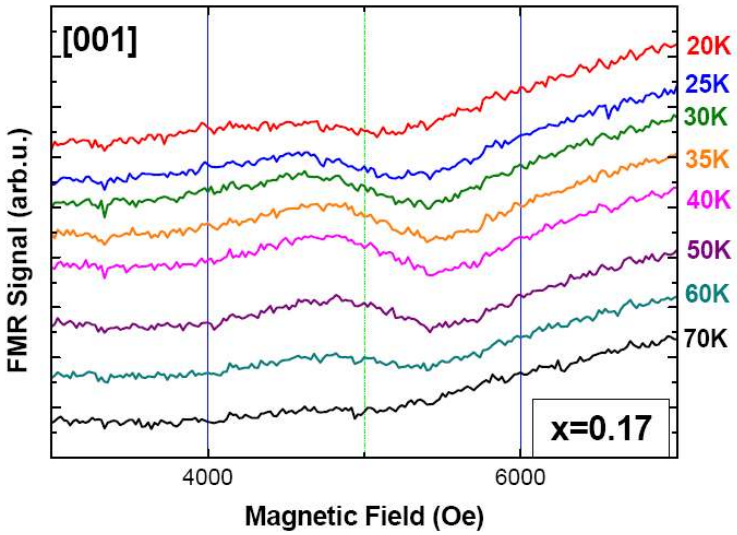


**Figure 5.6:** FMR spectra for applied field along the hard [001] direction of as-grown sample.B for temperatures from 20K to $T_C$

#### 5.4.1.2 Annealed samples

- Sample A (x=0.15)

Fig.5.7 shows the FMR spectra of annealed sample A at T=4K. The resonance field positions indicate the [001] and [1$\bar{1}$0] as the hard and easy axes respectively at this temperature. Note that while this easy axis was reported to be [100] for the reference sample (the standard sample with x=0.07)(cf. [3, 12] and section 4.9), there are some reports which present [1$\bar{1}$0] axis as the easiest one even for lower doping levels [13] (this fact is discussed in the section 3.4.3). This axis remains the easiest axis for all the temperature up to $T_C$. The extension of the resonance field from easy axis to hard axis is the same as the one observed for the standard 7% reference sample.

One should note that the shape of the spectra along [001] axis can be well fitted by the first derivative of two Lorentzian absorption curves (fig.5.7), which enables us to deduce the precise values of the resonance position and estimate the signal intensities. The superposition of more than one spectra is a common fact seen in FMR measurements on DMS structures and as discussed in previous chapters is attributed to the inhomogeneity of the magnetic moment distribution in different regions. Rappoport et al. [14] have attributed this inhomogeneity to the distribution of the hole concentration induced by the inhomogeneous distribution of the $Mn_{int}$ ions. However the metallic character of the samples puts this attribution in question. We can notice that these spectra appear in the order of their respective line-width,

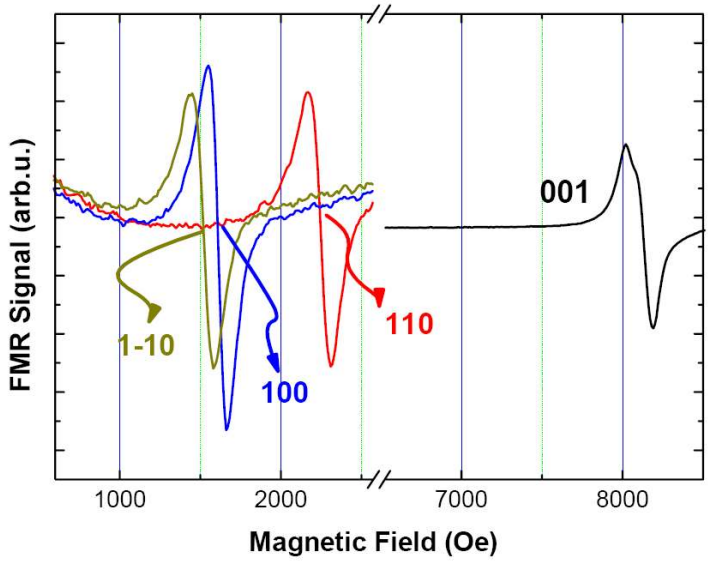


**Figure 5.7:** FMR spectra for high symmetry axes of sample.A (x=0.15) at T=4K

indicating a slight difference in their magnetic anisotropy fields. Hence even if we have to consider this superposition for further correct analysis of the line-width, the inhomogeneity of the sample is not large and the sample can be considered as a homogeneous one. This will be discussed in more detail in future sections 6.4.3. Moreover, these spectra do not present the same intensities and in this section we focus on the dominant spectra (i.e. the larger number of magnetic moments) which is representative of the sample.

In fig.5.8 the spectra are shown as a function of temperature for an applied field along the [001] direction of the sample. A closer attention to the form of the spectra show that as the temperature is increased, it deforms slightly from the single Lorentzian absorption shape. The reduction of the line-width with the temperature (for temperatures well below than the $T_C$) is well observed in all samples and is also reported in other similar works. This enabled us to detect at T=4K the complex spectra which were discussed in previous paragraph. At T=4K the total line-width of the spectra does not permit to distinguish them any longer. Since both spectra can be fitted separately by a Lorentzian shape, the relative volume of the dominant can be deduced. It is shown that as the temperature is increased, the resonance field for [001] (generally for all directions) shifts progressively to the value of Hr=3370Oe corresponding to the paramagnetic resonance field of manganese with g=2.00. (this feature is valid for high hole concentrations; see ref. [3] and section 4.9) Because of the presence of the external applied magnetic field there is a typical 10K difference between the empirical $T_C$ observed in FMR and the real critical temperature of the

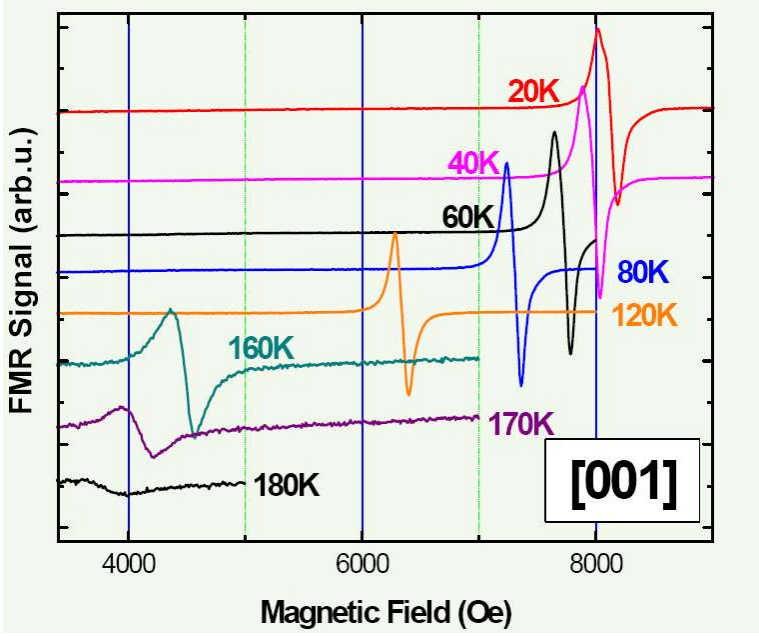


**Figure 5.8:** FMR spectra of sample.A (x=0.15) for H‖[001] for different temperatures

film. As usual, the total intensity of the spectra decreases with the temperature due to the reduction of the total magnetization of the sample.

- Sample B (x=0.17)

At T=4K the easy axis for this sample is along [100] direction. This reorientation of the easy axis compared to sample A is attributed to the modification of uniaxial stress and hole concentration in the sample [19]. Between 20K to 40K the easy axis reorients from [100] to $[1\bar{1}0]$(fig.5.9). In addition the resonance field for hard (/easy) axis is lower (/higher) compared to the ones of sample.A.

The other feature of this sample is the variation of the resonance field along hard axis as a function of temperature; from 4K to 10K there is a slight increase of resonance field (fig.5.10). This feature which was observed previously for low (intermediate) hole concentrations ($p<7\cdot10^{20}cm^{-3}$) illustrates the increase of the free charge carriers in this sample. The disappearance of the FMR signal around 140K is consistent with the $T_C$ value extracted from SQUID data for the counterpart of this sample [6].

- Sample C (x=0.21)

The monotonous decrease of the resonance field difference from easy to hard axis as function of doping level continues in this sample (Fig.5.11). Once more,

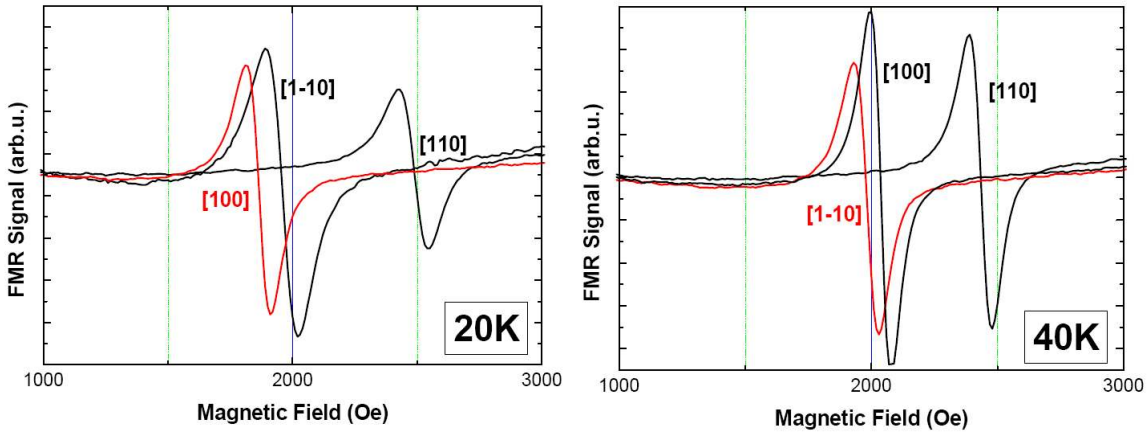


**Figure 5.9:** FMR spectra of sample.B (x=0.17) for H‖inplane axes at T=20K and 40K (the FMR spectra of easy axis are in red color)

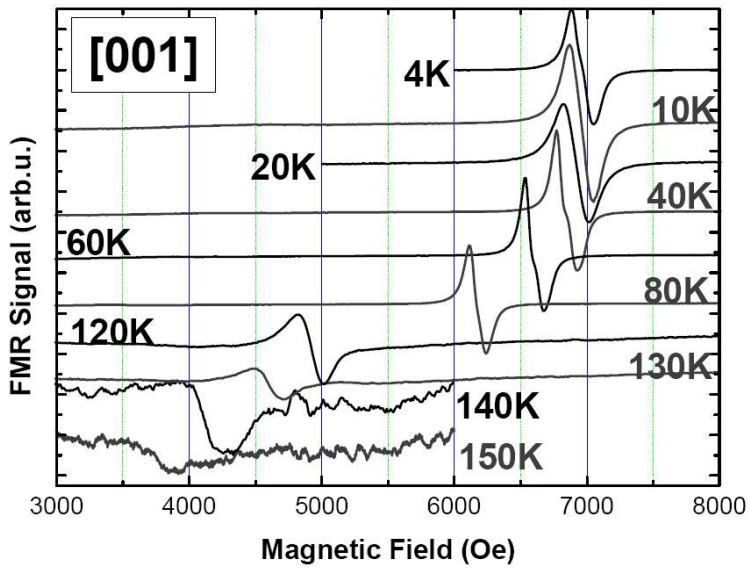


**Figure 5.10:** FMR spectra of sample.B (x=0.17) for H‖[001] as a function of temperature up to $T_C$ (for T=120 and 130 the gain of spectra are multiplied by factor 5 and for 140 and 150K by factor 50 for a better observation)

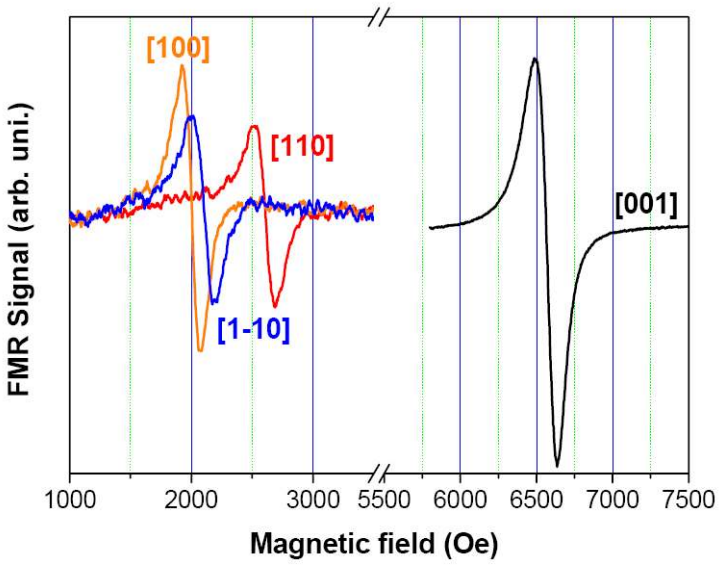


**Figure 5.11:** FMR spectra of sample.C (x=0.21) for H along high symmetry axes of the film axes at T=20 (note that at this temperature the axes [100] and [1$\bar{1}$0] are getting close to be equivalent)

one should notice here the enhancement of the resonance position from 4K to 20K. The easy axis is [100] at T=4K and reorients along [1$\bar{1}$0] direction between 20K to 60K; this observation is similar to the one made for sample B. The FMR spectra measured for the hard axis geometry at different temperature show a progressive increase of the total linewidth in the series. The FMR spectra can be fitted using a single Lorentzian line-shape. Either the increase in the linewidth for these samples have covered the separation of the former two spectra, or these samples have become more homogeneous due to the higher concentration of Mn. The disappearance of the FMR signal about T≈150K differs by 25K from what is expected from the TC measured by SQUID technique. The considerable enhancement of the total linewidth (4 to 6 times larger as compared to the reference sample),can be the sign of the existence of high magnetic inhomogeneities in the sample e.g. interstitial Mn centers which delay the disappearance of the remanent magnetization in the presence of an external applied field, inducing a difference of more than 10K as for the standard samples.

#### *5.4.1.3 FMR intensity*

It was mentioned that the SQUID measurements were not reported in details for these samples, especially as a function of temperature but this is essential for the quantitative analysis of the magnetic properties of these samples. In addition the very low thickness of the samples prevents us to deduce from squid measurements

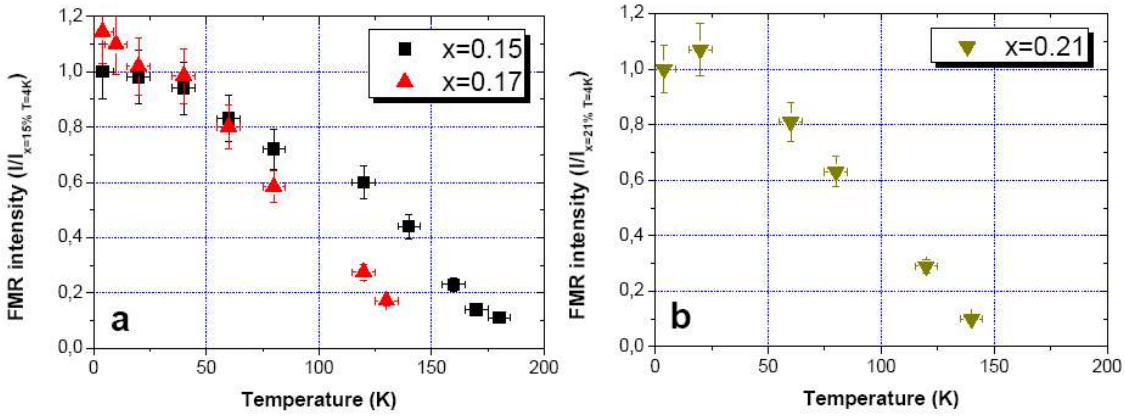


**Figure 5.12:** FMR intensity is proportional to the magnetization. The FMR intensities for samples of the series are normalized to the the intensity of sample.A at T=4K (a) and sample.C (b)

the magnetization value at higher temperature due to the dominating contribution of the substrate diamagnetism. In this case we used another approach to determine these values.

As it is discussed in section 2.1.4 and experimentally shown in section 4.9.3, the intensity of the FMR spectra (double integral) is proportional to the magnetization of the samples. Normalizing these value to the one measured at T=4K and considering the values of the SQUID measurements enable us to estimate the values of M as a function of temperature. Moreover, for the new sample.B which is different from the reported 10nm sample, normalizing the FMR intensity to the one obtained from the sample.A allows us to determine its total magnetization at any temperature.

Fig.5.12 shows the results. The magnetization of sample.B is higher than the one of sample.A which is different from the one indicated in ref [6]. Considering the results from RBS measurements in section 5.3, this might be due to the increase in the effective volume of the sample after the migration of the $Mn_{int}$ ions toward the surface as compared to the 10nm thick sample with the same doping level.

Samples A to C show similar values of magnetization despite the considerable increase of the doping level. This fact is probably due to the high rate of compensation, both electrical and magnetic, which increases with the doping level. As for injecting more Mn ions into the GaAs matrix the temperature of the substrate is decreased, the concentration of the As antisites could be higher. This, together with the higher magnetic compensation due to interstitial Mn ions, create a double compensation effect in this series.

## 5.5 g-factor measurements; comparison to mean field calculations

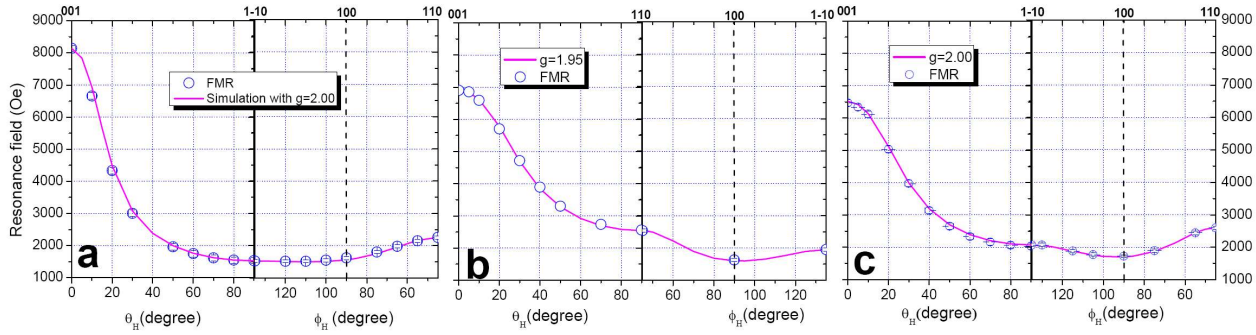


**Figure 5.13:** Simulation (lines) of the FMR resonance field (circles) as a function of angular variation of applied magnetic field orientation with respect to the film axes; for both out-of-plane (left) and in-plane (right) configurations. For each sample ((a)sample.A, (b)sample.B and (c) sample.C) the measured g-factor is indicated in on its graph. (T=4K)

For this series we made similar analysis as the one performed for the two previous series. We simulate the angular variation of the resonance fields and the g values were determined by the best fit of the angular variation. Fig.5.13 shows these simulations together with the deduced g-factor values for each sample at T=4K. For samples A and C the measured value is g=2.00. Whereas the sample.B presents an angular variation of the resonance field which matches better with g=1.95±0.01. The interpretation of these values will be postponed until more aspects of the measurements are elucidated.

In fig.5.14 the magnetic anisotropy field values which led to our simulations and g-factor measurements are shown as a function of temperature for different samples. The term $4\pi M_{eff}$ is introduced instead of the perpendicular uniaxial anisotropy field (cf. section 2.1.1). In each sample the $4\pi M_{eff}$ term is dominating. The value $4\pi M_{eff}$ of the reference sample is also displayed in each graph for comparison. The $4\pi M_{eff}$ term of the sample with x=0.15 is very close to one of the reference sample even though its doping level is two times higher. The dominating anisotropy term decreases with the Mn concentration. For samples B and C the lack of data point for higher temperature, due to excessive line broadening of the spectra, did not allow an analysis near $T_C$.

## 5.6 Magneto-crystalline anisotropy constants

Using the magnetization value obtained from SQUID measurements the four magnetocrystalline anisotropy constants were calculated. Fig.5.15 shows the value

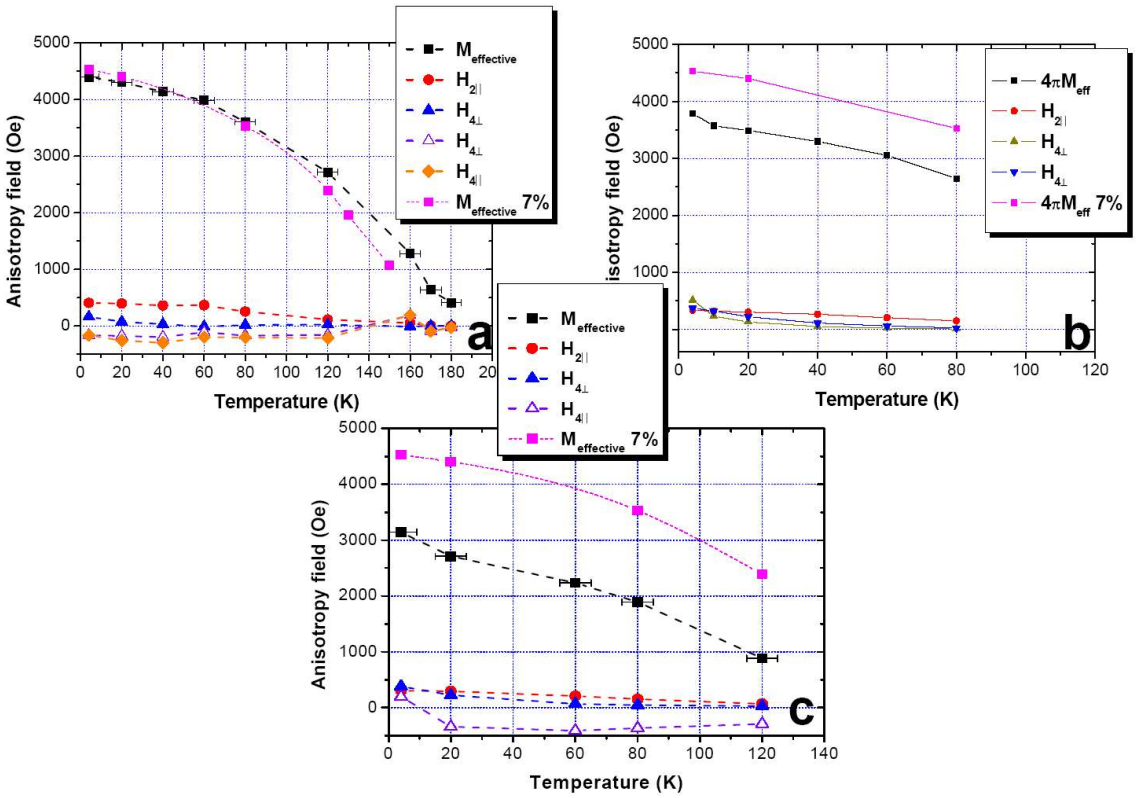


**Figure 5.14:** The magnetic anisotropy fields as a function of temperature for different samples((a)sample.A, (b)sample.B and (c) sample.C). The second $H_{4\perp}$ in sample.A is related to the second observed resonance field which is attributed to the inhomogeneity of the sample. The Other fields remain unchanged for this resonance.

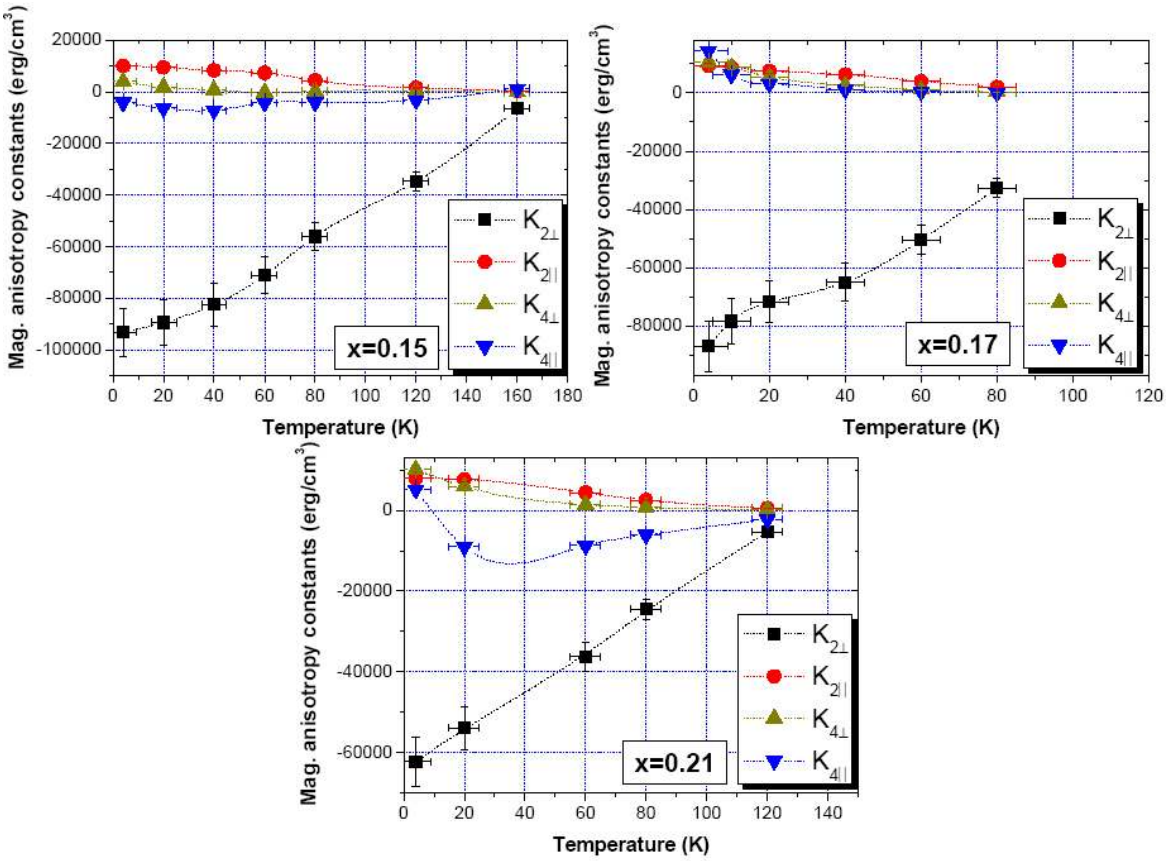


**Figure 5.15:** The magnetocrystalline anisotropy constants as a function of temperature for the samples of the series. The SQUID and FMR intensities are used for their determination. The lines are guides for the eyes.

of the four constants K as a function of temperature. The variation of the anisotropy constants is not following the same behavior in the three samples. In a first step we try to compare the results with the reference sample and in second step we will use some mean field theory results to interpret them.

### 5.6.1 Comparison to standard (x=0.07) sample and mean-field predictions

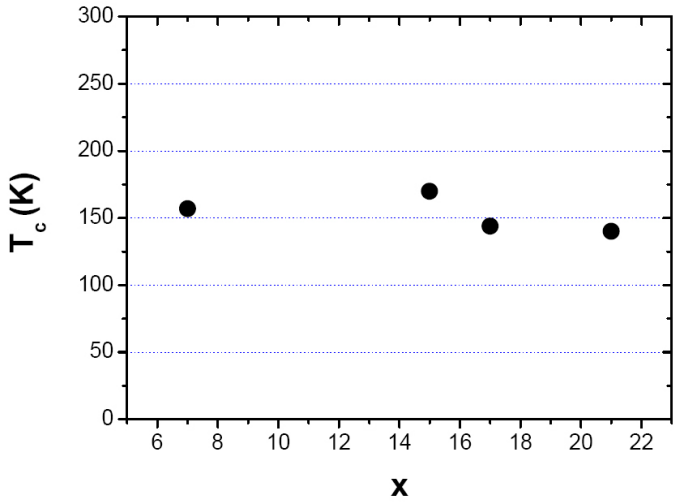


**Figure 5.16:** The measured values of Curie temperature via FMR as a function of the total Mn concentration.

The objective for growing layers with such high Mn concentration was to increase the Curie temperature. As was shown before, unfortunately the $T_C$ values are still far below room temperature and stay close to the previous limit of 180K(fig.5.16). Which process prevents the $T_C$ to increase further? The answer to this question lies in the result shown in the fig.5.17. In this figure we have drawn the effective concentration as a function of the total Mn concentration. This parameter is the ratio of the measured magnetization of the sample to the expected magnetization from a GaMnAs sample with the same Mn concentration, in which all the Mn ions are magnetically active.

$$x_{eff} = \frac{M_{measured}}{M_{expected}} \times x \tag{5.3}$$

The figure shows that in all samples the value is around 5% of substituted Mn. The fig.5.16 reveals that in all samples the $T_C$ value is the one expected for a sample with 4.5 to 5% of $Mn_{Ga}$ concentration. Using eq. 5.4:

$$x_{int} = \frac{x_{tot} - x_{eff}}{2} \tag{5.4}$$

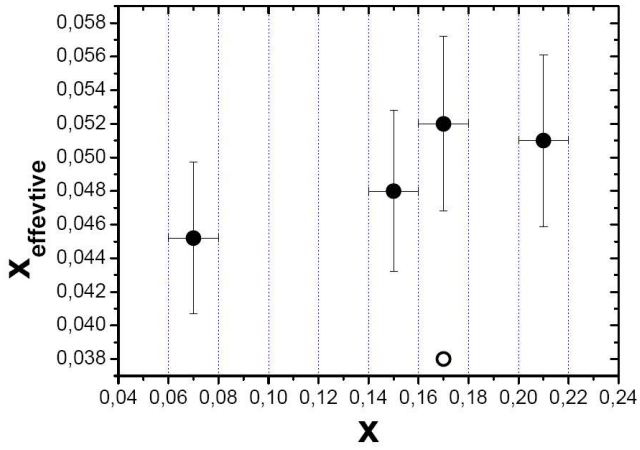


**Figure 5.17:** The concentration of the effective Mn ions ($x_{eff}$) as a function of total doping concentration x (filled circles). The empty circle is calculated with the measured magnetization for a 10nm thick sample doped with x=0.17 (note that sample B is 20nm thick).

and then subtracting the amount of interstitial ions from the total concentration, gives the concentration of $Mn_{Ga}$. This estimation is based upon the assumption of no electrical compensation from the $As_{antisite}$ defects. If we accept this hypothesis, a simple linear model linking the fraction of interstitial Mn to the total Mn concentration, allows to interpret our observations fig.5.18. This simple model explains the limitation of Tc by the magnetic compensation of substitutional Mn by interstitial Mn ions.

This conclusion shows that although the manganese ions have well been introduced in the GaAs matrix and do not precipitate after annealing, the interstitial fraction limits the magnetic performance. In the section 5.3 we showed that the interstitial manganese concentration has a profile that increases to the surface. At the same time the negative effect of the GaAs capping layer via creation of a barrier (repulsive Coulomb interaction between the n-type capping layer and p-type GaMnAs layer) for further out-diffusion of $Mn_{int}$ ions is known (cf. [15]). Very recently Novak et al. [16] has reported the possibility to increase the Curie temperature in samples with x=0.07 up to 176K via chemically removing the out-diffused Mn ions which oxide in ambient air, and successive annealing. Considering the high potential of MnAs to oxide, the same process can be applied for these heavily doped samples even with the precipitation of the MnAs clusters on the surface and this could be a way to increase the concentration of $Mn_{Ga}$ centers.

We can then discuss the dependence of Tc with the hole concentration predicted in the frame of the mean field model and which is a direct result of the Zener kinetic

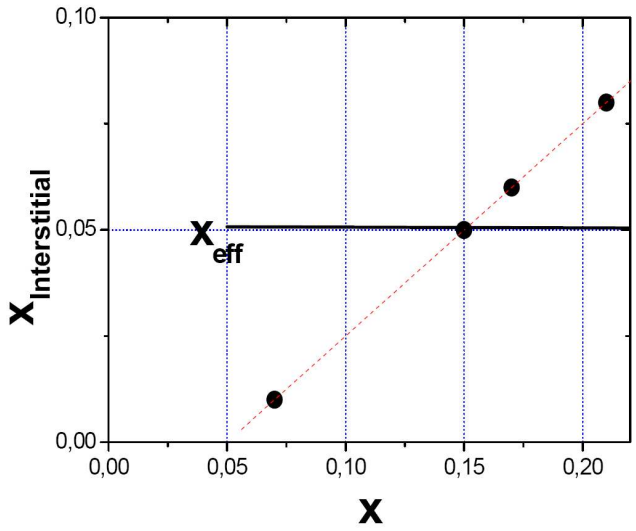


**Figure 5.18:** The measured concentration of the interstitial Mn ions ($x_{int}$) as a function of total doping concentration x. The thick solid line shows the resulting effective concentration. The red line is the linear fit to the measured data.

exchange model:

$$\frac{T_C}{x_{eff}} \propto p^{1/3} \tag{5.5}$$

For systems in which the compensation is high (our series) this relation appears to be valid. This relation was also in good agreement with the experimental results of the hydrogen passivated series. Considering the effective Mn concentration in that case which is nearly the same as in this series, it seems reasonable to use the relation 5.5 for a rough estimation of the hole concentration. The results are shown in fig. 5.19.

These results are normalized using the measured hole concentration of the reference sample of the hydrogen passivated series (sample.R). Our reference sample with x=0.07 has a slightly larger effective Mn concentration and a slightly higher hole concentration. Samples B and C despite of their considerably higher $x_{eff}$, reveal lower $T_C$ and hole concentrations. For sample C, this is consistent with the resistivity results. This could be attributed to the very high doping level together with the low thickness of the sample where the interstitial Mn ions do not have enough space to form a homogeneous layer near the surface, leading to a more inhomogeneous layer (as compared to sample.A).

For sample.B for which we have estimated the hole concentrations between the ones for sample C and D in the hydrogen passivated series, the determined g-factor is quite consistent with our previous results. However note that qualitatively, this feature can be described by considering that for such high concentrations, while

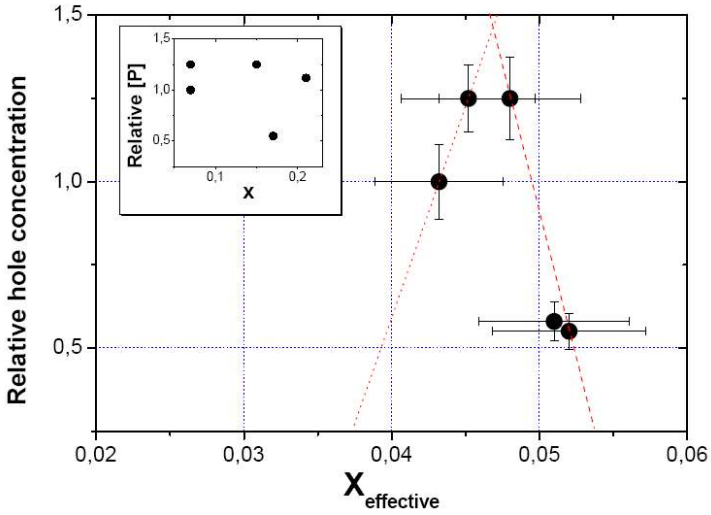


**Figure 5.19:** The estimated hole concentration using MF predictions and FMR measurements as a function effective x. The dotted line joins the two previous reference samples and the dashed line the samples in this series

the spatial distances between the $Mn_{Ga}$ magnetic moments decrease considerably, the polarization of the holes tends to vanish because of the deep position of the Fermi level in the valence band. More over the conductivity of the holes can be more complicated because of the higher rate of their scatterings. In this condition the system tends toward a RKKY model in which the mediation of magnetic order via the band carriers do not depend on their total polarization but mostly on the spontaneous antiferromagnetic coupling of a few numbers of them with the very close Mn centers. This interaction can be dominant over the probable superexchange interaction between the close Mn ions which tends to vanish their resulting moments. This qualitative description indeed requires theoretical calculations and support.

The magnetocrystalline anisotropy constants of the samples are presented as a function of effective x in fig.5.20. The reference samples are again added to the graph for comparison. We note that these constants depend on both the hole concentration and the lattice parameter. For a better vision on the different contributing parameters we have used the relation calculated by Abolfath et al. [17]: (eq. 4.5) whose validity is again verified experimentally in section 4.11.1:

$$\frac{\Delta a}{a} \propto \frac{K_{2\perp}}{[p]} \tag{5.6}$$

where $\Delta$a presents the change of the lattice parameter. This approach is important since once again the low thickness of our ultrathin film has not enabled us to deduce these values from the XRD measurements. Once again the results are

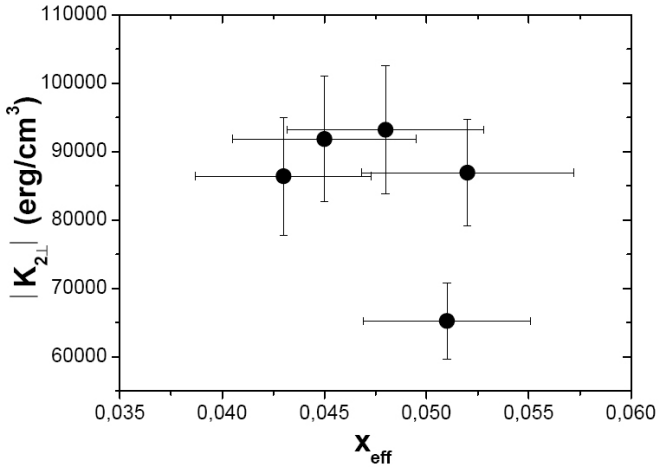


**Figure 5.20:** The uniaxial magnetocrystalline anisotropy constant ($K_{2\perp}$) as a function of $x_{eff}$

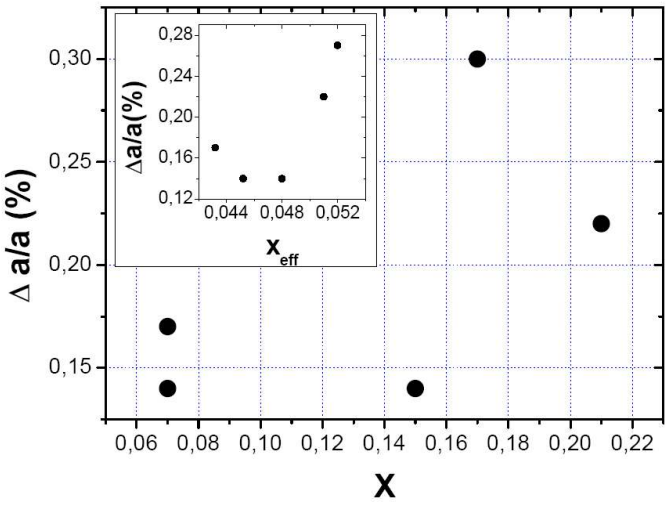


**Figure 5.21:** The estimated lattice parameter variation using MF predictions and FMR measurements as a function effective x. (inset: as a function of effective x)

normalized to those of the reference sample in the hydrogen passivated series 4.11.1 and they are shown in fig.5.19. Both latter figures show that the uniaxial anisotropy constant ($K_{2\perp}$) increases from sample.R (the reference sample in section 4.11.1) to the reference sample. Fig.5.19 reveals that this could be due to the increase in the hole concentration in the reference sample. The case of sample.A is the most particular one. Despite the fact that the doping level is increased twice, neither the lattice parameter nor the hole concentration is different from the reference sample with x=0.07. This is a very remarkable result of the annealing process which has provided us with a sample in which a large part of the interstitial ions have migrated to the upper layers, leaving an important part of the sample as an 5% doped sample. This feature is also observed in the following samples of the series. For samples B and C, although one might notice the increase in the lattice parameter compared to the previous member of the series, but it is crucial to consider the important difference in the doping level too. Zhao et al. have reported in 2005 the experimentally deduced relation between the doping level and the lattice parameter as follows ( [18]):

$$\Delta a = (0.26 \pm 0.08)x + (0.6 \pm 0.2)y + 1.05z \quad (A^o) \tag{5.7}$$

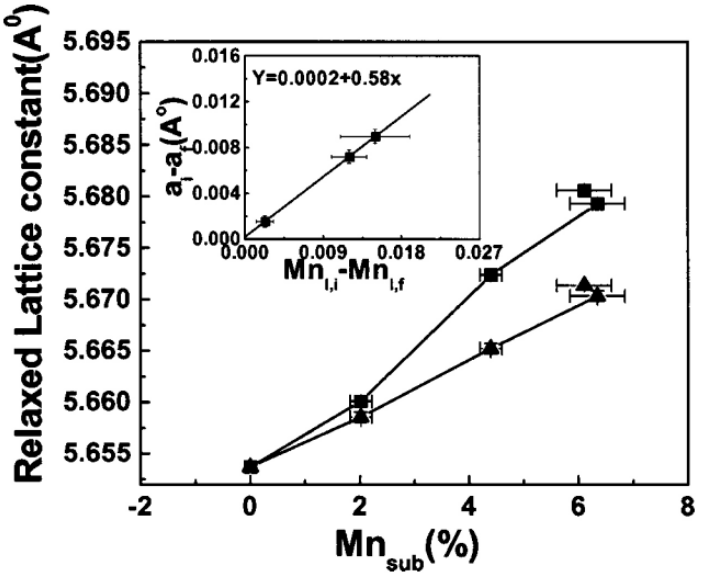


**Figure 5.22:** The contribution of interstitial and substitutional Mn ions to the modification of lattice parameter of the GaAs (from ref. [18])

where x, y and z are substitutional, interstitial and $As_{anti}$ share of the doping concentration. Their experimental results are shown in fig.5.22. Considering this

relation and the relatively high concentration of As antisites in our samples as compared to the samples grown at 250°$C$ (the density of the As antisites are lower than the Mn ions by a factor of 10), the samples A, B and C are similar to the sample with x=0.05.

In fig. 5.23, we would like to add a justification to our predicted results. This figure which shows the TEM image of sample.C, demonstrates the high quality of its crystal structure. At the interface the border between the substrate and the GaMnAs layer is difficult to distinguish. On the other hand at the top of the layer, about 1nm of the film from the surface is deformed. This is the region where the interstitial ions accumulated strongly.

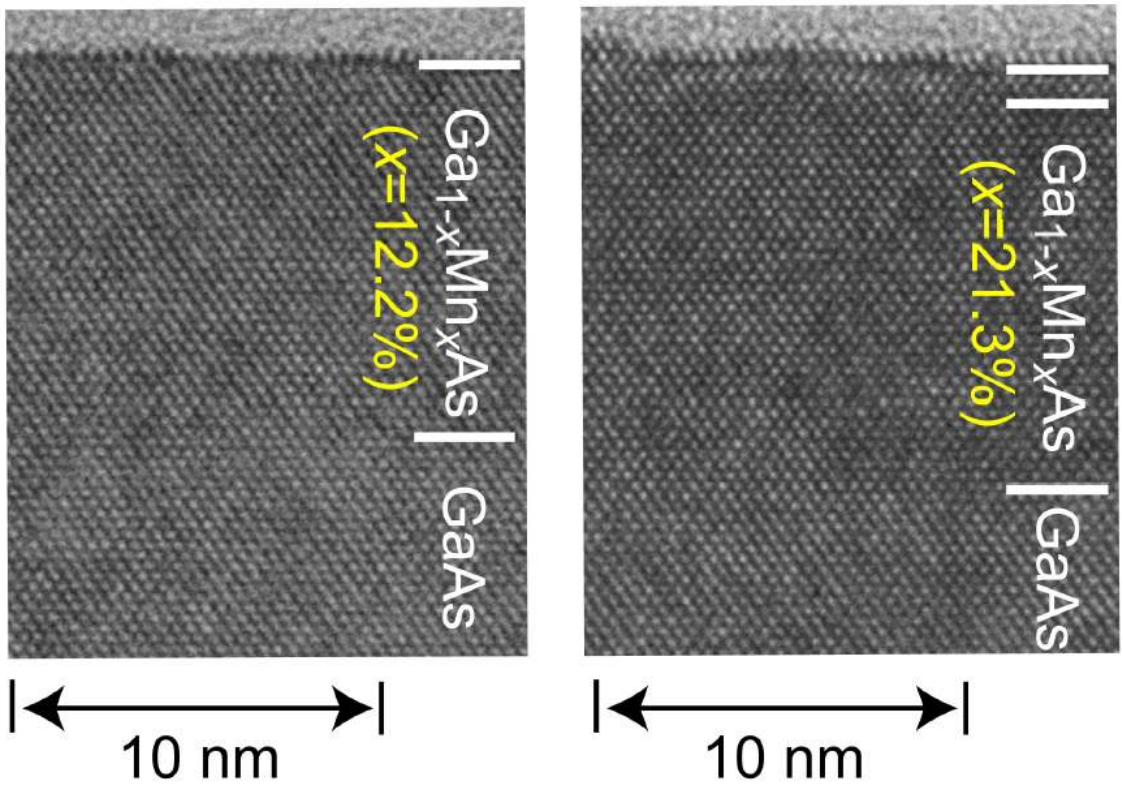


**Figure 5.23:** TEM image taken for the heavily doped samples x=0.125(left) and x=0.213 (right).

### *5.7 Conclusion*

To summarize this chapter, we presented the possibility to inject very high concentrations of manganese in GaAs matrix. We showed that the new GaMnAs sam-

ples with such high Mn concentrations, if well controlled, can provide single homogeneous layers without formation of undesirable second phases such as MnAs clusters.

We have investigated the effect of the additional manganese on the Curie temperature of GaMnAs thin films. Although no further increasing of $T_C$ was observed we concluded that it is still consistent with the mean-field theory predictions by introducing a new parameter : the effective Mn concentration which represents the density of magnetically active Mn ions. We observed that a linear increase of interstitial Mn ions with the doping level could explain the compensation of the substitutional Mn ions.

We propose that more sophisticated annealing processes such as multiple annealing could be a rather direct solution to further increase the Curie temperature in these heavily doped samples.

# Bibliography


[1] T. Jungwirth,J. Sinova, J. Masek et al. Rev Mod. Phys. 78, (2006).

[2] T. Jungwirth, J. Sinova, A.H. MacDonald, B.L. Gallagher et al. Phys. Rev. B 76, 125206 (2007).

[3] Kh. Khazen, H. J. von Bardeleben, and J. L. Cantin et al., Phys. Rev. B 77, 165204 (2008).

[4] M. Yokoyama, H. Yamaguchi et al., J. Appl. Phys. 97, 10D317 (2005).

[5] A. Kwiatkowski, D. Wasik et al., J. Appl. Phys. 101, 113912 (2007).

[6] S. Ohya, K. Ohno and M. Tanaka, Appl. Phys. Lett. 90, 112503 (2007).

[7] M. Tanaka, J. Vac. Sci. Technol. B 16, 2267 (1998);.

[8] J. Sadowski, R. Mathieu and P. Svedlindh, Appl. Phys. Lett. 78, 3271 (2001).

[9] J. Sadowski, J. Z. Domagala, J. Bak-Misiuk, S. Kolesnik, M. Sawicki, K. Swiatek, J. Kanski, L. Ilver, and V. Strom, J. Vac. Sci. Technol. B 18, 1697 (2000).

[10] Y. Horikoshi, M. Kawashima, and H. Yamaguchi, Jpn. J. Appl. Phys., Part 2 25, L868 (1986).

[11] Yu, K. M., W. Walukiewicz, T. Wojtowicz, W. L. Lim, X. Liu et al. , Phys. Rev. B 68, 041308R (2003).

[12] X. Liu and J. K. Furdyna, J. Phys.: Condens. Matter 18, R245 (2006).

[13] K. Y. Wang, M. Sawicki, K. W. Edmonds, R. P. Campion, S. Maat, C. T. Foxon, B. L. Gallagher, and T. Dietl, Phys. Rev. Lett. 95, 217204 (2005).

[14] T. G. Rappoport, P. Redlinski, X. Liu et al. Phys. Rev. B 69, 125213 (2004).

[15] M. B. Stone, K. C. Ku, S. J. Potashnik, B. L. Sheu, N. Samarth, and P. Schiffer, Appl. Phys. Lett. 83, 4568 (2003).

[16] K. Olejnik, M.H.S. Owen, V. Novak, J. Masek, A.C. Irvine, J. Wunderlich, T. Jungwirth arXiv:0802.2080v1 (2008).

[17] M. Abolfath, T. Jungwirth, J. Brum, and A. H. MacDonald, Phys. Rev. B 63, 054418 (2001).

[18] L. X. Zhao, C. R. Staddon, K. Y. Wang, K. W. Edmonds, R. P. Campion, B. L. Gallagher, and C. T. Foxon, Appl. Phys. Lett. 86, 071902 (2005).

[19] T. Dietl, H. Ohno, and F. Matsukura, Phys. Rev. B 63, 195205 (2001).

# 6

# Dynamics of Magnetization; Damping factor

[35]

In this chapter we will focus on the dynamics of the magnetization in different type of GaMnAs thin films. This topic is an important subject both fundamentally and from an application point of view since in spintronic devices the coupling between the electronic and magnetic states of the carriers and local moments is used. In particular in DMS systems where the magnetic properties are introduced by doping and the spin orbit interaction is strong quite different damping factors might be expected as compared to the classical ferromagnetic systems such as iron (Fe) and cobalt (Co).

Another important aspect is the timescale at which the magnetization can be switched. This is relevant for systems such as an M-RAM where nano- or some times picosecond magnetization reversals are required. Despite of its technological importance the so called damping process is still not fully understood in metals and of course even less in DMS materials.

We have to distinguish two different cases of damping, the small angle relaxation of the magnetization in a homogeneously magnetized thin film, which is measured by FMR spectroscopy and the complete magnetization reversal via domain wall motion such as is observed in Kerr microscopy. In a classical model, of a homogeneously magnetized film where the system can be treated as a macrospin, interactions such as spin-orbit, spin-spin and magnon-magnon are expected to contribute to the magnetization relaxation time. It seems not to be clear how the damping factor and the relaxation time are related as some researchers find a direct relation between the relaxation time and the damping and others claim a reciprocal relation.

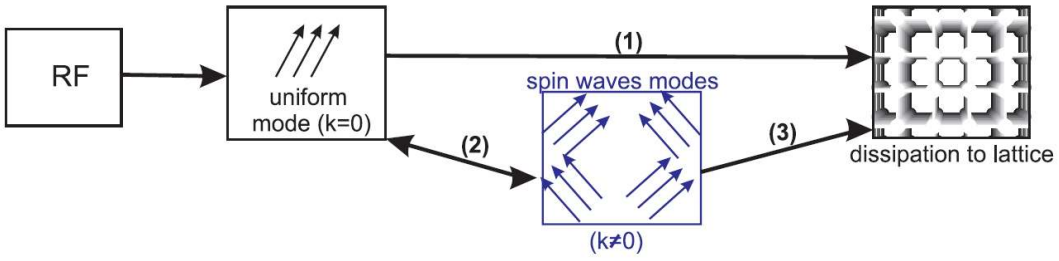


**Figure 6.1:** Schematic drawing of the possible paths of the relaxation of the magnetization precession [1]

## *6.1 Spin relaxation mechanisms*

We have presented in section 2.1.2 that for a small deviation of the magnetization from the effective magnetic field the relaxation process can be included in the LL equation of motion. In an FMR experiment the homogeneous microwave field couples to the uniform mode of magnetization, for which all spin precess in phase (wave vector k = 0). This uniform mode may not only decay via direct energy dissipation to the lattice, but also via energy transfer to the other spin-wave (k $\neq$ 0) modes (i.e. keeping the energy within the spin system), which then dissipate the energy to the lattice. The viscous damping is a direct energy dissipation to the lattice and is irreversible. Fig.6.1 shows the possible processes during magnetization relaxation. Path (1) indicates the viscous damping and path (2) denotes a decay into nonuniform spin-waves (k $\neq$ 0), which finally decay to the lattice via path (3). In other words path (2) indicates that the energy of the uniform mode might dissipate to the lattice via an intermediate reversible state. This state may include high energy magnons or Stoner excitations for instance.

These relaxation processes can be described by the Bloch-Bloembergen [2, 3] equation:

$$\frac{1}{\gamma}\frac{\partial \vec{M}}{\partial t} = -\left(\vec{M} \times \vec{H}_{eff}\right) - \frac{M_x}{\gamma T_2}\hat{i} - \frac{M_y}{\gamma T_2}\hat{j} - \left(\frac{M_z - M_s}{\gamma T_1}\hat{k}\right) \tag{6.1}$$

Here $T_1$ presents the direct dissipation to the lattice, the so-called longitudinal relaxation time, whereas $T_2$ is the transverse relaxation time(in this case the energy is scattered to the transverse components of the magnetization). A schematic illustration of both phenomena is given in Fig.6.2. The magnetization vector according to the LLG equation spirals toward the direction of the effective magnetic field (Fig.6.2 (a)). The length of $\vec{M}$ stays constant, while $M_z$ increases, whereas in the Bloch-Bloembergen case the z-component stays constant if $T_1 \succ\succ T_2$, since

the energy is scattered into the transverse components of the magnetization. The relaxation mechanisms can be generally divided into two categories which will be introduced briefly. They are important for the interpretation of the following experimental measurements. B. Heinrich and J. Bland have exposed these effects in detail in their book [4].

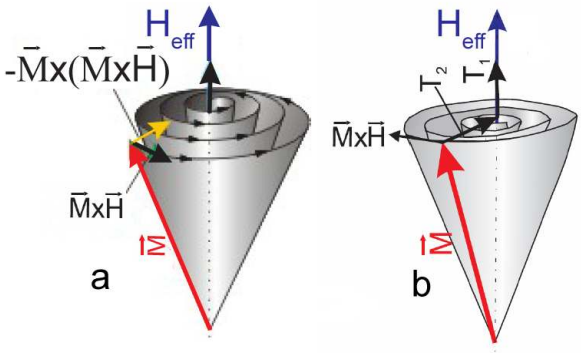


**Figure 6.2:** Schematic illustration of (a) LLG and (b) Bloch-Bloembergen damping

### 6.1.1 Intrinsic relaxation (Gilbert damping)

>In the LLG equation of motion all intrinsic relaxation mechanisms are expressed in one phenomenological parameter, the Gilbert damping factor which is the second term in the LLG equation. Small contributions such as phonon-drag and eddy currents are neglected in this description; it is the spin-orbit relaxation which plays the major role.

#### *6.1.1.1 Spin-orbit relaxation*

One mechanism for spin relaxation which has been proposed by Heinrich et al. [5] in 1967, is the s-d exchange interaction. In this model the interaction of itinerant s-p like electrons with localized d-spins can beobtained by integrating the s-d exchange energy density function.

$$H_{sd} = \sum_j \int_V J(\vec{r}_j - \vec{r})\vec{S}_{j,d} \cdot \vec{S}_S(\vec{r})dr^3 \tag{6.2}$$

where $J(\vec{r}_j - \vec{r})$ is the s-d exchange interaction between the spin density, $\vec{S}_S$, of s-p like itinerant electrons and the localized spins of the d-electrons,$\vec{S}_{j,d}$. j is the lattice site. Two different sets of electrons have to be considered. Those that are

mostly localized (here the d-electrons) and those which are itinerant (the s electrons). In reality the itinerant electrons are hybridized states of s-p and d electrons. The transverse interaction Hamiltonian involving only the rf-components of magnetization vectors is described by a three particle collision term:

$$H_{sd} = \sqrt{\frac{2S}{N}} \sum_{\vec{k}} J(\vec{q}) a_{\vec{k},\uparrow} a^{\dagger}_{\vec{K}+\vec{q},\downarrow} b_{\vec{q}} + h.c. \tag{6.3}$$

where N is the number of atomic sites, a (b) annihilates an electron (a magnon ) and $a^{\dagger}(b^{\dagger})$ creates an electron (a magnon). The arrows $\uparrow$ and $\downarrow$ show the spin direction (up and down, respectively). A schematic illustration of this process is shown in Fig.6.3

This relation indicates that the magnons and itinerant electrons are coherently scattered by the s-d exchange interaction, which results in an electron-hole annihilation pair.

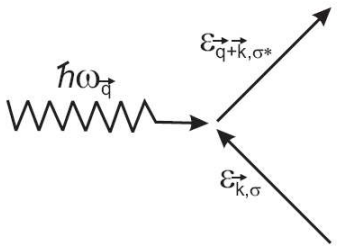


**Figure 6.3:** Illustration of the spin-flip scattering process.

This scattering (fig.6.3) does not lead to magnetic damping of magnons with the uniform mode (q = 0). The coherent scattering of magnons with itinerant electrons has to be disrupted by incoherent scattering with other excitations. The spin-flip hole-electron pairs can be incoherently scattered by thermally excited phonons. One can account for incoherent scattering by including a finite lifetime for the electron-hole pair (quasi-particle) excitation. Then, the electron-hole pair energy has an additional imaginary term:

$$\Delta\epsilon_{\vec{k},\vec{k}+\vec{q}} = \epsilon_{\vec{k}+\vec{q},\uparrow} - \epsilon_{\vec{k},\uparrow} + i\frac{\hbar}{\tau_{eff}} \tag{6.4}$$

where $\tau_{eff}$ is the effective lifetime and given by the spin-flip time of the electron-hole pair, $\tau_{sf}$. It is enhanced as compared to the momentum relaxation time $\tau_m$ which enters in the conductivity. The reason is that one needs to invoke spin-orbit interaction to flip the spin during the relaxation process of electron-hole pairs by phonons. For simple normal metals $\tau_{sf} = \tau_m/\Delta g^2$ [6], where $\Delta g$ is the deviation of the g-factor

from the free electron value. Another estimation of $\tau_{sf}$ can be obtained from the spin diffusion length. The spin diffusion length is a part of the spin accumulation process which occurs in the current perpendicular to plane giant magneto-resistance (CPP GMR) investigations [7–9] and is given by:

$$l_{sd} = \sqrt{\frac{\lambda_{FM}^{m} \nu_F \tau_{sf}}{6}} \tag{6.5}$$

where:

$$\frac{1}{\lambda_{FM}^{m}} = \frac{1}{2}\left(\frac{1}{\lambda\uparrow} + \frac{1}{\lambda\downarrow}\right) = \frac{ne^2\rho^*}{m\nu_F}$$

with $\lambda_{FM}^{m}$ is the effective momentum mean free path resulting from the momentum mean free paths of the majority $\lambda\uparrow$ and minority $\lambda\uparrow$ electrons. $\nu_F$ is the Fermi velocity of the electrons participating in the spin accumulation, n is the total density of conduction electrons. $\rho^* = \rho_{FM}(1-\beta^2)$ where $\rho_{FM}$ is the measured resistivity of the ferromagnet and $\beta$ is a bulk spin asymmetry coefficient. The rf susceptibility can be calculated by using the Kubo Green function formalism in the random phase approximation (RPA) [10].

$$G_{\vec{q},\vec{q'}} = \left\langle b_{\vec{q}} | b_{\vec{q'}}^{\dagger} \right\rangle = -i\theta(t-t') \left\langle \left[ b_{\vec{q}}(t), b_{\vec{q'}}^{\dagger}(t') \right] \right\rangle \tag{6.6}$$

$\theta(t-t')$, is the Heaviside step-function which is averaging over a grand-canonical ensemble and brackets are the commutative operator. The infinite chain of higher-order Green functions is determined using contraction over operators a and b.

By defining an additional Green function:

$$F_{\vec{k},\vec{k'},\vec{q}} = \left\langle a_{\vec{k},\uparrow} a_{\vec{k'},\downarrow}^{\dagger} | b_{\vec{q}} \right\rangle \tag{6.7}$$

the imaginary part of the Green function here presents the effective damping field then a sharp Fermi energy the Gilbert damping field can be written as [5]:

$$H_{eff}^{sf} = \frac{2\langle S \rangle}{Ng\mu_B} \sum_{\vec{k}} |J(\vec{q})|^2 \, \sigma(\epsilon_{\vec{k}} - \epsilon_F) \hbar\omega_{\vec{q}} \frac{\hbar}{\tau_{sf}} \frac{1}{\left(\hbar\omega + \epsilon_{\vec{k},\uparrow} - \epsilon_{\vec{k}+\vec{q},\downarrow}\right)^2} \tag{6.8}$$

here $\langle S \rangle = M_s(T)/M_s(0)$ presents the reduced spin, n is the density of states. According to the fact that the excitation energy of electron-hole pairs is dominated by the exchange energy in an uniform ferromagnetic resonance, the Gilbert damping field can be written as:

$$H_{eff}^{sf} = \frac{\hbar^2 \omega_{\vec{q}}}{2M_s\tau_{sf}} \sum_{\vec{k}} \delta(\epsilon_{\vec{k}} - \epsilon_F) \tag{6.9}$$

the Gilbert factor can be deduced from comparing this equation with the LLG equation of motion.

$$G = \frac{\chi_P}{\tau_{sf}} \tag{6.10}$$

The Pauli susceptibility of itinerant electrons $\chi_P$ in expressed by:

$$\chi_P = \left(\frac{\hbar\gamma}{2\pi}\right)^2 \int \vec{k^2}\delta(\epsilon_{\vec{k}} - \epsilon_F)d\vec{k} = 2\mu_B^2 n(\epsilon_F) \tag{6.11}$$

in which $n(\epsilon_F)$ is the density of itinerant electrons at the Fermi level. In a different approach Kambersky et al have proposed another model for spin-lattice relaxation [11, 12]. According to his model the intrinsic damping in metallic ferromagnets can be derived from the spin-orbit interaction Hamiltonian.

$$H_{so} = \frac{1}{2}\sqrt{\frac{2S}{N}}\xi \sum_{\vec{k}} \sum_{\alpha,\alpha',\sigma} \langle\beta\,|L_+|\,\alpha\rangle\, c^{\dagger}_{\beta,\vec{k}+\vec{q},\sigma} c_{\alpha,\vec{k},\sigma} b_{\vec{q}} + h.c \tag{6.12}$$

$\xi$ is presenting the spin-orbit interaction coefficient. $L_+ = L_x + iL_y$ is the right handed component of the atomic transverse angular momentum. The operators $c_{\beta,\vec{k}+\vec{q},\sigma}c^{\dagger}_{\beta,\vec{k}+\vec{q},\sigma}$ annihilates(creates) electrons in the appropriate Bloch states with the spin $\sigma$. $b_{\vec{q}}$ annihilates the spin-wave with the wave-vector $\vec{q}$. The $\alpha$ and $\beta$ subscripts represent the projected local orbitals of Bloch states. The rf susceptibility has been proposed to be calculated from the Kubo Green function formalism in RPA.

By this approach the effective damping field is given by the imaginary part on the dominator of the circularly polarized susceptibility:

$$\frac{G\omega}{\gamma^2 M_s} = \frac{\langle s\rangle^2}{2M_s}\xi^2 \left(\frac{1}{2\pi}\right)^3 \int d\vec{k^3} \sum_{\alpha,\beta,\sigma} \langle\beta\,|L_+|\,\alpha\rangle\,\langle\beta\,|L_-|\,\alpha\rangle$$

$$\times\sigma\left(\epsilon_{\alpha,\vec{k},\sigma} - \epsilon_F\right)\hbar\omega \frac{\hbar/\tau_m}{\left(\hbar\omega + \epsilon_{\alpha,\vec{k},\sigma} - \epsilon_{\beta,\vec{k}+\vec{q},\sigma}\right)^2 + (\hbar/\tau_m)^2}$$

The relaxation time $\tau_{sf}$ is replaced by the momentum relaxation time, $\tau_m$ which enters the conductivity of the ferromagnet. For intraband electron transitions for low frequency spin-waves ($q \prec\prec k_F$ ), the electron energy balance $\hbar\omega + \epsilon_{\alpha,\vec{k},\sigma} - \epsilon_{\beta,\vec{k}+\vec{q},\sigma} = \hbar\omega - (\hbar^2/2m)\left(2\vec{k}\cdot\vec{q} + q^2\right)$ can be significantly less than $\hbar/\tau_m$. After integration over the Fermi surface the Gilbert parameter can be approximated by:

$$G \approx \langle S\rangle \left(\frac{\xi}{\hbar}\right)^2 \left(\sum_{\alpha} \chi_P^{\alpha}\,\langle\alpha\,|L_+|\,\alpha\rangle\,\langle\alpha\,|L_-|\,\alpha\rangle\right)\tau_m \tag{6.13}$$

In this relation the Pauli susceptibility of those states which participate in intra-band electron transitions is the $\chi_P^\alpha$. It is clear for this relation that Gilbert damping in this regime is proportional to the inverse of the relaxation time, $1/\tau_m$, and therefore scales with the conductivity.

The electron-hole pair energy is dominated by the energy gap ,$\Delta\epsilon_{\beta,\alpha}$, by which the inter-band transitions are associated . For gaps larger than the relaxation frequency $\hbar/\tau_m$ the Gilbert damping can be approximated by:

$$G \approx \langle G \approx \langle S \rangle \rangle \sum_\alpha \chi_P^\alpha (\Delta g_\alpha)^2 \frac{1}{\tau_m} \tag{6.14}$$

In this limit, considering Elliot's relation for the spin-flip relaxation time ($\tau_{sf} = \tau_m/\Delta g^2$), the spin-orbit interaction results in a Gilbert damping coefficient similar to that found for s-d exchange interaction [6].

Note that the Gilbert damping factor estimated in this model is isotropic and temperature independent. FMR spectroscopy is the standard technique to measure the damping factor and we have used it in the case of GaMnAs.

### 6.1.2 Extrinsic relaxation (Two magnon scattering)

Two magnon scattering is the major reason for extrinsic relaxation in ferromagnetic metallic films. In this process the uniform FMR mode can be scattered to nonuniform modes ($\vec{k} \neq 0$) as shown in fig.6.1 by the path (2). The examples of studying this contribution to damping have reported in refs. [13–16].

The two-magnon scattering contribution can be extracted from the torque term (first) in the LLG equation and consequently, does not result from the relaxation term. The dispersion relation for spin-waves can be derived from eq. 2.2. The only consideration is that the dipolar field, which includes $K \neq 0$ magnons has to be added to the exchange field. Therefore, the effective field can be expressed as [17]:

$$\vec{B}_{eff} = H_{exchange} - \frac{\mu_0}{k^2}\vec{k}\left(\vec{k}\cdot\vec{m}\right) \tag{6.15}$$

with $\vec{m} = \vec{m}_0 exp(i\vec{k}\cdot\vec{r})$. The schematic illustration of the bulk spin-wave dispersion relation for different orientations of the applied magnetic field is presented in fig.6.4. It indicates a shift of the band by changing the measurement configuration from the perpendicular to the in-plane orientation of the external field. In the perpendicular configuration the bottom of the spin-wave band at k = 0 coincides with the FMR frequency and there exist no degenerate non-zero k spin-wave states at this frequency. In the parallel configuration the band has dropped down so that the top of the spin-wave band at k = 0 equals the FMR frequency. In this configuration there is an extended range of wave numbers degenerate with the uniform FMR mode.

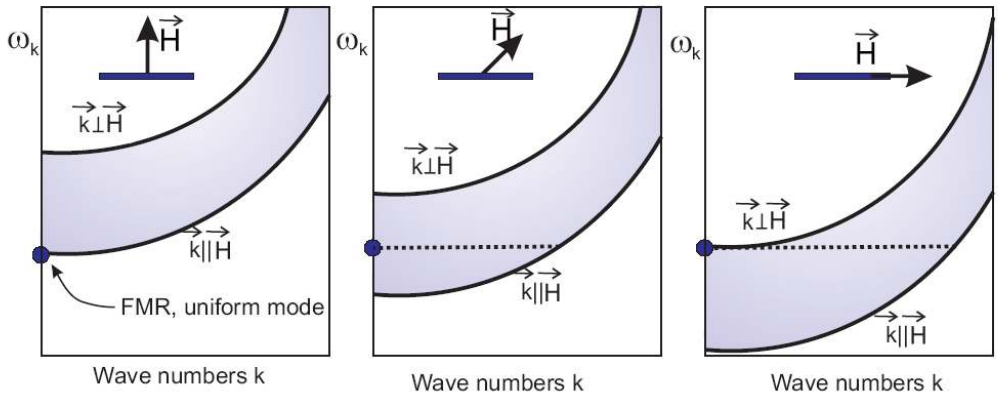


**Figure 6.4:** Schematic illustration of the spin-wave dispersion curve for different orientations of the applied magnetic field [1]

In the case of ultrathin films the wave vectors $\vec{k}$ are confined to the film plane. For a thin film with an effective out-of-plane anisotropy field, $4\pi M_{eff} = 4\pi M - \frac{2K_{2\perp}}{M}$, the magnon energies are given by Damon-Eshbach modes [18–22].

If the magnetic field is applied along an in-plane easy direction, then the dispersion relation can be expressed as:

$$\left(\frac{\omega_{K\|}}{\gamma}\right)^2 = \left(\frac{\omega}{\gamma}\right)^2 - \frac{1}{2}\mu_0 M\left[H - (H + \mu_0 M_{eff})sin^2\phi_{k\|}\right]k_\| + (2H + \mu_0 M_{eff})Dk_\|^2 \tag{6.16}$$

where, D is the exchange stiffness and $\pi_{k\|}$ is the angle between the in-plane component of wave vector $\vec{k}$ and $\vec{M}$.

Equation 6.16 indicates that in addition to the quadratic term there exists another linear term which is angle dependent. Moreover, this indicates that below a critical angle $\phi_{critical}$ given by:

$$sin^2\phi_{\vec{k}\|} \prec \frac{H}{H + \mu_0 M_{eff}} \Rightarrow \left|\phi_{\vec{k}\|}\right| \prec arcsin\left(\left(\frac{H}{H + \mu_0 M_{eff}}\right)^{1/2}\right) \tag{6.17}$$

the spin-wave band could be changed so that the minimum is not anymore at $k = 0$ and there are non-zero k spin-wave states degenerate with the uniform FMR mode. A schematic illustration of the spin-wave dispersion curve of an ultrathin film is given in fig.6.5.

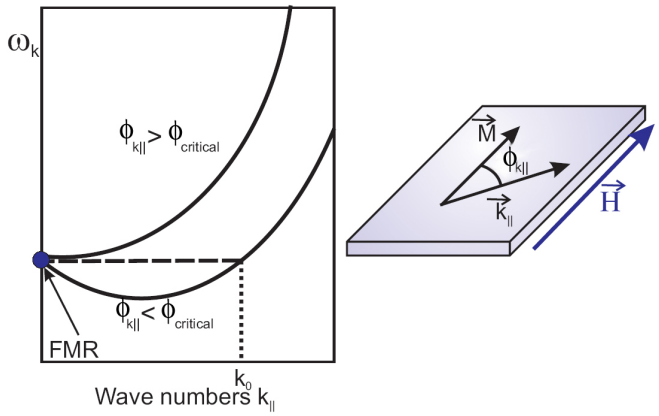


**Figure 6.5:** The in-plane spin-wave dispersion curve of an ultrathin film [1]

Contrary to the Gilbert contribution the frequency dependence of the linewidth due to two-magnon scattering is nonlinear. Its frequency dependency has been calculated by Arias and Mills [18, 22]. They have employed the Green's function formalism and defined a Green's function as:

$$S_{y,z}\left(\vec{k}_{\|},\vec{k'}_{\|},t\right)=i\frac{\theta(t)}{\hbar}\left\langle\left[m_y(\vec{k}_{\|},t),m_z^{\dagger}(\vec{k'}_{parallel},0)\right]\right\rangle \tag{6.18}$$

The operators are in the Heisenberg representation and z is the direction perpendicular to film plane. These authors derived the frequency dependence of the FMR linewidth due to the two-magnon scattering mechanism:

$$\Delta H_{pp}^{2mag}(\omega)=\Gamma arcsin\left(\sqrt{\frac{\sqrt{\omega^2+(\omega_0/2)^2}-\omega_0/2}{\sqrt{\omega^2+(\omega_0/2)^2}+\omega_0/2}}\right) \tag{6.19}$$

where $\omega_0$ is the resonance frequency corresponding to $\mu_0 M_{eff}$. $\Gamma$ represents the strength of the two-magnon scattering mechanism. For comparison matter in fig.6.6 the calculated frequency dependence of the FMR linewidth caused by different mechanisms is presented [1].

The author has used $\Gamma = 50mT$, $\mu_0 M_{eff} = 2.1T$,$g = 2.09$,$G = 6 \times 10^7 Hz$ for his calculations, and H is applied along the [100]-direction. $\Delta H(0)$ is the inhomogeneous broadening which will be discussed in the following section; it is considered frequency and angle independent. As can be deduced from these calculations the FMR linewidth broadening due to the Gilbert mechanism is a linear function of frequency, whereas the contribution caused by two-magnon scattering is nonlinear.

The two-magnon scattering requires the presence of scattering centers of the order of the spin-wave wavelength. This means that $\Gamma$ is not isotropic and that

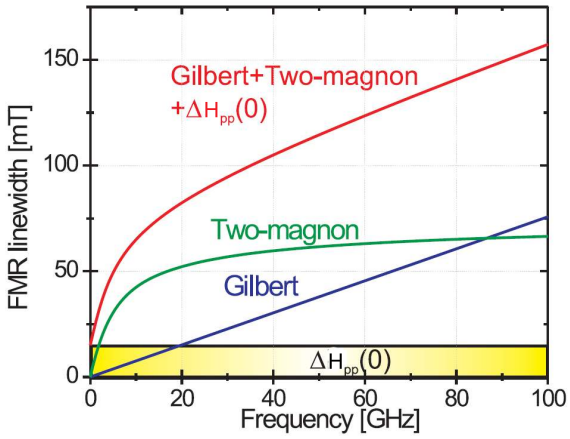


**Figure 6.6:** Calculated frequency dependence of the FMR linewidth for an ultrathin film with in-plane magnetization [1]

it depends on the crystallographic directions because the misfit dislocations in the crystal will be formed along particular direction(s) or in other words two-magnon scattering is angle dependent and depends on the direction of the network of misfit dislocations. In order to identify the angular dependence of two-magnon scattering, knowledge of the lattice structure is necessary. Note that in the case of GaMnAs films on GaAs which are grown by molecular beam epitaxy and can be assumed to be of high crystalline quality, the density of macroscopic defects responsible for this relaxation is expected to be negligible.

As it is shown in fig.6.6, the largest contribution of two magnon scattering occurs for low microwave frequencies (less than 10 GHz) and at higher frequencies the frequency dependence of the linewidth becomes linear again.

The two magnon scattering is efficient when the magnetization and the applied field are not aligned parallel. This occurs in the case of hard magnetic materials such as MnAs where the resonance field can be lower than the coercivity field, or in the case of intermediate orientations between the hard and easy axes; moreover it will become inefficient from a certain critical angle while approaching the out-of-plane directions [16]. Therefore to avoid the probable contributions of this process we have focused our studies on the measurements for the high symmetry axes of the sample.

The angular dependence due to two-magnon scattering for most cases should lead to a reduction of the linewidth with respect to the in-plane value. It will be shown that the results obtained in the GaMnAs samples show a quasi isotropic linewidth which indicates again that the two-magnon scattering contribution is small in our case.

## *6.2 Metals vs. Semiconductors*

In the semiconductors because of the strong spin orbit interactions one can expect higher values of the damping factor as compared to metallic systems. This feature is supposed to reduce also the coherence time of the spin polarised currents in these materials. While the former case can be desirable in the magnetization switching devices because of a faster switching, the latter process limits the interest of these materials for device applications. The transport (TMR and MR) measurements has already shown the possibility of injecting spin polarized currents in these materials with high (i.e. $\approx 80\%$ TMR in GaMnAs tri-layers) MR effects. Up to now only very few experimental and theoretical studies on the damping mechanisms in DMS materials have been published.

## *6.3 FMR broadening*

### 6.3.1 Inhomogeneous linewidth

The inhomogeneous, frequency independent linewidth can be further decomposed in three contributions, related to the crystalline imperfection of the film [23]:

$$\Delta H_{inhom} = \left|\frac{\delta H_r}{\delta \theta_H}\right| \cdot \Delta\theta_H + \left|\frac{\delta H_r}{\delta \phi_H}\right| \cdot \Delta\phi_H + \left|\frac{\delta H_r}{\delta H_{int}}\right| \cdot \Delta H_{int} \tag{6.20}$$

These three terms were introduced to take into account a slight mosaic structure of the metallic thin films defined by the polar angles $(\theta, \phi)$ and their distributions $(\Delta\theta, \Delta\phi)$- the first two terms in eq.6.20- and a distribution of the internal anisotropy fields Hint - the last term of eq.6.20. In the case of high quality epitaxial III-V films obtained by MBE growth like GaMnAs only the third component ($\Delta H_{int}$) is expected to play an important role. For most materials the inhomogeneous part is strongly sample dependent and can be smaller but also much larger than the intrinsic linewidth. In GaMnAs total linewidths at X-band between 100Oe and 1000Oe have been encountered which already indicates the importance of inhomogeneous broadening. The homogeneous linewidth will only depend on the intrinsic sample properties. This approach supposes that the inhomogeneous linewidth is frequency independent and the homogenous linewidth linear dependent on the frequency, two assumptions generally valid for high symmetry orientations of the applied field with a magnetization parallel to the magnetic field.

### 6.3.2 Homogeneous linewidth; Gilbert damping factor

The intrinsic magnetization relaxation can be described by one parameter, the Gilbert damping coefficient $\alpha$, which is defined by the LLG equation of motion for the magnetization:

$$\frac{1}{\gamma} \cdot \frac{d\vec{M}}{dt} = -\left[\vec{M} \times \vec{H}_{eff}\right] + \frac{\alpha}{\gamma}\left[\vec{M} \times \frac{d\vec{s}}{dt}\right] \tag{6.21}$$

with M the magnetization, $H_{eff}$ the effective magnetic field, $\alpha$ the damping factor, $\gamma$ the gyromagnetic ratio and $s$ the unit vector parallel to M.

The damping factor $\alpha$ is generally assumed to be a scalar quantity [4, 24]. It is defined for small angle precession relaxation such as occurring in FMR spectroscopy. This parameter can be experimentally determined by FMR spectroscopy from the variation of the uniform mode linewidth $\Delta H_{pp}$ with the microwave frequency. It is then expressed in the following form:

$$\Delta H_{pp} = \Delta H_{inhom} + \Delta H_{hom} = \Delta H_{inhom} + \frac{2}{\sqrt{3}} \cdot \frac{G}{\gamma^2 \cdot M} \cdot \omega \tag{6.22}$$

With $\Delta H_{pp}$ the first derivative peak-to-peak linewidth of the uniform mode of Lorentzian lineshape, $\omega$ the angular microwave frequency and G the Gilbert damping factor from which the magnetization independent damping factor $\alpha$ can be deduced as $\alpha = G/\gamma M$.

It should be underlined that in diluted magnetic semiconductor (DMS) materials like GaMnAs the damping parameter is not only determined by the sample composition $x_{Mn}$ [25]. It is expected to depend as well on:

1. the magnetic compensation which will vary with the growth conditions
2. the carrier concentration which is influenced by the presence of native donor defects like arsenic antisite defects or Mn interstitial ions [26]
3. the valence-band structure, sensitive to the strain in the film

Due to the high out-of-plane and in-plane anisotropy of the magnetic parameters [27] which further vary with the applied field and the temperature a rather complex situation with an anisotropic and temperature dependent damping factor can be expected in GaMnAs.

### *6.4 Linewidth study of different GaMnAs systems*

We have investigated this parameter in the GaMnAs systems studied in previous chapters, i.e. films with different strains, films with different hole concentrations and highly doped films.

Whereas the Gilbert damping factor has been determined for many metallic FM systems [24] only two experimental studies of its value in GaMnAs thin films has been published up to now [25, 28]. In one of these studies the inhomogeneous broadened linewidth has been assumed to be negligible and in the second one the

samples with rather lower quality (considering the reported $T_C$ and the measured spectra) have been used.

The GaMnAs/GaAs samples which were studied by us showed much smaller total linewidths than the one's of the previous cases. As explained above, in order to determine the $\alpha$ factor FMR measurements at at least two different microwave frequencies have to be done.

In our case FMR measurements were performed at 9.4 and 34.3 GHz (X-band and Q-band respectively) under standard conditions: 1 mW microwave power and 100 KHz field modulation. The angular variation of the FMR spectra was measured in the two rotation planes (110) and (001). The peak-to peak linewidth of the first derivative spectra were obtained from a lineshape simulation. The value of the static magnetization M(T) had been determined previously by a commercial superconducting quantum interference device (SQUID) magnetometer.

### 6.4.1 Reference $Ga_{0.93}Mn_{0.07}As$ sample

The reference sample is a compressively strained layer grown on a GaAs buffer layer; it consists of a $Ga_{0.93}Mn_{0.07}As$ layer of 50nm thickness has been grown at $250°C$ by low temperature molecular beam epitaxy (LTMBE) on semi-insulating (100) GaAs substrates. A thin GaAs buffer layer has been grown before the deposition of the magnetic layer. After the growth the sample was annealed at $250°C$ for 1h under air or nitrogen gas flow. The Curie temperature was 157K. Based on conductivity measurements the hole concentration is estimated in the $10^{20}cm^{-3}$ range. The peak-to-peak linewidth of the first derivative uniform mode spectra have been strongly reduced by the thermal annealing; in the non annealed sample the X-band linewidth was highly anisotropic with values between 150Oe and 500Oe at T=4K. After annealing it is reduced to an quasi isotropic average value of 70Oe at X-band.

In fig. 6.7 the typical low temperature FMR spectra at X-band (a) and Q-band (b) frequencies for the hard [001] axis orientation of the applied magnetic field. The spectra are characterized by excellent signal to noise ratios and well defined lineshapes. We see that at both frequencies the line-shape is close to a Lorentzian (compare the two Lorentzian and dispersion/absorption fits to the FMR spectrum in panel b). In addition to the main mode one low intensity spin wave resonance is observed.

The linewidth at X-band (fig. 6.8) is of the order of 50Oe to 75Oe with a weak orientation and temperature dependence. Above T>130K, close to the critical temperature, the linewidth increase strongly.

At Q-band we observe a systematic increase by a factor of two of the total linewidth (fig.6.9) with an increased temperature and orientation dependence. As generally observed in GaMnAs, the easy axis orientation gives rise to the lowest

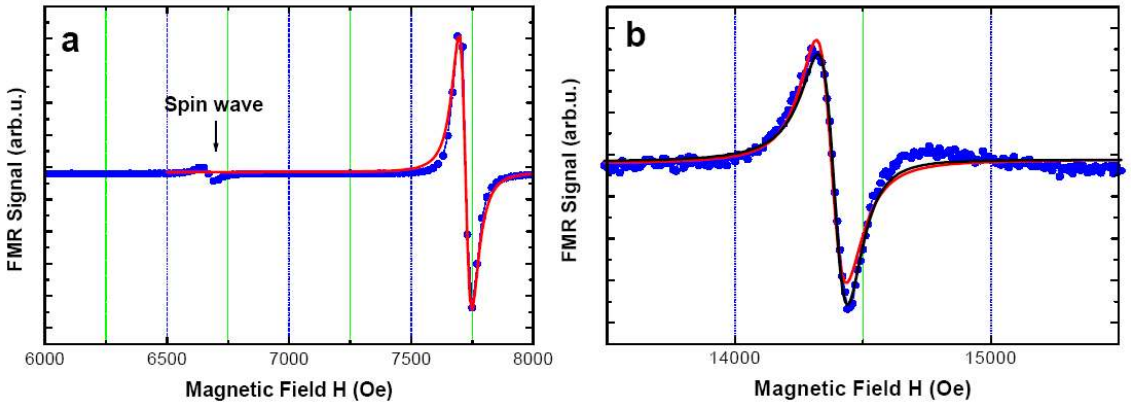


**Figure 6.7:** (a)X-band and (b) Q-band FMR spectrum of the GaMnAs/GaAs film taken at T=20K and for H ∥ [001]; the peak-to-peak linewidth is 60Oe and 117Oe respectively. The experimental spectrum is shown by circles and the Lorentzian lineshape simulation by a red line. In panel.b a simulated spectrum with dispersion/absorption lineshape is fitted (presented by black line) to the data as well.

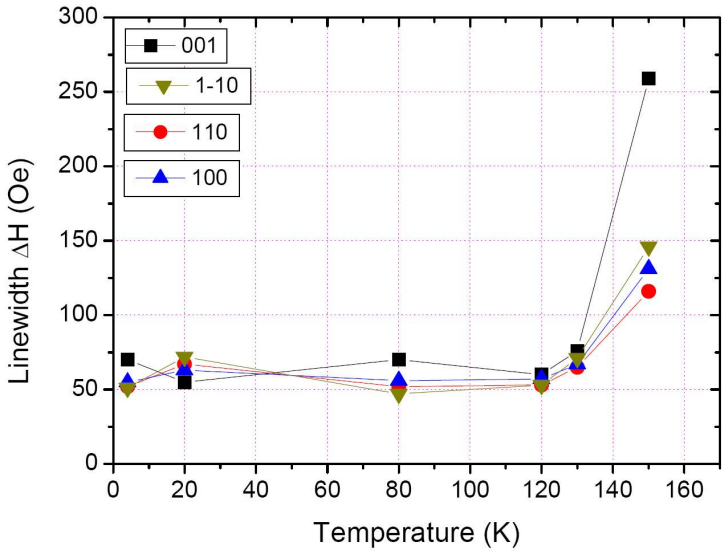


**Figure 6.8:** X-band peak-to-peak line widths for the GaMnAs/GaAs film for the four main field orientations squares, H∥[001] black squares, H∥[1-10] olive lower triangles, H∥[110] red circles, H∥[100] blue upper triangles.

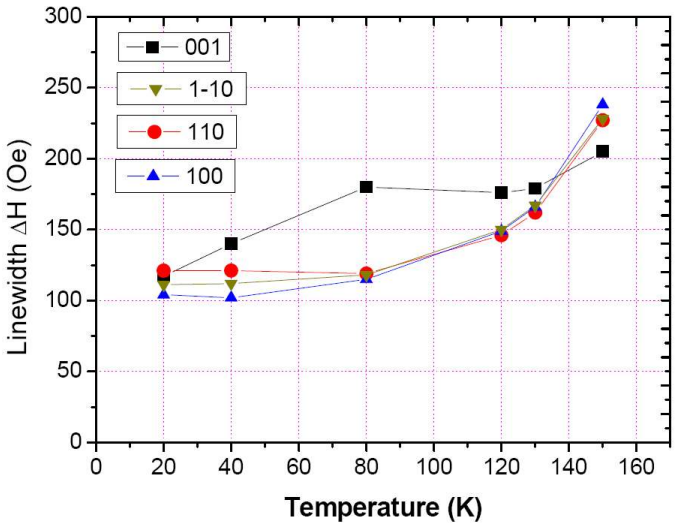


**Figure 6.9:** Q-band peak-to-peak line widths for the GaMnAs/GaAs film for the four main field orientations: H||[001] black squares, H||[1-10] olive lower triangles, H||[110] red circles, H||[100] blue upper triangles.

linewidth. At X-band the line-shape is perfectly Lorentzian (fig. 6.7). These linewidth are among the smallest ever reported for GaMnAs thin films, which reflects the high crystalline and magnetic quality of the film.

To determine the damping factor $\alpha$ we have plotted the frequency dependence of the linewidth for the different orientations and at various temperatures. An example is given in fig. 6.10 for T=80K; this allows us to determine the inhomogeneous linewidth obtained from a linear extrapolation to zero frequency and the damping factor from the slope. The inhomogeneous linewidth at T=80K is of the order of 30 Oe, i.e. 50% of the total linewidth at X-band. This shows that the approximation $\Delta H_{pp/inhom} << \Delta H_{pp/hom}$ which had been previously used [25] to deduce the damping factor from a single (X-band) frequency measurement is not fulfilled here.

The temperature dependence of the inhomogeneous linewidth is shown in fig. 6.11. Similar trends as for the total linewidth in the non annealed films are observed: the linewidth is high at the lowest temperatures, decreases with increasing temperatures up to 120K and increases again close to $T_C$.

From the slope of the linewidth variation with microwave frequency we obtain the damping factor $\alpha$ (fig.6.12). Its high temperature value is of the order of 0.010 but we observe a systematic, linear variation with the temperature and a factor two difference between the easy axis orientation [100] and the hard axis orientation [001].

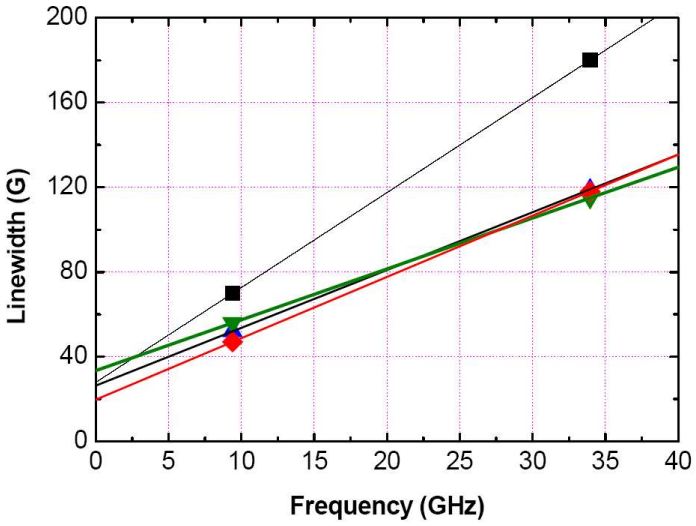


**Figure 6.10:** Peak-to-peak linewidth at 9GHz and 35GHz for the GaMnAs/GaAs film; T=80K and H‖[001] black squares, H‖[1-10] olive lower triangles, H‖[110] red circles, H‖[100] blue upper triangles.

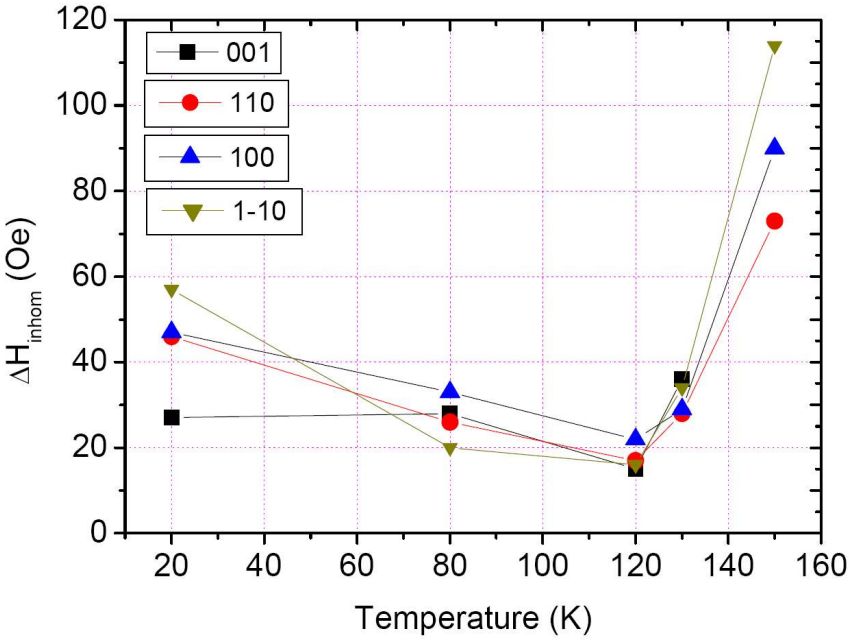


**Figure 6.11:** damping factor $\alpha$ as a function of temperature and magnetic field orientation; H‖[001] black squares, H‖[1-10] olive triangles, H‖[110] blue triangles, H‖[100] red circles

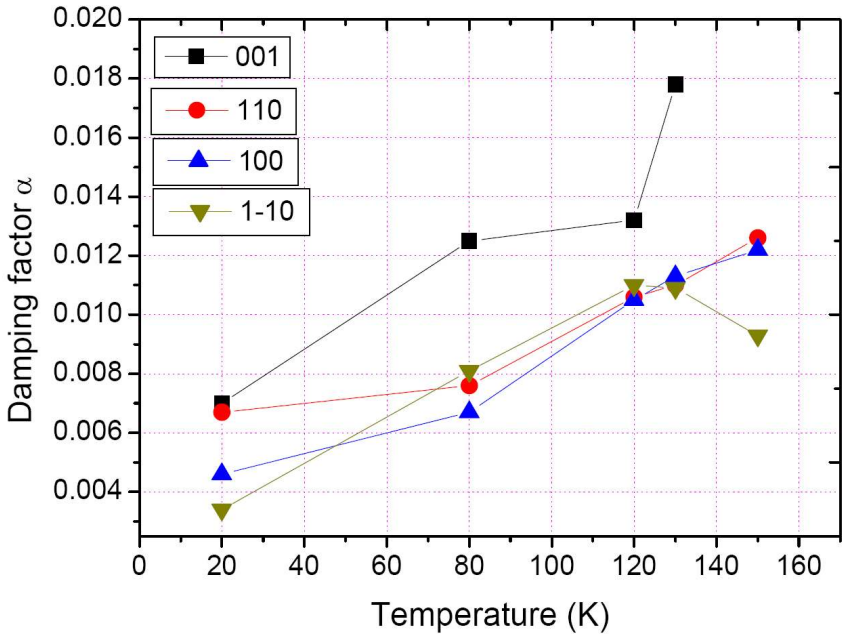


**Figure 6.12:** damping factor $\alpha$ as a function of temperature and magnetic field orientation; H‖[001] black squares, H‖[1-10] olive triangles, H‖[110] blue triangles, H‖[100] red circles

#### *6.4.1.1 discussion*

The numerical values of the $\alpha$-damping factor for this sample are significantly smaller than the one's predicted by the MF calculation [25] and the one's reported by [28]. The minimum value of the intrinsic damping for was found for the in plane orientation [1-10] of the sample.

### 6.4.2 Damping factor as a function of substrate induced strain

The second sample, a 50 nm thick $Ga_{0.93}Mn_{0.07}As$ layer on (100) $Ga_{0.902}In_{0.098}As$ has been grown under very similar conditions as the reference one; the main difference is a graded GaInAs buffer layer to avoid the formation of dislocations in the GaMnAs layer; for more details see ref. [29] and section 3.2.2. In this tensile strained layer the easy axis of magnetization is along the out-of-plane [001] direction. The layer has equally been annealed in order to reduce the electrical and magnetic compensation, to homogenize the layers and to increase the Curie temperature to $T_C$=130K.

Once again, based on the conductivity measurements the hole concentration is estimated in the $10^{20}cm^{-3}$ range. Similar measurements, as the reference sample (section 6.4.1), have been performed on this layer. In tensile strained GaMnAs films

the easy axis of magnetization ([001]) coincides with the strong uniaxial second order anisotropy direction. As the anisotropy field is higher than the resonance field at X-band no FMR spectrum can be observed at temperatures below T=80K for the easy axis orientation H‖ [001. For the other three orientations the resonances can be observed at X-band in the whole temperature range 4K to $T_C$. Due to the strong temperature dependence of the anisotropy constants and the parallel decrease of the internal anisotropy fields the easy axis resonance becomes observable at X-band for temperatures above 80K. In the films on GaInAs much higher linewidth are encountered than in the films on GaAs; the values are up to ten times higher indicating a strong inhomogeneity in this film. A second low field resonance is systematically observed at X-band and Q-band; it is equally attributed to a spin wave resonance.

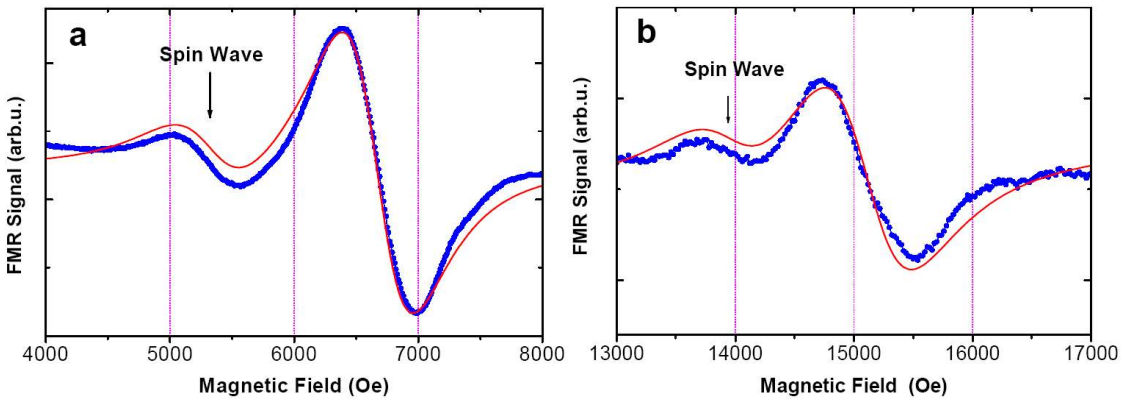


**Figure 6.13:** a)X-band and b)Q-band FMR spectra for the GaMnAs/GaInAs film at 25K and H‖[110] (hard axis); the low field spin wave resonance is of high intensity in this case.

Figures6.13.a,b show typical FMR spectra at X- and Q-band respectively. At both frequencies the line-shape can no longer be simulated by a Lorentzian but has changed into a Gaussian line-shape.

Contrary to the first case of GaMnAs/GaAs the X-band linewidth varies monotonously in the whole temperature region (fig. 6.14 ). We observe a linewidth of ≈600Oe at T=4K, which decreases only slowly with temperature; the linewidth becomes minimal in the 100 K to 140K range.

At low temperature the Q-band linewidth vary strongly with the orientation of the applied field with values between 500Oe and 700Oe. The lowest value is observed for the easy axis orientation. They decrease as at X-band only slowly with increasing temperature and increase once again when approaching the Curie temperature. At Q-band the easy axis FMR spectrum is observable in the whole temperature range.

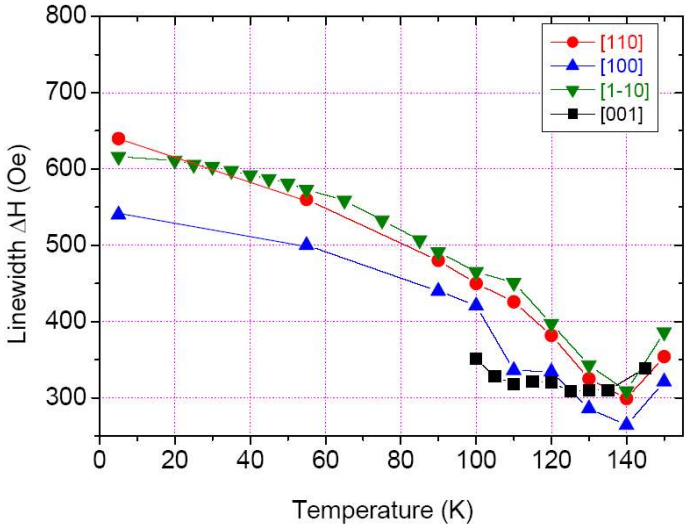


**Figure 6.14:** GaMnAs/GaInAs: X-band FMR linewidth as a function of temperature for the four orientations: H||[001] black squares, H||[1-10] olive lower triangles, H||[110] red circles, H||[100] blue upper triangles; the easy axis FMR spectrum is not observable below T=100K

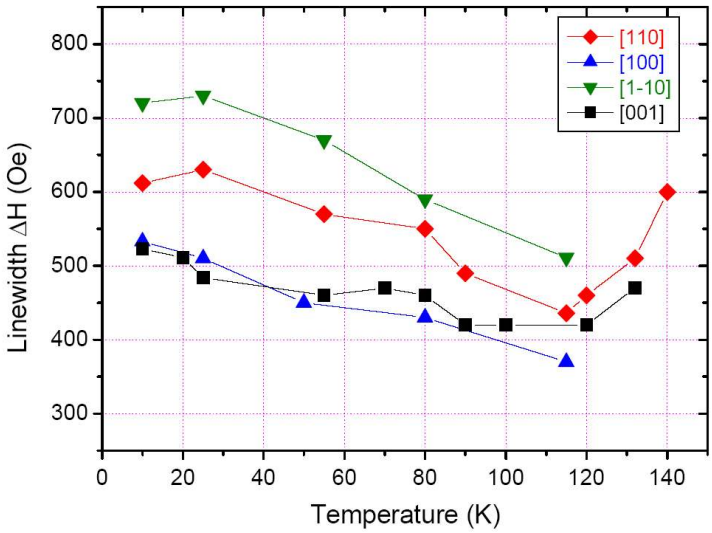


**Figure 6.15:** GaMnAs/GaInAs : Q-band FMR linewidth as a function of temperature for the four orientations : H||[001] black squares, H||[1-10] olive lower triangles, H||[110] red circles, H||[100] blue upper triangles

For this sample we observe especially at Q-band a systematic difference between the cubic axis linewidth and the one for the in-plane [110] and [1-10] field orientations (fig. 6.15 ). The most surprising observation is that for temperatures below T<100K the linewidth for H‖[100] and H‖[110] are comparable at X-band and Q-band and thus an analysis in the simple model exposed above is not possible. We attribute this to much higher crystallographic/magnetic inhomogeneities, which mask the homogeneous linewidth. The origin of the strong inhomogeneity is still unclear. The only orientation for which in the whole temperature range a systematic increase in the linewidth between X-and Q-band is observed is the H‖[1-10] orientation. We have thus analyzed this variation (fig. 6.16) according to eq.6.21.

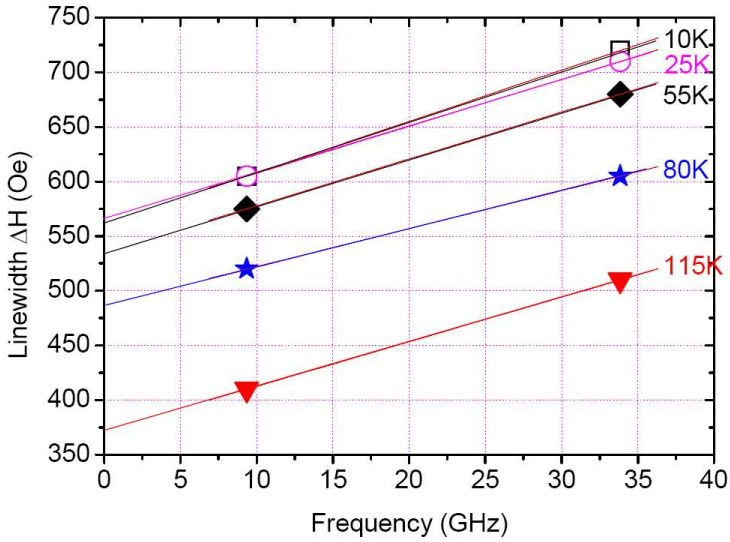


**Figure 6.16:** GaMnAs/GaInAs : FMR linewidth as a function of microwave frequency for H‖[1-10] at different temperatures; T=10K (squares), T=25K (circles) ,T=55K(spades), T=80K(stars), T=115K (triangles)

In spite of important differences in the linewidth the slope varies only weakly which indicates that the inhomogeneous linewidth is very temperature dependent and decreases monotonously with increasing temperature from 570Oe to 350Oe.

In the high temperature range (T≥100K) the easy axis orientation could also be analyzed (fig. 6.17). The inhomogeneous linewidth are lower than for the hard axis orientation at the same temperatures and are in the 300Oe range (fig.6.18). The inhomogeneous linewidth at 9Ghz is in the 50Oe range which is close to the values determined in the first case of GaMnAs/GaAs.

From the slope we obtain the damping factor which for the hard axis orientation is =0.010 in the whole temperature range (fig.6.19). This value is comparable to the one measured for the GaMnAs/GaAs film for H‖[110]. The damping factor for the

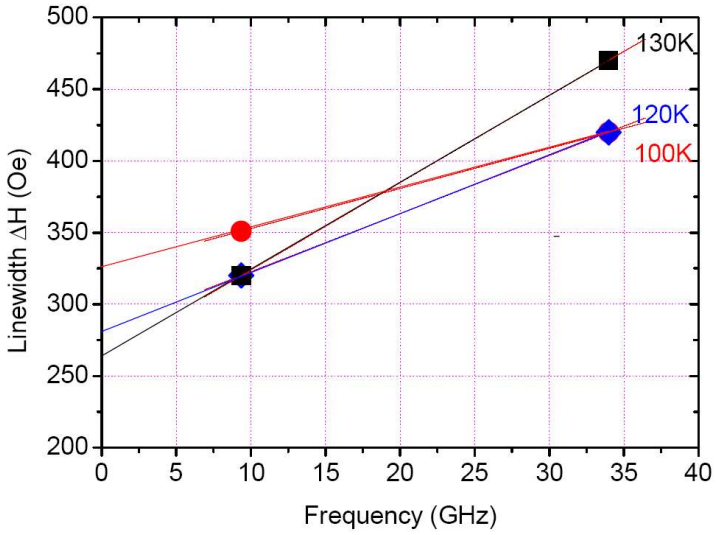


**Figure 6.17:** GaMnAs/GaInAs: FMR linewidth as a function of microwave frequency for H‖[001] (easy axis) at different temperatures; T=100K (red circles), T=120K (blue spades),T=130K(black squres);Q-band.

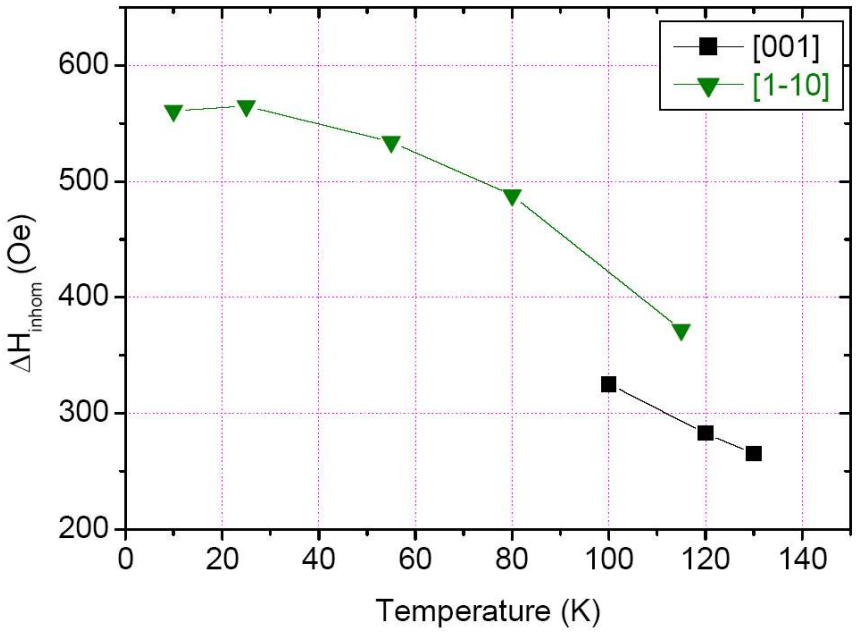


**Figure 6.18:** GaMnAs/GaInAs inhomogeneous linewidth as a function of temperature for two orientations of the applied field: H‖[001] squares and H‖[1$\bar{1}$0] lower triangles.

easy axis orientation is lower but increases close to $T_C$ as in the previous case.

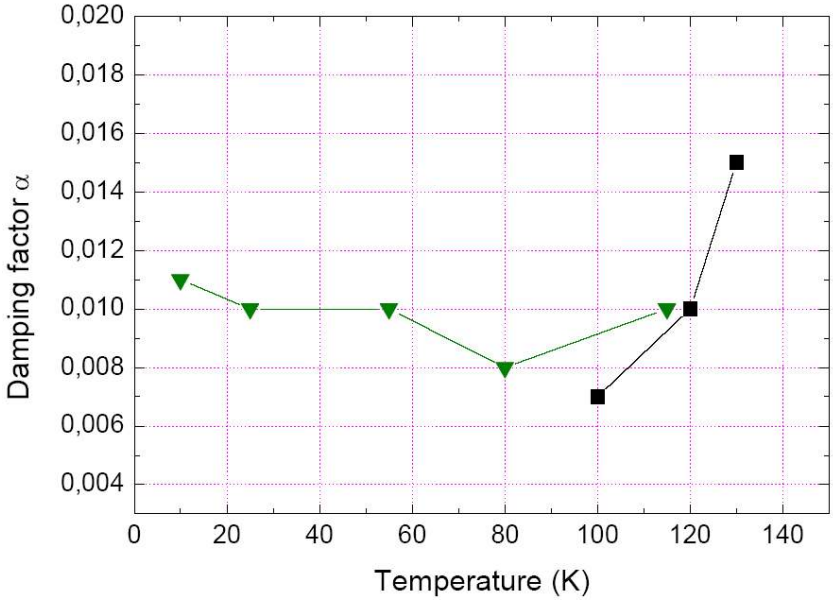


**Figure 6.19:** GaMnAs/GaInAs damping factor $\alpha$ as a function of temperature and magnetic field orientation; H||[001] squares, H||[1$\bar{1}$0] lower triangles.

### 6.4.2.1 Discussion

An estimation of the FMR damping factor has been made within a model of localized Mn spins coupled by p-d kinetic exchange with the itinerant-spin of holes treated by the 6-band Kohn-Luttnger Hamiltonian [25]. Note, that they take for the effective kinetic exchange field the value in the mean-field approximation, i.e. $H_{eff}$=JN<S>, so that their calculation are made within the RPA approximation. RPA calculations of have been made by Heinrich et al. [5] and has been used by Tserkovnyak et al. for numerical applications to the case of GaMnAs [26]. Both models however, are phenomenological and include one adjustable parameter: the quasi-particle lifetime $\Gamma$ for the holes in [25] and the spin-flip relaxation $T_2$ in [26]. These models do not take into account neither multi-magnon scattering nor any damping beyond the RPA. However, it has been argued elsewhere [30] that in diluted magnetic semiconductors such affects are important only at high temperature (i.e. at T>$T_c$). In particular, the increase of $\alpha$ in the vicinity of $T_C$ may be attributed to such effects that are beyond the scope of the models of references [25] and [5]. At low temperatures T«$T_C$ however, where the corrections to the RPA are expected to be negligible, the models of [25], [5] and [26] provide us with a numerical value of $\alpha$ in agreement with our experiments if we introduce reasonable values

of these parameters. For GaMnAs films with metallic conductivity, Mn concentrations of x=0.05 and hole concentrations of 0.5 $nm^{-3}$($5{\cdot}10^{20}cm^{-3}$) Sinova et al [25] predict an isotropic low temperature damping factor $\alpha$ between 0.02 and 0.03 depending on the quasi-particle life time broadening. Tserkovnyak et al [26] deduced an isotropic damping factor for a typical GaMnAs film with 5%Mn doping and full hole polarization of $\alpha \approx 0.01$.

The predicted values are rather close to the experimental values found in this study. Our results show further that the damping factor is indeed anisotropic in GaMnAs with a lowest value for the easy axis orientation and an increase of up to a factor of two for the hardest axis orientation.

Additional material related parameters are expected to further influence the damping factor. As the spin flip relaxation times will depend on the sample properties and in particular the presence of scattering centers we will not expect to find a unique damping factor even for GaMnAs/GaAs samples with the Mn composition x. More likely, different damping factors are expected to be found in real films and their values might be used to assess the film quality. In this sense the GaMnAs/GaAs film studied here is of course "better" than the one on GaInAs in line with the strong difference in the sample inhomogeneities.

The inhomogeneous linewidth originates from spatial inhomogeneities in the local magnetic anisotropy fields and inhomogeneities in the local exchange interactions. Given the particular growth conditions of these films, low temperature MBE, inhomogeneities will not expected to be negligible in these materials. If we had analyzed our X-band results of the GaMnAs/GaAs film in the spirit of [25], i.e. assuming a negligible inhomogeneous linewidth - ($\Delta H_{inhom}$=0)- , we would have obtained artificially increased damping factors. A further contribution might be expected from the intrinsic disorder in these films: as GaMnAs is a diluted magnetic semiconductor with random distribution of the Mn ions, this disorder will even for crystallographically perfect crystals give some importance to this term.

In the two previous publications on this subject higher values of the damping factor have been found. Matsuda et al [28] found damping factors between 0.02 and 0.06 in the T=10K to T=20K temperature range. They observed the same trends as we did concerning the anisotropy and temperature dependence of $\alpha$ : the lowest damping factor is seen for the easy axis orientation and its values increases with increasing temperatures. The films of their study were however significantly different: the Mn doping concentration was lower, x=0.03 and thus the hole concentration was equally lower and the critical temperature of the annealed film was only T=80K. The anisotropy in the inhomogeneous linewidth at T=20K was equally much higher, varying between 30Oe for the easy axis to 250Oe for the hardest axis [110]. In a second study Sinova et al [25] have measured a GaMnAs/GaAs sample with similar composition (x= 0.08) as the one studied here. Their damping factor for the annealed sample characterized by a critical temperature TC=130K was of the order

of =0.025 with only a slight temperature dependence between 4K and 80K and an increase close to TC. However these measurements were only done at one (X-band) microwave frequency and as explained above, the real value of $\alpha$ can be expected to be lower.

The damping factor $\alpha$ plays also an important role in the critical currents required to switch the magnetization in GaMnAs trilayers [25]. As this current is directly proportional to $\alpha$ it is important to minimize its value. Sinova et al. have estimated the critical current for realistic GaMnAs layers: based on values of $\alpha$ = 0.02, they estimated the critical current density to $J_C$=$10^5$Acm$^-$2. As the damping factor for the easy axis orientation at low temperature can even be lower,$alha$ = 0.003 as measured here, still smaller critical currents can be expected to be sufficient in high quality GaMnAs thin films.

Finally let us remark that the damping factor measured from the FMR linewidth is by definition different from the damping factor involved in the domain wall motion [31, 32].They can however be related by a proportionality factor. In general the damping factor of the domain wall motion is substantially higher than the one derived from FMR measurements..

### 6.4.3 Damping factor as a function of Mn concentration (x>0.1)

The magnetic scattering centers are ferromagnetic films are on the sources of damping of the magnetization. Thus the concentration of the manganese as the magnetic centers, in principle should modify the damping factor. In order to study the influences of this parameter on the damping factor we applied the FMR measurements via two different (9 and 35GHz) micro-wave frequencies on the heavily doped samples. The detailed magnetic and transport properties of the samples are mentioned in chapter 5 and the experimental details are mentioned in previous section. The samples contain the total magnetic moment concentration of x=0.15, 0.17 and 0.21%. The FMR studies are compared in both bands for different orientations of applied field with respect to the crystal high symetry axes as a function of temperature.

Fig.6.20 presents the total FMR linewidth of the sample with 15% of total manganese as a function of temperature for X and Q-band measurements for magnetic field applied along [001] (hard axis) and [110] (intermediate axis) axes. The curves show a quasi-equal $\Delta$H for low temperatures; where for intermediate tmperatures the values due to the two bands separate slightly. Again as the case was shown in section 6.4.1, the linewith increases rapidly close to $T_C$.

The linewidth variation as a function of the orientation of applied field with respect to the film orientation for its out-of-plane rotation is shown in fig.6.21 in X-band frequency measurements. The linewith of the spectra of the GaMnAs with x=0.07 from previous section is inserted as a comparison. Note the progressive in-

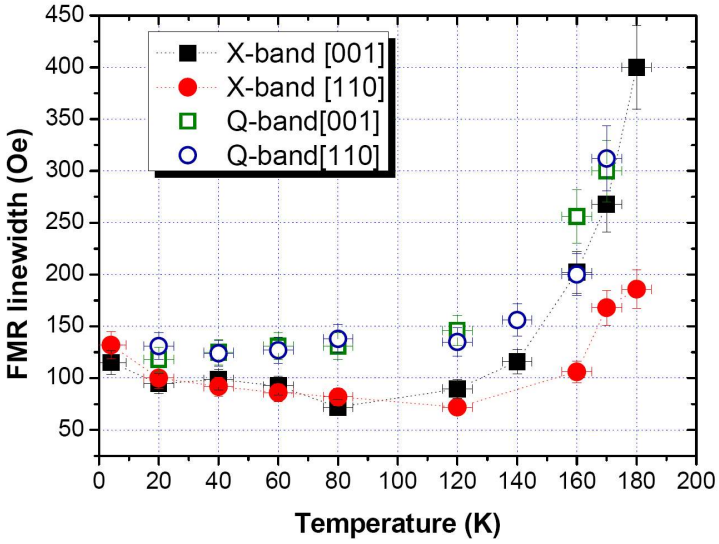


**Figure 6.20:** FMR total linewith of the GaMnAs sample with x=0.15 as a function of temperature for applied field direction parallel to [001] (squares) and [110] (circles) in two applied microwave frequency measurements

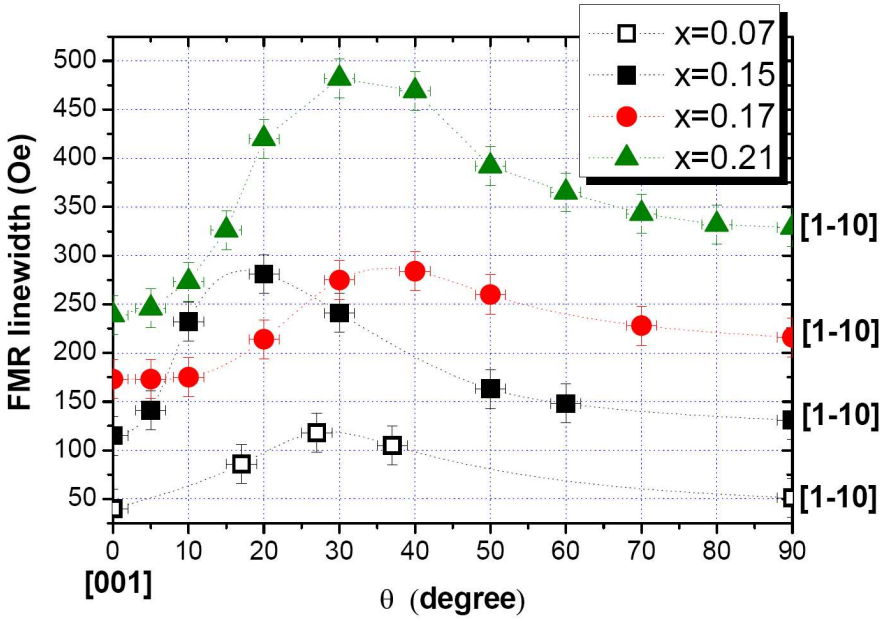


**Figure 6.21:** total FMR linewidth as a function of rotation of applied field in [110] plane for different concentration of Mn.

crease of the linewith as a function of total manganese concentration. The linewidths present the almost same behavior as a function of angular variation of the applied field; while for H||high symmetry axes the linewidth have their minima values, they increase as applied field is rotated away from these axes.

As it is explained in detail in section 6.3, The total FMR linewidth can be separated into four parts (field-dragging, mosaicity, two-magnon scattering and the gilbert broadening). Note except for the still more complicated case of damping contribution all other three vanish for the high symmetry axes. For these samples as the fig.6.21 presents, the difference of the linewidth along the [001] and [110] is small. This is an indication that in our epitaxied samples the two magnon scattering broadening process is negligible. This fact provides us to decompose our resulted linewidths into two frequency dependent and independent contributions and due to the linear dependency of the damping component with frequency be able to discuss the issue in more details. However, in general all frequency independent process stronger for field applied along intermediate axes where the magnetization varies strongly, magnetization and the applied field have the largest separation and the mosaicity become important because of the well separation of the local resonance fields of the mosaic-like regions.

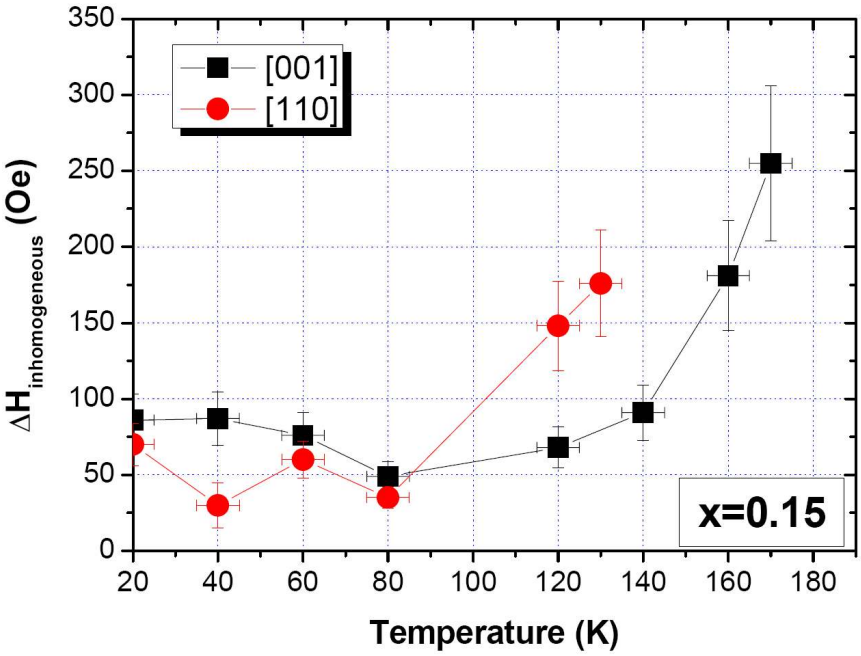


**Figure 6.22:** Inhomogeneous component of the total FMR linewidth for applied field along [001] and [110] axes of the GaMnAs with x=0.15 as a function of temperature.

The measured inhomogeneity contribution to the linewidth ($\Delta H_{inh}$) for sample

with x=0.15 is shown in fig.6.22. Along both hard and intermediate axes its value is almost the same and merely fix up to T≈100K from where it starts to increase abruptly. This feature is almost the same for all samples in this series and the previous one. As a function of total Mn concentration the ($\Delta H_{inh}$) do not present a considerable variation. One may just notice a very slight one which is retained as a function of temperature (fig.6.23). In addition to all other parameters we have already measured in these samples this feature is considered to another evidence to indicate the structural quality of these samples. Comparing $\Delta H_{inh}$ for these samples which is in the order of 70 to 90Oe for T=20K with the reference sample GaMnAs with x=0.07 who presents $\Delta H_{inh}$ ≈45Oe at this temperature reveals this aspect. Note that the increase in inhomogeneous linewidth for the sample with x=0.21 is even less than the increase in the total Mn concentration compared to the sample with x=0.15. Our predicted results about the lattice parameter variation in sample x=0.17 can be once more obsreved from another aspect via comparing its $\Delta H_{inh}$ with other samples.

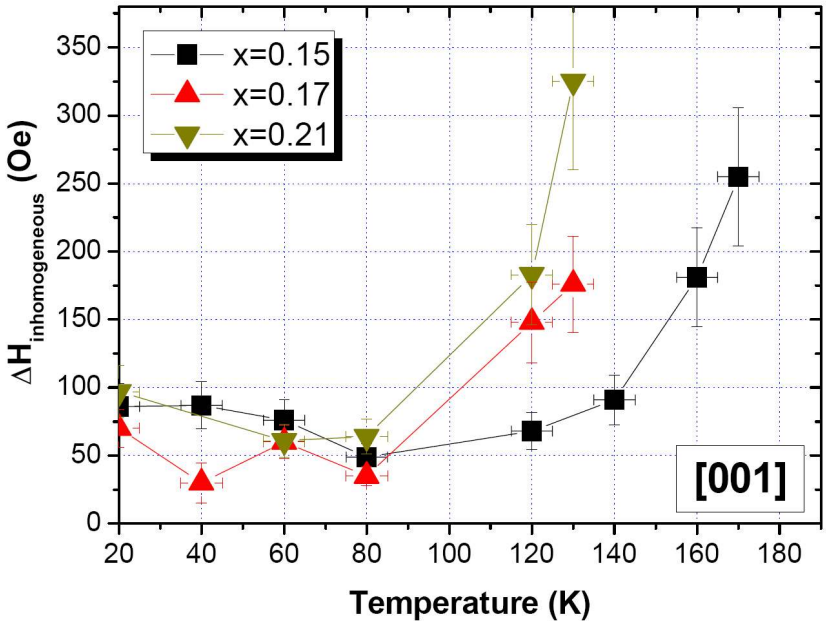


**Figure 6.23:** $\Delta H_{inh}$ as a function of temperature for diffrent total Mn concentration measured along [001] axis of the films.

The linewidth decrease slowly by as temperature increase from 20K to 80K and then strat to increase up to $T_C$.

The damping factor $\alpha$ measured for heavily doped GaMnAs samples as a function of temperature is shown in fig.6.24.

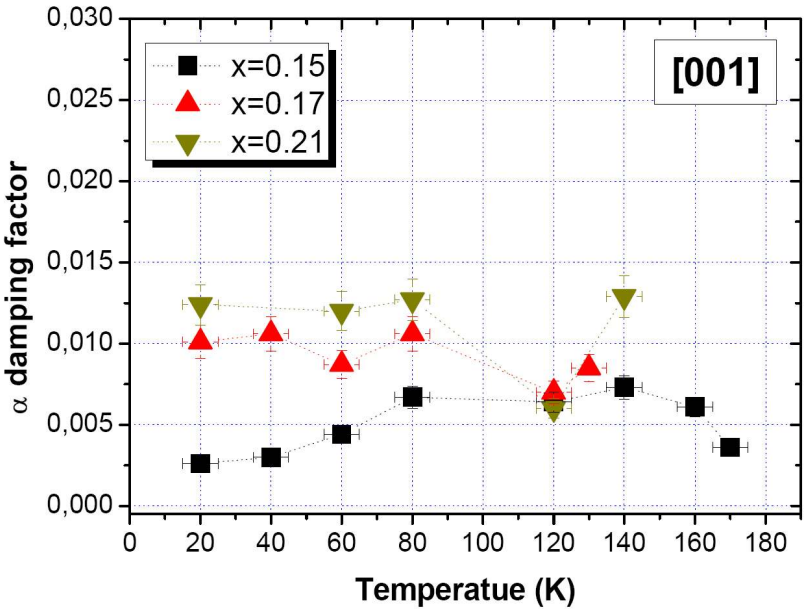


**Figure 6.24:** $\alpha$-damping factor as a function of temperature along the [001] hard axis for GaMnAs samples with different indicated Mn concentrations.

As one deduces immediately, The damping factor along [001] is increased progressively with the total manganese concentration. In this step we would like to remind the reader about the magnetic properties of these samples. In section 5.6.1 we have shown that the reason for which the Curie temperature has not increased considerably, with the enhancement of the Mn concentration is lied in the definition of the effective x value (the concentration of magnetically active manganese ions) which was almost fix for all three samples in the series. This is the indication of a progressive compensating process as a function of Mn concentration (x). The compensation of the manganese ions although passivate their magnetic contribution to the ferromagnetic order but it does not annihilate them. The Mn magnetic moments are present and their contribution to the relaxation process via dipole-dipole interaction persists.

Nevertheless, as the transport, g-factor and magnetization measurements reveal the hole concentration and the relevant carrier polarization are expected to vary from one sample to other. Comparing the results with the reference sample shows that the damping factor in sample with x=0.15 at T=20K (=0.003) is less than the one some the same conditions in reference sample (=0.0088) by a factor 3. This reduction, despite the increase in total Mn concentration can be explained by the simultaneous reduction of spin-orbit coupling (predicted by measured g-factor value g=2.00) for this sample. For x=0.17 the damping factor is very close to the x=0.07

one (=0.010), for this sample there is a competition between the Mn concentrations and the carrier polarizations (spin-orbit) which is reduced compared to the x=0.07 sample.

$\alpha$ factor retains more or less its fix value up to temperatures close to $T_C$. The same measurements and results for the [110] axis of GaMnAs sample is mentioned in fig.6.25.

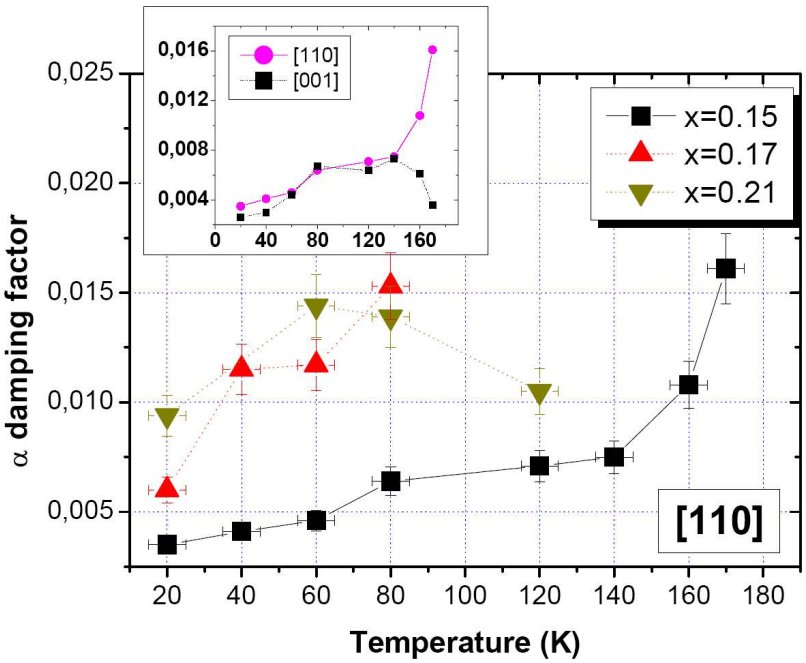


**Figure 6.25:** $\alpha$-damping factor as a function of temperature along the [110] inplane axis for GaMnAs samples with different indicated Mn concentrations. Inset: the damping factor as a function of temperature measured along [001] and [110] axes in GaMnAs with x=0.15.

The damping factors of the samples have kept their respective order; they increase as a function of doping level. Note that the same a the case along [001] axis here the samples with x=0.17 and x=0.21 presents close values in all investigated temperatures. The damping factors related to two higher samples are reduced by a factor 2/3 at T=20K. This case in which the damping factor along hard axis is higher than the one along easier axes is contradictory to what is measured for the case of the reference sample in previous section (6.4.3) but it is well consistent with the reported anisotropic $\alpha$ for Fe and Sm thin layers [24]. This case is explained straightforward by Farle: The magnetization precessing around the easy axis is more viscously damped, since it has to move into an unfavorable hard direction. For the magnetic field along the hard axis M precesses toward the easy direction and is less damped.

This feature changes as function of temperature. The sample with x=0.21 the same as the one with x=0.15 do not show any considerable variation of damping factor value along to axes.The inset of fig.6.25 compares the damping factors for sample with x=0.15 along two high symmetry axes. The respective damping values are almost the same until T≈140K. This feature can be considered as a limit between the previously studied reference sample and the the other highly doped sample in which the higher damping factor changes from easy to hard axes of magnetization. For the x=0.17 sample, the damping factor along in-plane [110] continues to increase and from T≈60K its case is the same as the reference sample. In order to more understand the situation we like to turn the reader's attention toward the second evidence of the anisotropic behavior of damping factor. Beside the fact that the magnitude of the $\alpha$ factor in axis-dependent, one can observe from figs.6.12 (for reference sample), 6.24 and 6.25 that the these factors present different temperature dependencies. One deduces that while the $\alpha$ along an axis in each sample tends to increase as the temperature approaches $T_C$, the other one tends to slightly decrease in this regime. Once more this feature, reminds one of the theoretical approach that Sinova et al. applied for damping factor calculation in 2004 [25]. They calculated $\alpha$ as a superposition of intra and inter-band spin-orbit interaction. Note that in their calculation as one component decreases with temperature enhancement the other increases.

Although the nature of damping factor and the models trying to explain this factor in ferromagnetic systems is well complicated, such quasi-systematic measurements may result in the elucidation of different parameters affecting this phenomenological factor and the way they affect it. Thus in this essay we tried not to limit the research to determine the corresponding $\alpha$-factor value of each series, but also try to attribute at least a qualitative model supporting their variation as a function of these parameters. The results that we presented up to this section together with the detailed magnetic properties of each sample enables us to nearly separate the measured samples in two categories.

1. **The reference sample** (x=0.07) with lower Mn concentration but with a considerably high hole concentration which indicates the dominant carrier contributed spin-orbit relaxation process

2. **The heavily doped samples** (x=0.15 and 0.21) with higher Mn concentration and lower hole polarization which results in the domination of dipole-dipole relaxation process.

It worth noting that in both mentioned categories the both interactions are competing for the resulted damping factor. While in the highly doped samples constant values are measured for damping factor in low temperatures, for the samples with lower g-factors the samples present anisotropic relaxation factors.

### 6.4.4 Damping factor as a function of hole concentration

Damping factor is measured as a function of the hole concentration to investigate the effect of this important parameter on the relaxation process of magnetization. Moreover as the proposed application of the hydrogen passivation and the application of different hole concentrations to modify the magnetic properties in the spintronics devices depends strongly on the affect of these parameters on the dynamic of the magnetization, this study is of great importance. *A priori*the reduction of the charge carrier concentration, which are the main resposibles of the scattering processes (via spin-orbit interaction), should reduce the damping factor in the samples. Fig.6.26 presents the calculated isotropic damping factor for GaMnAs as a function of hole concentration for different Mn doping levels (x<0.1). As it is clearly shown the damping factor for all doping levels is predicted to increase as a function of hole concentration.

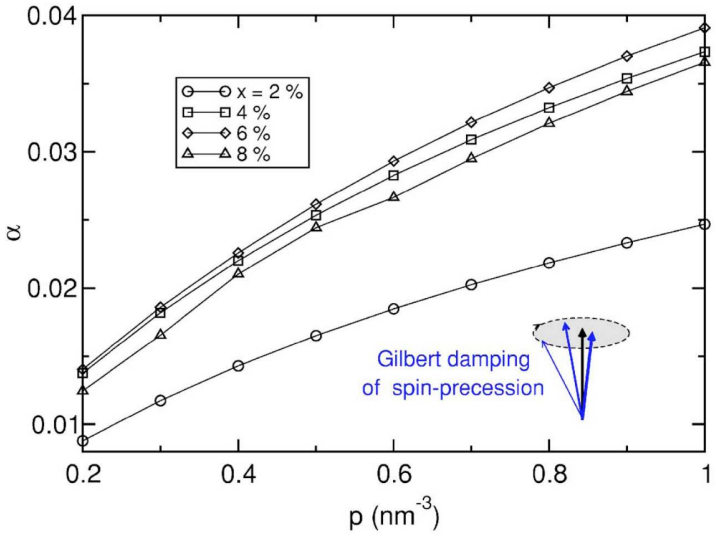


**Figure 6.26:** Calculated $\alpha$-damping factor as a function of hole concentration for GaMnAs layers containing different Mn densities. The calculations are made by comparing the linear response of a magnetic system to weak transverse fields in terms of the phenomenological constants of micromagnetic theory and the dissipative part of the quantum-mechanical susceptibility. [25]

This investigation have performed on the hydrogen passivated series whose magnetic properties are studied in detail in chapter 4. The same procedure as the previous section is applied (comparison of the measurements by two X and Q-band microwave frequency). Here we limit our self only to the final results. The case of sample.B did not studied in this section via FMR because of the very large linewidths that this sample presents even in X-band measurements and prevent us to obtain reliable values.

In FMR measurements performed via Q-band MW frequency, the samples present the same comportment as the two previous studied samples (The resonance fields shift to higher values and their respective distance is respected). The very particular case of course is the sample.R (reference sample). As was mentioned in fig.4.16, this sample presents some inhomogeneity attributed satellite resonances in its spectrum for applied field along its hard axis. These satellites are superposed on the main uniform mode for higher temperatures and constitute a single spectrum. The case was decomposed into 6 Lorentzian-form components (cf. fig.4.16). In measurements performed via 35GHz microwave frequency however, the case is completely different. As It is shown in fig.6.27, the FMR spectrum for applied field along [001] direction of this sample is composed of two spectra with comparable intensities.

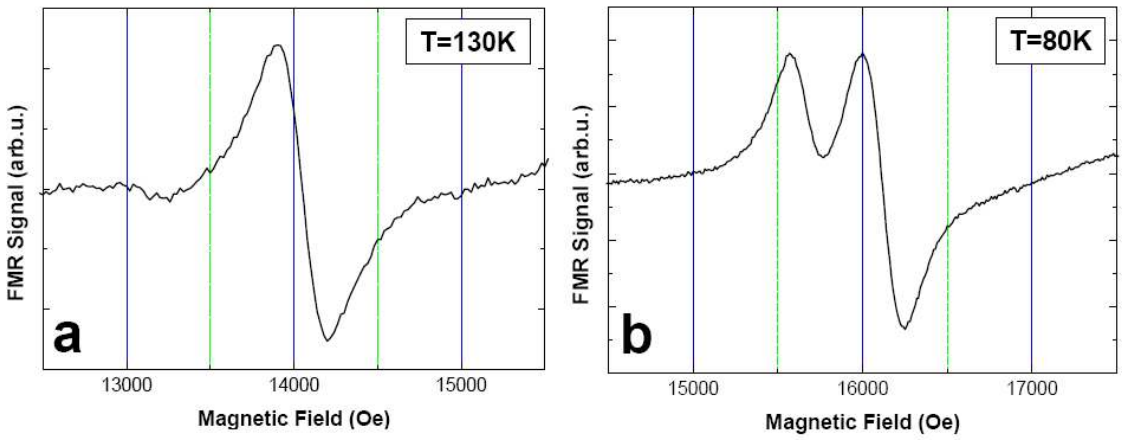


**Figure 6.27:** FMR spectra of sample.R for applied field parallel to hard [001] axis for (a) T=130K and (b) T=80K

As it is presented as a function of temperature and also as the field is rotated toward in-plane directions (not shown here) these spectra are superposed. The angular and temperature evolution of the spectra reveals that the origin of the second spectra is the same inhomogeneities in the sample as observed in X-band measurements. The increase in linewdth as a function of enhancement of microwave frequency superposes all those small spectra together to create this second high intensity spectrum observed in fig.6.27. Observing such behavior reveals that maybe the application of AC fields of lower frequencies be an appropriate technique to investigate the inhomogeneities in the ferromagnetic thin films, as their better separation due to the decrease in linewidth makes them more visible.

Considering the fact that these two spectra possess comparable intensities and in order to avoid the neglect of any important information because of a bad approximation we have treated the parameters measured for this sample twice; once for

each of the resonances.

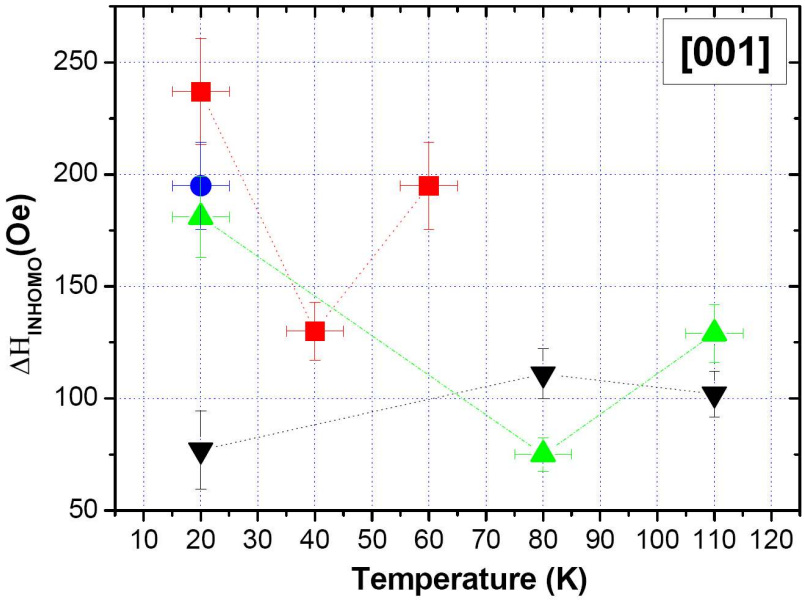


**Figure 6.28:** Inhomogeneity contribution part of the total FMR broadening measured along [001] axis for sample.C (squares) sample.D (circles) Sample.E (upward triangles) and sample.R (downward triangles)

Comparing the linewidths measured in the two frequencies conditions, one can distinguish the inhomogeneity part of the total linewidth for different hole (/hydrogen) concentration as is shown in fig.6.28 and 6.29.

In previous sections 6.4.2 and 6.4.3, we observed that the inhomogeneous linewidth is almost isotropic in each sample. In fig.6.28, it is shown that as a function of hydrogen concentration the inhomogeneity part of the linewidth of the spectra measured along [001] direction of the film increases progressively. This increase is even more distinguishable while comparing the reference sample (which was not exposed to hydrogen treatment) with other samples, indicating the immediate influence of the hydrogen diffusion to the GaMnAs matrix, which is more than a factor 2. While $\Delta H_{inh}$ along this axis pass through a minimum before increasing for temperatures near $T_C$ for the hydrogen passivated samples, it seems to be constant or slightly increased for the reference sample.

Along the [110] in-plane direction the average increase in inhomogeneity linewidth is observed once more. However in this direction while the inhomogeneity of sample.C remain constant as a function of temperature, for the reference sample it decreases slightly.

In fig.6.30 the related damping factor as a function of the hole concentration, measured along two axes of the samples is shown. In both axes the damping factor

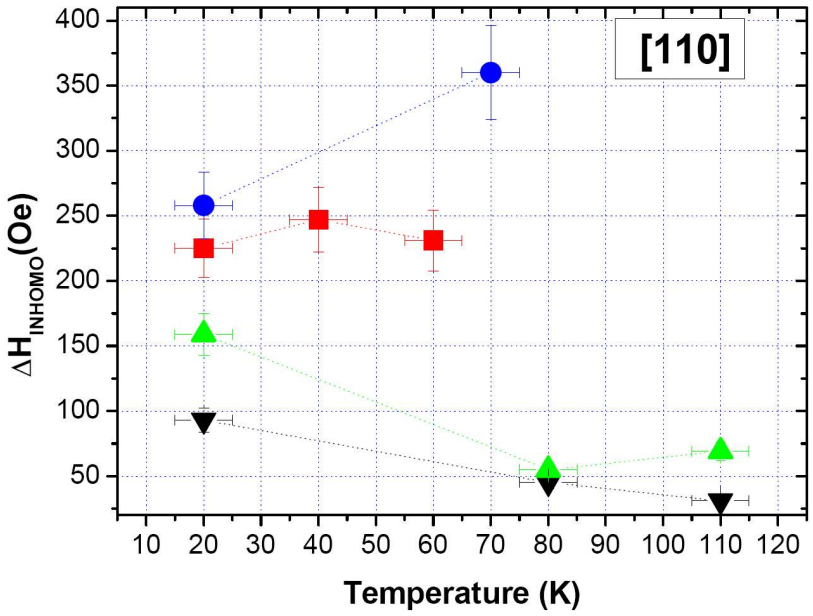


**Figure 6.29:** Inhomogeneity contribution part of the total FMR broadening measured along [110] axis for sample.C (squares) sample.D (circles) Sample.E (upward triangles) and sample.R (downward triangles)

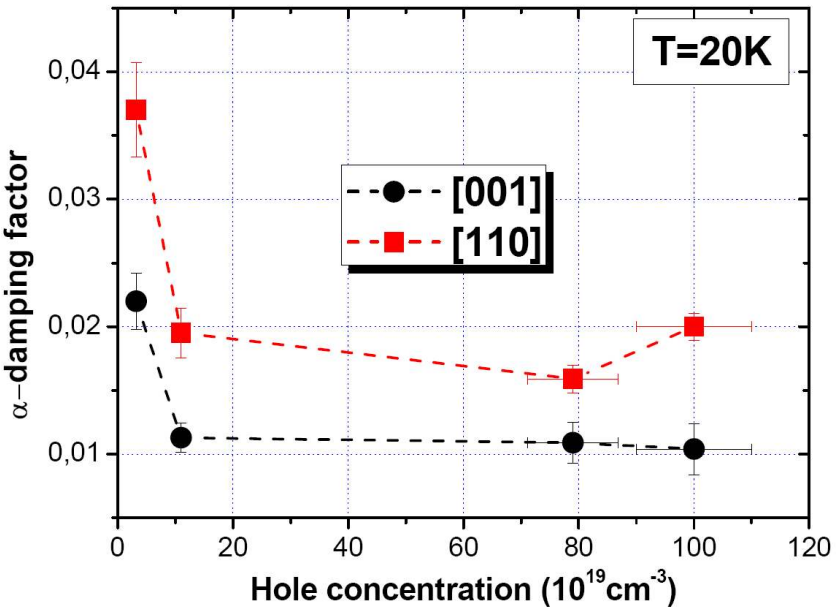


**Figure 6.30:** $\alpha$-damping factor as a function of hole concentration along [001] (circles) and [110] (squares) at T=20K

tends to decrease as the hole concentration is increased; as the hole concentration varies by a factor 30 from sample.C to the reference sample, the damping factor decreases by a factor 2. The feature is observable for both [001] and in-plane axes. At first sight this might seems contradictory what we were expecting (fig.6.26) and to the origins of damping.

In section 4.10, we presented the measured effective g-factor for all the samples in this series. There we mentioned how from these values and the two other parameters provided through mean field calculation for these samples, we estimated a gradual diminution of the hole polarization from ≈80% for sample.B to 20% for sample.R. This decrease of the polarization directly affect the coupling between the holes and the manganese magnetic moments and the dampin factor [25]. It worth noting how the curves due to g-factor measurements look similar to these curves. The values for each sample in two direction decreases as the carrier density enhances, resembeling to the same fact which was discussed in previous section 6.4.3, that while the polarization tends to reduce, $\alpha$ is found isotrope in GaMnAs systems. The other particular situation is the reversed order of the axes from the relaxation point of view. In two other series (sections 6.4.1 and 6.4.3) the higher value of damping factor was measured along the [001] hard axis, whereas in this series the higher damping is related to the [110] direction. This feature is more consistent with the reports on anisotropic damping factor in metallic samples [33, 34]. Farle have explained this situtation simply by asumming that while the applied field is along an easy axis the magnetization should precess and move through the hard axis (normal to former) which is more visquese and provide more relaxation conditions, therefor result in a higher damping factor along this axis.

The g-factor was found to get saturated at g=1.9 for this series, after that for two other series with higher expected hole concentrations this value again tends to increase toward g=2.00, section 4.10 and 5.5. The source of cross over for this reversal then very probably lies whithin this regime variation.

As as function of temperature along [001] direction the samples present a gilbert factor which increases softly before it decreases for temperatures close to T=$T_C$ (fig.6.31). Its variation as a function of temperature is more important for the sample with lower hole concentration. Note again that this behavior is a one of the two typical ones which has been detected for damping along high symmetry axes in these three series. The other typical behavior is found for [110] axis of reference sample, where the damping continues to increase for temperatures close to $T_C$ with a larger gradient (fig.6.32). As for the two previous cases, this is attributed to the competition between the inter and intra band contributions to the total damping which we expect to be anisotropic.

Note that as a function of temperature the difference between the measured $\alpha$ along two axes reduces considerably for sample.C where as in sample.E it is less clear.

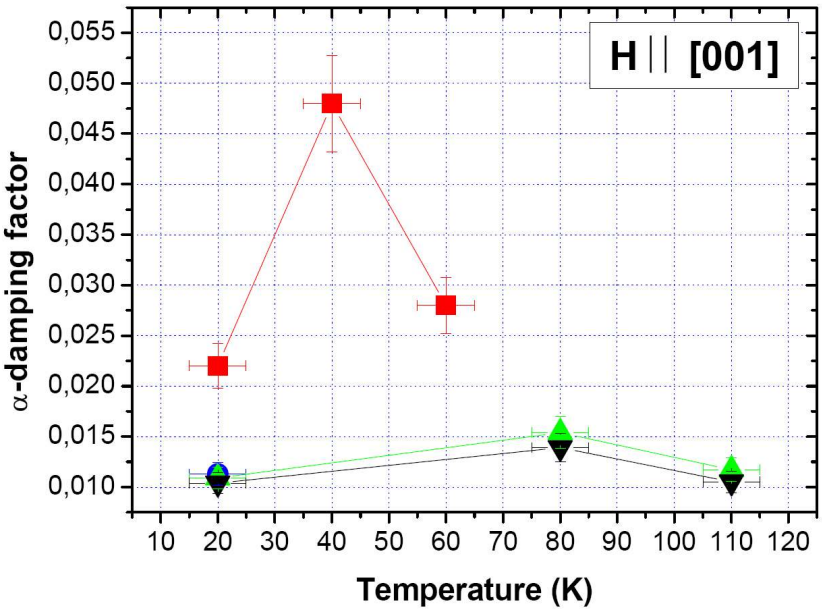


**Figure 6.31:** $\alpha$-damping factor as a function of temperature along [001] axis for sample.C (squares) sample.D (circles) Sample.E (upward triangles) and sample.R (downward triangles)

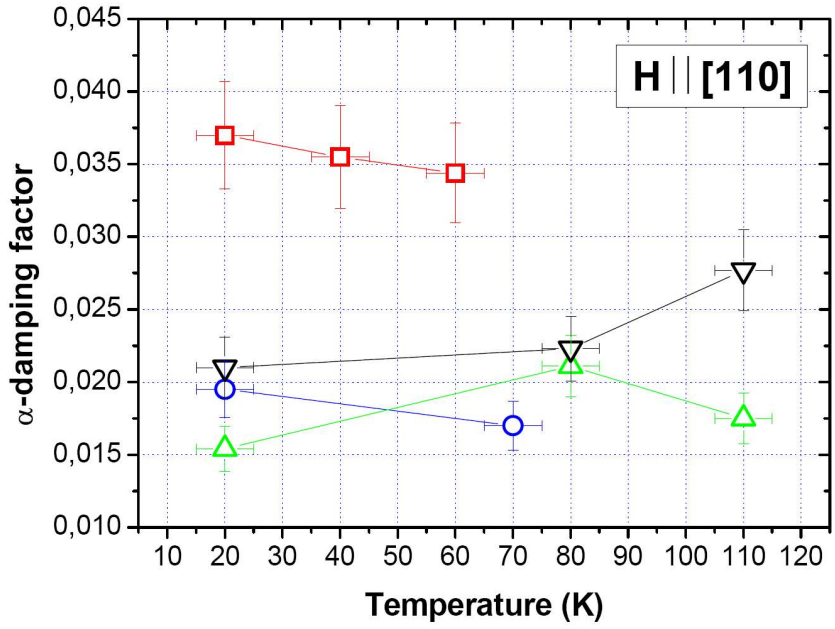


**Figure 6.32:** $\alpha$-damping factor as a function of temperature along [110] axis for sample.C (squares) sample.D (circles) Sample.E (upward triangles) and sample.R (downward triangles)

## *6.5 Conclusion*

As a brief conclusion, in this chapter the we studied the parameters leading to broadening the FMR linewidth were studied. The two inhomogeneity contribution and damping parts of the linewidth were distinguished and separated.

relaxation mechanisms of magnetization and the relevant damping factor were determined for a sample with the highest Curie temperature, together with the effect of hole and Mn concentrations on this parameter and as a function of temperature. The conditions of experiments were adjusted so that to reduce as much as possible the effect of extrinsic relaxation mechanisms.

As a general result we observed that the Gilbert damping factor present an anisotropic character, not only by its value, but also from its evolution as a function of temperature. Also we found that for our samples the damping factor is considerably lower than the theoretical calculations (by factor 10 along easy axis of the reference sample at T=20K).

The strain did not led to a significant modification of the damping factor. However the sample under tensile strain presents much higher inhomogeneity broadening. While the effect of increasing Mn impurities which leads to higher damping factors, coherent with the theoretical predictions, the decreasing of damping factor with hole concentration is in contradiction with them. Moreover, while in intermediate hole concentrations the easy axis present damping factor higher than the hard axis (consistent with the case of standard metallic samples) In higher hole concentration the case is inversed.

While in all theoretical models the exchange interaction is considered isotropic and the calculation are based on this assumption, our results clearly show an anisotropy of the damping factor. The anisotropy of the valence band in GaMnAs has a crucial influence on the magnetic properties of this material and one of the consequences this anisotropy is definitely an anisotropic exchange interaction.

We have attributed this anisotropy to the competition between the inter and intra band spin-orbit interaction contributions to the total damping factor. The low damping factor was explained qualitatively by using the results on the polarization of the holes and the lower Mn-Mn exchange integrals.

Finally, we comment that while the two-magnon scattering effect depends on the spin-wave dispersion relation and as it was mentioned in chapter 3, it's case must be different to the standard case of metallic systems and needs further theoretical calculation. However our results show that (by comparing the in-plane and out-of-plane linewidths) this contribution must be weak for the standard GaMnAs/GaAs layers.

# Bibliography


[1] "Magnetic monolayers on semiconducting substrates: an in situ FMR study of Fe-based heterostructures" kh. Zakeri, PhD thesis, Universitat Duisburg-Essen (2007).

[2] F. Bloch, Phys. Rev. 70, 460 (1946)

[3] N. Bloembergen, Phys. Rev. 78, 572 (1950).

[4] B. Heinrich and J. A. C. Bland, Ultrathin Magnetic Structures II-III, Springer, Heidelberg (1994).

[5] B. Heinrich, D. Fraitova and V. Kambersky, Phys. Stat. Sol. (a) 23, 501 (1967).

[6] R. J. Elliot, Phys. Rev. 96, 266 (1954).

[7] L. Piraux, S. Dubois, A. Fert, and L. Belliard, Euro. Phys. J. B 4, 413 (1998).

[8] S. D. Steenwyk, S. Y. Hsu, R. Loloee, J. Bass and W. P. Pratt, J. Magn. Magn. Mater. 170, L1 (1997).

[9] S. Dubois, L. Piraux, J. M. George, K. Ounadjela, J. L. Duvail and A. Fert, Phys. Rev. B 60, 477 (1999).

[10] R. Kobu, M. Toda and N. Hashitsume, Statistical Physics II Nonequilibrium Statistical Mechanics, Springer, Heidelberg (1992).

[11] V. Kambersky, Can. J. Phys. 48, 2906 (1970).

[12] V. Kambersky, Czech. J. Phys B 26, 1366 (1976).

[13] M. E. Schlomann, J. Phys. Chem. Solids 6, 242 (1958).

[14] M. Sparks, R. Louden and C. Kittel, Phys. Rev. 122, 791 (1961).

[15] C. E. Patton, C. H. Wilts, and F. B. Humphrey, J. Appl. Phys. 38, 1358 (1967).

[16] Kh. Zakeri, J. Lindner, I. Barsukov et al., Phys. Rev. B 76, 104416 (2007).

[17] M. J. Hurben and C. E. Patton, J. Appl. Phys. 83, 4344 (1998).

[18] R. Arias and D. L. Mills, Phys. Rev. B 60, 7395 (1999).

[19] R. Arias and D. L. Mills, J. Appl. Phys. 87, 5455 (2000).

[20] R. D. McMichael, M. D. Stiles, P. J. Chen, and W. F. Egelhoff, J. Appl. Phys. 83, 7037 (1998).

[21] R. P. Erickson and D. L. Mills, Phys. Rev. B 46, 861 (1992).

[22] D. L. Mills and R. Arias, Physica B 384, 147 (2006).

[23] C. Chappert,K. LeDang,P. Beauvilain,H. Hurdequint and D. Renard, Phys. Rev. B 34, 3192 (1986).

[24] M. Farle, Rep. Prog. Phys. 61, 755 (1998).

[25] J. Sinova, T. Jungwirth, X. Liu, Y. Sasaki, J. K. Furdyna, W. A. Atkinson and A. H. MacDonald, Phys. Rev. B 69, 085209 (2004).

[26] T. Y. Tserkovnyak, G. A. Fiete, B. I. Halperin, Appl. Phys. Lett. 84, 5234 (2004).

[27] Kh. Khazen, H. J. von Bardeleben, and J. L. Cantin et al., Phys. Rev. B 77, 165204 (2008).

[28] Y. H. Matsuda, A. Oiwa, K. Tanaka and H. Munekata, Physica B 376-377, 668 (2006).

[29] L. Thevenard, L. Largeau, O. Mauguin et al. Phys. Rev. B 73, 195331 (2006).

[30] A. Mauger, D. L. Mills, Phys. Rev. B 29, 3815 (1984).

[31] S. C. Chen and H. L. Huang, IEEE Transactions on Magnetics 33, 3978 (1997).

[32] H. L. Huang, V. L. Sobolev, and S. C. Chen, J. Appl. Phys. 81, 4066 (1997).

[33] Z. Celinski and B. Heinrich, J. Appl. Phys. 70 5935 (1991).

[34] F. Schreiber ,J. Pflaum ,Z. Frait et al. Solid State Commun. 93 965-8 (1995).

[35] "Damping and magnetic anisotropy of ferromagnetic GaMnAs thin films" Kh. Khazen, H. J. von Bardeleben, and J. L. Cantin et al. submitted to Phys. Rev. B.

# 7

# Conclusion

This thesis presents a study of the static and dynamic magnetic properties of GaMnAs thin layers as a function of three important parameters:

- the strain in the film, induced by the lattice mismatch with the substrate
- the hole concentration
- the Mn concentration

These layers were investigated by X-band and Q-band FMR spectroscopy our principal technique as well as in special cases by complementary techniques: SQUID magnetometry, Rutherford back scattering (c-RBS), PIXE, XPS, magneto-optical Kerr effect microscopy and ERDA.

The samples were obtained in collaboration from different laboratories in France, Czech Republic and Japan. Most of these samples had been characterized by X-ray diffraction and transport measurements in the laboratories were they were grown.

The main results obtained can be summarized as follows

- The effect of strain :

We have studied in great detail the magnetic anisotropies of typically 50nm thick GaMnAs layers with comparable but opposite compressive or tensile stress induced by the substrate (GaAs/GaInAs). The easy and hard axes of magnetization have been determined at T=4K and as a function of temperature between 4K and the Curie temperature. From the angular variation of the uniform mode resonances the magnetocrystalline anisotropy constants have been determined as well as their variation with temperature. Whereas we were able to evidence differences in the magnetocrystalline anisotropy and easy magnetization axes direction, our results show that the intrinsic magnetic parameters of the films such as the g-factor, the Curie temperature and the $J_{MnMn}$ exchange integral are very similar in the two cases. By choosing the substrate it is thus possible to modify and adjust the magnetic

anisotropies of the layer. The results are in good agreement with the predictions of Zener mean field theory. This functionality has no equivalence in metallic systems where the demagnetization fields are dominant for thin film geometries. Spin wave resonances were equally observed. Their study revealed a particular and complex dispersion relation of the magnons in this material. The spinwave observed in the in-plane geometry can not be described by the inhomogeneity models usually applied for conventional out-of-plane modes. However, they fit well with the classical model of surface pinned modes proposed by Kittel. From these measurements we determined the stiffness factor and the J Mn-Mn exchange integral. The results agreed with those obtained from magneto-optical Kerr effect microscopy measurements. The value of J is at least 5 times lower than the predicted and measured values for the as-grown samples with lower Mn concentrations. We have attributed this difference to the lower level of polarization for samples with higher Mn and hole concentrations. Finally, we would like to note that the DMS character of the layers should modify the classical dispersion relation of the spinwaves which is based on the assumption of the periodic localization of the spins.

- The effect of the hole concentration :

The micromagnetic parameters of ferromagnetic 50nm thick strained $Ga_{0.93}Mn_{0.07}As$ films have been investigated as a function of the hole concentration which was modified by hydrogen passivation by three orders of magnitude. The variation of the basic parameters, i.e. the critical temperatures, easy axes of magnetization and the anisotropy constants have been determined. Their numerical values and their variation with the hole concentration and the temperature are in good agreement with the prediction of the kinetic Zener model for all the samples in the metallic and in the impurity band conduction regime. The FMR spectra broaden rapidly when the hole concentration is decreased; their anisotropic linewidth reflects the symmetry of the valence band structure.

By measuring the g-factor and using a phenomenological model based on the Zener kinetic exchange-type ferromagnetism, we have shown the gradual decrease of the free hole polarization level with the hole concentration. Direct measurements of the polarization in these samples are being performed at this moment (via Andreev reflection technique) to verify this issue which would explain the low Mn-Mn exchange integral and the alteration of ferromagnetic properties of highly doped samples.

The anisotropy constants and their evolution as a function of temperature were determined. This enabled us to test the validity of results obtained in the frame of the mean-field theory which relate the anisotropy constants to their microscopic origins.

For the fully passivated paramagnetic sample we have determined the value of the superexchange integral of nearest neighbour Mn-Mn ions. We find a weak anti-

ferromagnetic interaction with a value of -5K.

- The effect of Mn concentration :

We have shown that GaMnAs layers grown with very high Mn concentrations do not show undesirable second phases such as MnAs clusters. Once again, the FMR technique allowed us to measure the magnetization of less than 20nm thick GaMnAs layers, not accessible to conventional SQUID measurements due to its insufficient sensitivity. Although the mean-field theory predicts higher Tc for such heavily doped layers, no increase of $T_C$ was observed. We have investigated the reason for this discrepancy and proposed a simple model of a linear increase of interstitial Mn ions with the total doping level which would lead to high compensation of the substitutional, magnetically active, Mn ions. By introducing an effective Mn concentration, we concluded that our results are still consistent with the mean-field theory predictions. The results suggest that more sophisticated annealing procedures such as multiple annealing, would be more efficient for interstitial Mn out diffusion and should lead to the expected higher Curie temperature.

- Damping factor :

We have studied the magnetization relaxation via the brodening of the uniform mode FMR linewidth.

The Gilbert damping factor and inhomogenous linewidth were determined for various types of samples. In particular we have investigated the effect of the hole and Mn concentrations on the damping factor. Our results show a minimum daming factor of 0.003. Angular variation measurements show further that the Gilbert damping factor is anisotropic and varies with the temperature. The values obtained are considerably lower than the theoretical ones (by a factor of 10 along easy axis at T=20K).

The strain did not lead to a significant modification of the damping factor. However the sample under tensile strain presents a much higher inhomogeneous brodenning. Increasing the Mn concentration leads to higher damping factors, in agreement with theoretical predictions. But the observed decrease of the damping factor value with the hole concentration is in contradiction with them. Moreover, while for intermediate hole concentrations the easy axis present damping factor higher than the hard axis (as in the case of metallic samples for ex.), for higher hole concentration, the opposite is observed.

In the mean field theory models the exchange interaction is considered to be isotropic. We do believe that this approximation has eliminated some important aspects. The anisotropy of the valence band in GaMnAs has a crucial influence on the magnetic properties and should lead to an anisotropic exchange interaction.

We have observed that the damping factor is anisotropic for samples with high hole polarization and nearly isotropic for lower polarization We have attributed this anisotropy to the competition between the inter and intra band spin-orbit interaction contributions to the total damping factor. The low damping factor was explained qualitatively by using the results on the polarization of the holes and the lower Mn-Mn exchange integrals.

### *7.1 Perspectives*

We have studied GaMnAs single layers as a function of several parameters, which provided us which numerous information about the correlation between structural, electrical and magnetic properties of these systems. Spintronic devices based on GaMnAs such as spin valves require the growth of multilayer structures which might also easily be studied by FMR spectroscopy. One of the powerful aspects of FMR is its capability to evidence the interlayer exchange interactions which should be studied for the basic trilayer structure GaMnAs/GaAs/GaMnAs. Other interesting extensions of this study are the investigation of different III-V alloy systems and patterned structures such as wires.

# Conferences

- Organizer of monthly de spintronics/magnetism
- **2008 Nanomagnetism and spintronics summer school** (Prague- Czech republic ) Poster
- **2008 ELECTRONIC MATERIALS CONFERENCE** (Santa Barbara, US) Oral presentation
- **INTERMAG 2008 CONFERENCE** (Madrid-Spain) Posters
- **Forth international school and conference on Spintronics and quantum information technology** (Hawaii-USA) Poster
- **Journée Scientifique C'nano IdF - axe Electronique de Spin** Poster
- **10th Joint MMM/INTERMAG conference (Baltimore-USA)** Articles+ Poster
- **28th International conference of Physics of Semiconductors** (Vienna-Austria) Article+ Poster
- **GDR-SESMA conference of Magnetism and Semiconductors Associated Spin** (THALES-Paris) Poster
- **Dumont D'Urville workshop** (Marseille - France) Oral presentation
- **Spintronics summer-school** (Montpelier-France) Poster
- *Invited speaker* to "**Second Conference and Workshop on Nanoelectronics**" Tehran-IRAN

# Publications

- *"Ferromagnetic resonance study of GdN thin films with bulk like and extended lattice constants"*, Kh.Khazen, H.J. vonBardeleben, J.L. Catin, A. Bittar et al. ***Phys. Rev. B.*** 74 245330 (2006)

- *"Dependence of magnetic anisotropies and critical temperature on the hole concentration in ferromagnetic GaMnAs thin films"*, Kh. Khazen, H.J. von-Bardeleben, J.L. Cantin, L. Thevenard et al., ***IEEE. Trans. Mag.*** 43 (2007)

- *"Evolution of the Magnetic Anisotropy with carrier density in Hydrogenated (Ga,Mn)As"*, L.Thevenard, Kh.Khazen et al. ***Phys. Rev. B'*** 75, 195218 (2007)

- *"Expansion and collapse of domains with reveres magnetization in GaMnAs epilayers with perpendicular magnetic easy axis"*, A. Dourlat, V. Judi, C. Gourdon, Kh. Khazen, H.J. vonBardeleben et al. ***IEEE Trans. Mag.*** 43, 3022 (2007)

- *"Tunning the hole density of GaMnAs by hydrogenation"*, A. Lemaitre, Kh. Khazen et al. ***Proceedings of 28th international conference on the Physics of Semiconductors*** (2006)

- *"Domain structure and magnetic anisotropy fluctuations in (Ga,Mn)As: Effect of annealing"*, A. Dourlat, C. Gourdon, Kh. Khazen et al., ***J. Appl. Phys.*** 102, 023913 (2007)

- *"Determination of the micromagnetic parameter in (Ga,Mn)As using domain theory"*, C. Gourdon, V. Jeudi, Kh.Khazen et al. ***Phys. Rev. B*** 76, 241301(R) (2007)

- *"Experimental determination of domain wall width and spin stiffness constant in ferromagnetic (Ga,Mn)As with perpendicular easy axis"*, A. Dourlat, V. Judi, C. Gourdon, Kh. Khazen, H.J. vonBardeleben et al., ***Physica E*** 40, 1848 (2008)

- *"Ferromagnetic resonance of GaMnAs thin films with constant Mn and variable free-hole concentrations"*, Kh.Khazen, H.J.vonbardeleben et al. ***Phys.Rev. B***, 77, 165204 (2008) **(EDITORS' SUGGESTION)**

- *"Damping and magnetic anisotropy of ferromagnetic GaMnAs thin films"*, Kh.Khazen, H.J.vonBardeleben et al. submitted to ***Phys. Rev. B.*** arXiv:0809.4644

# Acknowledgments

Before any statement I should thank ***God*** for everything I have, for every opportunity I have come across during my life, for everything I am and for each moment I have lived is a gift from him. Most of all I want to thank him for giving me the chance to meet all the following persons and be grateful to them.

I would like thank my first teachers, my beloved parents ***Hossein Khazen*** and ***Fereshteh Shams***. The ones who dedicated their youth and spend all their energy for raising me. I want to thank them for all their compassionate efforts, worries, cares, encouraging and guiding. For all the nights they spent near my bed when I was ill and for all the credits they gave me for my successes. For every time they picked me up from school and for the famous shiny red apples I would find in my bag. For their all-aspects supports which helped me to live in France and fulfill the first level of my scientific life. For the incredibly generous patience they had during all these years. And above all, my dear angels thank you for teaching me how to look, how to think and how to live.

I would like to extend my sincere gratitude to all members of my dissertation committee which honored me by their presence and contribution to the defense event:

- My referees:

***Prof. Bret Heinrich***, from "*Simon Fraser university*" of Canada, for all helpful discussions, comments and guidelines he provided us with. Dear Bret, thanks for having recieved us warmly and shared your time and long precious experiences with us.

***Prof. Tomas Jungwirth*** from "*Nottingham university*" of United kingdom and the "*Academy of Science*" of Prague. I know that Tomas is always too busy because of his world wide and numerous collaborations, but still too kind and generous to spend a part of his time on this thesis. Specially his vast knowledge on magnetic semiconductors has provided me with a wide perspective to the field.

- And my examiners:

***Prof. Claude Chappert***, the director of "*Insitut d'Electronique Fondamentale*" in Orsay, who despite of his very heavily charged schedule accepted our invitation. His very large experience on the applied spintronics and his previous contribution to the FMR spectroscopy field allowed us to benefit from his helpful comments.

***Prof. François Gendron***, the director of the "UFR de Physique" in "*Pierre and Marie Cuire university*" of Paris, who was the president of the committee.

***Dr. Alain Mauger***, the director of research in "*Institut de Minéralogie et de Physique des Milieux Condensés*". His large contribution to magnetic semiconductors from his PhD in 1980 until now, in addition to his friendly and kind character was two major reason why I could knock on his door at any time of the day and benefit from his original ideas and comments on the subject.

And most of all I should address my deepest, warmest and most special acknowledgments to **Dr. Hans Jurgen vonBardeleben**, My supervisor. His large contribution to FMR and EPR spectroscopy fields specially on semiconducting systems was a precious luxury from which I benefited a lot. In addition his outstanding character of being precise, punctual and very social not only have made his group a remarkably well-known group in this field but also was a great pattern for me. It was his own credits and his confidence in me which encouraged me to further delve into international collaborations. However, when my words comes to Jurgen it is hard to be cruelly formal. Dear Jurgen, I want to thank you not only because you were a wondrous mentor and supervisor one can ever have, not only because you learned me how to look, how to think, how to act and how to express myself as a scientist, not only for giving me so much credits as I entered your laboratory and having so much confidence in me and not only because you were always there for hundreds of my questions... but also for being my *best* friend, I want to specially thank you for that box of "bonbon".

It was a great honor for me to have the scientists, whose works have always been the reference of my (and many others) researches, as the referees of my thesis; and I do appreciate your participation in one the most important days of my professional life.

I must also acknowledge:

***Prof. Anne-Marie Cazabat*** for accepting me in her doctoral school: " *Physique de la particule au solide : modËles et expériences* and her in-time supports; also for her kind receives each time I was in her office.

***Prof. Claudine Noguera*** for receiving me in her laboratory: "*Insitut des NanoSciences de Paris (INSP)*" and her kind replies and feedbacks to my emails.

***Dr. Jean Louis Cantin***, my second supervisor, an outstanding colleague and moreover my dear friend during these three years. Thank you dear Jean-Louis for all our friendship, for the unforgettable moments we had together in the lab and in missions, for helping me through my apply for the ATER position and for all learned from you. Thank you and sorry for all the time you passed on editing my thesis and

you could have profited from the swimming pool and for listening to my warm-up presentations despite all the tiredness you felt after you classes. And thanks for ordering me a cheese cake while I was dying to have one of those chocolate towers.

I should thank all the members of our research axis: "*Couches nanométriques : formation, interfaces et défauts (CONFID)* " in INSP, for receiving me warmly between them and having helped me in many affairs, specially ***Dr. Ian Vickridge***, the director of this axis for supporting me in different occasions and helped me through the RBS and PIXE measurements. Indeed, none of my many international collaborations could be fulfilled without his kind attentions and supports; Also my dear colleague ***Murat Cubukcu*** who is, for the moment, continuing this project. I wish him an excellent thesis.

Although officially a thesis is attributed to one person, everyone knows that fulfilling such a heavy work in less than three years is not possible without the help, supports and collaborations of many people, to whom I am infinitely grateful:

***Dr. Laura Thevenard*** and ***Dr. Aristide Lemaitre*** and all dear colleagues from "*Laboratoire de Photonique et de Nanostructures*" in Marcoussis for supporting us with many of GaMnAs samples and transport measurements. Dear Laura, I wish you to shine during your postdoc period as you did during your thesis and hope to see your further successes anywhere you work as the permanent researcher. Dear Aristide, thank you for all helpful discussions we had, for all the remarkable samples you provided us with and for being open to all our requests upon the samples and experiments. Also thank you for all the good memories of Hawaii which was formed upon your presence and management.

***Dr. Catherine Gourdon*** and ***Prof. Vincent Jeudi*** and ***Alexandre Dourlat*** for the wall-domain studies and the Kerr effect measurements on the GaMnAs samples. I would like to thank Cathrine also for accepting Sanaz as her future PhD student which allowed us to work near each other and made this subject as our family affair. Dear Alexandre, I wish you a glorious thesis defense, the one that you deserve and hope to see you in higher scientific levels in near future.

***Dr. Vit Novak*** and his research team in "Academy of Sciences" in Prague-Czech republic, for having confidence in me from the first days I started my scientific career and sharing his very high quality GaMnAs samples with me which was the reference sample for all my measurements.

***Dr. Yasushi Hoshino*** from "*Kanagawa University*" of Japan, who has helped us through RBS measurements and analysis.

***Dr. Javier Garcia Lopez*** from "*National Accelerator Center*" of Sevilla-Spain, for the RBS and PIXE measurements. Dear Javier thank you for your warm hospitality in Sevilla and for the very nice moments I had there. I hope that this friendship and collaboration continues for the many coming years.

***Prof. Tanaka*** and D***r. Shinobu Ohya*** from "*Tokyo University*" of Japan for providing us with the first homogeneous series of heavily doped samples grown in

the world.

***Prof. Nitin Samarth*** from "*Pennsylvania State University*" of US. Dear Nitin thank you for your interest and confidence and sharing your GaMnAs/MnAs samples and results with us and also for the very interesting and helpful discussions, comments you provided me with in Spintech and in Santa-Barbara. I hope that our friendship and collaboration continues in the coming years.

***Prof. Tomasz Dietl*** for "*Polish Academy of Sciences*" of Poland, first of all for all his excellent lectures and presentations I have attended and also for his collaboration for the calculation of the effective g-factor in hydrogen passivated series, which was performed in collaboration with his colleague ***Dr. Cezary Sliwa***. I am also very grateful to the very interesting discussions we had and to his remarkable character of being open to discussions and questions.

***Dr. Jean-Marie George***, the Director of research in "*Thales-CNRS mixed research laboratory*" and his previous PhD student ***Dr. Marc Elsen*** for the TMR and SQUID measurements on GaMnAs trilayers.

***Prof. Joe Trodahl***, *Dr. Ben Ruck*, ***Dr. Simon Granville*** and ***Dr. Tony Bittar*** from "*Victoria university*" of New Zealand, for the GdN samples and the DUDU workshop which was organized by their efforts in Marseille.

***Dr. Monge*** for helping me with the Mathlab programming for energy surfaces of GaMnAs.

Moreover A very special thanks goes out to all the great researchers and scientist I had the honor to discuss with them and beneficiate from their knowledge and large experiences such as:

***Prof. Hideo Ohno***, from "*Tohoku university*" of Japan, also for his comments, guidelines and his interest in our publications.

***Prof. David Awschalom*** and also ***Dr. Roberto Myers*** from "*University of California Santa-Barbara*" for their warm hospitality and discussions during our visit to their laboratory.

***Prof. Stephan vonMolnar*** from "*Florida State University*".

***Prof. Ali Yazdani*** from "*Princeton University* ".

***Prof. Michel Farle*** "***Duisburg-Essen university***" of Germany., for dedicating a considerable part of his time during the Intermag 2008 conference to discuss with me and for his patience in helping me through different interpretations of my results.

***Dr. Jorg Wunderlich*** from "*Cambridge university*", ***Prof. Albert Fert*** from "*Thales-CNRS mixed research unit*", ***Prof. Bernard Clerjaud***, ***Dr. Massimiliano Marangolo*** And many others whose names have certainly missed in this limited text and asked them to accept my apologies.

Appreciation also goes out to:

**Prof. Annick Whuler** and P***rof. William Sacks*** for accepting my spouse Sanaz as the Master student, which provided us a perfect environment to continue

our research works. I can hardly name many other professors and directors who work and care more for their students than Annick and William, as I have seen their work closely and have felt the effect of their presence on the discipline and value of the SMNO master. Dear William maybe this is where I can also thank you for all your supports not only for Sanaz but also for me in getting the ATER position after my thesis.

I am deeply indebted to my dear friend ***Dr. Kamran Behnia*** from "*Laboratoire de la physique quantique*" in ESPCI, because of his confidence, all he has done in the frame of friendship and for all his kind supports without whom continuing this thesis would have been a very difficult affair.

***Prof. Andrea Guazzi*** from "*IMPMC*" laboratory of "*Pierre and Marie Curie*" university for accepting to be in charge of my thesis defense file and for his great help in facilitating the administrative procedures.

***Prof. Didier Gourier*** and ***Dr. Laurent Binet*** from "*Ecole Nationale superieur de Chimie de Paris (ENSCP)*" for accepting me in their laboratory for the period of my ATER position and giving me the opportunity to enlarge my experiences by collaborating with them and their dear colleagues.

And very special thanks to all my colleagues in INSP laboratory, my second family, for warmly receiving me as a member of their scientific family, for all the great memories the made for me there, for all their supports, cares and helps. I should individually thank: ***Dr. Bernard Croset*** for being great friend and for all his language lessons, remarks and very interesting discussions we had, ***Dr. Tristan Cren*** and D***r. Geoffroy Prévot*** specially for helping us to invite Bret Heinrich to Paris. ***Dr. Dimitri Roditchev*** for helping us in repairing our cryostat because of his skills and large experience in working with devices at liquid helium temperature. ***Dr. Yves Borensztein*** for his excellent organizations of PhD student affairs and seminars. ***Dr. David Martina*** for helping my through various problems specially adapting myself with LATEX and French slangs and of course thank you for that "carte de sejour". ***Dr. Lionel Bureau*** for letting me use his PhD LATEX package. ***Vincent Dubost***, ***Dr. François Debontridder***, ***Francis Breton*** and all the people I used to meet and discuss during the coffee breaks for making the atmosphere more delightful by their jokes, talks and guides. ***Dr. Bernard Pajot*** for sharing his CDs and utility programs with me. ***François Rey*** and ***Corrine Poisson*** in "*Service informatique*" for their excellent network organization. ***Elisabeth Martin***, ***Christelle Caron***, ***Natalia Bonnet***, ***Lucdivine Collin***, ***Catherine Dematteis*** and ***Valerie Guezo*** who has helped me a lot in administration affairs and not to forget the people in mechanics workshop who provided us with the tools.

I also thank France for being a great host for me during these years and of course the beautiful Paris which, by her fascinating beauty created delightful and romantic moments of walking in its streets and relaxing in its cafÈs after the work.

Here is a chance to thank all my friends who helped me with organizing the

ceremony after the defense specially: ***Reza***, ***Setayesh***, ***Shahram***, ***Banafsheh***, ***Yassaman*** and ***Sholeh***.

I also want to thank a special person my beloved sister ***Roxana*** whose presence in my life has always been a spiritual support and many times discussions with her has opened new points of view to me. I wish you glorious days specially in your researches as I believe that you are the one who deserve to be on the top. Neither I would forget "aghaye poopeye aziz".

And the Last but not at all the least, is my dear spouse ***Sanaz Haghgou***. My dear Sanaz, I thank you for all the courage and self confidence you invoked in me. I thank you for giving me the reason to try harder and for all the wonderful moments you created for me with your presence. I am thankful for all you did when I was ill. I am deeply sorry and grateful for the moments you spent alone while I was working in the lab, for tolerating an unbearable PhD student writing his thesis, for managing the home all alone despite you were passing a hard time with your master courses and for all the nights I came home you were awake waiting for me despite your tiredness. I thank you for all the love you take into my life which was the source of my energy for fulfilling this thesis. I wish you the most glorious thesis one would have and hope one day I can do the same you did for me.

**11 July 2008, Amphitheater of INSP**
**Khashayar Khazen's thesis defense**
From right to left: Tomas Jungwirth, Alain Mauger, Bret Heinrich, Claude Chappert, Jurgen von Bardeleben and Khashayar Khazen